Technische Universität Braunschweig

Christian Kuhlmann

Dual frequency Magnetic Particle Imaging Scanner

Hardware for mobilityMPI

Dissertation
Braunschweig 2018

Berichte aus dem **Institut für Elektrische Messtechnik und Grundlagen der Elektrotechnik** Band **59**

Hrsg. Prof. Dr. Meinhard Schilling

Dual frequency Magnetic Particle Imaging Scanner

Hardware for mobilityMPI

Von der Fakultät für Elektrotechnik, Informationstechnik, Physik
der Technischen Universität Carolo-Wilhelmina zu Braunschweig

zur Erlangung des Grades eines Doktors

der Ingenieurwissenschaften (Dr.-Ing.)

genehmigte Dissertation

von	Dipl.-Ing. Christian Kuhlmann
aus	Herford

eingereicht am	28.03.2018
mündliche Prüfung am	24.08.2018
1. Referent:	Prof. Dr. rer. nat. Meinhard Schilling
2. Referent:	Prof. Dr. rer. nat. Achim Enders
Druckjahr:	2018

Dissertation an der Technischen Universität Braunschweig,
Fakultät für Elektrotechnik, Informationstechnik, Physik

ISBN Printausgabe: 978-3-86387-937-2

Meinen Eltern Renate und Gerhard und meiner Schwester Heike von Herzen,
Dr. Krishnabhakdi und Herrn Brinkmann-Boyagian in tiefer Dankbarkeit,
Katharina in Liebe.

Kurzfassung

Magnetic Particle Imaging (MPI) ist eine neue tomographische Bildgebungsmethode, welche magnetische Nanopartikel als Marker (Tracer) nutzt und zahlreiche potentielle Anwendungsmöglichkeiten in der Medizin und medizinischen Forschung bietet. Es könnte dabei potentiell in der Lage sein, die bestehenden radiologischen Methoden der Einzelphotonen-Emissionscomputertomographie (SPECT) und der Positronen-Emissions-Tomographie (PET) zu ergänzen oder zu ersetzen. Durch seine vergleichbare Auflösung im Bereich weniger Millimeter und seine hohe zeitliche Auflösung mit mehreren Bildern pro Sekunde ist es für viele Anwendungen geeignet, welche hohen Kontrast ohne anatomisches Hintergrundsignal benötigen. Da MPI ohne ionisierende Strahlung arbeitet, bietet eine Substitution von radiologischen Untersuchungen Vorteile für Patient und medizinisches Personal.

Eine Herausforderung, abgesehen von der erforderlichen hohen Sensitivität um mit den bestehenden Verfahren konkurrieren zu können, ist die Entwicklung von Anwendungsmöglichkeiten, die über die Fähigkeiten der etablierten Methoden hinausgehen. Ein möglicher Vorteil von MPI ist das Vorhandensein der Nanopartikel, welche z.B. durch Funktionalisierung der Oberfläche so modifiziert werden können, dass sie kontrolliert mit ihrer Umgebung interagieren. Durch das Ausnutzen der Partikeldynamik können diese Interaktionen magnetisch mit MPI gemessen werden und es kann somit eine räumliche Darstellung des Partikelzustands gewonnen werden. Dies wiederum ermöglicht eine quantitative funktionale Bildgebung mit MPI.
Mehrere Punkte müssen dafür erfüllt sein: Zum einen werden geeignete biokompatible Nanopartikel als Tracer benötigt, welche die gewünschte Oberflächenfunktionalisierung besitzen und sich magnetisch für die Bildgebung mit MPI eignen. Das dynamische Verhalten dieser Partikel muss dabei z.B. über geeignete Modelle gut vorhersagbar sein, so dass sich zuverlässig Rückschlüsse auf die Umgebung aus dem magnetischen Signal gewinnen lassen. Des weiteren werden MPI Scanner benötigt, welche für die Bestimmung der Mobilitätsinformation aus dem Partikelsignal geeignet sind.

Die vorliegende Arbeit beschreibt die Entwicklung und Anwendung eines MPI Scanners, welcher speziell für die Demonstration und Erforschung der funktionalen Bildgebungsmöglichkeiten mit MPI unter Ausnutzung der Mobilitätsinformation der Partikel entworfen wurde. Dieses Konzept, welches als mobility MPI (mMPI) bezeich-

net wird, kann durch verschiedene Verfahren realisiert werden, welche gemeinsam haben, dass sie die *Brownsche* Relaxation der Partikel ausnutzen, um Informationen über den Partikelzustand zu gewinnen. Ein Verfahren ist dabei die Verwendung von zwei unterschiedlichen Anregungsfrequenzen, was die Separation der Partikeldynamik von der räumlichen Verteilung ermöglicht. Dadurch, dass die Partikelrelaxation stark frequenzabhängig ist und viele Partikel einen zusätzlichen Signalbeitrag durch die *Néelsche* Relaxation beinhalten, ist somit eine Trennung von räumlicher und funktionaler Information im Partikelsignal möglich. Da alle aktuellen MPI Scanner Sende- und Empfangsschaltungen besitzen, welche an die Anregungsfrequenz angepasst sind, erfordert das Mehrfrequenz mMPI Hardwareerweiterungen gegenüber konventionellen Scannern.

Ausgehend von einem Mehrfrequenz-Spektrometer (MPS) für magnetische Nanopartikel, welches später für Voruntersuchungen an verschiedenen Partikelsystemen genutzt wurde, beschreibt die vorliegende Arbeit detailliert das Design und die Konstruktion des mMPI Systems und seiner Komponenten. Mehrere nützliche Entwurfsverfahren, wie z.B. eine Methode zur präzisen Vorhersage der parasitären Effekte bei den verwendeten Anregungsspulen, wurden im Zuge des Design-Prozesses entwickelt. Außerdem erwähnenswert ist das Design der Sende- und Empfangsfilter, welche hohe Dämpfungswerte im Sperrbereich bei guter Linearität ermöglichen, was eine essentielle Voraussetzung für MPI Bildgebung ist. Die Entwicklung einer volldifferentiellen Empfangsspule ist ein weiterer interessanter Aspekt des mMPI Scanners. Alle Komponenten wurden ausgiebig charakterisiert und gegen die Anforderungen getestet.

Der neue Scanner wurde ausgehend von konventionellen ein- und zweidimensionalen MPI Bildern genutzt, um die Eignung von MPI für die räumlich aufgelöste funktionale Bildgebung mittels Partikeldynamik zu untersuchen. Proben mit verschiedenen Viskositäten wurden verwendet, um den Effekt verschiedener Bindungszustände nachzubilden.

Abstract

Magnetic Particle Imaging (MPI), being a new tomographic imaging modality based on magnetic nanoparticle tracers, offers potential applications in medicine and medical research that may complement or even replace current radiological methods such as single-photon emission computed tomography (SPECT) and positron emission tomographie (PET). Offering similar spatial resolution in the millimeter range and high temporal resolution with several images per second, it is well suited to be useful for many applications that require high contrast with no interfering anatomical background signal. Since MPI doesn't rely on ionizing radiation, substitution of radiological methods benefits the safety of patients and medical staff.
One of the challenges, besides delivering high sensitivity that can compete with these existing methods, is to provide capabilities that surpass what is currently possible with tracer based imaging systems. A possible advantage of the MPI method is the presence of nanoparticle tracers that can be modified to interact in well defined ways with their environment through surface functionalization. By exploiting particle dynamics, these interactions can be measured magnetically using MPI and can provide a spatially resolved map of particles states, enabling functional imaging on a quantitative basis.
Several points need to be addressed in order to enable functional imaging with MPI: Suitable biocompatible tracers need to be developed that possess the desired surface functionalization and are suitable for MPI, particle dynamics of these tracers need to be well understood and modeling techniques should be available to predict particle behavior accurately enough to derive useful information from the particle signal, and MPI scanners suitable for the task of detecting particle mobility need to be constructed.

This work describes the development and application of a MPI scanner that is designed specifically to demonstrate and further research the functional imaging capability of MPI through the measurement of particle mobility information. This concept, called moblity MPI (mMPI), can be realized through several techniques, all of which are based on the *Brownian* relaxation mechanism. One of these techniques involves the use of multiple excitation frequencies, that can be used to separate information on the spatial distribution from particle dynamics. Since the particle relaxation is inherently dependent on the excitation frequency and since for many particle tracers an additional contribution from the *Néel* relaxation exits, acquiring the same image at several drive frequencies can provide the additional data required for functional and

spatially resolved MPI. Since all current MPI scanners rely on transmit and receive chains that are tuned to the excitation frequency, the scanner hardware needs to be adapted for this multi-frequency approach.

Starting from the design of a multi-frequency magnetic particle spectrometer (MPS) that was later used to carry out pre-experiments on suitable tracer systems, this thesis describes in detail the design and construction of a mMPI system and its components. Several useful design techniques, such as a method for the accurate prediction of excitation coil parasitics, have been developed for this task. Other noteworthy aspects are the design of transmit and receive filters that offer high stop band attenuation and good linearity as required for MPI. The development of a fully differential receive coil completes the effort to provide a system suitable for the demonstration of mMPI. All system components have been thoroughly characterized to validate that the requirements have been met.

After acquiring conventional one- and two-dimensional MPI images, the new scanner was used to investigate the capability of MPI to provide spatially resolved information on particle mobility. Samples with different viscosities have been used to that end to simulate the effect of different binding states on the particles.

Glossary

AC	alternating current
ACS	AC susceptibility
ADC	analog-to-digital converter
BNC	bayonet Neill-Concelman
BPF	bandpass filter
BSF	bandstop filter
C0G	$\pm$ 30 ppm/K temperature drift ceramics class
CAD	computer aided design
CMRR	common-mode rejection ratio
CT	computed tomography
CTRL	control
CW	continuous wave
DAC	digital-to-analog converter
DC	direct current
DF	drive field
DI	de-ionized
DIN	Deutsche Industrie Norm
EM	electro magnetic
EMC	electro magnetic compatibility
EMI	electro magnetic interference
ENBW	equivalent noise bandwidth
FD	freeze dried
FDA	fully differential amplifier
FEM	finite elements method
FFL	field free line
FFP	field free point
FFT	fast fourier transform
FOV	field of view
FWHM	full width half maximum
GEN	generator
GUI	graphical user interface
HD2	second harmonic distortion
HD3	third harmonic distortion

HF	high frequency
IEEE	Institute of Electrical and Electronics Engineers
IR	infra red
IT	information technology
LC	inductor capacitor
LTX	transmit coil
LNA	low noise amplifier
MNP	magnetic nanoparticle
MPI	magnetic particle imaging
mMPI	mobility MPI
MPS	magnetic particle spectroscopy / spectrometer
MRI	magnetic resonance imaging
MRX	magnetic relaxometry
NF	noise figure
OpAmp	operational amplifier
PA	power amplifier
PCB	printed circuit board
PCI	peripheral component interconnect
PEEC	partial element equivalent circuit
PET	positron emission tomography
PNS	peripheral nerve stimulation
PSF	point spread function
PVC	polyvinyl chloride
RF	radio frequency
RLC	resistor inductor capacitor
SAR	specific absorption rate
SF	selection field
SFDR	spurious free dynamic range
SI	Système international d'unités
SMB	subminiature version B
SMPS	switching mode power supply
SNR	signal to noise ratio
SPECT	single-photon emission computed tomography
SPICE	simulation program with integrated circuit emphasis
SRF	self-resonant frequency
SVD	singular-value decomposition
THD	total harmonic distortion
THD+N	total harmonic distortion and noise
TOSM	through-open-short-match
TWMPI	travelling wave MPI
VCO	voltage controlled oscillator
VNA	vector network analyzer
VOI	volume of interest

Symbols

$\boldsymbol{A}$		MPI system matrix
$a_{i,j}$		MPI system matrix component
b	Hz	bandwidth
B	T	magnetic flux density
$\boldsymbol{B}$	T	magnetic flux density vector
$bei_\nu z$	1	*Kelvin* function ($\Im\left\{ J_\nu \left(z \exp \frac{3\pi j}{4} \right) \right\}$)
$ber_\nu z$	1	*Kelvin* function ($\Re\left\{ J_\nu \left(z \exp \frac{3\pi j}{4} \right) \right\}$)
c	mol/L	concentration
$\boldsymbol{c}$	mol/L	spatial concentration vector
C	F	capacitance
$C_{\mathbf{tt}}$	F	turn-to-turn capacitance
χ	1	magnetic susceptibility
χ_0	1	initial or dc susceptibility
$d_{\mathbf{c}}$	nm	particle core diameter
$d_{\mathbf{h}}$, $d_{\mathbf{hyd}}$	nm	particle hydrodynamic diameter
$d_{\mathbf{o}}$	m	litz wire bundle diameter
$d_{\mathbf{s}}$	m	strand conductor diameter
δ	m	skin depth
$D_{\mathbf{cu}}$	m	conductor diameter
$D_{\mathbf{in}}$	m	insulation diameter
$\boldsymbol{e_s}$	m	desired field direction vector
E_k	1	complete elliptic integral of the second kind
E_i	V	network potential at port i
E_n	V	voltage noise source
$\boldsymbol{E}$	V/m	electric field vector
ε	F/m	permittivity ($\varepsilon_0\, \varepsilon_{\mathrm{r}}$)
ε_0	F/m	vacuum permittivity ($8.854187817 \cdot 10^{-12}$ F/m)
$\varepsilon_{\mathbf{r}}$	1	relative permittivity
f	Hz	frequency
F_k	1	complete elliptic integral of the first kind
G	T/m	magnetic field gradient
$\boldsymbol{\Gamma}$	1	*Tikhonov* matrix

γ	1	regularization factor
γ_s	1	conductor-diameter to skin-depth ratio
H	$\mathrm{A/m}$	magnetic field
H_C	$\mathrm{A/m}$	coercivity or critical field
$H(j\omega)$	1	Transfer function in the frequency domain
$H(s)$	1	Transfer function in the *Laplace* domain
i	A	current (time domain or time varying)
j		imaginary unit, the result of $\sqrt{-1}$
I	A	current (frequency domain or static)
$\boldsymbol{I}$	1	identity matrix
J	1	Bessel function
k_R	1	impedance scaling factor
$k_{m,n}$	1	inductive coupling coefficient
K	$\mathrm{J/m^3}$	anisotropy constant
k_B	$\mathrm{J/K}$	*Boltzmann*'s constant ($1.38 \times 10^{-23}\,\mathrm{J/K}$)
L	H	inductance
$\mathcal{L}$	1	*Langevin* function
$\mathscr{L}$	$1/\mathrm{Hz}$	*Laplace* transform
l_t	m	average turn length
m	$\mathrm{Am^2}$	magnetic moment
$\boldsymbol{m}$	$\mathrm{Am^2}$	magnetic moment vector
M	$\mathrm{A/m}$	magnetization
$\boldsymbol{M}$	$\mathrm{A/m}$	magnetization vector
$M_{i,j}$	H	mutual inductance
$\boldsymbol{M_0}$	$\mathrm{A/m}$	equilibrium magnetization vector
M_S	$\mathrm{A/m}$	saturation magnetization
μ_o	$\mathrm{T\,m/A}$	vacuum permeability ($4\pi \times 10^{-7}\,\mathrm{Vs/Am}$)
μ_r	1	relative permeability
N	1	particle number
N_t	1	number of turns
N_L	1	layer count
$\boldsymbol{\nu}$	1	correction vector
η	$\mathrm{Pa\,s}$	dynamic viscosity
η_1	1	external porosity factor
η_2	1	internal porosity factor
N_A	$1/\mathrm{mol}$	*Avogadro* constant ($6.022 \times 10^{23}\,1/\mathrm{mol}$)
n_d	$1/\mathrm{m^3}$	particle number density
n_s	1	number of strands in litz wire
p	1	litz wire packing factor
Φ	Wb	magnetic flux
r_cu	m	copper radius
r_in	m	insulation radius
Q	C	electric charge
R	Ω	resistance

$R_{\mathbf{ac}}$	Ω	AC resistance
$R_{\mathbf{dc}}$	Ω	DC resistance
R	m	radius
res		residue
ρ	$1/\mathrm{m}$	nanoparticle density
$\rho(j\omega)$	1	reflection coefficient
s	Hz	complex frequency parameter of the *Laplace* transform
S	Hz	transformed complex frequency variable
$s_{\mathbf{g}}$	m	(half) gap width
s_{ij}	1	scattering network parameter port j to i
$\boldsymbol{S}$	1	scattering parameter network matrix
σ	Hz	real part of the complex s parameter
σ	S	specific conductivity
$\sigma(t)$		*Heaviside* function
dS	m^2	differential surface element
T	K	absolute temperature
T	s	period
$T_{\mathbf{Rep}}$	s	repetition period (frame length)
t	s	Time
$t_{\mathbf{o}}$	m	distance between adjacent windings
$t_{\mathbf{s}}$	m	strand spacing
$t(j\omega)$	1	transmission coefficient
τ	s	time constant
τ_0	s	characteristic time constant for spin reversals
$\tau_{\mathbf{B}}$	s	*Brownian* time constant
$\tau_{\mathbf{m}}$	s	time constant of measurement technique
$\tau_{\mathbf{N}}$	s	*Néel* time constant
$\tau_{\parallel}$	s	time constant of relaxation parallel to the external field
$\tau_{\perp}$	s	time constant of relaxation perpendicular to external field
$\tau_{\mathbf{eff}}$	s	effective time constant
u	V	voltage (time domain or time varying)
U	V	voltage or voltage potential (frequency domain or static)
$\mu_{\mathbf{r}}$	1	relative permeability
V	m^3	volume (1 µL = 1 mm^3)
V	V	source voltage
V_c	m^3	volume of the particle core (1 µL = 1 mm^3)
V_{P}	m^3	particle volume
$\boldsymbol{v}_{\mathbf{meas}}$	V	spectal voltage amplitude vector
$\boldsymbol{v}_{\mathbf{cal}}$	V	spectral received voltage signal during calibration
v_{f}	1	particle volume fraction
ω	rad/s	angular frequency
ω_0	rad/s	mid or corner angular frequency
ξ	1	ξ factor
$\boldsymbol{\xi}$	1	ξ vector

y_{ij}	S	admittance network parameter ij
$\boldsymbol{Y}$	S	admittance network matrix
z_{ij}	Ω	impedance network parameter ij
$\boldsymbol{Z}$	Ω	impedance network matrix
Z	Ω	impedance

Schematic symbols

This document uses European resistor 

and inductor symbols 

, which are indicated as empty or filled boxes respectively. However, when inductors are used to generate or pick-up magnetic fields as their primary function, a more graphical symbol 

is used instead.

Contents

CHAPTER 0

Introduction

Since its invention in 2005 [1], Magnetic Particle Imaging (MPI) has seen significant developments as a tomographic imaging technique. Offering high temporal and spatial resolution [2, 3], the ability to track nanoparticle labeled cells [4] and having commercial preclinical scanners available [5], MPI is a versatile technique for medical research.
It achieves spatial resolutions in the mm range and frame-rates of more than 100 frames per second, allowing e.g. the study of blood perfusion in real time [6]. This fast image rate can be traded for high sensitivity to low tracer concentrations through longer measurement intervals in the range of several minutes, allowing applications such as cell tracking [7].

Because MPI utilizes the nonlinear magnetization of superparamagnetic nanoparticles to achieve a spatially encoded signal, it does not suffer from anatomical background signals and achieves high contrast [4], making it comparable to radiological methods like positron emission tomography (PET) or single-photon emission computed tomography (SPECT). Unlike these, it does not rely on ionizing radiation, making it safer to use for clinic personnel and patients.

Magnetic nanoparticles (MNP), which are the tracers for MPI, have been shown to have a multitude of biomedical applications [8, 9], which range from hyperthermia [10, 11] to functionalization [12, 13] and their use in immunoassays [14, 15]. Combining these applications with MPI would enhance the method with functional imaging capabilities. A promising step in that direction would be to have a means to measure the particle environment. Using particle functionalization, this directly translates to the measurement of the mobility of the particles in the surrounding media. Through the *Brownian* relaxation process, this information is accessible via magnetic measurements, which has been successfully demonstrated using other magnetic techniques, which operate in a similar frequency and amplitude range as MPI

[16]. The presence of a second, internal relaxation behavior, however (namely the *Néel* process), makes it necessary to acquire additional information to reconstruct spatial and mobility information at the same time, but also opens the opportunity to image completely immobilized particles and therefore separate spatial and functional data. One approach that provides this additional information exploits the different time constants of the external and internal particle relaxation processes. Acquiring two images of the same specimen but using different excitation frequencies, the differences between the acquired images (with the *Néel* relaxation contribution removed) are directly linked to the changed relaxation behavior due to the binding reaction [17]. The removal of media dependent signal changes is also a prerequisite to achieve truly quantitative imaging in MPI with non-functionalized particles.
As a result, to accomplish quantitative imaging of the particle relaxation behavior, an MPI scanner with two or more excitation frequencies is desirable. It is therefore the goal of this work, to demonstrate spatially resolved particle mobility imaging, by realizing a suitable dual frequency mobility MPI (mMPI) scanner.

Chapter 1 starts by introducing the properties of magnetic nanoparticles, including their dynamic behavior (section 1.1.4), which is important for understanding the mMPI principle. It also explains how their non-linear magnetization allows to achieve spatially resolved MPI images through suitable encoding fields (section 1.2.2). Starting from the preconditions for the successful application of the mMPI technique, the basic theory relevant for the construction of such a device is reviewed (section 1.2.5). Similar to general purpose MPI scanners, parasitics of hardware components play an important role and are therefore also covered (section 1.3). Measuring the small non-linear response of MNPs requires a purely sinusoidal transmitted signal without harmonic content in the first place. Since currently available amplifiers are not capable of producing such a signal directly, filtering is an important aspect of MPI system design. The relevant theory of passive filters is therefore reviewed as well (section 1.4). Since MPI hardware has seen several improvements during the course of this thesis, a review of the developments by other groups is given in section 1.6, focusing on technical aspects relevant to scanner design.
Chapter 2 describes the construction of a magnetic particle spectrometer (section 2.1) that can be used to evaluate particle behavior in a zero-dimensional experiment. The chapter continues with the design of the mMPI scanner (section 2.2). It provides details on the construction of the drive coil system (section 2.2.3) and presents a method to accurately predict coil performance and parasitics (section 2.2.3.5). As mentioned before, filter circuits are a central concern in MPI system design. Consequently, the design procedure for the transmit- (section 2.2.5) and receive filters (section 2.2.7.2) is explained in detail. The latter are intimately coupled to the receive coil, which was constructed using a novel, fully differential arrangement (section 2.2.7.1). To verify the performance of individual components, extensive measurements were performed, which are summarized in section 2.3.
The imaging results achieved with the new mMPI scanner, as well as selected MPS measurements are given in chapter 3. The work closes with chapter 4, that provides a summary as well as ideas for future research and development.

CHAPTER 1

Basics

1.1 Magnetic Nanoparticles

This section will discuss fundamental properties of magnetic nanoparticles (MNP). The focus will be on theoretical concepts relevant for the context of this work, with emphasis on iron-oxide nanoparticles. Starting with the effect of superparamagnetism, simple models to describe particle relaxation processes, as well as the macroscopically observed magnetization behavior of superparamagnetic particle ensembles will be given. The nonlinear nature of this effect and its applications will then be discussed in more detail in the following sections.

1.1.1 Superparamagnetism

Ferromagnetic bulk material exhibits magnetic domains, which are characterized by spin-collinearity of the atoms [18]. These regions are formed due to strong short-range magnetostatic interactions (called exchange interaction) that energetically favor parallel spin orientations. However, long-range magnetostatic interactions in the bulk material compete with these short range terms, so that domain walls are formed in a way that minimizes the global magnetic energy in the material. This gives rise to the creation of magnetic flux closures [18], so that the externally observed magnetization is zero if no additional field is present. The number of domains is limited by the surface tension energy, introduced by the transition layer the domain wall constitutes[19].
With an external magnetic field applied, domain walls are shifted in favor of those domains aligned with the external field, to minimize the magnetic energy. At very high fields, all spins are aligned with the field, and the material experiences saturation. After the field is removed again, not all domains return to their previous state and a part of the magnetization is retained by the material, an effect known as remanence.

Particles made from ferromagnetic materials show similar behavior down to a size of ≈100 nm. Below that diameter, long-range interactions are no longer a significant contribution and therefore a single magnetic domain is formed, leading to a dramatically changed behavior: With all spins in the same direction, these nanoparticles exhibit saturation without external fields, leading to a macroscopic magnetization.
The orientation of the magnetization is influenced by anisotropy effects. The most simple approach is to assume an uniaxial anisotropy [18], e.g. due to the crystal structure or the shape anisotropy of a prolate ellipsoid, leading to an "easy axis" and perpendicular "hard axis"[1)]. Without external influence, the magnetization is oriented either parallel or anti-parallel to the easy axis, minimizing the total energy. With an external field applied opposite to the magnetization, the magnetization vector turns out of the easy axis until the external field is strong enough to overcome the energy barrier imposed by the anisotropy, and therefore the magnetization flips.
The energy required to turn the magnetization is

$$E_{\text{ani}} = -K\,V\cos^2\alpha \tag{1.1}$$

where K is the anisotropy constant, V is the particle volume and α is the angle between the magnetization vector and the easy axis.

The magnetic field required to overcome the energy barrier and flip the magnetization can be reduced by the presence of thermal fluctuations. These random events, even though they have no predominant direction in the time average, have a chance of being directed parallel to the applied field direction. Therefore, as the temperature is increased, the probability of the particle magnetization flipping at field energies below the anisotropy barrier rises. Sufficiently high temperatures allow particles to flip even with no external field present, once the thermal energy $k_{\text{B}}T$ is greater than KV [18]. This statistical process can be characterized by the spin relaxation time

$$\tau_S = \tau_0 \exp\left(\frac{KV}{k_{\text{B}}T}\right) \tag{1.2}$$

where τ_0 is a characteristic time constant for spin reversals (the inverse of the attempt frequency [20]) in the order of 10^{-9} to 10^{-12} s [21]. k_{B} is the *Boltzmann* constant and T the absolute temperature.

Since these disturbances are a probabilistic effect, the time window, within which a particle is observed, greatly influences the perceived behavior of the particles. When many flipping events occur during the observation window, the *perceived* magnetization of the particle disappears. This effect is known as superparamagnetism, since the particle magnetization behaves similar to a paramagnetic material: without external field, no magnetization is observed, whereas the application of an external field (and therefore adding another energy that thermal fluctuations have to overcome) results in a distinct direction of the magnetization vector's time average, making it observable.
The temperature, above which for a given observation method superparamagnetic

[1)] Or, more precisely, a hard plane.

behavior is observed, is called the blocking temperature T_B. It can be expressed as

$$T_B = \frac{K\,V}{k_B} \frac{1}{\ln\left(\frac{\tau_m}{\tau_0}\right)}, \tag{1.3}$$

where τ_m is the characteristic measurement time of the observation technique [18].

1.1.2 Core-shell model

Since the following sections will be dealing with nanoparticles in a colloidal solution, we have to discuss how particles can be stabilized for use under such conditions. Owing to the constant magnetization magnitude of superparamagnetic nanoparticles, there is a tendency for them to build larger structures that minimize the total energy, similar to the domains encountered in bulk material. This effect is known as agglomeration and we seek to avoid it as it can dramatically change particle behavior and lead to coagulation. For use in biological systems, this is even more important since large agglomerates of particles could e.g. block blood vessels and cause severe harm to the subject.

To reduce attractive particle interaction, it is common to add a non-magnetic shell around the magnetic core. If sufficiently large, it will separate the particles enough so that thermal fluctuations can always break particle assemblies. Figure 1.1 depicts a nanoparticle enclosed by a shell. We distinguish the size of the magnetic core d_c from the outer diamater of the shell d_{shell}. When the particle is dispersed in an aqueous solution, it is common that molecules from the solution stick to the surface of the shell e.g. by electrostatic forces, increasing its effective diameter. We denote this diameter as hydrodynamic diameter d_{hyd} of the particle.

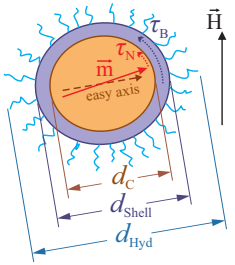

Figure 1.1: Core-shell model of a magnetic nanoparticle showing core diameter d_c, shell size d_{shell} and hydrodynamic diameter d_{hyd}, magnetic moment $\boldsymbol{m}$ and easy axis. Relaxation processes are also symbolized: τ_B, τ_N are the relaxation times discussed in section 1.1.4.

Assuming that an ensemble of such particles is sufficiently diluted in an aqueous solution, we can completely neglect particle interaction. We still need, however, to deal with the statistical process that governs particle behavior, as well as particle to particle parameter variations.

Even though up to now we have assumed that the core of our particles is uniform, this does not need to be the case. In the case of a single core structure it is still possible that the chemical composition changes throughout the core [22], often as a consequence of the synthesis procedure. Moreover, it is possible to incorporate several crystallites of magnetic material into a common shell, which is called a multi-core particle.

1.1.3 Size Distribution

Currently available fabrication processes of magnetic nanoparticles invariably lead to a size distribution, although it may be very narrow. Very often, a log-normal distribution will describe this with reasonable accuracy [23]. While the reasons for the formation of the log-normal distribution are still subject of research [24], it is nevertheless useful to model real-world particle systems.

Especially when multiple large cores are incorporated into a common shell, multimodal distributions are encountered, each centered around the respective core size of the cluster.

1.1.4 Particle Relaxation

1.1.4.1 Néel relaxation

Observing a large particle ensemble, the aforementioned behavior can be described by its statistical average. This gives rise to a macroscopic relaxation time constant with which the particle ensemble reacts to external fields, though the behavior of individual particles remains governed by statistics.
The relaxation of the internal particle magnetization of the ensemble, without rotation of the crystallographic matrix, is called *Néel* relaxation and can be described by the *Néel* relaxation time constant [20]

$$\tau_{\mathrm{N}} = \tau_0 \exp\left(\frac{K\,V_c}{k_{\mathrm{B}}T}\right) = \tau_0 \exp\left(\frac{K\,\pi {d_c}^3}{6k_{\mathrm{B}}T}\right). \tag{1.4}$$

Here, V_c is the volume of the particle core with diameter d_c and K its anisotropy constant. τ_0 is the inverse of the attempt frequency as in (1.2).

1.1.4.2 Brownian relaxation

Magnetic nanoparticles in suspensions gain the ability to move within the medium. As a consequence, in addition to the aforementioned rotation of the magnetization vector, the particle can also rotate as a whole to align the magnetic moment with the external field. For an ensemble, the average relaxation time purely governed by particle movement, is called the *Brownian* relaxation time [25]

$$\tau_{\mathrm{B}} = \frac{3V_{\mathrm{hyd}}\eta}{k_{\mathrm{B}}T} = \frac{\pi {d_{\mathrm{hyd}}}^3\eta}{2k_{\mathrm{B}}T}, \tag{1.5}$$

where V_{hyd} is the hydrodynamic volume of the particle with hydrodynamic diameter d_{hyd}, and η is the viscosity of the medium.
Using τ_{B}, the exponential relaxation process can be described phenomenologically. This consideration is valid as long as the observation timescale is much larger than the processes that achieve thermal equilibrium.

1.1.4.3 Effective relaxation time constant for combined Néel and Brownian relaxation

When both *Brownian* and *Néel* relaxation are in effect, the resulting relaxation time is dominated by the shorter time constant, following the equation [19]

$$\tau_{\text{eff}} = \frac{\tau_{\text{B}} \cdot \tau_{\text{N}}}{\tau_{\text{B}} + \tau_{\text{N}}}. \tag{1.6}$$

The effective relaxation time constant for typical nanoparticle parameters as a function of the cores size is depicted in figure 1.2, in addition to the individual *Brown* and *Néel* relaxation time constants.

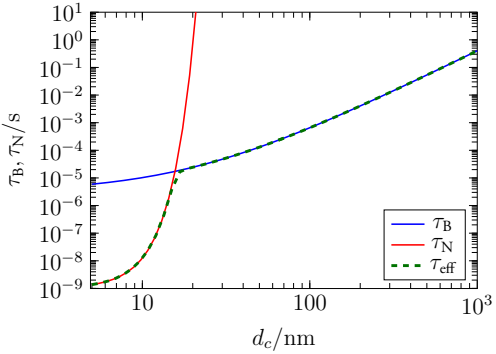

Figure 1.2: *Brown* and *Néel* time constants for different core diameters d_c, assuming a constant shell thickness of 10 nm, $K = 20\,\text{kJ/m}^3$ and $\eta = 1\,\text{mPa s}$ at $T = 300\,\text{K}$.

1.1.4.4 Static magnetization response of superparamagnetic particles

Above the blocking temperature T_{B} and neglecting anisotropy effects, the mean dipole moment in the direction of an external field H of a superparamagnetic nanoparticle with the magnetic moment m can be described by $m \cdot L(\xi)$, where $L(\xi)$ is the *Langevin* function

$$\mathcal{L}(\xi) = \coth(\xi) - \frac{1}{\xi}, \tag{1.7}$$

with the parameter

$$\xi = \frac{\mu_0 m H}{k_{\text{B}} T} \tag{1.8}$$

[20]. It is the (thermal) equilibrium solution of the *Landau-Lifshitz* equation for uniaxial anisotropy. As can be seen from figure 1.3, the magnetic moment shows nonlinear magnetization behavior similar to ferromagnetic materials, except that no

hysteresis occurs. This aspect is similar to paramagnets, but since the magnetic moment of superparamagnets is much higher, saturation is already observed (at room temperature) at moderate field strengths. This nonlinear behavior will be the focus of the measurement techniques discussed in the following chapter.

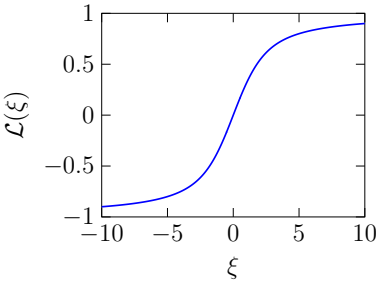

Figure 1.3: Langevin function

1.1.4.5 Dynamic magnetization response of superparamagnetic particles

To model the dynamic magnetization response of a superparamagnetic particle ensemble, it is necessary to solve the stochastic differential equations that result when applying *Brownian* perturbations on top of the *Landau-Lifshitz* equation. A linearized solution of this problem for the (quasi)-equilibrium state is obtained through the effective field method. The following is a simplified summary of the derivations described in [19].

The effective field method

The effective field method, as explained by *Raikher* and *Shliomis* [19], is the application of a method lend from thermodynamics onto rigid dipole magnetics. *Leontovitch* [26, Ch. 3] introduced it to convert an arbitrary non-equilibrium state of a thermally uniform system into the equilibrium state by introducing an "appropriate" field, which achieves the transformation into the equilibrium. The idea is that the internal (statistical) parameters (the entropy) of the system are not affected by the introduction of said field, therefore allowing their determination from the equilibrium values.

Applied to the topic of magnetic systems, *Raikher* and *Shliomis* identify the internal state to be the particle magnetization $\boldsymbol{M}$, as obtained as solution of the *Landau-Lifshitz* equation. In applying an effective field that puts the system in an equilibrium state, the equilibrium solution of the *Landau-Lifshitz* equation with applied thermal fluctuations may be used, simplifying the problem.
Using this idea, the relaxation process becomes a sequence of quasi-equilibrium states, each with its individual effective field. The effective field tends to the applied external

field and when settled the solution obtained converges to the equilibrium solution under these external field conditions. In the next step, the effective field is assumed to be such that it can be derived by applying a uniform correction field on top of the applied field. From this assumption, a dependence between the effective field and the true field as a function of time can be derived.

Linearizing the problem, i.e. considering only small excursions from the equilibrium state, the effective field $\boldsymbol{\xi}_e$ can be expressed as sum of the applied field $\boldsymbol{\xi}$ and a small correction vector $\boldsymbol{\nu(t)}$, which puts the system back into equilibrium. Here $\boldsymbol{\xi}$ is the vectorial form of (1.8), aligned with the external field [19]:

$$\boldsymbol{\xi}_e = \boldsymbol{\xi} + \boldsymbol{\nu(t)}. \tag{1.9}$$

From there it follows that the non-equilibrium contribution to the magnetization $\boldsymbol{m}$ is [19]

$$\boldsymbol{m} = \boldsymbol{M} - \boldsymbol{M_0} = n\mu \left[\frac{\boldsymbol{\xi}_e}{\xi_e} \mathcal{L}(\xi_e) - \frac{\boldsymbol{\xi}}{\xi} \mathcal{L}(\xi) \right], \tag{1.10}$$

where $\boldsymbol{M_0}$ is the equilibrium magnetization and $\boldsymbol{M}$ is the instantaneous magnetization. μ is the magnetic moment and n is the number density of particles.

To avoid dealing with the inverse of the Langevin function, *Raikher* et al. use a linear approximation and arrive, after splitting the nonequilibrium part into components parallel and perpendicular to the external field, at a differential equation for the total magnetization $\boldsymbol{M} = \boldsymbol{M_0} + \boldsymbol{m}$ [19]:

$$\frac{d}{dt}\boldsymbol{M} = -\frac{1}{\tau_{\parallel} H^2} \boldsymbol{H} \left[(\boldsymbol{M} - \boldsymbol{M_0})\, \boldsymbol{H} \right] - \frac{1}{\tau_{\perp} H^2} \left(\boldsymbol{H} \times (\boldsymbol{M} \times \boldsymbol{H}) \right), \tag{1.11}$$

where

$$\tau_{\parallel} = \frac{d \ln \mathcal{L}}{d \ln \xi} \tau_{\mathrm{B}}, \tag{1.12}$$

$$\tau_{\perp} = \frac{2\mathcal{L}}{\xi - \mathcal{L}} \tau_{\mathrm{B}} \tag{1.13}$$

are the relaxation times in the corresponding directions. *Raikher* et al. also note that for strong fields $\xi \gg 1$ the transverse relaxation time $\tau_{\perp} = \frac{2\tau_{\mathrm{B}}}{\xi}$ exceeds the longitudinal relaxation time $\tau_{\parallel} = \frac{\tau_{\mathrm{B}}}{\xi}$ by a factor of 2.

It is also useful to consider the case of one-dimensional AC excitation. In this case, the term $\boldsymbol{H} \times (\boldsymbol{M} \times \boldsymbol{H})$ always evaluates to zero and (1.11) reduces to

$$\frac{d}{dt} M = -\frac{1}{\tau_{\parallel}} \left(M - M_0 \right). \tag{1.14}$$

Separation of nonlinearity and dynamics

While the effective field method is a powerful tool that works for one-dimensional as well as for three-dimensional field conditions, the qualitative behavior of magnetic

nanoparticles under strong one-dimensional AC fields may be approximated by separating the nonlinear magnetization behavior from the dynamics.

By assuming that under AC conditions, the dependence described by the *Langevin* equation still holds, dynamic effects can be applied a posteriori through a temporal convolution of the nonlinear response with an exponential relaxation term [27]:

$$M(t) = M_0 \mathcal{L}\left(\xi \sin(\omega t)\right) * \frac{1}{\tau_{\text{eff}}} \exp\left(-\frac{t}{\tau_{\text{eff}}}\right) \sigma(t) \tag{1.15}$$

where $*$ denotes the temporal convolution and $\sigma(t)$ is the *Heaviside* function, which we use to enforce causality on the relaxation term.

In the *Laplace* domain with the complex frequency variable $s = j\omega + \sigma_d$, this corresponds to the multiplication of the spectral response of the Langevin function under sinusoidal excitation with a first order dynamic system viz. $H(s) = \dfrac{1}{1 + s\,\tau_{\text{eff}}}$.

Unfortunately, no closed-form analytical expression for the *Fourier* or *Laplace* transform of aforementioned $\mathcal{L}\left(\xi \sin(\omega t)\right)$ response is available. However, a numerical calculation is easily achieved. The resulting dynamic response is included in figure 1.4 on page 15, which is discussed in the following section.

1.2 Magnetic Particle Spectroscopy and Magnetic Particle Imaging

Devices known as *Magnetic Particle Spectrometer*[2)] (MPS) and *Magnetic Particle Imaging scanner* (MPI) are in more general terms setups that allow the observation of MNP responses under large signal AC field conditions. The difference between them is that imaging devices usually have larger sample areas and possess means to achieve spatial resolution within these. The most common method for spatial encoding is the addition of a gradient field that contains a field free region (either a line or a point), but arrays of excitation or receive coils are also possible.

The spectrometer evaluates the response at a single spatial position only, usually without any gradient fields or DC field offsets present.

The following sections will briefly explain MNP signal generation in these devices, as well as image encoding and reconstruction in case of the imaging setup. Detailed information on their construction will follow in chapter 2 on page 61, while theoretical concepts relevant for the implementation are presented in sections 1.3 to 1.5.

1.2.1 Harmonic generation by MNPs

As mentioned before, no closed-form expression for the magnetization response of an AC driven *Langevin* function is available in the frequency domain. To gain more insight than is possible from numerical solutions, we use an approximation by starting with the *Langevin* function (1.7) and using a *Taylor* expansion around the origin to

[2)] Also known as *Magnetic Particle Relaxometer*.

express its nonlinearity:

$$\mathcal{L}(x) = \frac{x}{3} - \frac{x^3}{45} + \frac{2x^5}{945} - \frac{x^7}{4725} + \frac{2x^9}{93555} - \frac{1382x^{11}}{638512875} + ... \tag{1.16}$$

When we insert a sinusoidal excitation field, we can also use common identities for trigonometric functions to expand the polynomial:

$$\begin{aligned}
\sin^2 x &= \frac{1}{2}\left(1 - \cos 2x\right) \\
\sin^3 x &= \frac{1}{4}\left(3\sin x - \sin 3x\right) \\
\sin^4 x &= \frac{1}{8}\left(\cos 4x - 4\cos 2x + 3\right) \\
\sin^5 x &= \frac{1}{16}\left(\sin 5x - 5\sin 3x + 10\sin x\right)
\end{aligned} \tag{1.17}$$

With this we arrive at

$$\begin{aligned}
\mathcal{L}(sin(\omega t + \varphi)) \approx\ & 0.3179\sin(t\omega + \varphi) + 4.9573\cdot 10^{-3}\sin(3t\omega + 3\varphi) \\
& + 1.1178\cdot 10^{-4}\sin(5t\omega + 5\varphi) + 2.6715\cdot 10^{-6}\sin(7t\omega + 7\varphi) \\
& + 6.0257\cdot 10^{-8}\sin(9t\omega + 9\varphi) + \ldots .
\end{aligned} \tag{1.18}$$

It becomes apparent that the polynomial will generate harmonics of the fundamental frequency ω_1, that drop in amplitude with the order of the harmonic. Also, any phase shift on the fundamental increases proportionally with the harmonic order.

Repeating these steps for a sine with an offset of 2 and a *Taylor* expansion of $\mathcal{L}(\xi)$ around that point, truncated after the 5^{th} element, we arrive at

$$\begin{aligned}
\mathcal{L}(2 + sin(\omega t + \varphi)) \approx\ & 0.51463 + 0.17805\sin\left(\omega t + \varphi\right) \\
& + 2.25551\cdot 10^{-2}\cos\left(2\omega t + 2\varphi\right) - 1.28177\cdot 10^{-3}\sin\left(3\omega t + 3\varphi\right) \\
& + 1.28895\cdot 10^{-4}\cos\left(4\omega t + 4\varphi\right) - 4.56198\cdot 10^{-5}\sin\left(5\omega t + 5\varphi\right) + \ldots
\end{aligned} \tag{1.19}$$

The offset gives rise to even ordered harmonics. It also creates phase offsets for odd and even harmonics. However, the propagation of fundamental phase shifts onto harmonics stays proportional to the order.

It should be noted that even though these considerations adequately explain the qualitative effects observed experimentally, they are insufficient to accurately predict the resulting signal. The deviations increase with the order of the harmonics. The *Taylor* expansion is also very limited in the amplitude range around the evaluation point ($|\Delta\xi| \leq 2$) for which the expansion shows reasonable agreement with the original *Langevin* function. Otherwise, piecewise linearization has to be used, further complicating the results.

Figure 1.4 visualizes the generation of harmonics by magnetic nanoparticles using a numerical approach based on (1.15) and will be covered in more detail in the following sections.

1.2.2 Spatial encoding

To extract spatial information from the nanoparticle response, a (static) encoding field can be applied to make the responses of different points distinguishable.

1.2.2.1 Image encoding considered from the frequency domain

Spacial encoding through use of a gradient field

As we have learned from section 1.2.1, applying a DC offset changes the harmonic content of the response signal of the MNPs. Beyond a simple change, the generated harmonic signal is characteristic for the individual offset, so that every offset value produces a unique[3)] spectral response. This has been shown by *Rahmer* et al. [28] for an ideal particle system exhibiting as *signum* magnetization response.

Aforementioned behavior can be exploited by covering a volume of interest (VOI) with a gradient field. Since the amplitude of the magnetization signal from the particles has its maximum around the origin of the magnetization curve, it is useful to have a field free region in the VOI, which can have the shape off a field-free-line (FFL) or field-free-point (FFP). With this setup, superimposing a homogeneous, pure sinusoidal field with no DC offset (called the drive field DF) on the gradient, every point in the VOI now shows a unique harmonic response [28]. Since the sinusoidal field shifts the position of the FFP in space, the resulting response for the whole volume can be maximized in amplitude by making the drive field sufficiently strong so that the FFP is shifted throughout the whole VOI. As the particles in the instantaneous field free region exhibit zero-field relaxation conditions, the gradient can also be seen as a way to "select" particles at the FFP, and is therefore called the *selection field* (SF) in MPI terminology.

Gathering encoding information

To put the encoding scheme to good use, it is necessary to know the spectral response that belongs to each spatial position. By positioning a point sample of nanoparticles at one and only one point in the field of view (FOV), the response of that position can be acquired. The sample can then be moved around to acquire the response of every point in the volume. This is called a calibration scan.

In formula, we extract a vector $\boldsymbol{v}_{\mathrm{cal},k}$ with h harmonic components $v_{\mathrm{cal},j,k}$ at multiples of the fundamental frequency $\omega_1 = 2\pi f_1$ from the received voltage signal $v_{\mathrm{cal},k}(t)$ at each point k:

$$\boldsymbol{v}_{\mathrm{cal},k} = \begin{pmatrix} v_{\mathrm{cal},1,k} & v_{\mathrm{cal},2,k} & \dots & v_{\mathrm{cal},h,k} \end{pmatrix}^{\mathrm{T}} \tag{1.20}$$

We then collect these vectors in the so called *system matrix* $\boldsymbol{A}$ at each of the p spatial points in the VOI:

[3)] if the phase is included

$$\boldsymbol{A} = \begin{pmatrix} \boldsymbol{v}_{\text{cal},1} & \boldsymbol{v}_{\text{cal},2} & \dots & \boldsymbol{v}_{\text{cal},p} \end{pmatrix} = \begin{pmatrix} a_{1,1} & a_{1,2} & \dots & a_{1,p} \\ a_{2,1} & a_{2,2} & \dots & a_{2,p} \\ \vdots & \vdots & \ddots & \vdots \\ a_{h,1} & a_{h,2} & \dots & a_{h,p} \end{pmatrix} \tag{1.21}$$

This principle is visualized in figure 1.4 on page 15 (cf. [28]) which depicts the generated spectra at different positions in the imaging volume. The first and second column show the position within the static gradient and the local field conditions respectively. For each of these points the resulting dynamic magnetization curve (column 3) and the corresponding time domain waveform (column 4, cyan) are shown. Since coils are usually employed for signal reception, the time derivative of the magnetization is also included (column 4, red), as well as its amplitude (column 5, purple) and phase (column 5, green dots) spectrum. In the last column, the parametric curve of the received signal over the FFP position, which is used for X-space reconstruction (see section 1.2.3.2 on page 17), is plotted.

Reconstruction principle

An arbitrary distribution of magnetic nanoparticles inside the VOI can be reconstructed from the superposition of the generated responses, if the response at each[4] point in the VOI is known. This means, that an image of the particle distribution can be acquired by measuring the total harmonic signal produced by the particles. The VOI thus becomes the available imaging volume and is therefore called the field of view of the imaging device. Particles outside the FOV do not contribute to the image: as they remain in saturation all the time, the signals produced by them are very small (cf. bottom row of figure 1.4 on page 15).

Mathematically, we have a received signal $v_{\text{meas}}(t)$ that contains a superposition of all the signals from nanoparticles in the FOV. As before, we can extract the harmonic amplitudes $\boldsymbol{v}_{\text{meas}}$. With the known system matrix, acquired by a prior calibration scan, we can express this superposition by introducing the concentration vector $\boldsymbol{c}$ that contains the MNP concentration c_k at each point k:

$$\boldsymbol{v}_{\text{meas}} = \boldsymbol{A}\boldsymbol{c} \tag{1.22}$$

Obtaining an image is thus the process of inverting the system matrix $\boldsymbol{A}$ to calculate $\boldsymbol{c}$:

$$\boldsymbol{c} = \boldsymbol{A}^{-1}\boldsymbol{v}_{\text{meas}}. \tag{1.23}$$

Unfortunately, due to noise, the conditioning of the system matrix and the low pass character of the system, there is no exact algebraic solution for this inverse problem.

[4] or a sufficiently high number

The inversion of $\boldsymbol{A}$ leads to a high-pass characteristic, which tends to further amplify noise at the upper system bandwidth, giving frequency components with low SNR too much weight. As analytical inversion as well as standard least-squares minimization are unable to solve this kind of problem, regularization should be performed to suppress noise dominated solutions. Section 1.2.3.1 will briefly discuss methods that allow us to perform this step.

1.2.2.2 Image encoding considered from the time domain

The same encoding and reconstruction principle we have considered before can also be viewed from the time domain perspective. Here we will briefly discuss the idea, while a mathematical treatment is provided in the corresponding section on the reconstruction algorithm, section 1.2.3.2 on page 17.

The setup we will assume in the following is the same as for the frequency domain approach (cf. section 1.2.2.1 on page 12): A field free point (or line) produced by a static gradient in the center of the field of view, that is moved through the FOV via an sinusoidal drive field. Only this time, we take a look at the time domain waveform of the received signal of a point sample (columns 4 and 6 in figure 1.4) and notice that every time the FFP crosses the particle sample, the magnetization of that sample has a zero-crossing and the (inductively) received signal has an extremum.

Plotting the received signal over the position of the FFP (column 6), we see a direct relationship with the sample position. Ideally, a maximum is observed where the sample is positioned, but due to particle relaxation, the images of each scan direction exhibit a slight lag. Since this is a systematic deviation, only depending on the particle system used, it can be removed from the image if the relaxation behavior of the particles is known. This corresponds to the relaxation information included in the calibration scan of the frequency domain method. Similarly, the widening of the maximum due to the finite slope of the magnetization curve can be addressed.

The time domain method also works for multiple samples in the FOV [29], as can be seen from the reconstruction algorithm.

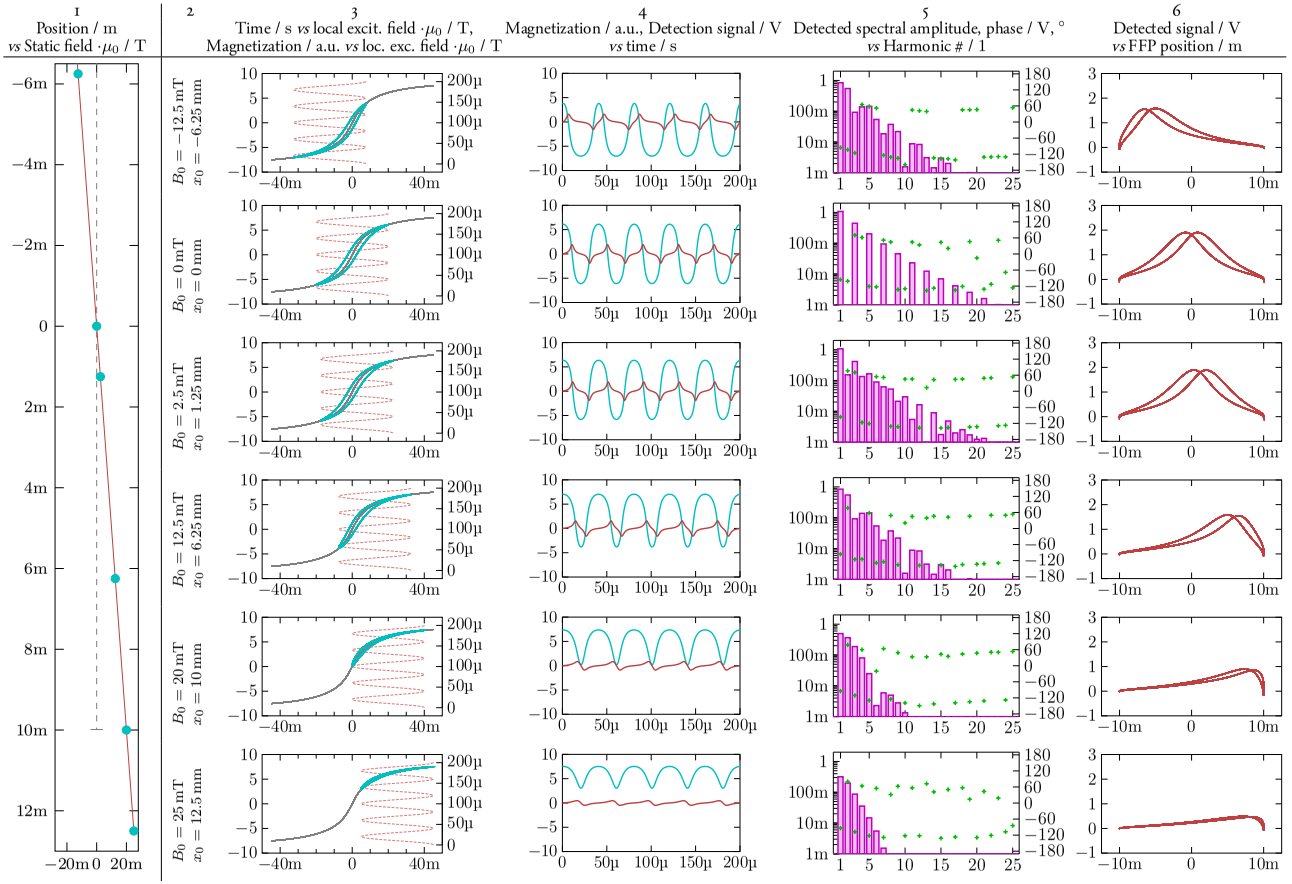

Figure 1.4: MPI signal encoding scheme: 1,2: Position along gradient; at individual positions: 3: Drive field and (dynamic) magnetization curve, 4: Time domain magnetization, received signal, 5: Spectral amplitude, phase (dots) of received signal, 6: X-Space response. (cf. [28])

1.2.3 Image reconstruction algorithms

1.2.3.1 Reconstruction in the frequency domain (system matrix or f-space approach)

Starting from the image equation that connects the desired concentration vector $\boldsymbol{c}$ with the received harmonic component vector $\boldsymbol{v}_{\text{meas}}$

$$\boldsymbol{v}_{\text{meas}} = \boldsymbol{A}\boldsymbol{c} \tag{1.24}$$

we can deduce that we will have to deal with an ill-posed and ill-conditioned problem. The reasons for this are

1. To counter noise and system drift, we would like to use more harmonic components than are required for the solution of the problem. Thus the problem will be overdetermined.
2. The nonlinear dependency creating the harmonics results in large changes in the harmonic content even for small changes of the gradient field, i.e. small sample displacement, leading to a high condition number of the system matrix and an ill-conditioned problem.
3. The low-pass characteristic of the system, which especially affects higher order harmonics that determine the spatial resolution, results in noise amplification once the system matrix is inverted. This worsens the conditioning.

To solve the inverse problem, regularization should be performed to penalize solutions that are governed by system noise. With this addition, least-squares minimization is able to solve the over-determined problem.

Tikhonov regularization is routinely used for MPI reconstruction [30]. In its most basic form, it adds the norm of the solution vector multiplied with a regularization factor to the total residual error of a least squares problem:

$$\|\boldsymbol{A}\boldsymbol{c} - \boldsymbol{v}_{\text{meas}}\|_2^2 + \|\boldsymbol{\Gamma}\boldsymbol{c}\|_2^2 \tag{1.25}$$

where $\boldsymbol{\Gamma}$ is called the *Tikhonov* matrix and often implemented as $\gamma\boldsymbol{I}$, with $\boldsymbol{I}$ being the identity matrix and γ being the regularization factor.
This penalizes solutions for $\boldsymbol{c}$ with large norms, which correspond to small entries in $\boldsymbol{A}$ that are most likely affected by noise.

Thus the concentration is found as [30]

$$\boldsymbol{c} = \arg\left\{\min_{\boldsymbol{c}} \|\boldsymbol{A}\boldsymbol{c} - \boldsymbol{v}_{\text{meas}}\|_2^2 + \|\gamma\boldsymbol{I}\boldsymbol{c}\|_2^2\right\} \tag{1.26}$$

The solution of this least-squares problem can be calculated using singular value decomposition (SVD). Details about the practical numerical calculation of the SVD can be found in [31] and [32]. For speed considerations, when solving with large system matrices, iterative methods such as the modified *Kaczmarz* algorithm can be used [30, 33].

For two- or three-dimensional imaging, slightly different frequencies are used for the individual axes, forming a *Lissajous* trajectory and allowing easy distinction between the axis components in the frequency domain. Consequently, in addition to the harmonic content of the individual axes, intermodulation products can be found in the received signal, increasing the number of available harmonics. This is important in consideration of the square or cubic growth of unknowns for 2d or 3d system matrices. More detailed discussion of individual trajectories is provided in section 1.2.4.2 on page 19.

To some extent, a system matrix acquired through modeling techniques [34, 35] can also be used for reconstruction. Hybrid matrices calculated from both experimental data and model simulations [36] can be used to reduce noise in the system matrix and decrease the required number of calibration measurements.

1.2.3.2 Reconstruction in the time domain (x-space approach)

Analog [37] to the reconstruction in the frequency domain, image reconstruction can also be performed in the time domain, which is known as x-space reconstruction [29]. This approach starts with less generalized assumptions on scanner setup and particle behavior to arrive at a more obvious relationship between the received signal and the reconstructed image. However, non-ideal particle and system properties have to be taken into account [27], to achieve the same image quality as the calibration based approach using a system matrix. At this point we will briefly review the basic idea behind the x-space approach, while multi-dimensional x-space reconstruction [38], as well as the removal of relaxation effects [39] are beyond the scope of this introduction.

We start with the assumption of a linear, time-invariant gradient field $-Gx$ in x direction, that has a value of zero at the origin. Superposition of a homogeneous, time-varying magnetic field $H_0(t)$ results in a shift of the field free point:

$$H(x,t) = H_0(t) - Gx \tag{1.27}$$

$$H(t) - Gx = 0 \Rightarrow x_{\text{FFP}}(t) = \frac{H(t)}{G} \tag{1.28}$$

We can then express the time-varying field using the spatial position of the field free point:

$$H(t) = Gx_{\text{FFP}}(t). \tag{1.29}$$

Therefore the total field becomes

$$H(x,t) = G\left(x_{\text{FFP}}(t) - x\right). \tag{1.30}$$

Assuming a nanoparticle density $\rho(x,y,z) := \rho(x)\,\delta(y)\delta(z)$ along the x-axis, we can calculate the density of magnetic moments (thus the magnetization M) using

the Langevin function

$$M(x,y,z,\,t) = \rho(x,y,z)\,m\,\mathcal{L}\left(\frac{\mu_0 m H(x,t)}{k_\mathrm{B}T}\right) \tag{1.31}$$

$$= \rho(x,y,z)\,m\,\mathcal{L}\left(\frac{\mu_0 m G\,(x_\mathrm{FFP}(t)-x)}{k_\mathrm{B}T}\right) \tag{1.32}$$

The generated flux in x-direction is the surface integral

$$\Phi(x,t) = \iint\limits_S B\,dS = \iint\limits_S \mu_0 M\,dS \tag{1.33}$$

$$= \int\limits_{-\infty}^{\infty}\int\limits_{-\infty}^{\infty} \mu_0\,\rho(x)\,\delta(y)\delta(z)\,m\,\mathcal{L}\left(\frac{\mu_0 m G\,(x_\mathrm{FFP}(t)-x)}{k_\mathrm{B}T}\right) dy\,dz$$

$$= \mu_0\,\rho(x)\,m\,\mathcal{L}\left(\frac{\mu_0 m G\,(x_\mathrm{FFP}(t)-x)}{k_\mathrm{B}T}\right). \tag{1.34}$$

Then, using a detector with homogeneous spatial sensitivity[5)] $S(x) = S_0 = \frac{1}{\mathrm{m}}$, the total measured flux becomes

$$\Phi_\mathrm{tot}(t) = \int S_0\,\mu_0\,\rho(x)\,m\,\mathcal{L}\left(\frac{\mu_0 m G\,(x_\mathrm{FFP}(t)-x)}{k_\mathrm{B}T}\right) dx \tag{1.35}$$

$$= S_0\,\mu_0\,\rho(x)\,m\;*\,\mathcal{L}\left(\frac{\mu_0 m G}{k_\mathrm{B}T}x\right)\Bigg|_{x=x_\mathrm{FFP}(t)} \tag{1.36}$$

where $*$ denotes the spatial convolution in x.

In the common case, where a coil is used as detector, the resulting voltage is the time derivative according to *Faraday*'s law:

$$V(t) = -\frac{d\Phi_\mathrm{tot}}{dt} = -S_0\,\mu_0\,\rho(x)\,m\;*\,\dot{\mathcal{L}}\left(\frac{\mu_0 m G}{k_\mathrm{B}T}x\right)\Bigg|_{x=x_\mathrm{FFP}(t)} \frac{\mu_0 m G}{k_\mathrm{B}T}\dot{x}_\mathrm{FFP}(t) \tag{1.37}$$

The image equation can be found by defining the time derivative of the *Langevin* function as the point spread function PSF and removing all other terms from the equation by means of normalization:

$$\mathrm{Img}\,(x_\mathrm{FFP}(t)) = \frac{V(t)}{-S_0\,\mu_0\,m\,\frac{\mu_0 m G}{k_\mathrm{B}T}\,\dot{x}_\mathrm{FFP}(t)} \tag{1.38}$$

$$= \rho(x) * \dot{\mathcal{L}}\left(\frac{\mu_0 m G}{k_\mathrm{B}T}x\right)\Bigg|_{x=x_\mathrm{FFP}(t)}. \tag{1.39}$$

[5)] This sensitivity had to be introduced to fix a unit error in the original derivation. Alternatively, the integral in (1.36) can be replaced by a sum of the flux picked up by individual windings, which will not alter the unit and results in $S(x)$ being dimensionless, but also makes the convolution in (1.36) less obvious.

Therefore we can arrive with an image by calculating (1.38), possibly applying a deconvolution to improve resolution.

Since according to (1.39), the derivative of the *Langevin* function is the PSF of our image, it is worth taking a closer look. A common criterion to evaluate the resolution of a system is the full-width-half-maximum (FWHM) value of a point sample that is acquired with that system. For the *Langevin* function, we find the derivative

$$\frac{d}{d\xi}\mathcal{L}(\xi) = \frac{1}{x^2} - \operatorname{csch}(x)^2 = \frac{1}{x^2} - \frac{1}{\sinh(\xi)^2} \tag{1.40}$$

Using *L'Hospital*'s rule[6] we find the maximum value of $\frac{1}{3}$ at the origin and can determine the value of $\xi = \pm 2.0805$ where it has dropped to half of the maximum value. This allows us to determine the resolution of the scanner as

$$\mathrm{FWHM}_{\mathcal{L}} = \xi_{\mathrm{FWHM}} = 4.161 = \frac{\mu_0 m G}{k_\mathrm{B} T} x_{\mathrm{FWHM}} \tag{1.41}$$

$$x_{\mathrm{FWHM}} = \xi_{\mathrm{FWHM}} \frac{k_\mathrm{B} T}{\mu_0 m G} \tag{1.42}$$

which tells us that the spatial resolution is anti-proportional to the gradient strength of the scanner and the magnetic moment of the particles.

As mentioned before, relaxation effects should be removed from the image, either through a deconvolution with a PSF kernel that includes relaxation effects, or by using the superposition of a forward and a backward scan [27, 40].

1.2.4 Two-dimensional and three-dimensional imaging

1.2.4.1 Decoupling of signals produced by different axes

The transition from one-dimensional scans to two- or three-dimensional ones can be accomplished by choosing a slightly different frequency for every active axis. The superposition of several spatially orthogonal fields with different frequencies results in a two- or three-dimensional *Lissajous* movement pattern of the field free point.

Due to the different frequencies, it is easy to distinguish between the harmonics of different axes in the frequency domain. However, since now a surface or a volume is covered, the number of pixels or voxels increases with the power of the dimensions used. Since the pure harmonics of each axis can only be observed up to a certain number, they are insufficient to provide enough entries in the system matrix to allow reconstructions. Inclusion of inter-modulation products of different axes, created by the mixing on the nonlinear magnetization curve, allows to extract enough frequency components to reconstruct images in 2-d or 3-d.

1.2.4.2 Trajectories

As mentioned in the previous section, use of a separate drive frequency for each excitation axis produces a *Lissajous* trajectory for the FFP. The choice of frequencies

[6] Also known as L'Hôpital's rule, according to current French orthography.

however is not arbitrary. Apart from technical requirements, which will be covered in the hardware design part, the density of the pattern as well as the repetition time, after which the FFP has returned to its initial position and direction, are of interest.

Figure 1.5 visualizes the movement of a field free point through the imaging area or volume. Figure 1.5a shows the movement in two dimensions, moments before the FFP (cross) returns to its origin and completes the trajectory, while fig. 1.5b shows the FFP at the same time under three dimensional excitation. The added third frequency increases the repetition time necessary to reach the same point within the volume, therefore the trajectory in fig. 1.5b is far from complete.

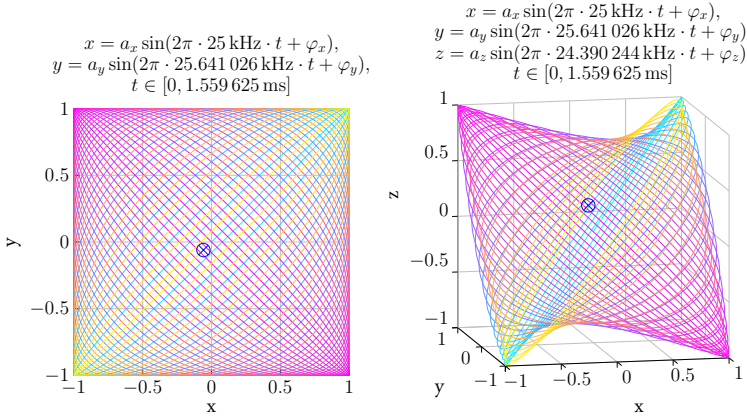

(a) Two-dimensional excitation

(b) Three-dimensional excitation

Figure 1.5: Lissajous trajectory for two and three-dimensional excitation. Time is visualized via color from cyan over magenta to yellow.

The procedure for selecting drive frequencies and calculation of repetition times can be performed as follows: After choosing a base frequency f_{Base} with the corresponding period T_{Base}, each frequency is calculated from the base by dividing it by an integer fraction N_x, N_y, N_z. This corresponds to the requirement that the periods T_x, T_y, T_z of the constructed drive frequencies are integer multiples of the base period. The dividers N_x, N_y, N_z should be chosen so that they are not integer multiples or divisors of each other. Calculation of the repetition time is then simply finding the least common multiple of the associated axes' divisors and multiplying that number by T_{Base}:

$$T_{\text{Rep}} = \text{lcm}\,(N_x, N_y, N_z) \cdot T_{\text{Base}} \tag{1.43}$$

where lcm returns least common multiple.

The density of the trajectory, which is important for pixel and voxel size and therefore affects image resolution, can be estimated for the two-dimensional case

$$x_{\text{FFP}}(t) = a_x \sin(\omega_x t) = a_x \sin\left(\frac{2\pi}{T_{\text{Base}} N_x} t\right) \tag{1.44}$$

$$y_{\text{FFP}}(t) = a_y \sin(\omega_y t) = a_y \sin\left(\frac{2\pi}{T_{\text{Base}} N_y} t\right) \tag{1.45}$$

by first considering the intersections of the x-axis at

$$t = \frac{N_y}{2} T_{\text{Base}} n \tag{1.46}$$

where $n \in \mathbb{N}^0$.
Since (assuming no phase-shift) the origin is always an intersection with the x-axis, we seek the smallest value of $a_x \sin\left(\left[\frac{N_y}{N_x} n\right] \pi\right)$ that is different from zero. Since the sine value is periodical in 2π this equals finding the smallest, non-zero value of $\frac{N_y}{N_x} n \mod 2$. Since N_x, N_y are integers, the smallest possible value for this is $\frac{1}{N_x}$. However, if N_x and N_y have common dividers, this becomes

$$x_{1,\text{FFP}} = a_x \sin\left(\frac{\gcd(N_x, N_y)}{N_x} \pi\right) \tag{1.47}$$

where gcd returns greatest common divider.
It is therefore useful to pick an even divider[7] N_x and use $N_x \pm 1$ for N_y, N_z. For the y axis, the estimation results in

$$y_{1,\text{FFP}} = a_y \sin\left(\frac{\gcd(N_x, N_y)}{N_y} \pi\right) \tag{1.48}$$

and the density can be approximated by $\sqrt{(x_{1,\text{FFP}})^2 + (y_{1,\text{FFP}})^2}$ in the two-dimensional case.

The estimations (1.47), (1.48) for the trajectory density are also convenient for the three-dimensional case, although they are less exact there and the result should be multiplied by $\sqrt{3/2}$ to account for the third axis. It should also be noted that while the trajectory is denser at the edges, due to lower slew-rate of the sine there, the resolution in these areas is usually inferior to the center, owing to the reduced number of particle harmonics generated at the FOV edges (cf. figure 1.4 on page 15).

1.2.5 Particle dynamics and mobility MPI

In this section we will briefly review the fundamental concepts of mobility MPI. Since this work focuses on the implementation of a MPI scanner suitable to acquire mobility information, we will mostly restrict the scope to the aspects that influence hardware design. The interested reader is directed to the PhD thesis of Thilo Viereck [17] for in-depth information on mMPI reconstruction and modeling techniques.

[7] Otherwise, 2 will always be a common divider for two of the three.

1.2.5.1 Mobility MPI concept

The basic idea behind mobility MPI (mMPI) is to provide functional imaging capabilities for MPI by measuring the Brownian relaxation time τ_B, which itself is dependent on the viscosity of the particle environment and the hydrodynamic diameter.

In its simplest form, this means differentiating between particles which can rotate freely within the medium and those that are completely immobilized. The range in between can be achieved by either varying the viscosity of the medium or by varying the hydrodynamic diameter. The latter method can be used e.g. in homogeneous binding assays, where functionalized groups on the particle surface bind with a molecule of interest, increasing the particle diameter in the process and thus the hydrodynamic size.
A similar concept has been successfully demonstrated using magnetic relaxometry experiments [41], and also employing a rotating field setup [42]. The benefit of applying the same idea on the MPI process is the perspective of spatially resolved data. Such information is especially valuable if the experiment can be performed in vivo.

1.2.5.2 Requirements for mobility MPI (mMPI)

Taking into account the fundamental dynamic particle behavior discussed in section 1.1.4 on page 6, especially the effective relaxation time constant (1.6), it becomes apparent that mMPI requires that a significant fraction of particles exhibit relaxation governed by the *Brownian* relaxation process, i.e. $\tau_B \ll \tau_N$. Otherwise the *Néel* relaxation, which is only dependent on the particle's magnetic core and temperature, will prevent observation of the mobility information. Figure 1.6 illustrates the parameter range suitable for mMPI. It should be noted however, that the field dependence of the time constants has not been included in these graphics, i.e., the values are only accurate for small field values. Since as of this writing, the field dependency has only been investigated for a small parameter range and a limited number of particles systems, it is not possible to apply the necessary corrections to large areas of the parameter space. In order to estimate the influence of the field dependency on the aforementioned results, the following can be considered: Experimental results by *Dieckhoff* et al. for the single core particle system SHP 25 (Ocean Nanotech, San Diego, CA, USA) with 25 nm core size evaluated at up to 9 mT showed a dependency of the *Néel* time constant that followed [43]

$$\tau_{N,H} = \frac{\tau_N}{\sqrt{1 + A\,\xi^C}}, \tag{1.49}$$

where the fit parameters $A = 1.97$ and $C = 3.18$ yielded the best fit [43]. For this particle system and typical field conditions used for MPI, ξ is in the range of 15, yielding an effect in the order of factor $\tau_{N,H}/\tau_N = 0.0096$. For the *Brownian* time constant, similar investigations based on the *Fokker-Planck* equation by *Yoshida* et al. [44] resulted in

$$\tau_{B,H} = \frac{\tau_B}{1 + 0.126\,\xi^{1.72}}. \tag{1.50}$$

Evaluating this formula as before for $\xi = 15$ gives $\tau_{B,H}/\tau_B = 0.0914$. Therefore, for the SHP 25 particle system, the relevant correction factor at 25 mT would be $\tau_{B,H}/\tau_{N,H} = 9.51$. Considering that figure 1.6 shows 25 orders of magnitude, a factor of 9.5, although relevant, only leads to a relatively small shift. Again, it should be noted that this correction factor is only known for this specific particle system and a very limited set of parameter and field conditions. A more general correction is currently not available and existing models provide inconsistent results.

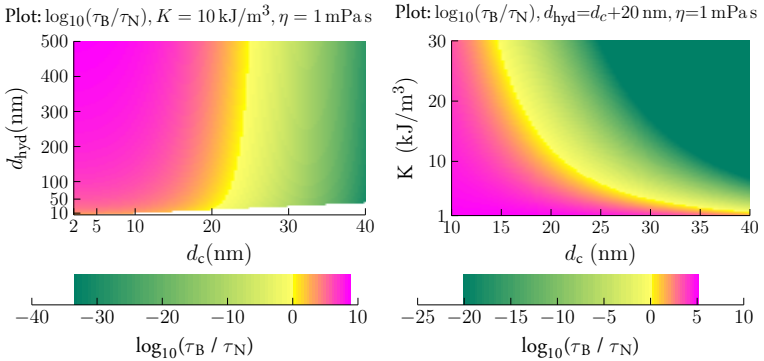

(a) $\frac{\tau_B}{\tau_N}$ depending on d_c, d_{hyd} (b) $\frac{\tau_B}{\tau_N}$ depending on d_c, K

Figure 1.6: Orders of magnitude between τ_B and τ_N with emphasis on d_c and a) d_{hyd}, b) K. Green and light yellow areas mark the parameter range where mMPI can be performed. $T = 294.15\,\mathrm{K}$

Returning to the general matter of mMPI preconditions, another necessary condition is to excite the particles at frequencies ω well below the inverse of the *Brownian* time constant $\frac{1}{\tau_B}$ [17], which directly limits the maximum drive frequency. It is, however, possible to combine faster excitation signals with a superimposed slow modulation to reveal Brownian relaxation [17], although additional reconstruction effort is required for this.

1.2.5.3 Particle dynamics under multi-dimensional excitation

When we expose a magnetic nanoparticle to two alternating external fields in different spatial directions, it is reasonable to assume that the same fundamental concepts of particle dynamics, as we have discussed in section 1.1.4 on page 6 still apply. Unfortunately, exact calculation of the ensemble magnetization (now being a three-dimensional vector), using the underlying stochastic differential equations, becomes much more involved in that case.

The effective field method, which we have reviewed in section 1.1.4.5 on page 8, is able to cover dynamic relaxation effects under 3-d field conditions, but does not

include *Néel* relaxation. Considering the exponential dependency of the *Néel* constant with the core diameter, it is reasonable to assume that a large quantity of particles will either be dominated by the *Brownian* relaxation or by *Néel* relaxation. The small number of particles where *Brownian* and *Néel* time constants fall into the same order of magnitude allows the separation of those particles which always relax through the *Néel* process, from the *Brownian* fraction. The *Néel* process dominated particles can be treated as a background or baseline signal [17], and therefore be subtracted before evaluating mobility effects.

Implementations of models including both relaxation behaviors, which are able to predict the response of large particle ensembles under three dimensional excitation, are at the time of this writing not available and are still subject of contemporary research. We will therefore restrict ourselves to simpler models or experimental data.

1.2.5.4 Techniques for mobility MPI

As we have learned from the previous section, we need to separate particles with relaxation behavior predominantly governed by the *Néel* process from those that are relaxing mostly due to the *Brownian* process and are therefore suitable for mMPI. To exclude their response from our evaluation we need additional information, since we still want to reconstruct spatially resolved particle concentration as well.

Several techniques to accomplish this are discussed by *Thilo Viereck* [17] and will be summarized here:

Multi-Frequency Approach

The chronologically first idea was adapted from AC susceptibility measurements and depends on multiple excitation frequencies. For a known particle system, drive frequencies above and below the inverse of the *Brownian* time constants are chosen. When the same spatial distribution is examined, differences in the reconstructed image must be a consequence in differences of the Brownian time constant and therefore particle mobility. The contribution of fast *Néel* particles, that are always part of the image, can be considered as constant and therefore vanishes when the difference is used. Analyzing simulated data it becomes apparent that the phase of the image data is of major importance [17]. This can also be verified by experimental data, see section 3.1.3.

F-Space Approach

Starting from a conventional MPI reconstruction in the frequency domain, the effect of particle relaxation on the system matrix can be studied.
Similar to the previous discussion, it turns out that response of the particles relaxing through the *Néel* process constitutes a system matrix of their own, which is included in the total received signal. This can be determined by experiments using freeze-dried particles, where the Brownian process has been blocked. Consequently, the Brownian

part of the system matrix can be calculated by subtracting the "*Néel*"-matrix from the matrix containing both contributions. Again, a complete system matrix is revealed. Alternatively, model based data can be used to construct the *Brownian* matrix [17].

X-Space Approach

Continuing from the observations made from figure 1.4 on page 15, more specifically the shift of the maximum of the point spread function due to dynamics, the mobility of particles can be estimated using this effect [45]. In addition to the delayed maximum, there is also a decrease in amplitude.
Since the PSF is usually viewed on a linear scale, the most prominent visible effects arise from the fundamental and low-ordered harmonics. They are mainly dependent on the slew-rate of the field, so that increasing the drive field amplitude at a constant frequency gives very similar results to an increased drive field frequency at constant amplitude [46].
The actual location of the tracer material can be deduced from a scan in different directions. In the simplest case, a forward and backward scan can be used. Knowing that the concentration distribution is the same for both scans, relaxation effects can be removed and the spatial distribution can be recovered [17]. For complex excitation scenarios, such as *Lissajous* trajectories, this simple scheme is inaccurate as the curvature of the FFP movement also influences the response.

Vector acquisition (3-dimensional data acquisition)

By measuring all spatial components of the magnetization signal, the instantaneous direction of the particle magnetization can be compared to the local field conditions at the spatial point of the particles. Any differences that arise must be due to a dynamic lag of the magnetization and therefore particle relaxation effects. Thus it is possible to deduce mobility information from this comparison [17]. However, the dependency between the resulting signal and the dynamics is more convoluted, once more than a single sample populates the FOV. As of this writing, no separation technique in the case of a spatial distribution has been presented for this method. It is however, an excellent tool to verify modeling techniques by comparing the estimated magnetization direction to experimental data.

Direct Approach

Extending the previous idea of vector acquisition and considering the unique field conditions at every point of the FOV due to the gradient field, the field changes according to the FFP *Lissajous* trajectory can be seen as a relaxation experiment. In contrast to classical magnetorelaxometry (MRX), only the transient behavior is observed and no steady state is reached. Again, reconstruction of a particle distribution becomes challenging.

Color MPI

In addition to the above techniques, the color-MPI reconstruction technique, originally proposed for the differentiation between several particle types [47], can be applied to mobility information [48]. The basic idea is to combine the system matrices of different particles to a compound matrix that is used to reconstruct the data acquired from a mixture of aforementioned particles.
To gain additional information, as required for the reconstruction of spatial distribution and separation of particle types at the same time, different excitation parameters can be used. Originally, different drive field amplitudes have been used [47],[49]. However, to reveal mobility information, different drive frequencies can be used either in addition or as a replacement for different amplitudes, so that this technique becomes similar to the multi frequency approach, as far as the experimental setup and execution is concerned. Despite that, the process of data evaluation between color MPI and the multi-frequency approach is different.

1.2.5.5 Implementation of mMPI

Considering the different techniques proposed for mMPI and reviewing their requirements, it can be concluded that the setup necessary for their implementation has close resemblance to traditional MPI scanners. To have a wide variety of techniques available, a multi frequency system is desirable, as well as vectorial signal reception. Additionally, a FFP setup is preferable to a FFL due to the simpler field conditions and fewer particles that contribute to the receive signal at any given instant. The construction of such a setup will be the main topic of this work and will be discussed in detail in chapter 2.

1.3 Passive Components

This chapter briefly reviews parasitic properties and equivalent circuits for passive components relevant for the construction of a MPI scanner. Since the design of power amplifiers, which are specifically engineered to meet the requirements of a MPI scanner is not feasible over the course of this work, the system has to cope with the performance limits of available amplifiers and improve signal quality by means of passive filters. The main focus here is on linearity, since this is the most crucial aspect of MPI hardware and at the same time one of the most difficult to achieve properties in a high-power amplifier.

Considering filter design, parasitics such as losses and self-resonances become important, which ultimately determine the performance and bandwidth limit of the realized filter. While this may sound rather basic, achieving high linearity, high power capability and the necessary bandwidth at the same time proves to be a challenging combination.

1.3.1 Capacitors

Capacitors exhibit more subtle non-ideal properties than inductors. Compared to coils, their overall performance is often closer to that of the ideal component [50]. However, their tendency to exhibit intrinsic non-linear effects deserves closer attention when used for MPI applications.

1.3.1.1 RLC Capacitor Model

The basic equivalent circuit for a capacitor is depicted in figure 1.7 and shows elements that model its losses as well as its series resonance at $\omega_{\text{srf}} \approx \frac{1}{\sqrt{L_s C}}$. The parallel resistance R_p can often be neglected for applications in the kHz range.

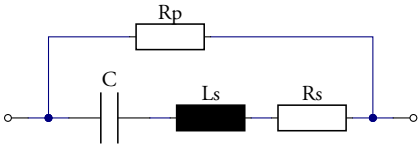

Figure 1.7: Equivalent circuit of a basic capacitor model, incorporating losses and self-resonance.

The most deciding factor for the performance of a capacitor is its dielectric material, which we will cover next.

1.3.1.2 Dielectric Absorption

Most capacitor types use a dielectric other than air or vacuum. While reducing the required component size considerably, almost all dielectrics in use for capacitors exhibit

an effect called dielectric absorption, where charge is stored in the dielectric that is not released instantly when the capacitor is discharged. Therefore, after removing the low-impedance load that discharged it, the voltage of a capacitor will *recover* to some degree, as the charge in the dielectric is released [51]. For AC applications, dielectric absorption manifests itself as additional, frequency dependent losses [52] and can be modeled by introducing parameters that scale with $s^{\frac{m}{n}}$, where $\frac{m}{n} \in (0;1)$ [53, 54]. Whether dielectric absorption will be responsible for distortions is highly dependent on the application. While in passive circuits the variation of the capacitance with the applied voltage (see next section) will most likely dominate the nonlinear effects, switching applications like zeroing integrators, sample and hold circuits and VCOs can exhibit nonlinear effects due to dielectric absorption [55–57].

1.3.1.3 Nonlinearities in capacitors

As mentioned in the previous section, the properties of many dielectrics depend on the applied voltage (and therefore the applied electric field). Ceramics are especially prone to this effect. It should be noted that even temperature compensated ceramics (such as C0G) are affected. To complicate matters further, the voltage dependent effects are highly unrelated to the behavior over temperature [58], so that the manufacturers' datasheet for the individual component type has to be checked.

Foil capacitors on the other hand, together with mica dielectrics, achieve much better linearity and low dielectric absorption. Contrary to mica capacitors, foil capacitors are available in a wide range of values [51]. Polypropylene capacitors have proven especially useful for MPI [59]. To minimize non-linear effects it is beneficial to choose capacitors with sufficient high voltage and current ratings, since aging of polypropylene capacitors causes harmonic distortion [60]. Since there is usually also a derating with operating frequency and ambient temperature, parallel and series arrays are often required to achieve sufficient headroom to the maximum ratings. Another source for nonlinearity in capacitors is mechanical deformation under the electrostatic forces subjected to the electrodes [61]. Stiff mechanical construction helps to reduce these effects. To this end, round foil capacitors tend to perform better than rectangular types.

1.3.2 Coils

For MPI applications, coils are used for three different purposes:

1. as magnetic field generators for static or AC fields (cf. section 2.2.3 on page 82)
2. as receive coils to detect magnetic fields (cf. section 2.2.7.1 on page 111)
3. as filter coils to construct inductors to realize a specific transfer function (cf. section 2.2.5 on page 102 and section 2.2.7.2 on page 114)

Since each of these applications has slightly different requirements, individual optimization techniques will be given in the corresponding sections. At this point, we limit our scope to generalized aspects that lay the foundation for further considerations.

As we have seen in section 1.2.2, spatial encoding in MPI relies on the non-linearities of the magnetic nanoparticle tracers. Because the system should not mask the non-linearities of the particles, highly linear components are required, which prohibits ferromagnetic core materials from being used in all coils in the system subjected to dynamic fields. Therefore, from this point onward, air-core coils are considered if not explicitly stated otherwise.

1.3.2.1 RLC coil model

Similar to the capacitor, we can model losses and parallel self-resonance of a coil at $\omega_{\text{srf}} \approx \frac{1}{\sqrt{LC}}$ by using a simple R-L-C-model, as depicted in figure 1.8. The impedance of this one-port element is

$$Z = \frac{L\, R_{\text{par}} s + R_{\text{ser}}\, R_{\text{par}}}{C_{\text{par}} L\, R_{\text{par}}\, s^2 + (C_{\text{par}} R_{\text{ser}}\, R_{\text{par}} + L)\, s + R_{\text{par}} + R_{\text{ser}}}. \tag{1.51}$$

This model does not take the following aspects into account, some of which we will incorporate/consider in later sections or chapters:

1. Losses due to the skin effect, which would result in a resistance scaling with frequency proportional to $\sqrt{f}$
2. Losses due to the proximity effect
3. Losses due to the dielectric surrounding the coil windings. Especially if these losses are due to coolants, the mechanisms may be of electrochemical nature, with no closed form expression available to model them.
4. Second and higher order resonances, as well as resonances with the environment.
5. Inductive coupling of several coils in an assembly due to non-ideal orthogonality or insufficient spacing due to practical limitations

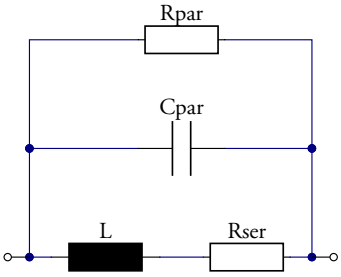

Figure 1.8: Equivalent circuit of a basic coil model, incorporating losses and self-resonance (cf. [62]).

1.3.2.2 Skin-effect, Proximity-effect

The skin effect describes a phenomenon in electrical conductors that carry time-varying currents, where self-induced eddy currents created by the associated magnetic field partially compensate the current flow in the conductor, leading to a non-uniform current distribution across the conductor's surface. This leads to high current densities at the surfaces of the conductor while the current with increasing depth drops exponentially. For round, homogenous conductors, the exponent is determined by the negative ratio of depth from the surface divided by the skin depth δ.

As a result, the effective cross sectional area of the wire is reduced, leading to additional resistive losses. In the kHz regime, this can be partially offset by the usage of litz wire, which consists of isolated individual wire strands. By increasing the wire's surface area, the losses of the skin effect can be reduced.

The proximity effect describes a similar influence on the current distribution in conductors, but differs from the skin effect with regard to the origin of the responsible magnetic fields. In case of the proximity effect, the magnetic fields are caused by other conductors in close proximity of the wire (hence the name). Unlike the skin effect, it not only depends on the geometry of the influenced conductor, but also the arrangement of nearby conductors and conductive surfaces, since they all affect the magnetic field conditions. The proximity effect also reduces the active conductor cross section and results in additional resistive losses.

Skin- and proximity effect losses can be incorporated using a equivalent circuit modeling approach outlined by *Kim* et al. [63]. However, numerical simulation is required for all but the most simple geometries, if no empirical data for the losses are available.

If the simulated geometry accurately describes the actual coil, field simulation results closely match measured data. To accomplish this, it is necessary to model individual wires in a coil, to properly account for the proximity effect. The helix structure can often be neglected, so that boundary conditions for a revolved model can be chosen for solenoid and Helmholtz coils. In the case that litz wire is used, the effective μ_r method [64] is sufficient to account for the stranding in the frequency range of MPI. Figure 1.9 shows simulated data, acquired with the FEMM package [65, 66], in comparison with measured results for a single layer solenoid coil with 43 windings, using litz wire composed of $45 \times 0.2\,\mathrm{mm}$ strands. As is apparent in fig. 1.9b, the real part of the coil impedance is accurately predicted by the simulation up to the self-resonance. The figure depicts the simulation results of several models: A simple model where the cross sectional outline of the coil is given and the simulation package assumes uniformly arranged wiring within that area (Simp.), and a model of individual wires (Indiv.). In both cases, litz wire was used as conductor. Both models were investigated with two different boundary conditions that showed a rectangular or circular shape. The results are compared to measured data (Meas.) and generally show good agreement up to the first resonance. The simple model is influenced by the boundary conditions, which is a result of the larger mesh size generated by the program, while the complex model using individual wires remains unaffected by them. It also

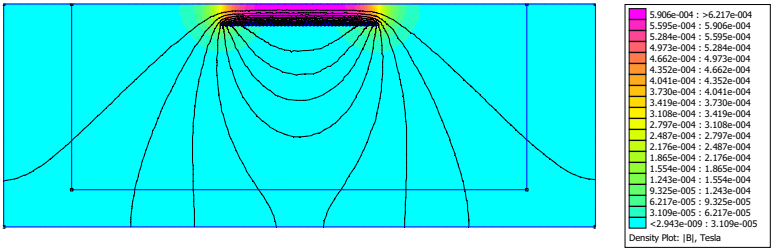

(a) Simulation model (rotated by 90 degree, the topmost line is the symmetry axis of the axisymmetric problem)

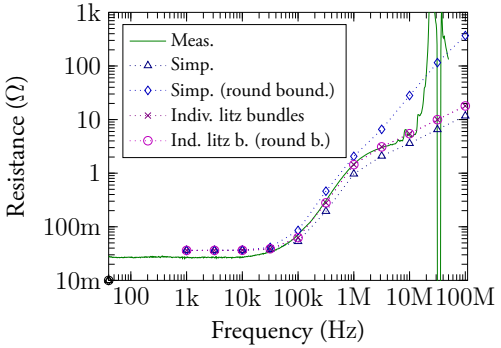

(b) Simulation results for AC coil losses in comparison with measured data.

Figure 1.9: Accurately determining skin- and proximity effect losses in the regime up to 1 MHz: Simulation with individual litz wire bundles, each simulating strands with the effective μ_r method in comparison with simpler models only simulating the total wire package and measured data. Details on the graphs are given in the text.

shows more accurate results because of the better incorporation of the proximity effect. Another useful property is the estimation of stray capacitances between conductors when using the same geometry for an electrical simulation.

With the relative deviation below that of the DC resistance error, ac losses only pose a problem for geometries where a full 3-dimensional simulation is required to determine the field conditions (e.g. toroidal coils). Due to the complexity of such simulations, modeling individual wires is currently not feasible for the intended application.

To achieve the same field conditions for the constructed coil, careful positioning of the connecting wires is required, since they also contribute to the proximity effect. The best practice is therefore to keep both connecting wires short and in close prox-

imity so that their fields tend to cancel each other and the losses they cause can be neglected.

1.3.2.3 Self resonant frequency

The self resonant frequency of air core inductors is lower than that of coils with soft magnetic cores of the same inductance value. This is due to the higher number of turns required to achieve that inductance value, which consequently leads to an increased number of inter-turn capacitances. Multi-layer coils are especially affected, since the inter-layer voltages exceed the inter-turn voltages, leading to larger displacement currents bypassing the coil structure. The total effective self capacitance of these coils is thus dominated by inter-layer capacitances [67].

1.3.2.4 Effects of Surrounding Medium

Unfortunately, dielectric and media losses are not as easily modeled as those caused by the skin- or proximity-effect, especially if the coil windings are surrounded by a coolant such as water. Usually, a complex frequency dependency is observed in the resistance of a coil in these cases, which can only be expressed by several frequency terms with fractional exponents [54] and cannot be described accurately using the simple RLC model of figure 1.8, even if it is extended to include frequency dependent copper losses in R_{ser}. This is due to the electrochemical nature of these losses, which make model creation from measured data a difficult task. This complex behavior is used in the field of electrochemical impedance spectroscopy to evaluate the process of chemical reactions. A good overview of the models used for that task is given by *Gómez-Aguilar* et al. [54]. For MPI applications, where a low resistance is desirable, the effect can be mitigated by using wire servings that isolate the wires from the coolant (cf. figure 1.10).

Influence of conductivity of the surrounding medium

In case of liquid coolants, ions within these can also be subject to eddy current losses or ohmic losses if they are in direct contact with windings at different potential. Since the conductivity is usually very low compared to metals, their contribution is often negligible in presence of other loss mechanisms. They can, however, influence the quality factor of parallel coil resonances in a similar way as the finite non-zero parallel conductivity of capacitors does.

Influence of the dielectric on losses

Since accurate prediction of the influence of the dielectric on losses is often not feasible, prototyping is an adequate method to estimate the effects and has been used throughout this work. Nevertheless, geometry and manufacturing can have a large impact and are difficult to prototype with reasonable effort.

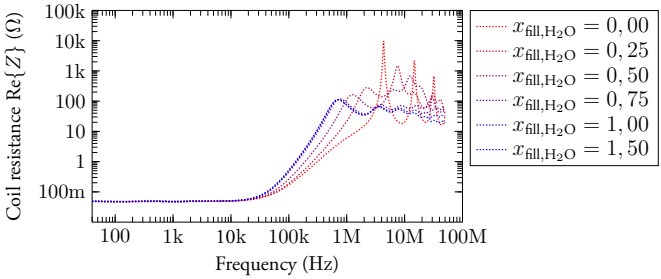

(a) Litz wire coil with silk serving

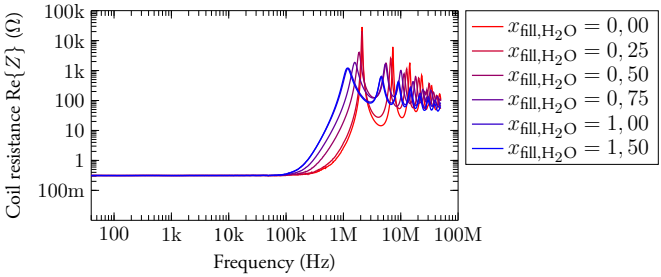

(b) Litz wire coil with mylar serving

Figure 1.10: Change in resistance and self resonant frequency when immersing a solenoid coil up to a certain fraction of its height in water, (a) for litz wire with silk serving and (b) for litz wire with mylar serving. Note the higher quality factor and reduced shift of the resonance with the Mylar for the immersed coil.

It is possible to mitigate the influence of the coolant dielectric by separation. Using wires with polymer coating can reduce the effects of the coolant and thus help with the prediction of coil parameters.

Influence of the dielectric on the self resonance

The influence of the dielectric on the self resonant frequency of a coil (cf. figure 1.10) can be predicted through simulation methods [68] or by means of calculating the turn-to-turn capacitances, using the (approximated) winding geometry [69]. The accuracy depends on the complexity of the geometry and the ability to model it accordingly. Manufacturing tolerances and shape variations (especially when using litz wire) limit accuracy. Simulation of individual wires (as with AC loss modeling) is required to adequately represent the coil. Additionally, this offers deeper insight into mutual inductances and capacitances between windings. For solenoid coils, reasonably accurate

prediction of the first parallel resonance and series resonance is possible if the coil is precisely modeled (cf. section 1.3.2.7 and section 2.2.3.5 on page 92).

1.3.2.5 Nonlinearities in Coils

Unlike capacitors, coils can be effectively constructed in such a way that nonlinear effects have such low magnitudes, that they become negligible. This requires air core coils or coil formers made of non-ferromagnetic materials, since even a non-saturated ferromagnetic core generates enough harmonic content to prevent MPI imaging. As a consequence, flux leakage is much higher, so that toroidal windings should be used for all coils, except field generators, to minimize stray fields as much as possible. Separation to other coils and metallic surfaces is necessary as well and the surrounding environment should be free from ferromagnetic materials. Similarly, coolants should be carefully chosen. Mineral oils and de-mineralized water have been found to produce acceptable results. If litz wire is employed to reduce skin effect losses, careful manufacturing is required, since the arcing at a single broken strand of a litz wire bundle can introduce harmonics of the fundamental and therefore generate substantial non-linearity. Another factor for non-linearities are mechanical vibrations, which can be minimized by covering the coil e.g. in pouring resin, therefore preventing movement of individual wires relative to each other. Coils should also be fixed to a solid structure to prevent movement relative to other parts of the system.

1.3.2.6 Magnetic Field and Homogeneity

Homogeneous fields are required for MPI Imaging, especially when generating drive fields. Salmon et. al. [70] identify three criteria to express the field homogeneity in a volume by a single quantity:

1. Non-uniformity, defined as the root-mean-square deviation in the desired direction $\boldsymbol{e}_s$ from the mean field magnitude, evaluated at all points of interest $\boldsymbol{r}_k$.

$$NonUni = \frac{\sqrt{\sum_{k=1}^{N} \left(\left(\boldsymbol{B}_{(\boldsymbol{r}_k)} - \overline{\boldsymbol{B}_{(\boldsymbol{r})}} \right) \cdot \boldsymbol{e}_s \right)^2 \over N-1}}{\overline{\left| \boldsymbol{B}_{(\boldsymbol{r})} \right|}} \tag{1.52}$$

   The same can also be calculated for the magnitude. In case of good alignment of $\boldsymbol{e}_s$ and $\boldsymbol{B}_{(r)}$ in the sample volume, this yields the same result.

2. Peak-to-peak (in-)homogeneity, the difference between the maximum and minimum field magnitude in the desired direction $\boldsymbol{e}_s$, relative to the center value $\boldsymbol{B}_{(\boldsymbol{r}_c)}$

$$Inh = \frac{\max\limits_{\boldsymbol{r}} \left(\boldsymbol{B}_{(\boldsymbol{r})} \cdot \boldsymbol{e}_s \right) - \min\limits_{\boldsymbol{r}} \left(\boldsymbol{B}_{(\boldsymbol{r})} \cdot \boldsymbol{e}_s \right)}{\left| \boldsymbol{B}_{(\boldsymbol{r}_c)} \cdot \boldsymbol{e}_s \right|} \tag{1.53}$$

3. Relative uniformity, the percentage of areas with magnitudes within a certain range around the center value, e.g. $\pm 5\%$

In addition to these, for MPI, two additional quantities are of use:

4. Directional nonuniformity, the average of the magnitude of the angle between the actual field vector and the vector of the desired direction $\boldsymbol{e}_s$.

$$DirNonUni = \frac{180°}{\pi} \sum_{k=1}^{N} \frac{\arccos\left(\frac{\boldsymbol{B}_{(r_k)}}{\left|\boldsymbol{B}_{(r_k)}\right|} \cdot \boldsymbol{e}_s\right)}{N} \tag{1.54}$$

where $\arccos\left(\frac{\boldsymbol{B}_{(r_k)}}{\left|\boldsymbol{B}_{(r_k)}\right|} \cdot \boldsymbol{e}_s\right)$ calculates $\measuredangle\left(\boldsymbol{B}_{(r_k)}, \boldsymbol{e}_s\right)$.

5. Maximum directional nonuniformity, the maximum of the magnitude of the angle between the actual field vector and the vector of the desired direction $\boldsymbol{e}_s$.

$$MaxDirNonUni = \max_{r} \left\{ \arccos\left(\frac{\boldsymbol{B}_{(r_k)}}{\left|\boldsymbol{B}_{(r_k)}\right|} \cdot \boldsymbol{e}_s\right) \right\} \frac{180°}{\pi} \tag{1.55}$$

The criteria listed above are easily applied to simulation results and can serve to objectively quantify the field homogeneity of the design. However, verifying these results experimentally for an implemented coil is challenging, since few magnetic sensors exist that will accurately measure the magnetic flux density vector at a point small enough to give precise data for comparison. Perpendicularity and relative position of the sensor axes is also an issue that limits measurement accuracy.

1.3.2.7 Predicting coil impedances

Although for the MPI coil system the homogeneity and harmonic purity of the magnetic drive field is one of the major goals, the coil impedance also has a major influence. Besides determining power losses and maximum drive frequency through the self resonant frequency, it also affects the design of the transmit filters and influences their effectiveness above the drive frequency. Since the latter is of utmost importance to achieve a clean drive signal, predicting the impedance of drive coils as early as possible in the design process is beneficial.

Several works exist that have established methods to predict coil impedances of solenoid coils either through simulation methods [68, 71] or analytical formulae [69, 72, 73]. Since both, slightly bend and reinforced solenoids as well as the individual coils of *Helmholtz* pairs can be approximated as an ideal solenoid coil, they apply to the drive coils used here (cf. section 2.2.3). For the modeling in this work, an approach based on these methods has been used that was adapted to include the effect of liquid coolants and was implemented to be used in conjunction with common circuit solvers. Section 2.2.3.5 on page 92 explains the details of the developed method while this section briefly reviews the techniques it extends.

Modeling stray capacitances analytically

Massarini et al. have developed a model for the stray capacitance between coil windings, assuming a staggered pattern and densely packed windings [69]. For a basic cell with an active angle of $\frac{\pi}{6}$ to its neighboring windings, they arrive at the turn to turn capacitance C_{tt} [69]

$$C_{\mathrm{tt}} = \varepsilon_0 l_t \frac{2\varepsilon_{\mathrm{r,in}} \arctan\left[\frac{\left(-1+\sqrt{3}\right)\left(2\varepsilon_{\mathrm{r,in}}+\ln\frac{D_{\mathrm{in}}}{D_{\mathrm{cu}}}\right)}{\left(1+\sqrt{3}\right)\sqrt{\left(2\varepsilon_{\mathrm{r,in}}+\ln\frac{D_{\mathrm{in}}}{D_{\mathrm{cu}}}\right)\ln\frac{D_{in}}{D_{cu}}}}\right]}{\sqrt{2\varepsilon_{\mathrm{r,in}}\ln\frac{D_{\mathrm{in}}}{D_{\mathrm{cu}}} + \left(\ln\frac{D_{\mathrm{in}}}{D_{\mathrm{cu}}}\right)^2}} \tag{1.56}$$

Here $\varepsilon_{\mathrm{r,in}}$ is the relative dielectric constant of the insulation, D_{in} its outer diameter and D_{cu} the diameter of the conductor.

Hole et al. [73] have presented similar calculations that assume the stacking of wires of different layers. However, when applying the results to water cooled coils, the approach of *Massarini* yielded results that were in better agreement with FEM modeling and measured data [74].

Analytic calculation of self- and mutual inductance

For the special case of a solenoid coil, the self inductance of individual windings can be calculated accurately using elliptic integrals and expressed in closed form [75, 76] as

$$L_m = \mu_0 R \left(\ln\left(\frac{8R}{r_{\mathrm{cu}}}\right) - 2 + \frac{Y}{2}\right), \tag{1.57}$$

where R is the coil radius and Y is a parameter that accounts for the current distribution in the wire. It has a value of 0 when assuming surface currents and $\frac{1}{2}$ for a homogeneous current density across the wire cross section (e.g. for litz wire). μ_0 is the vacuum permeability.

To calculate the mutual inductance between the coaxial windings, *Maxwell*'s formula can be used. Assuming two wire loops m, n with radii R_m and R_n and axis positions z_m, z_n, the mutual inductance can be calculated as [75, 77]

$$M_{m,n} = 4\pi\sqrt{R_m R_n}\left(\left(\frac{2}{k} - k\right)F_k - \frac{2}{k}E_k\right) \tag{1.58}$$

$$k = \frac{2\sqrt{R_m R_n}}{\sqrt{(R_m + R_n)^2 + (z_m - z_n)^2}}. \tag{1.59}$$

Here F_k and E_k are the complete elliptic integrals of the first and second kind respectively with the parameter k.

Modeling of coil losses

For the case of solenoid coils, *Reatti* et al. and *Bartholi* et al. have developed a closed form expression that determines AC losses due to the skin- and proximity effect and calculates the AC resistance of a solenoid coil made of litz wire as [78, 79]

$$\begin{aligned} R_{\mathrm{ac}} = \; & R_{\mathrm{dc}} \frac{\gamma_{\mathrm{s}}}{2} \left[\frac{1}{n_{\mathrm{s}}} \frac{ber\,\gamma_{\mathrm{s}}\; bei'\gamma_{\mathrm{s}} - bei\,\gamma_{\mathrm{s}}\; ber'\gamma_{\mathrm{s}}}{ber'^{2}\gamma_{\mathrm{s}} + bei'^{2}\gamma_{\mathrm{s}}} \right. \\ & + \left\{ (-2\pi) \left(4 \frac{{N_L}^2 - 1}{3} + 1 \right) n_{\mathrm{s}} \left({\eta_1}^2 + {\eta_2}^2 \frac{p}{2\pi n_{\mathrm{s}}} \right) \right. \\ & \left. \left. \cdot \frac{ber_2\gamma_{\mathrm{s}}\; ber'\gamma_{\mathrm{s}} + bei_2\gamma_{\mathrm{s}}\; bei'\gamma_{\mathrm{s}}}{ber^2\gamma_{\mathrm{s}} + bei^2\gamma_{\mathrm{s}}} \right\} \right], \end{aligned} \tag{1.60}$$

where the DC resistance of the wire is $R_{\mathrm{dc}} = \frac{4 N_{\mathrm{t}} l_{\mathrm{t}}}{n_{\mathrm{s}} \sigma \pi {d_{\mathrm{s}}}^2}$. l_{t} is the average length of a single turn, N_{t} the total number of turns, n_{s} is the strand count of the litz wire, d_{s} the diameter of a single strand's conductor and σ its conductivity. $\gamma_{\mathrm{s}} = \frac{d_{\mathrm{s}}}{\delta\sqrt{2}}$, $\delta = \sqrt{\pi f \mu_0 \mu_r \sigma}^{-1}$ is the skin depth, μ_r the relative permeability of the strands and f the frequency. N_{L} is the layer count. The external porosity factor is $\eta_1 = \frac{d_{\mathrm{o}}\sqrt{\pi}}{2 t_{\mathrm{o}}}$, and $\eta_2 = \frac{d_{\mathrm{s}}\sqrt{\pi}}{2 t_{\mathrm{s}}}$ is the internal porosity factor, d_{o} is the outer diameter of the litz wire bundle without serving, t_{o} is the distance between adjacent windings, t_{s} the spacing between strands, and $p = N_{\mathrm{t}} \frac{{d_{\mathrm{s}}}^2}{{d_{\mathrm{o}}}^2}$ is the litz wire packing factor. *ber* and *bei* are the *Kelvin* functions.

The derivatives of the *Kelvin* functions can be calculated according to [80]

$$ber'_{\nu} z = \frac{-ber_{\nu-1} z + ber_{v+1} z - bei_{v-1} z + bei_{v+1} z}{2\sqrt{2}} \tag{1.61}$$

$$bei'_{\nu} z = \frac{+ber_{v-1} z - ber_{v+1} z - bei_{v-1} z + bei_{v+1} z}{2\sqrt{2}}. \tag{1.62}$$

Equivalent circuit model

To predict the total coil impedance from the individual distributed (parasitic) elements, *Grandi* et al. [72] and *Hole* et al. [73] have suggested a model of lumped components that represent the properties of individual turns. It is depicted in figure 1.11. This model is valid until the wavelength of the frequencies of interest becomes significant compared to a single turn length. It is, however, possible to extend the frequency range by dividing each turn into finer segments that are used to derive model components and making additional adjustments to account for retarded fields. This is a subset of the method of partial element equivalent circuits (PEEC) [81].

1.3.3 Modeling Resonant circuits

Building passive ladder filters with bandpass and bandstop characteristic naturally leads to parallel and series resonant circuits in the design. Since, up to now, we have

modeled the components only up to the first resonance[8] (either a series resonance for capacitors or a parallel resonance for coils), the combination of models of several components can deviate from measured data from the first resonance onward. Fortunately, the next higher resonance is often formed by the interaction of the parasitic elements of the building blocks, i.e. a series or parallel resonance between the parallel capacitance of an inductance and the series inductance of a capacitor. Often, resonances beyond that will fall outside the frequency span of interest and can therefore be neglected. In case that higher order effects should be taken into account, the aforementioned simple models can be extended to incorporate additional parasitics. Figure 1.12 shows the combination of a more sophisticated coil model with an ideal capacitor (C_3).

Comparing simulation results with measured impedance data, as is shown in figure 1.13 on page 40, the model proves describe the magnitude and phase response up to the 5^{th} resonance reasonably well. In addition to higher order resonances it also models skin effect losses by a L-R ladder structures as suggested in [63].

However, the development of such sophisticated models is laborious, since for every added lumped element in the parasitic model all previously identified elements need adjustments to their values. Additionally, the circuit beyond the second order parasitic becomes ambiguous in the way that different implementations or value combinations exist that achieve frequency responses with the same residual quadratic error sums. Due to that it is not possible to deduce the origin of these parasitics without additional experiments. In general, even for first order parasitics, caution is advised when attributing the model elements to the actual construction: since the distributed nature of the effects which cause the parasitics is neglected by the model, limited insight can be provided from their values. Experimental variation of construction parameters is necessary to verify the origin of parasitics identified by the model.

[8] With the exception of the solenoid coil modeling. While the equivalent network can model arbitrary coil geometries, there are no established analytical formulas for the parasitic elements of more complex shapes such as toroid coils. Therefore the fitting of first order models remains relevant, especially for coils in filter circuits.

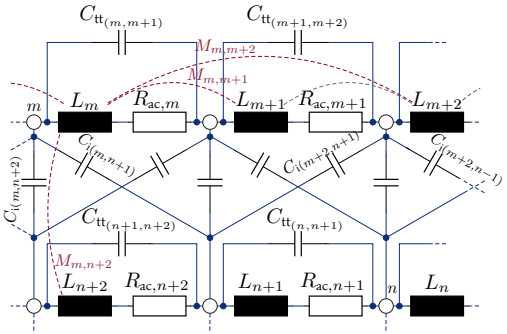

Figure 1.11: Lumped component network of a coil as suggested by *Grandi* et al. [72].

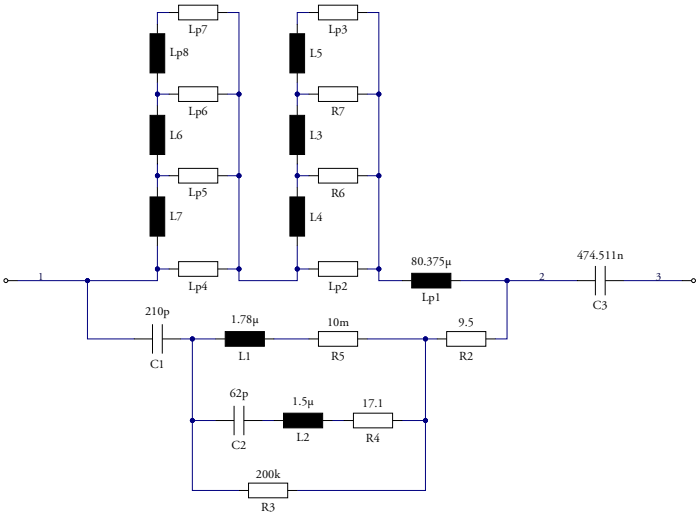

Figure 1.12: Schematic of an advanced model for a resonant circuit with a complex coil model and an ideal capacitor (C3).

1.3.4 Determining model values from measured data

For the simple RLC coil and capacitor models, model parameter extraction from measured complex frequency domain impedance data can be automated. A *MATLAB* script with GUI front-end has been developed to ease this task. It is based on the `tfest` command of the *System Identification Toolbox*, which employs an iterative approach to solve a non-linear least-squares problem for the coefficients of a transfer function of a specified order, so that it fits the measured data best. To guarantee good agreement with the measured data, weighting should be used so that each measured datapoint is weighted by the inverse of its magnitude. This ensures that large values won't dominate the result, since, for our model, every frequency point is of equal importance. The convergence can be improved by letting the algorithm first determine initial values and then refine these during a second series of iterations. Alternatively, initial values can be entered by the user. Entering the correct order of magnitude usually ensures convergence. Resonances beyond the first should be excluded through proper weighting since they will deteriorate the fit for simple models.

This automated approach is suitable up to an order of 3 for the denominator of the transfer function. Fits for higher order responses become increasingly unstable and may even diverge for well chosen initial values. Although an automated fitting process should be possible, it would require additional information on the model type to set boundary conditions (e.g. parameter ranges for parasitics in dependence on the

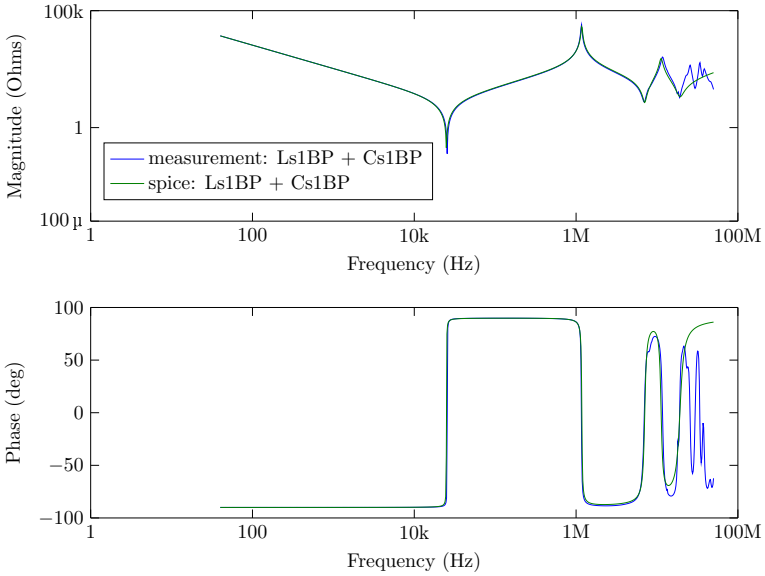

Figure 1.13: Frequency response of the model shown in figure 1.12, compared to the measured original data.

main element value). For the work at hand, this task was rarely performed and thus model creation by hand was acceptable for high-order transfer functions.

Another approach is possible by constructing a more elaborate model that takes the component geometry into account. By extracting parasitics between individual geometric features, lumped component networks can be constructed that are valid beyond the first resonant frequency as explained before and in section 2.2.3.5. Impedance measurements are then only used to verify the accuracy of the model and determine parameters that are difficult to predict, such as dielectric losses. Since the simulation has determined most of the unknowns, the required fit has only a few remaining parameters and is therefore stable.

1.4 Filter Design Theory

In this section we will review the process of filter design and synthesis, following the procedure presented by *Su* in [82]. It is assumed that the reader is familiar with basic network theory, as well as stability criteria such as *Hurwitz* polynomials. After a short introduction of the inverse *Laplace* transform, we will start by reviewing criteria for filter responses, followed by thereof derived transfer functions. A synthesis procedure is presented that allows us to design LC-ladder filter structures that implement the aforementioned responses. Active filters play a minor role for MPI hardware, with the notable exception of the receive chain, for which we review the Twin-T structure.

1.4.1 The (inverse) Laplace Transform

Since for MPI imaging and reconstruction the frequency domain is of major importance, it is convenient to discuss many system components also in the frequency domain. Consequently we shall make frequent use of the *Laplace* transform to express frequency domain signals and transfer functions. Since filter theory is essentially about the synthesis of adequate transfer functions and their realization through a set of standard components, the *Laplace* transform is used by many works on filter design. A good introduction, to which this section frequently refers, is outlined by *Starič* and *Margan* [83].

While it is expected that the reader is familiar with the basic concept of the *Laplace* transform

$$F(s) = \mathscr{L}\left(f(t)\right) = \int_0^\infty f(t)\, e^{-st}\, dt, \tag{1.63}$$

we will summarize a few important equations that facilitate the application of the inverse Laplace transform [83]

$$f(t) = \mathscr{L}^{-1}\left(F(s)\right) = \int_{c-j\infty}^{c+j\infty} F(s)\, e^{st}\, ds \tag{1.64}$$

that we will utilize to derive time domain responses for given frequency domain responses and excitations.

Cauchy's residue theorem lets us calculate the contour integral in the complex plane around the pole at $s = a$ of the function G(s)

$$G(s) = \frac{F(s)}{s-a} \tag{1.65}$$

$$\oint_C \frac{F(s)}{s-a} ds = 2\pi j \cdot F(a) = 2\pi j \cdot \lim_{s\to a} \left\{(s-a)\cdot G(s)\right\} = 2\pi j \cdot \operatorname{res}\left\{G(s)\right\} \tag{1.66}$$

where res $= F(a)$ is called the residue of G at a.
We can write for the **residue for a single pole** at $s = a$:

$$\text{res}\,\{G(s)\} = \lim_{s\to a}\{(s-a)\cdot G(s)\} \tag{1.67}$$

If multiple poles are present as in $G(s) = \frac{F(s)}{(s-a)^n}$, $F(s)$ can be expressed by its *Taylor* series around a as

$$\begin{aligned} F(s) =& (s-a)^n G(s) \\ =& \frac{F(a)}{0!} + \frac{F'(a)\cdot(s-a)}{1!} + \frac{F''(a)\cdot(s-a)^2}{2!} + \dots \\ &+ \frac{F^{(n-1)}(a)\cdot(s-a)^{n-1}}{(n-1)!} + \dots . \end{aligned} \tag{1.68}$$

Therefore G(s) follows as

$$\begin{aligned} G(s) =& \frac{F(a)}{0!(s-a)^n} + \frac{F'(a)}{1!(s-a)^{n-1}} + \frac{F'(a)}{2!(s-a)^{n-2}} + \dots \\ &+ \frac{F^{(n-1)}(a)}{(n-1)!\,(s-a)} + \dots . \end{aligned} \tag{1.69}$$

With the shortcut for the constant $F^{(i)}(a) =: A_{-(n-i)}$ we can express $G(s)$ by its *Laurent* series

$$G(s) = \sum_{m=-n}^{\infty} A_m (s-a)^m, \quad m,n \in \mathbb{N}^0 \tag{1.70}$$

and it can be proven [83] that only the term $A_{-1} = \frac{F^{(n-1)}(a)}{(n-1)!}$ of the series contributes to the integral $\oint_C G(s)\,ds$, therefore

$$\begin{aligned} \oint_C G(s)\,ds &= \oint_C \frac{F(s)}{(s-a)^n}\,ds = 2\pi j\, A_{-1} \\ &= 2\pi j\,\text{res}\left\{\frac{F(s)}{(s-a)^n}\right\} \\ &= 2\pi j\,\frac{F^{(n-1)}(a)}{(n-1)!} \\ &= 2\pi j \lim_{s\to a}\frac{1}{(n-1)!}\left[\frac{d^{(n-1)}}{ds^{(n-1)}}\,(s-a)\,G(s)\right]. \end{aligned} \tag{1.71}$$

and the **residue for a repeated pole with multiplicity** n follows as

$$\begin{aligned} \text{res}\,\{G(s)\} &= \text{res}\left\{\frac{F(s)}{(s-a)^n}\right\} \\ &= \frac{F^{(n-1)}(a)}{(n-1)!} = \lim_{s\to a}\frac{1}{(n-1)!}\left[\frac{d^{(n-1)}}{ds^{(n-1)}}\,(s-a)\,G(s)\right]. \end{aligned} \tag{1.72}$$

Considering a function $F(s)$ with n poles, the *Cauchy-Goursat* theorem allows to perform counterclockwise integration around a contour encircling all poles on the complex plane by dividing the contour in a counterclockwise part around all poles and individual clock-wise circles around the individual poles. Because the distance to the poles can be made arbitrarily small, the integral of the original contour and the compound contour can be proven to be equal. This identity allows to express the contour encircling all poles by the sum of clockwise integrals around the poles:

$$\oint_C F(s)\,ds = \oint_{C_{s_1}} F(s)\,ds + \oint_{C_{s_2}} F(s)\,ds + \ldots + \oint_{C_{s_n}} F(s)\,ds \tag{1.73}$$

As before, the individual integrals can be expressed by the residues of F at these poles:

$$\oint_C F(s)\,ds = 2\pi j\,[\mathrm{res}_1 + \mathrm{res}_2 + \ldots + \mathrm{res}_n] = \sum_{i=1}^{n} \mathrm{res}_i \tag{1.74}$$

Finally, for a rational function of the complex variable s

$$F(s) = \frac{s^m + b_{m-1}s^{m-1} + \ldots + b_1 s + b_0}{s^n + a_{m-1}s^{n-1} + \ldots + a_1 s + a_0}, \quad n - m \geq 1 \tag{1.75}$$

the identity

$$\oint_C F(s)\,e^{st}\,ds = \int_{c-j\infty}^{c+j\infty} F(s)\,e^{st}\,ds \tag{1.76}$$

can be shown between the integral encircling all poles and the line integral along the imaginary axis, making use of the *Cauchy-Goursat* theorem

This leads to the **expression of the inverse Laplace transform** as

$$f(t) = L^{-1}\{F(s)\} = \int_{c-j\infty}^{c+j\infty} F(s)\,e^{st}\,ds = \sum_{i=1}^{n} \mathrm{res}_i\left\{F(s)\,e^{st}\right\} \tag{1.77}$$

for all rational functions where the number of poles exceeds the number of zeros by at least one.

When we consider stable causal systems (where the number of poles is greater or equal to the number of zeros), the responses to all common excitations (sine, step, triangle, etc.) satisfy this criterion, with the impulse response being an exception and requiring an additional pole for the aforementioned methods to work.

1.4.2 Filter responses

1.4.2.1 The Butterworth response: Maximally flat amplitude response

To obtain a frequency response of a low pass filter, that is maximally flat in the pass-band, *Butterworth* [84] suggested a transfer function of the form $|H(s)| = \left(1 + \left(\frac{s}{s_0}\right)^m\right)^{-1}$, remarking that with increasing order m this function will approach unity increasingly well for all values $0 \leq s < s_0$, and will approach zero for $s > s_0$.

In more mathematical terms, it can be shown [82] that for a transfer function of the form

$$|H(j\omega)|^2 = \frac{1}{1+\omega^{2n}} \tag{1.78}$$

the magnitudes of the first $2n-1$ derivatives at $\omega = 0$ are zero, since

$$|H(j\omega)| = \left(1+\omega^{2n}\right)^{-\frac{1}{2}} \tag{1.79}$$

$$= 1 \cdot \left(\omega^{2n}\right)^0 - \frac{1}{2}\left(\omega^{2n}\right)^1 + \frac{3}{8}\left(\omega^{2n}\right)^2 - \frac{5}{16}\left(\omega^{2n}\right)^3 + \frac{35}{125}\left(\omega^{2n}\right)^4 + \ldots, \tag{1.80}$$

which can be easily shown using binomial expansion

$$(1+x)^r = \sum_{k=0}^{\infty} \binom{r}{k} x^k, \quad \binom{r}{k} = \frac{\prod_{m=0}^{k-1} r-m}{k!}. \tag{1.81}$$

Thus this is the flattest achievable low-pass response using a causal system represented by a rational function of the selected order.

1.4.2.2 The Bessel-Thomson response: Maximally flat group delay

Similar to the way the *Butterworth* response achieves maximum gain flatness, the *Bessel-Thomson* response seeks for maximally flat group-delay, also known as envelope delay. With the group delay defined as $\tau_{ed} = \frac{d}{d\omega} \arg\{H(s)\}$, we realize that our goal is to approximate the delay operator using a rational function. Since in the Laplace domain [85]

$$\mathcal{L}\{f(t-\tau_d)\} = e^{-\tau_d s}\, \mathcal{L}\{f(t)\} \tag{1.82}$$

we seek to approximate $e^{-\tau_d s}$ by a rational function. To facilitate this, *Storch* [86] has used the identity $\cosh x + \sinh x = e^x$, therefore

$$H_d(s) = e^{-\tau_d s} = \frac{1}{\sinh(\tau_d s) + \cosh(\tau_d s)} \tag{1.83}$$

Normalizing with $\tau_d = 1$ (which we can revert by scaling s) and using an all-pole rational function for our approximation, we want

$$H_n(s) = \frac{K}{M(s)+N(s)} \approx H_d(s) \tag{1.84}$$

with $M(s)$ being an even and $N(s)$ being an odd polynomial[9]. With the series

$$\cosh(s) = \sum_{n=0}^{\infty} \frac{1}{(2n)!} s^{2n} \qquad = 1 + \frac{1}{2!}s^2 + \frac{1}{4!}s^4 + \dots \quad \text{and} \tag{1.85}$$

$$\sinh(s) = \sum_{n=0}^{\infty} \frac{1}{(2n+1)!} s^{2n+1} = s + \frac{1}{3!}s^3 + \frac{1}{5!}s^5 + \dots \tag{1.86}$$

we perform a continued fraction expansion of $\frac{\cosh s}{\sinh s}$: Starting with a normal polynomial long division *at the lowest order* of s we then process the inverse of the remainder-divided-by-divisor fraction and repeat the long division until we reach the desired order, i.e. the desired number of results.
The division results are then taken as inverse and added back up until we reach the first result [86]:

$$\frac{\cosh(s)}{\sinh(s)} = \frac{1}{s} + \cfrac{1}{\frac{3}{s} + \cfrac{1}{\frac{5}{s} + \ddots + \cfrac{1}{\frac{2n-1}{s}}}} \tag{1.87}$$

By simplifying the compound fraction we get an even numerator and an odd denominator polynomial, which we must simply add to reach our desired $H_n(s)$ according to (1.84).

As *Su* remarks [82], the lowpass characteristic of the result is determined by the choice of an allpole function in (1.84) and not inherent to the minimum group delay criterion. It can be converted into an allpass characteristic by replacing the numerator of H_n by it's denominator polynomial with $-s$ substituted for s.

It should also be noted that, in contrast to the Butterworth response, the transfer function of the Bessel-Thomson response is readily available, while for the Butterworth characteristic we have only determined an expression for its magnitude. The following synthesis procedure therefore will include a step that determines a transfer function for a given magnitude response.

1.4.3 A filter synthesis procedure for passive filters

In this section we will briefly review a method to obtain a passive LC-ladder structure from a given transfer function. The ubiquity of personal computers enables new methodologies that grant the designer a larger degree of freedom at the cost of requiring symbolic math software and numerical methods to dimension complex networks in acceptable time [87]. To gain additional insight, we will use a more traditional approach, which, for the standard responses we will employ, delivers the same results.

[9] Because of (1.85) and (1.86) as we'll see soon.

1.4.3.1 Obtaining a transfer function $H(s)$ from a given magnitude response $|H(\omega^2)|$

We start the procedure [82] for finding $H(s)$ for a given $|H(j\omega)|$ by considering

$$|H(j\omega)|^2\Big|_{\omega^2=-s^2} = \left.\frac{A\left(\omega^2\right)}{B\left(\omega^2\right)}\right|_{\omega^2=-s^2} = H(s)\cdot H(-s) \tag{1.88}$$

Since $H(s)$ should be a rational function in s, we can split it into its numerator and denominator polynomials

$$H(s) = \frac{P(s)}{Q(s)} \tag{1.89}$$

and therefore

$$P(s)P(-s) = A(\omega^2)\Big|_{\omega^2=-s^2}, \quad Q(s)Q(-s) = B(\omega^2)\Big|_{\omega^2=-s^2} \tag{1.90}$$

$P(s)$ and $Q(s)$ are polynomials with real coefficients, thus their zeros are either real or complex conjugate pairs. As a consequence, the products $P(s)P(-s)$ and $Q(s)Q(-s)$ can only have groups of zeros:

(a) For real zeros, all zeros in the left halfplane have a complementing zero in the right halfplane.

(b) Complex zeros that do not lie on the imaginary axis appear in groups symmetric about both the real and imaginary axis.

(c) Purely imaginary zeros only appear with even multiplicity (as they are a special case of complex zeros where the mirror pairs coincide).

To translate from the magnitude response to a transfer function, it is necessary to

1. Replace all instances of ω^2 in $A(\omega^2)$, $B(\omega^2)$ with $-s^2$ and every ω with $\frac{s}{j}$
2. Factor $A(-s^2)$, $B(-s^2)$ to determine their zeros and group them into
   a. real zeros $(s+a)(s-a)$,
   b. complex zeros with non-zero real part $(s^2+as+b)(s^2-as+b)$ where $a^2 < 4b$,
   c. imaginary zeros $\left(s^2+{\omega_i}^2\right)^2$.
3. Construct the $P(s)$ and $P(-s)$ polynomials by
   a. choosing the real zeros of $A(-s^2)$ from one halfplane for $P(s)$ and those of the other for $P(-s)$
   b. choosing the complex zeros of $A(-s^2)$ from one halfplane for $P(s)$ and those of the other for $P(-s)$
   c. assigning one half of the multiplicity of the imaginary zeros of $A(-s^2)$ to $P(s)$ and the other to $P(-s)$

The choice of zeros does not affect the magnitude response. To achieve a minimum phase function however, only zeros from the left halfplane should be selected for $P(s)$.

4. Distribute the zeros of $B(-s^2)$ into $Q(s)$ and $Q(-s)$, similarly to the procedure for P. Since $Q(s)$ is the denominator of our network function, the choice of only left-halfplane zeros for $Q(s)$ is mandatory to satisfy the *Hurwitz* criterion and construct an unconditionally stable network function, as required for passive networks. $Q(-s)$ receives the right-halfplane zeros.

5. Multiply $P(s)$, $P(-s)$ by $\sqrt{a_n}$, the square root of the coefficient of the highest order of ω in the $A(\omega^2)$ polynomial. Correspondingly, $Q(s)$, $Q(-s)$ should be multiplied with $\sqrt{b_m}$, the square root of the coefficient of the highest order of ω in the $B(\omega^2)$ polynomial. This is necessary to retain the gain of $H(jw)$ in $H(s)$, since we have constructed it using only zero locations and therefore lost the common factor in the coefficients. This step will not yield any difference for the following synthesis procedure, since the factors will always be unity, but is required in general.

Using (1.89) we arrive at the desired $H(s)$.

1.4.3.2 Synthesis procedure: Cauer realization

A very straight forward method for the synthesis of LC-ladder filters is the *Cauer* expansion.
It either works through continued pole removal at infinity (meaning, the order of the denominator of the transfer function exceeds the order of the numerator by at least one), which is known as *Cauer* 1 realization, or through the continued removal of poles at the origin (when the numerator order exceeds the order of the denominator by at least one), called *Cauer* 2 realization. A precondition for both realizations is that the transfer function to be realized is a lossless function [82].
In both cases, the removal of the pole creates a zero at the same place for the remainder. Inverting the remainder therefore leads to another pole there, so that the removal step can be repeated until the whole transfer function has been processed.

In other words, the *Cauer* realization converts a transfer function into a continued fraction expansion by repeatedly removing poles at infinity (*Cauer* 1) or at the origin (*Cauer* 2). With each step, it toggles between impedance and admittance plane. The values of the removed poles therefore directly correspond to inductances (*Cauer 1*: impedance plane, *Cauer* 2: admittance plane) or capacitances (*Cauer* 1: admittance plane, *Cauer* 2: impedance plane). Elements of the impedance plane are added to the filter structure as series elements, while results from the admittance plane are added as shunt elements. *Cauer* 1 expansions consequently realize low-pass networks, while *Cauer* 2 expansions create high-pass structures.

1.4.3.3 Synthesis procedure: Foster's preamble

Another important algorithm for the synthesis of LC-ladder filters is *Foster*'s preamble [82]. It allows the repeated removal of poles and zeros at infinity from a given transfer or impedance function. In addition, complex poles on the imaginary axis can also be removed by the algorithm. The removed pole (or pair of complex poles) can be translated into a network element, leaving a simplified remainder behind which can be processed again by using *Foster*'s preamble.

Often, the removal of a pole at infinity for an impedance will produce new a zero there. Thus if we invert the remainder (and therefore change to the admittance plane) the admittance will have a pole at infinity. Removal of this pole very often produces another zero at infinity. Changing back to the impedance plane by inverting the remainder we, again, have a pole at infinity etc. until only complex pole pairs remain. Those can then be removed in a similar manner by calculating their residues and substracting the pole (pair). The calculation of the corresponding residues is no different from the expressions derived in (1.67) and (1.72).

For the algorithmic implementation of *Foster*'s preamble (as well as for the implementation of the other procedures in this chapter), some important considerations have to be kept in mind:

1. Where numeric methods are used (usually required for orders ≥ 3), general rules for the handling of floating point values apply. Especially, comparisons have to account for numeric roundoff errors.
2. It is beneficial to suppress very small imaginary and real parts that appear in consecutive steps, when a purely real or complex value can be expected for a variable or coefficient. Otherwise these errors accumulate.
3. Transfer functions should be normalized to the coefficients of s^0. Very small coefficients should be dropped, especially in the remainder functions after pole subtraction. Otherwise, the order of the remainder will not be reduced and *Foster*'s preamble will not yield a simplified remaining network. Thus, successive steps will fail.
4. Pole-zero cancellation should be performed after every step, taking small numeric deviations into account.

1.4.3.4 Synthesis procedure: Singly terminated LC ladder filters

To create a LC ladder structure that is terminated at one end, which implements a given lossless transfer function, we need to take a closer look at the input impedance when looking into the network from the termination:
Figure 1.14 shows a lossless twoport (the LC ladder we want to realize), represented by its Y-parameters and driven by a voltage source. From the very definition of the Y-parameters we know

$$I_2 = y_{21} E_1 + y_{22} E_2 \tag{1.91}$$

but since port 2 is connected to a resistor, the voltage drop in relation to the current of that branch must satisfy *Ohm*'s law

$$E_2 = -I_2 R_2. \tag{1.92}$$

Substituting this into (1.91) and rearranging the terms we arrive at [82]

$$\frac{I_2}{E_1} = \frac{y_{21}}{1 + y_{22} R_2} \tag{1.93}$$

We now follow *Su* [82] and consider the transmission zeros of $T_{21}(s) = \frac{I_2}{E_1}$. It is obvious that the zeros of y_{21} are also zeros in T_{21}. In addition, T_{21} will have zeros at the private poles of y_{22}, i.e. the poles that are present in y_{22} but not in y_{21}. Network

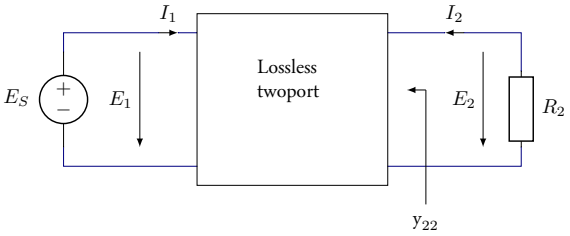

Figure 1.14: Singly terminated filter network, used to derive the relationship between the input impedance Z_{22} of port 2 and the transfer function (cf. [82]).

theory also states that y_{21} must either have an odd ordered numerator polynomial and an even ordered denominator polynomial, or vice versa. Knowing that y_{22} must be a lossless function, we can rearrange T_{21} into one of two forms

$$T_{21}(s) = \frac{P(s)}{Q(s)} = \frac{K N_1(s)}{M_2(s) + N_2(s)} \qquad \text{or} \tag{1.94}$$

$$T_{21}(s) = \frac{P(s)}{Q(s)} = \frac{K M_1(s)}{M_2(s) + N_2(s)} \tag{1.95}$$

where all M polynomials are purely even ordered and all N polynomials have only odd terms. In both cases we can rearrange the terms to satisfy the conditions for y_{21}:

$$T_{21}(s) = \frac{\frac{K N_1(s)}{M_2(s)}}{1 + \frac{N_2(s)}{M_2(s)}} \quad \text{or} \quad T_{21}(s) = \frac{\frac{K M_1(s)}{N_2(s)}}{1 + \frac{M_2(s)}{N_2(s)}} \tag{1.96}$$

where it becomes easy to identify the y parameters

$$y_{21} = \frac{K N_1(s)}{M_2(s)}, \quad y_{22} = \frac{N_2(s)}{M_2(s)} \quad \text{or} \quad y_{21} = \frac{K M_1(s)}{N_2(s)}, \quad y_{22} = \frac{M_2(s)}{N_2(s)} \tag{1.97}$$

We can now use e.g. the *Cauer* 1 expansion to realize a network that satisfies y_{21}, y_{22} from (1.97). When doing so, because we deal with Y parameters, we start in the admittance plane and the next step in the expansion continues in the impedance plane. A similar procedure can be used for filters driven by a current source, where Z parameters are used instead and the expansion starts in the impedance plane.

1.4.3.5 Synthesis procedure: Doubly terminated LC ladder filters

To obtain a LC-ladder network that is terminated at both ends with equal resistors $R_1 = R_2$, which implements a desired lossless transfer function $|H(s)|^2$, the following procedure [82],[88] can be used.

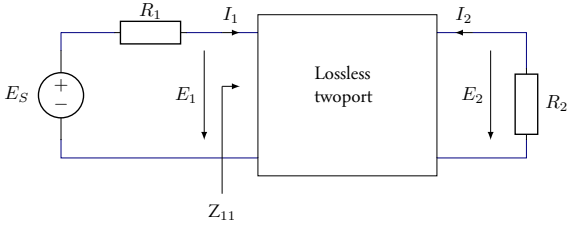

Figure 1.15: Doubly terminated filter network, used to derive the relationship between the input impedance Z_{11} and the transfer function as well as the reflection coefficient (cf. [82]).

First, it is useful to note the maximum power the source can deliver (for equal terminations $R_1 = R_2$), and the maximum power appearing at the load (see figure 1.15)

$$P_{\max} = \frac{E_S R_2}{R_1 + R_2} \frac{E_S}{R_1 + R_2} \overset{R_1 = R_2}{=} \frac{|E_S|^2}{4R_1} \tag{1.98}$$

$$P_2 = \frac{|E_2|^2}{R_2} \tag{1.99}$$

The transmission coefficient, that takes the double termination into account, therefore is

$$|t(j\omega)|^2 = \frac{P_2}{P_{max}} = \frac{4R_1}{R_2} \left| \frac{E_2}{E_S} \right|^2 \leq 1. \tag{1.100}$$

The reflection coefficient is simply

$$|\rho(j\omega)|^2 = 1 - |t(j\omega)|^2. \tag{1.101}$$

Looking into the two-port we identify the complex input impedance Z_{11}

$$Z_{11}(j\omega) = R_{11}(\omega) + jX_{11}(\omega) \tag{1.102}$$

and note the maximum input current into the network

$$I_1 = \frac{E_S}{R_1 + Z_{11}(s)}. \tag{1.103}$$

Then the power delivered to Z_{11} must be that consumed by its real part

$$P_1(j\omega) = |I_1|^2 R_{11}(j\omega) = \frac{|E_S|^2 R_{11}(\omega)}{|R_1 + Z_{11}(j\omega)|^2} \overset{\text{lossless twoport}}{=} P_2(j\omega) \tag{1.104}$$

We can now calculate the transfer coefficient and the reflection coefficient (cf. (1.100))

$$\begin{aligned} |t(j\omega)|^2 &= \frac{\frac{|E_S|^2 R_{11}(\omega)}{|R_1+Z_{11}(s)|^2}}{\frac{|E_S|^2}{4R_1}} = \frac{4R_1 R_{11}(\omega)}{|R_1 + Z_{11}(s)|^2} \\ &= \frac{4R_1 R_{11}(\omega)}{|R_1 + R_{11}(\omega)|^2 + |X_{11}(\omega)|^2} \end{aligned} \tag{1.105}$$

$$\begin{aligned} |\rho(j\omega)|^2 &= \frac{|R_1 + R_{11}(\omega)|^2 + |X_{11}(\omega)|^2}{|R_1 + R_{11}(\omega)|^2 + |X_{11}(\omega)|^2} - \frac{4R_1 R_{11}(\omega)}{|R_1 + R_{11}(\omega)|^2 + |X_{11}(\omega)|^2} \\ &= \frac{|R_1 - R_{11}(\omega)|^2 + |X_{11}(\omega)|^2}{|R_1 + R_{11}(\omega)|^2 + |X_{11}(\omega)|^2} = \frac{|R_1 - Z_{11}(\omega)|^2}{|R_1 + Z_{11}(\omega)|^2}. \end{aligned} \tag{1.106}$$

This magnitude equation can be satisfied by choosing

$$\rho(s) = \pm \frac{R_1 - Z_{11}(\omega)}{R_1 + Z_{11}(\omega)} \tag{1.107}$$

which can be rearranged[10] for

$$Z_{11}(s) = R_1 \frac{1 \mp \rho(s)}{1 \pm \rho(s)} \tag{1.108}$$

Solving the network equations determined from figure 1.15, we arrive at[11]

$$\frac{E_2}{E_S} = \frac{z_{21} R_2}{(z_{11} + R_1)(z_{22} + R_1) - z_{21} z_{12}} \tag{1.109}$$

and can deduce that the transmission zeros of z_{21} are also the transmission zeros of the transfer-coefficient. This fact, together with the discovery of private poles at the input, lays the foundation of the analysis procedure presented by *Casson* et al. [87]. The synthesis procedure can now be formulated as follows

1. If a transfer function is available, we first obtain $|t(j\omega)|^2 = \left| H(s)|_{s=jw} \right|^2$

[10] In [82] the signs of the sums in the numerator and denominator are reversed. Here we have chosen the signs so that (1.107) and (1.108) are consistent.

[11] The corresponding equation in [82] misses R_2.

2. We use (1.101) to obtain $|\rho(j\omega)|^2$
3. Using the procedure outlined in section 1.4.3.1 on page 46, we obtain $\rho(s)$
4. Equation (1.108) is used to calculate the input impedance Z_{11} of the network. Depending on whether the upper or lower signs are chosen, we arrive at a minimum-capacitor or minimum-inductor implementation.
5. *Foster*'s preamble (section 1.4.3.3 on page 48) is used to repeatedly remove poles and zeros at infinity (corresponding to inductors and capacitors respectively) or pole pairs or zero pairs on the $j\omega$ axis (corresponding to series or parallel LC-circuits).
   Since we have designed Z_{11} to contain the termination resistor, the last remainder will be a purely real number with the value of R_2.

1.4.3.6 Frequency-transformation and frequency- and impedance-scaling

The synthesis procedure we have outlined so far is capable of generating networks for low-pass, high-pass, band-pass and band-stop responses. However, since we would like to reduce the computational effort and strive for algorithmic stability, it is convenient to first determine the elements of a *normalized low-pass* filter (corner angular frequency at $\frac{1}{\mathrm{s}}$ and 1 Ω termination) and apply frequency-transformation, frequency scaling and impedance scaling on the result to arrive at the desired filter.

Filter characteristic transformation				
	Prototype LP	high-pass	band-pass	band-stop
series element	L_S	$\frac{1}{\omega_0 \cdot L_S}$	$\frac{b}{\omega_0^2 \cdot L_S}$ $\frac{L_S}{b}$	$\frac{b \cdot L_S}{\omega_0^2}$ $\frac{1}{b \cdot L_S}$
shunt (or parallel) element	C_P	$\frac{1}{\omega_0 \cdot C_P}$	$\frac{b}{C_P \cdot \omega_0^2}$ $\frac{C_P}{b}$	$\frac{b \cdot C_P}{\omega_0^2}$ $\frac{1}{b \cdot C_P}$
frequ. variable	$S = \frac{s}{\omega_0}$	$S = \frac{\omega_0}{s}$	$S = \frac{1}{b}\frac{s^2+{\omega_0}^2}{s}$	$S = \frac{b \cdot s}{s^2+{\omega_0}^2}$

low-pass: frequency scaling		
	$\omega_c = 1$	$\omega_c = \omega_0$
L	L	$L' = \frac{L}{\omega_0}$
C	C	$C' = \frac{C}{\omega_0}$

all types: impedance scaling		
	$R_1, R_2 = 1\Omega$	$R_1, R_2 = k_R\,\Omega$
L	L	$L' = k_R\, L$
C	C	$C' = \frac{C}{k_R}$

Table 1.1: Overview of filter prototype transformations (cf. [82], [88])

The required steps to transform a prototype low-pass filter into the desired response are summarized in table 1.1. Changing the low-pass corner frequency from unity to ω_0 is a simple matter of scaling the frequency variable. When transforming from low-pass to high-pass, we invert and scale the frequency axis, projecting the origin on infinity and vice versa[12]. For the bandpass transformation, the low-pass response is projected in a way that the origin is mapped to the center of the desired passband at ω_0 (and $-\omega_0$) and infinity of the low-pass prototype maps to the origin as well as $\pm\infty$. The corner frequency points of the prototype map to two points separated by the desired bandwidth b and two mirror points on the negative half of the $j\omega$ axis. For the bandstop case, the mapping is similar but in this case the stop band corner frequency of the prototype maps to two points separated by b. From these mappings (formulas of the transformations are given in table 1.1), the relationships of the filter poles (and therefore its elements) can be deduced. The results of these transformations on the filter elements are apparent in the circuits and values in table 1.1.

All filter types can be impedance scaled to achieve the desired termination resistor values. Impedance scaling does not affect the transfer function, but does however, affect input and output impedances, as well as the range of element values.

For Bessel filters, to arrive at the prototype elements as found in the literature from the transfer function derived from (1.84), we need to apply frequency scaling, so that for $s = j \cdot 1\,\frac{1}{\mathrm{s}}$ the magnitude of the transfer function becomes $\frac{1}{\sqrt{2}}$ (cf. [89]). This step is not required for Butterworth type filters, since their transfer function already satisfies this requirement.

Prototype elements are found by applying the synthesis procedure outlined before to a (normalized) transfer function of the desired response, using $R_1 = R_2 = 1\,\Omega$ termination.

1.4.4 Active filters

Filters are categorized as active, when an active device, usually a transistor or operational amplifier, contributes to the realization of the filter function. With the help of positive or negative feedback it is possible to construct *simulated elements*. Especially integrated circuits benefit from the replacement of inductors by capacitors in conjunction with gyrators [87].

1.4.4.1 The Twin-T filter

The Twin-T filter [90], which is a modified version of the Sallen-Key notch filter, is suitable for the application in the MPI receive chain. This sets it apart from many other active filter circuits, that fail to achieve the required linearity, dynamic range or bandwidth.

[12] More precisely, the response is also flipped on the $j\omega$ axis around the origin, so that the low-pass passband on the negative part of the $j\omega$ axis maps to the high-pass passband on the positive projected axis $j\Omega$. Because of the symmetry of the response, this flipping has no influence on the magnitude response.

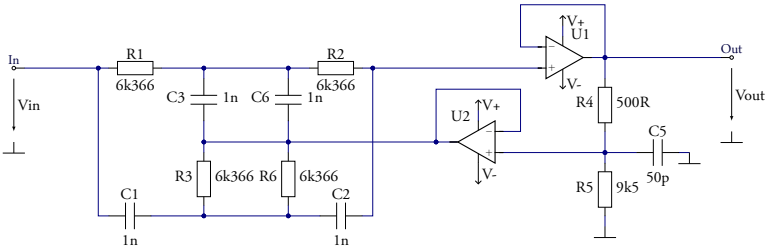

Figure 1.16: Active Twin-T bandstop filter

The basic circuit is shown in figure 1.16. Its transfer function can be derived from basic nodal analysis of the circuit as

$$\frac{V_{\text{in}}}{V_{\text{out}}} = \frac{C^2R^2s^2 + 1}{C^2R^2s^2 + 4CR\frac{R_4}{R_5+R_4}s + 1} \tag{1.110}$$

assuming $R_1 = R_2 = R_3 = R_6 = R$ and $C_1 = C_2 = C_3 = C_6 = C$.

Its suitability for the receive chain derives from the fact that its passive network already provides substantial attenuation at the input of the forward amplifier, relaxing the requirement on the op-amp's dynamic range and THD. This becomes easily recognizable by examining the passive network without the amplifiers, with the center node tied to (AC) ground:

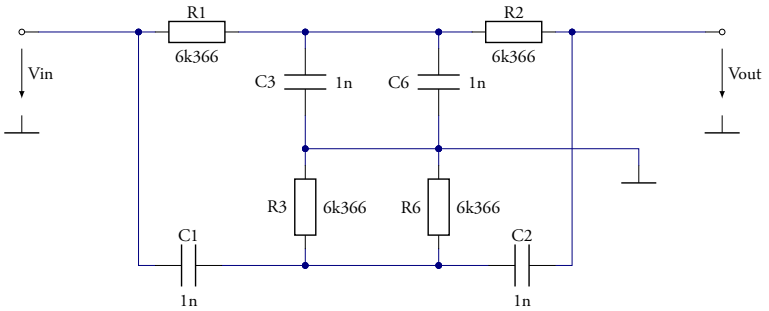

Figure 1.17: Passive Twin-T circuit

Again, performing nodal analysis, the transfer function is found as

$$\frac{V_{\text{in}}}{V_{\text{out}}} = \frac{C^3\,R^3\,s^3 + C^2\,R^2\,s^2 + CRs + 1}{C^3\,R^3\,s^3 + 5C^2\,R^2\,s^2 + 5CRs + 1} \overset{(C\,R\,s+1)}{=} \frac{C^2\,R^2\,s^2 + 1}{C^2\,R^2\,s^2 + 4CRs + 1} \tag{1.111}$$

which closely resembles (1.110), except for the additional dampening factor $\frac{R_4}{R_5+R_4}$ that controls the Quality factor Q of the circuit.

This idea can be taken a step further by changing the gain of the forward amplifier from unity to an arbitrary value, which is then accounted for by modifying the divider R_4, R_5 to achieve an (apart from the gain factor) unchanged overall response. The modified circuit is depicted in figure 1.18.

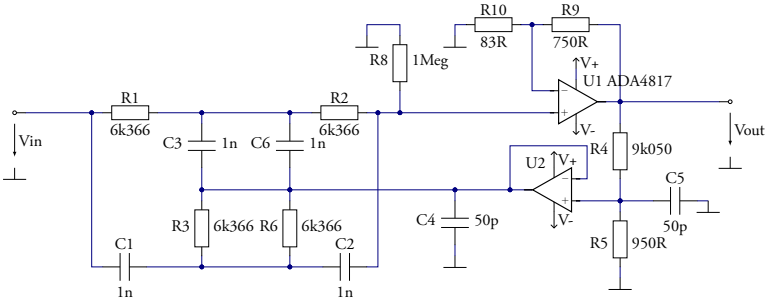

Figure 1.18: Modified Twin-T circuit with gain

From (1.110) or (1.111), the center frequency is found as

$$\omega_0 = \frac{1}{CR} \tag{1.112}$$

and for (1.110) the quality factor is determined as

$$Q = \frac{R_5 + R_4}{4R_4} \tag{1.113}$$

by comparing with a normalized second order system.

The divider network of figure 1.18 is recalculated such that

$$\frac{{R_5}^*}{{R_4}^* + {R_5}^*} = \frac{R_5}{R_4 + R_5}\frac{1}{G} \Rightarrow \left[{R_4}^* = \frac{(G-1)\,R_5 + GR_4}{G}, {R_5}^* = \frac{R_5}{G} \right] \tag{1.114}$$

where $G = \frac{R_f+R_g}{R_g}$ is the Gain of the forward amplifier.

This modification is beneficial for the filter's noise performance. The capacitors C_4, C_5 are used to stabilize the circuit and have been neglected in the previous analysis. Given their small values, their influence on the overall transfer function in the frequency span of interest is marginal.

1.5 System Design

1.5.1 Noise Calculations

Sensitivity is always a key element for acquisition systems. Very often, noise is the limiting factor that determines the lowest signal levels observable.

A very good introduction into noise processes, noise sources and modeling techniques is given by *Motchenbacher* [91]. For this work, we assume that the reader is familiar with the basic procedures of working with noise quantities. Therefore we will only briefly review some design concepts, which we will use later on.

1.5.1.1 Input referred noise

An important parameter for optimizing the signal to noise ratio (SNR) of a system, is the input referred noise. By reflecting all noise contributions back to the input, the smallest detectable signal level can easily be estimated.

1.5.1.2 Signal-to-noise ratio

The signal-to-noise ratio (SNR) is defined as the ratio of the power of the payload signal to the noise power. It is useful to evaluate the SNR at the input of a system to determine the limitations of the signal source, as well as the output, where it characterizes the performance of the complete system. The ratio of the input SNR to the output SNR is often used as a figure of merit and commonly called the noise figure (NF) of a system [91]. While useful to evaluate the noise performance of individual components (e.g. amplifiers), the noise figure is usually not a good indicator to optimize the system's total noise performance [91], since it masks the noise contribution by the source.

1.5.2 Shielding and Electromagnetic Interference

One key aspect of MPI system design is the requirement to deal with large excitation signals and weak receive signals simultaneously. Apart from nonlinearities in the drive field itself, interference from other stages of the transmit chain are a major concern that can limit system sensitivity. Proper grounding and, in many cases, shielding is required to mitigate these effects. Additionally, the wide-band nature of the MPI receive signal complicates efforts to make the receive chain immune to interfering signals. Especially switching mode power supplies (SMPS), which generate frequencies that fall directly into the receive bandwidth, are an issue. Because they are used in a wide range of lab equipment, careful signal routing is even more essential. Among general EMC design guidelines, the current loop technique [92] is of importance to reveal and avoid coupling of spurious signals into the receive chain by carefully planning return current paths. Another matter that comes into play when building equipment for MPI applications is the choice of materials. Apart from the obvious requirement to ban all ferromagnetic materials from the transmit and coil section of the setup, the high currents and voltages generated by MPI setups require careful selection of

conductor and shielding materials, as well as proper pairing of materials, to avoid contact degradation over time [93]. This is important since poor contacts can exhibit strong nonlinear effects (e.g. arcing) when subjected to high currents.

1.6 Previous and contemporary developments in MPI system design

This section will give a short overview over the system development efforts that have taken place in the MPI community. Contrary to the introduction, it will have a more technical focus and will highlight the works that have influenced this thesis.

1.6.1 Scanner types

As mentioned in section 1.2.2, there are currently two different gradient shapes in use with MPI scanners: Field free point (FFP) and field free line (FFL). Historically, FFP scanners were the first conceived scanner design, as presented by *Gleich* et al. [1], while the field free line concept started as a rather theoretical concept that was proposed with an arrangement of 32 coils by *Weizenecker* et al. [94]. *Knopp* et al. were able to simplify the concept to an assembly with 8 coils [95] for full 3d scanning, or even 4 coils if the object to be imaged can be rotated to acquire the whole volume [96]. Using these simplifications it was possible to significantly reduce the power consumption of FFL type scanners and harness their increased SNR [97].
Special cases of the FFP scanner are the traveling wave MPI, that uses a coil array to act both as selection field and drive field generators, presented by *Vogel* et al. [98], as well as the single sided scanner constructed by *Sattel* et al. [99]. The latter requires only access to one side of the object that is to be imaged, being advantageous for large subjects or hand-held applications at the cost of gradient strength and quality compared to conventional two-sided scanners with similar transmit chain parameters.

Another classification of MPI scanners can be the available clear bore size. As of this writing, scanners for mice and rabbit sized specimens have been introduced, with commercial rabbit sized systems available for preclinical research. Human sized scanners have been proposed as design studies [100] for FFL type scanners by *Bringout* et al. and presented as prototype devices for clinical use by *Rahmer* et al. [101].

Hybrid scanners constitute another design class. They can be divided in to scanners that utilize a common set of field generators as demonstrated by *Franke* et al. [102, 103] for a FFP type scanner combined with MRI or *Klauer* et al. [104] for TWMPI in combination with MRI, and scanners that combine two separate imaging systems. For systems that combine MPI with non-magnetic imaging modalities, such as CT, the differentiation between integrated and combined scanners has to be based on whether the specimen has to be moved for both imaging modalities to cover the same volume. Handheld devices, such as ultrasound imaging devices, can also be combined with MPI scanners [105].

1.6.2 Selection field generation

Selection field generation for MPI is commonly performed by (gradient-field) *Maxwell* coils and/or permanent magnets. The arrangement determines whether a FFP or FFL is generated. Early systems avoided the use of ferromagnetic materials in the scanner

while new, upscaled, designs for rat or human sized scanners started to use carefully shielded soft-magnetic materials to achieve high gradient strengths and to reduce fringing fields even at larger bore sizes [106, 107].

Permanent magnets have also been used both for FFP and FFL generation [108], as well as in hybrid designs in conjunction with gradient *Maxwell* coils [17].

Another distinguishing feature is the presence of focus fields that are able to apply a (DC) shift to the FFP or FFL to increase the image size by stitching several images together.

1.6.3 Drive field generator design and transmit circuitry

Several concepts are pursued considering the drive field generators. The majority of FFP and FFL system uses *Helmholtz* coil pairs or solenoid coils to generate the homogenous drive field. Implementations differ in cooling concepts, which range from air cooled coils [109] over water cooled litz wire [17, 110], water cooled rigid copper tube [111] to oil cooled coils [112].
Single sided scanners have also been demonstrated [99, 113] using two D-shaped drive coils to form a FFP.

Closely related to the drive field generators is the transmit chain circuitry. Although many authors choose not to reveal their dimensioning procedures of individual elements, several basic concepts can be deduced from the structures found in the literature: Parallel resonant circuits [114] tend to call for smaller drive coil inductances to achieve high quality factors and therefore high current gain, while series resonant circuits favor medium to large drive coil inductances to achieve the required field strengths using smaller currents. Transformers can be used to increase the applied voltage to the drive coil circuitry [115] and perform impedance matching.
Depending on the winding count of the drive coil, design optimization is either best performed through mathematical description of the coil by spherical harmonics [116] or by numerical or analytic evaluation of the resulting fields, taking coil parasitics into account. The latter concept will be discussed in more detail in section 2.2.3.

Apart from using the drive coil in a resonant circuit, impedance matching is often achieved by using additional capacitors parallel to a series excitation circuit [113, 117], a concept that is also used in MPS instrumentation (cf. section 2.1.4). The impedance of the drive coil circuit is also a major concern when designing transmit filters. Similar to the drive coil design, very few authors specify the design procedure or the element values of their filters. For the scanner presented in this work, the procedure to design the filter circuitry and achieve impedance matching is detailed in section 2.2.5. Apart from passive filtering, the active suppression of spurious signals in the drive field has been applied by several groups [118, 119] and was evaluated for the current design as well, cf. section 2.2.8.4.

1.6.4 Drive field frequencies

Since the first MPI demonstration [1], 25 kHz has been the most widely used drive field frequency, since it is outside of the frequency range that the human ear can perceive. While higher frequencies up to 150 kHz have been used for MPI scanners [115], mainly to avoid peripheral nerve stimulation in human subjects [120, 121], there is an additional burden coming from the nonlinearity of the available power amplifiers as the frequency is increased. This is an inherent property of the feedback loops employed in these devices. Since at the required power levels, voltage feedback architectures are the only ones available, the available feedback decreases as the gain rolls off after the open loop pole of the amplifier. This decreasing feedback leads to reduced correction of output errors and therefore increased non-linearity as the excitation frequency rises.

Another noteworthy influence of the drive frequency are the observed particle dynamics. With rising drive field frequency, the *Néel* process increasingly governs the behavior of common particle systems in use for MPI, while at lower frequencies a significant signal portion may stem from the *Brownian* process [122]. As outlined in section 1.2.5.2, low drive frequencies are therefore useful for mobility MPI. The scanner presented here is, to the knowledge of the author, the first dual frequency MPI scanner. It allows investigation of changed particle dynamics through the use of different drive frequencies with all other imaging parameters unchanged.

1.6.5 Receive chain arrangements

Signal reception in previously presented MPI scanners follows two different approaches. Some systems utilize the drive coils to pickup the particle signal, which is separated from the drive field signal by a suitable passive network [115]. Other designs use a dedicated receive coil to pick up the particle signal, which can also be constructed as a gradiometer [117, 123]. Hybrid approaches are also possible, where one axis uses the drive coil and others have dedicated receive coils [124]. This work is to the knowledge of the author the first to propose a two-axis gradiometric receive coil and extend the gradiometer concept to a fully differential coil design (cf. section 2.2.7.1).

CHAPTER 2

Hardware Design and Characterization

In this chapter the hardware design as well as the characterization/verification process will be presented. It will start with the Magnetic Particle Spectrometer (MPS) and will continue with the mobility MPI (mMPI) scanner. Since the fundamental concepts are very similar, many techniques from the MPS chapter will be continued and expanded in the mMPI scanner design section.

After giving an overview over the system components, coil system design will be of central interest for both techniques, since a large part of the performance is dependent on the field generators and receivers.
Another topic of major importance is signal conditioning, as well on the transmit as on the receive end of the signal chain.
Thermal management and handling of interference signals will also be a concern in the design process. The former will also influence coil design and performance as section 2.2.3.1 on page 83 will show.

A great deal of effort will be spent on predicting real world component behavior. Although limitations to this end exist, as comparison with measured data will reveal, it is adequate to further advance this topic as it has the capability to improve MPI hardware beyond the individual scanner design, through a refined design process.

2.1 Magnetic Particle Spectroscopy

As discussed rather generally in section 1.2 on page 10, the idea behind a MPS system is to generate large magnetic AC fields and measure the magnetization response of magnetic nanoparticles subjected to them.

2.1.1 System components

Being first described as a means to characterize magnetic nanoparticles for MPI [125, 126], it has proven to be also useful as a more general characterization technique.

Figure 2.1 shows a block diagram depicting the typical components of a MPS system. The central components are the excitation coil, which generates a large, homogeneous magnetic AC field, as well as the receive coil that picks up the magnetic nanoparticle particle response. Often, gradiometric or differential coils[1)] are employed to suppress direct feed-through from the excitation field.

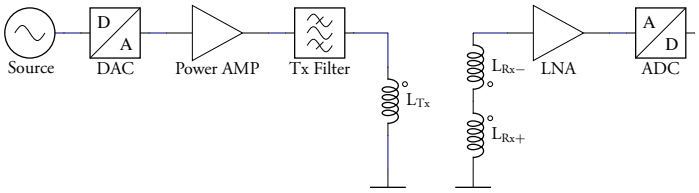

Figure 2.1: Overview over the components of a typical MPS system.

Since the current required in the excitation coil far exceeds the current output of generally available signal sources, a power amplifier is employed. With typical total harmonic distortion performance of power amplifiers in the 0.1% ($-60\,\mathrm{dBc}$) range above 1 kHz, adding filters to the excitation path is beneficial as it improves spectral purity and therefore system sensitivity.
Another component that improves sensitivity is the receive amplifier, which should have low intrinsic noise and high linearity. Reducing the capacitive loading of the receive coil by the data acquisition system and (coaxial) cabling, it also improves the measurement bandwidth.
Optionally, field generators for static fields can be added, which is useful to simulate field conditions at different positions within the FOV of a MPI with a spectrometer. Additional AC-fields can also be added through separate field generators, which allows a MPS to be used for MPI system matrix acquisition [128], although the majority of MPS systems does not possess that capability and the boundaries to a MPI scanner operated on a single sample position are blurred for such systems.

2.1.2 Design goal

At the beginning of the system design, several design goals were formulated to specify the requirements for the MPS system:

1. MPS system capable of (discrete) drive frequencies ranging from 10 kHz to 100 kHz

[1)] The difference being essentially the length of the baseline compared to the distance to the field source [127].

2. Drive field strengths of 30 $\mathrm{mT_{pk}}$
3. Gradiometric or differential receive coil to measure the fundamental frequency component of the particle signal
4. Modular setup
5. High linearity, as required for the measurement principle.

Since the excitation coil is on one hand the most central part of the system design, and therefore difficult to change at later design stages, it should be one of the first components to design. On the other hand it is also the part with the most critical requirements. The following section will discuss its design procedure.

2.1.3 Transmit Coil Design

2.1.3.1 Requirements

Considering the measurement principle of a MPS, as well as our design goals, several requirements can be derived for the transmit coil:

1. The coil should produce fields with high homogeneity over the extent of the sample.
   Since MPS measures a non-linear field dependency, every deviation from the nominal value has the potential to disproportionately affect the measured quantity.
2. The coil must not exhibit any nonlinear effects. It should reproduce the signal from its driving current without adding any distortion.

Taking technical requirements into account, this list can be extended for a practical implementation:

3. Since large AC fields are required, the coil needs to be able to carry the current required for the intended field strength, which is usually in the tenths of mT. More strictly, it should handle this current without excessive heat generation, which would cause cooling problems. It is important to include skin- and proximity effect losses (cf. section 1.3.2.2 on page 30 f.). If the surrounding medium is not air, dielectric losses and a reduced self resonant frequency might become relevant as well.
4. The driving current and/or[2)] self induced voltage must match the capabilities of the intended driving power amplifier. If the imaginary part of the coil impedance is canceled at the excitation frequency by a suitable series capacitor, the critical quantity is the product of the required current and (residual) resistance of this circuit. However, a transformer may be required if the impedance of the resonant circuit cannot be directly driven by the amplifier.
5. Apart from the ability to allow for samples and receive coils of a specified size, the coil also has to fit in the complete system setup.

[2)] Depending on whether the coil is directly connected to the amplifier or whether a series or parallel resonant circuit is used.

Table 2.1 on page 66 lists the targeted values for the different performance parameters, along with the achieved results.

2.1.3.2 Design procedure

From the requirements enumeration it is clear that coil losses should be kept at a minimum to reduce thermal load on the coil system and minimize requirements for the power amplifier.
Skin effect losses are a major concern for frequencies above 1 kHz, and were a limiting factor for a preceding design [129]. Therefore, litz wire should be used to avoid losses due to reduced effective copper area at higher frequencies. There is, however, a trade-off to be made between choosing finer litz strands to reduce skin effect losses, or choosing larger strand diameters to decrease total wire thickness for the same copper area: due to the fixed lacquer thickness, finer strands have a lower percentage of copper area to total wire surface. Thus, to be able to carry the same amount of current (below the skin-effect onset), the total wire diameter is larger for finer strands, which leads to a bulkier coil and a reduced coil constant. So for the same generated field amplitude, coils of finer litz wire with the same copper area require more excitation current, partially defeating the reduced losses.
From these considerations it becomes clear that a maximum excitation frequency should be chosen for MPS drive coil design. With that in mind, there exists an optimum for the stranding that reduces overall losses at the maximum operating frequency [130]. However, the required field homogeneity within the sample volume and maximum tolerated coil dimensions also have an influence on the optimum. To this end, a numerical simulation was used in favor of analytical methods [131] to determine and optimize skin effect losses in conjunction with field homogeneity. Analytical expressions [130, 131], however are a good way to estimate a reasonable parameter range for numerical evaluation.

Using an automated design environment based on the femm package [66] and it's Lua-script and MATLAB link, a large part of the parameter space could be explored.

Homogeneity optimization

Since homogeneity was another primary design goal, a trade-off between a compact (and therefore short) solenoid excitation coil and a longer design with better homogeneity had to be made. A downside of the longer coil are a lowered coil constant and reduced self-resonant frequency. Changing the coil former geometry from cylindrical to a mirrored conical frustum as depicted in fig. 2.2a on page 67 showed promising results, since for a short solenoid coil the inhomogeneity in the sample volume is mainly a result of the truncation: when moving on the center axis from the symmetry point to either direction, the field drops off. By increasing the winding radius of the conductors in proximity of the symmetry plane, their flux is distributed over a larger area and the field maximum at the center point can be flattened, allowing a larger homogeneous field area for the same coil length. Although total wire length and in-

ductance increase slightly, this is preferable to a solenoid coil with increased length (and the same total wire length), since the sample volume is easier to access.
Using this design, inhomogeneity[3)] within a cylindrical sample volume with 10 mm diameter and 20 mm height could be decreased from 2.59% for a conventional solenoid coil to 1.43%, using a coil angled by 6.6°. In addition, the maximum directional field deviation also reduces from 0.68° to 0.39°. In both cases, 4 layers and 28 turns around an inner diameter of 15 mm were used. For a smaller sample volume with 10 mm height, the reduction is more moderate from 0.82% to 0.66%. A smaller angle of $\approx 4°$ would further improve the performance of the $h = 10\,\mathrm{mm}$ sample volume at the cost of a larger inhomogeneity for the larger sample volume. The availability of a larger homogeneous area was deemed beneficial, e.g. if the need for larger sample vials should arise and was therefore chosen for the final design.
It should be noted however, that the coil constant is slightly reduced with increasing angle, resulting in a 9% increase in required excitation current for the same field strength for an angle of 6.6°.

The choice of litz wire stranding also plays a role for the field homogeneity, since a coil with more, but thinner windings is generally preferable to one with thicker wire. Taking all of the above into account, an optimum was found using 405 strands with a diameter 0.71 mm covered by silk serving.

2.1.3.3 Final design

Figure 2.2 shows a drawing of the final coil former design as well as the winding configuration. Mylar foil of 50 µm thickness was used between the layers to prevent arcing, especially at the upper excitation frequency of 100 kHz where the self induced voltage over the coil exceeds 2 kV. The coil former was manufactured by the institute's workshop using polyvinyl chloride (PVC). Key performance parameters are listed in table 2.1. A measured impedance plot is given in figure 2.3 on page 67.

100 kHz was chosen as the maximum excitation frequency, which was used for optimization. For short intervals <5 s, 150 kHz was determined to be a safe limit for the final coil at the nominal drive amplitude of $30\,\mathrm{mT_{pk}}$.
As can be seen from the values, most requirements where met or exceeded. When different design parameters and figures of merit were available, the stricter criterion was chosen. This is especially important for homogeneity considerations, for which maximum deviation was deemed more important than *rms* figures. Very good agreement between simulation results and measured data can be found for the real part of the impedance, i.e. the resistance, at frequencies below the self resonance. As seen in the theory section, accurate modeling of individual wires is required to arrive at these results. The procedure used to predict the parasitic capacitance will be outlined in section 2.2.3.5 on page 92 and values are merely given for completeness at this point.

[3)] Calculated according to (1.53).
[4)] Calculated using the resistance at 100 kHz.

Parameter	Requirement	Simulation	Measurement
Sample diameter d Sample height h	$> 8\,\mathrm{mm}$ $> 8\,\mathrm{mm}$	$10\,\mathrm{mm}$ $20\,\mathrm{mm}$	
Inhomogeneity (1.53)	$< 2\,\%$	$1.43\,\%$	n/a
rms non-uniformity (1.52)	$< 2\,\%$	$0.35\,\%$	n/a
Max. directional Inhomogeneity (1.55)	$< 2°$	$0.39°$	n/a
Field per unit current	n/a	$1.874\,\mathrm{mT/A}$	$2.101\,\mathrm{mT/A}$
Required current for $30\,\mathrm{mT_{pk}}$	$< 19\,\mathrm{A}$	$16.019\,\mathrm{A}$	$14.28\,\mathrm{A}$
Resistance (10 kHz)	n/a	$110.93\,\mathrm{m\Omega}$	$117.3\,\mathrm{m\Omega}$
Resistance (25 kHz)	n/a	$117.37\,\mathrm{m\Omega}$	$122.2\,\mathrm{m\Omega}$
Resistance (50 kHz)	n/a	$140.40\,\mathrm{m\Omega}$	$146.8\,\mathrm{m\Omega}$
Resistance (100 kHz)	n/a	$232.47\,\mathrm{m\Omega}$	$264.2\,\mathrm{m\Omega}$
Thermal losses (100 kHz, $30\,\mathrm{mT_{pk}}$)	$< 100\,\mathrm{W}$	$60.22\,\mathrm{W}$	$53.87\,\mathrm{W}$ [4)]
Inductance	n/a	$119.461\,\mu\mathrm{H}$	$124.39\,\mu\mathrm{H}$
Parasitic parallel capacitance	n/a	$96.73\,\mathrm{pF}$	$67.21\,\mathrm{pF}$
Parasitic DC series resistance	n/a	n/a	$114.2\,\mathrm{m\Omega}$
Parasitic parallel resistance	n/a	n/a	$25.14\,\mathrm{k\Omega}$
Self resonant frequency	$> 1\,\mathrm{MHz}$	$1.481\,\mathrm{MHz}$	$1.75\,\mathrm{MHz}$

Table 2.1: Requirements, simulation results and measurements for the MPS transmit coil with 4 layers and 28 windings per layer, angled by 6.6°. $405 \times 0.71\,\mathrm{mm}$ strands and 1×52 silk serving were chosen for the wire. Equivalent circuit elements according to figure 1.8.

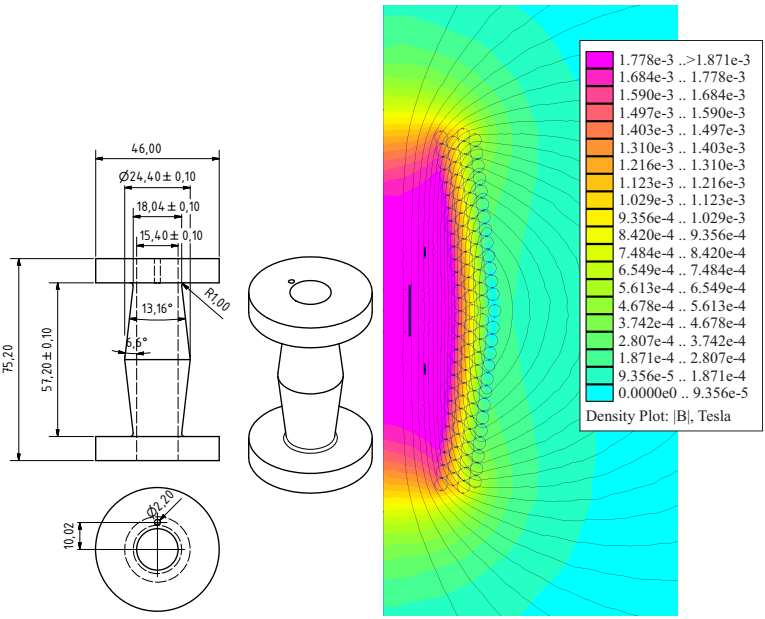

(a) Coil former (b) femm simulation

Figure 2.2: MPS excitation coil: coil former and results of quasi-static magnetic FEM simulation. The space between individual wires in the simulation corresponds to the additional silk serving around the wire strand package.

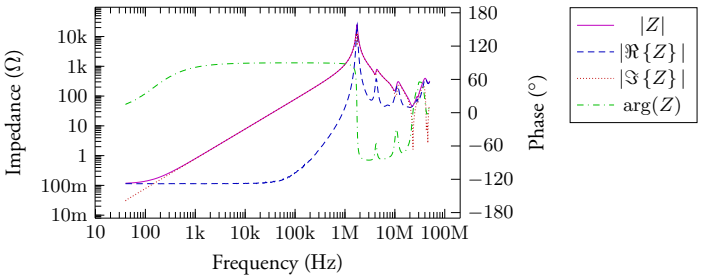

Figure 2.3: Impedance plot over frequency of the MPS transmit coil

2.1.4 Power amplifier and matching circuit

Driving 16 A of excitation current through the 124 µH excitation coil would require 1.2 kV at 100 kHz. While impedance matching to the power amplifier using a transformer is possible in theory, the linearity requirement prohibits the usage of soft magnetic core materials, making this option unattractive. Instead, a resonant circuit is used to compensate the transmit coil's reactance. Since the system is targeted at multiple excitation frequencies, individual matching networks for each frequency are required. A beneficial side effect of the resonant circuit is its frequency selectivity. Additional filtering of the excitation signal is performed by using an additional low-pass filter structure. More sophisticated filters were tested and have proven useful, but are only justified at frequencies above 25 kHz, where the linearity of the power amplifier noticeably decreases. Figure 2.4 depicts the structure of the simple resonant filtering and matching circuit and table 2.2 shows the chosen element values. Component dimensioning was performed by simulating the system using the commercial *AWR Microwave Office* design environment. The excitation coil was included using its one port *s*-parameters, measured with an *Agilent 4294A* impedance analyzer [132]. Figure 2.3 depicts the measured coil impedance over frequency, which was used for the simulations.

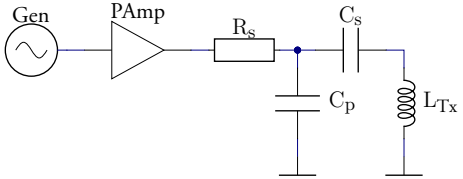

Figure 2.4: MPS filter and matching circuit

Frequency	R_S		C_P		C_S
10 kHz	1.0 Ω	25.0	µF	2.045	µF
25 kHz	1.0 Ω	12.0	µF	327.238	nF
50 kHz	1.0 Ω	6.0	µF	81.809	nF
100 kHz	1.0 Ω	3.0	µF	20.452	nF

Table 2.2: Element values of the resonant MPS circuits for different excitation frequencies.

For the power amplifier, an *AE Techron* 7224 amplifier [133] is used. The gain is set to 50%, which corresponds to a gain of $\frac{10\,\mathrm{V}}{\mathrm{V}}$. The amplifier has a small-signal bandwidth of 300 kHz and a large-signal bandwidth of 60 kHz. THD is specified as lower than 0.1% for DC to 30 kHz [133].

2.1.5 Receive Coil Design

For the receive coil of the MPS system, a differential detection coil was chosen to suppress fundamental feedthrough into the receive signal. To provide easy access to the sample, the compensation coil's diameter was increased compared to the sensing coil. Basic trimming was achieved by appropriate winding counts, determined using the aforementioned simulation framework. To provide even better compensation, mechanical movement of the lower compensation coil allows zeroing the output signal. To this end, the reduced field strengths at the ends of the excitation coil proved quite useful, since they reduce the necessary baseline length. This is desirable, as it reduces the susceptibility to external fields. Figure 2.5 shows the receive coil assembly inside the base frame after removing the excitation coil. Parameters of the individual coils and for the differential assembly are given in table 2.3, an impedance plot is shown in figure 2.6 on page 71. Further impedance plots of the perpendicular receive coils and the input impedance of the low noise amplifier are given in section B.1.

Parameter	**Sensing coil (I)**	**Compensation coil 1 (II)**	**Compensation coil 2 (III)**	**Assembled receive coil (I-II-III)**
Inductance L	54.5 µH	16.42 µH	14.63 µH	75.94 µH
parasitic parallel capacitance Cp	17.45 pF	10.5 pF	10.59 pF	22.46 pF
Parasitic series resistance Rs	1.64 Ω	1.01 Ω	1.02 Ω	3.31 Ω
Parasitic parallel resistance Rp	38.7 kΩ	31.6 kΩ	35.5 kΩ	52.5 kΩ
Self resonant frequency	5.2 MHz	12.1 MHz	12.8 MHz	3.853 MHz

Table 2.3: Parameters of individual MPS receive coils and the main receive coil assembly.

As can be seen from the data, the self resonant frequency of the unloaded coil is well above 3 MHz. However, this is reduced to 2 MHz once it is connected to the receive chain (cf. section 2.1.7).

2.1.6 Coil system chassis

The main task of the chassis is the accurate alignment of transmit and receive coils. It should also allow easy access to the sample and support future expansion of the system with additional coils or measurement options. To this end, a sturdy PVC cube with bayonet mounts in the circular wall openings was created. Using the bayonet system, additional coils or measurement instruments can be mounted on the frame at two sides and on top. They can be removed and re-mounted without additional tools, while at the same time repeatable positioning is ensured.

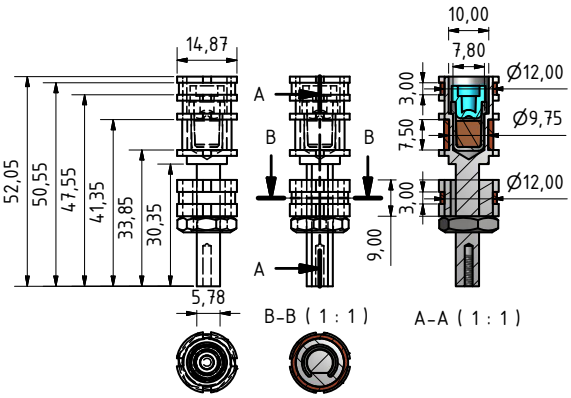

(a) Drawing

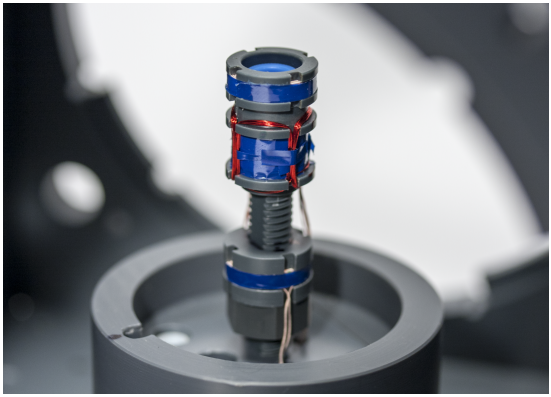

(b) Photograph

Figure 2.5: a) Technical drawing and b) image of the receive coil assembly of the MPS system, showing the trimmable differential receive coil for the axial field component and saddle coils for perpendicular directions.

The chassis also serves as a mounting place for the breakout PCB, which interconnects the receive coils with SMB coaxial connectors.

2.1.7 Receive amplifier

The signal picked up by the differential receive coil is amplified by a receive amplifier. There are several benefits to this approach compared to a direct connection to the ADC card:

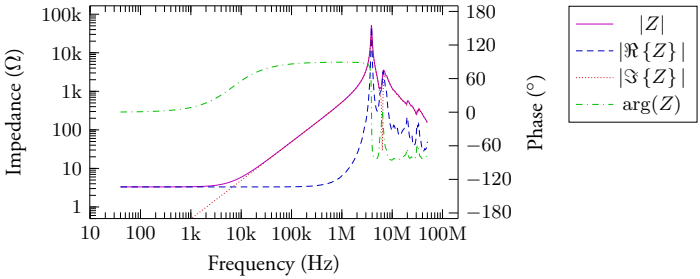

Figure 2.6: Impedance plot of the assembled receive gradiometer of the MPS setup.

(a) Mounted bayonet extensions (b) Chassis open

Figure 2.7: Photographs showing the complete MPS system assembly inside the chassis with a) mounted sidewall bayonets, b) removed sidewalls. (b): © IEEE 2015, [134].

1. By choosing an amplifier with low equivalent input noise, the signal can be amplified above the noise floor of the ADC card, reducing the system noise level referred to the magnetic input signal.
2. The signal can be limited. This is important in the case that an imbalanced receive coil (due to an inter-winding short or cabling fault) outputs large voltages which might damage the ADC card.
3. It decouples the receive coil from the coaxial cabling to the ADC card, as well as from the ADC card's input capacitance.

While the first two points are easily recognized as beneficial, we should elaborate a bit more on the last one: To achieve maximum sensitivity, the sense coil winding count should be maximized. However, this increases the coil's inductance and lowers the self resonant frequency of the coil. Every capacitive load on the coil further adds to the parasitic parallel capacitance of the coil and lowers the self resonant frequency. As can be seen from the values in table 2.3 on page 69, to keep the self resonant frequency above 2 MHz, a maximum capacitive load of 64.75 pF is tolerable. This agrees well with typical input capacitances of the employed amplifier boards in the 20 pF range,

but does not work well with the 317.8 pF input capacitance of the ADC card[5]. The gain of the receive amplifier stages should be moderate (2–20), to keep distortions at a minimum. Higher closed loop gains, which would reduce the amount of negative feedback, would decrease linearity and interfere with the measurement results.

2.1.8 Data acquisition and excitation current controller

The resonant nature of the transmit circuitry comes with the disadvantage of a large sensitivity to the quality factor of the resonance. Variations in loss mechanisms, e.g. due to expected thermal changes under operating conditions, can therefore have a noticeable impact on the resultant excitation current for a given power amplifier output level. To counter these variations, the excitation current is measured by means of a commercially available *Sensitec CMS3025* current sensor, which uses an AMR sensor bridge to measure the magnetic field surrounding a conductor to determine the current. The galvanically isolated nature of this measurement principle as well as the negligible feedback on the measured circuit ensure that there are no additional loss mechanisms introduced in the transmit circuit.
The analog output of the current sensor is acquired by a *National Instruments PCI-6133* ADC card, which is also used to acquire the signal from the receive chain. Using digitally implemented integral controllers, phase and amplitude of the excitation current are actively kept at their specified values. This ensures that, even in the presence of thermal drift, the excitation current meets its nominal amplitude and phase. Additionally, it can be used to monitor system parameters, such as settling time.

2.1.9 MPS System characterization

2.1.9.1 System calibration

To perform a complete system calibration, two goals need to be accomplished:

1. The conversion factor between the magnetic moment of a sample to the received voltage has to be determined.
2. The frequency dependency (transfer function) of the ratio between received voltage to magnetic moment (or magnetic field) has to be known.

The second task can be carried out in arbitrary units as long as a calibration sample is available for at least one frequency point to perform the first task.

The transfer function of the MPS receive chain was characterized using a custom built wideband voltage controlled current source. Its schematic circuit is depicted in the appendix in figure A.1 on page 176. It was used to imprint current into a calibration solenoid coil which was designed to be positioned within the sense coil of the MPS. The calibration coil's diameter and height correspond to the size of the microtiter vials used for nanoparticle samples. Figure 2.8 shows the frequency dependency of the receive chain's field sensitivity. As is apparent from the values, the

[5] Most likely a result of the shielded cable from the BNC breakout box to the PCI slot bracket.

receive coil acts as an ideal coil with frequency proportional voltage gain and 90° phase shift up to 500 kHz. From that point onwards, a slight deviation starts to build up until resonance is observed at 2 MHz.

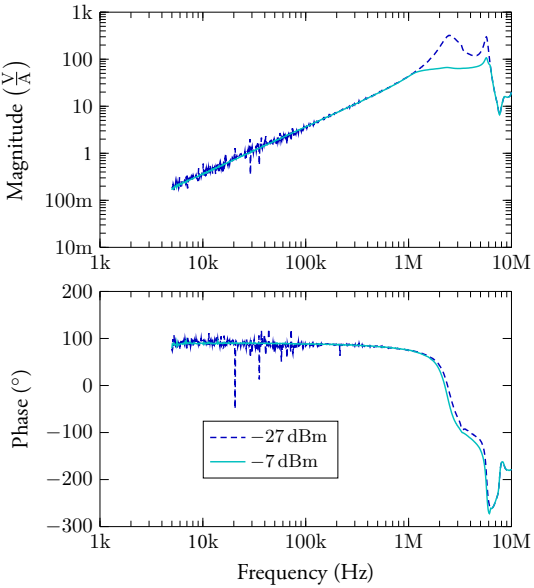

Figure 2.8: Transfer function of the MPS receive chain, driven by the calibration coil and the custom built current source. The transfer function was measured at two power levels to achieve either low noise at the lower frequency end or observe the self resonance at higher frequencies that would otherwise saturate the receive amplifier.

The absolute value of the MPS sensitivity can be determined by measuring the fundamental signal obtained from a dysprosium oxide (Dy_2O_3) sample with known mass of 0.3704 g and 150 µL volume. Using the known mass susceptibility of dysprosium of $3.0186 \times 10^{-6}\ m^2/kg$ (cf. [135], converted to SI units) the volume susceptibility of the dysprosium sample can be calculated as $0.007454029 + 0j$. From the known volume and the applied field strength, the magnetic moment of the sample is calculated and related to the measured signal amplitude. For 25 kHz and $B_0 = 25\,mT$ the received amplitude of the Dy_2O_3 sample is 262.043 mV and 90.903° (relative to the excitation current). In combination with the transfer function of figure 2.8 this achieves a full calibration. The calculations are detailed in eqs. (2.1) to (2.7).

$$\boldsymbol{m} = \boldsymbol{M}V = \chi_{\text{vol}}\, \boldsymbol{H}\, V \tag{2.1}$$

$$\chi_{\text{vol},\text{Dy}_2\text{O}_3,\text{SI}} = 4\pi\chi_{\text{vol},\text{Dy}_2\text{O}_3,\text{CGS}} \tag{2.2}$$

$$\chi_{\text{vol},\text{Dy}_2\text{O}_3,\text{CGS}} = \chi_{\text{mass},\text{Dy}_2\text{O}_3,\text{CGS}} \cdot \rho_{\text{Dy}_2\text{O}_3} \tag{2.3}$$

$$\chi_{\text{mass},\text{Dy}_2\text{O}_3,\text{CGS}} = \chi_{\text{mol},\text{Dy}_2\text{O}_3,\text{CGS}} \,/\, m_{m,\text{Dy}_2\text{O}_3} \tag{2.4}$$

$$\chi_{\text{mol},\text{Dy}_2\text{O}_3,\text{CGS}} = 89600 \cdot 10^{-6} \frac{\text{cm}^3}{\text{mol}} \quad \text{cf. [135]} \tag{2.5}$$

$$m_{\text{mol},\text{Dy}_2\text{O}_3} = 373.00 \frac{\text{g}}{\text{mol}} \quad \text{cf. [136]} \tag{2.6}$$

$$\rho_{\text{Dy}_2\text{O}_3,\text{Sample}} = \frac{m_{\text{Sample}}}{V_{\text{Sample}}} = \frac{0.3704\,\text{g}}{150 \cdot 10^{-9}\text{m}^3} = 2469.33 \frac{\text{kg}}{\text{m}^3} \tag{2.7}$$

2.1.9.2 Random measurement error

The random error of the system has been evaluated using a dilution series down to a minimum of 1 mmol/L. Figure 2.9 shows the normalized data for 25 kHz with the standard deviation shown as error bars. The standard deviation is estimated using the empirical variance determined from 10 repetitions. Unsurprisingly, the phase measurement at low concentrations shows larger errors than the amplitude. This is especially true for higher harmonics, where the phase error of the fundamental is multiplied with the order of the harmonic (cf. section 1.2.1). For the third and fifth harmonic, the standard deviation of the magnitude, relative to the amplitude, is below $\pm 0.26\%$ for all measurements in the dilutions series and the phase error is below $\pm 0.27°$.

The same procedure has been carried out at the other excitation frequencies. The results are depicted in figure 2.10 on page 76. Due to the increasing non-linearity of the power amplifier, low concentrations have increased uncertainties at higher excitation frequencies and very low concentrations cannot be observed any more. This originates from the fluctuating amplitude and phase of the background spectrum from the amplifier. Similar to the observations before, the amplitude shows smaller deviations and continues to be stable at high excitation frequencies.
As can be seen from figure 2.10, the results at all frequencies coincide well when normalized to the iron mass of the sample. The steeper slope of the harmonics and the change in phase as the excitation frequency is increased is a result of particle dynamics. For the employed FeraSpin multi-core particles this effect is comparably small owing to the wide crystallite size distribution in the core [137]. A similar, more pronounced effect of the excitation frequency on particle behavior due to dynamics will be demonstrated in section 3.1 on page 151 for single core particles.

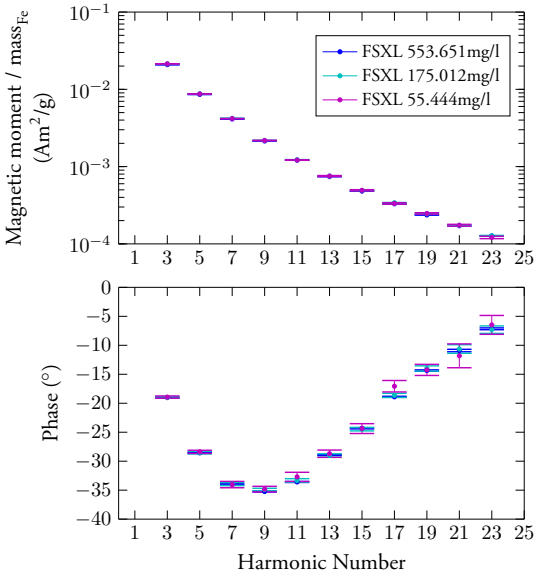

Figure 2.9: Random error determination for a dilution series down to 1 mmol/L using FeraSpin XL particles at 25 kHz and 25 mT excitation amplitude. The results have been converted to absolute values using the procedure from section 2.1.9.1 and normalized to the iron mass. Error bars show the standard deviation based on 10 repetitions.

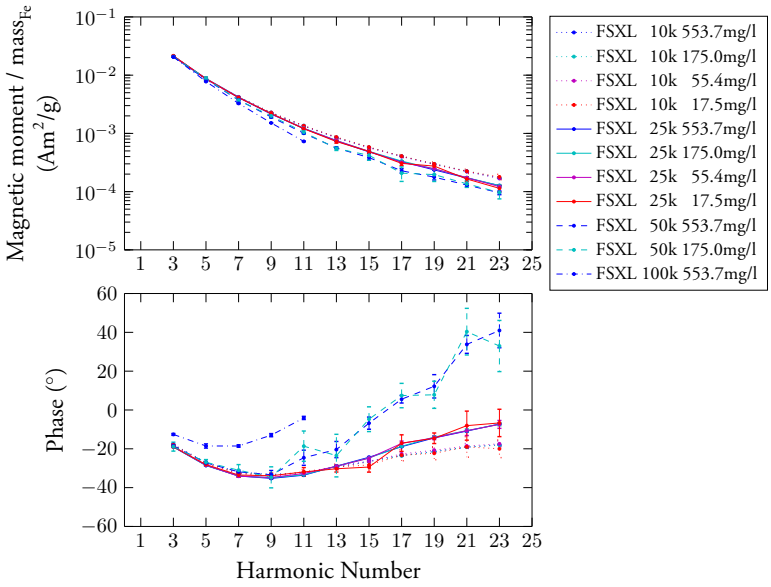

Figure 2.10: Random error determination for a dilution series down to 0.3 mmol/L using FeraSpin XL particles at 10 kHz, 25 kHz, 50 kHz, 100 kHz and 25 mT excitation amplitude. The results have been converted to absolute values using the procedure from section 2.1.9.1 and normalized to the iron mass. Error bars show the standard deviation based on 10 repetitions.

2.2 Magnetic Particle Imaging

The following sections describe the implementation of a mMPI scanner with two active axes. Since it is the successor of two other systems built at the institute, it is commonly designated as third generation MPI (MPIv3) system.

After a short overview, key design goals and procedures are presented for this scanner. Emphasis will be on field generator and filter design, as well as on aspects that differ from other MPI scanners, such as the receive coil configuration or the dual drive frequencies.
Scanner frame, gradient field generators and the drive coils were designed as part of the master thesis of *Sebastian Draack* [138], which contains additional constructional details. Most parts were manufactured in-house by the institute's workshop, due to the unavailability of stock components that fit the minimum requirements, such as non-ferromagnetic construction materials.

2.2.1 System components and system overview

The components of a MPI system can be grouped into five categories:

1. Transmit chain: Signal generation (GEN), power amplifier (PA) and bandpass filtering (BPF) to create a pure sine.
2. Coil/field generator system: Field generators for gradient and drive fields (LTX), receive coils (LRXS) and compensation coils (LRXC) to pick up the magnetic sample response and suppress fundamental feed-trough from the drive field.
3. Receive chain: Filter remaining fundamental feed-through (BSF), amplify the receive signal using a low-noise amplifier (LNA) and digitize it (ADC).
4. System control and data processing: Control system parameters such as drive current, generate measurement sequences, store and process data, reconstruct images (CTRL). Arguably, signal generation and acquisition can also be sorted under system control.
5. Auxiliary equipment: Mechanical support, power supplies for receive amplifiers, supply filtering and shielding.

Figure 2.11 shows an overview of the system components. Color has been used to group parts into the identified categories.

As this system is intended for the demonstration of mMPI imaging, it should enable as many mMPI imaging modes (cf. section 1.2.5.4 on page 24) as possible. Therefore, a scanner with two drive frequencies is built, so that the multi-frequency mMPI approach is available. Consequently, parts of the transmit and receive chain need to be present for each drive frequency.
For easier evaluation of particle dynamics in case of the direct mMPI approach, a FFP design is chosen, even though a FFL scanner would offer higher SNR under certain conditions [116, 139].

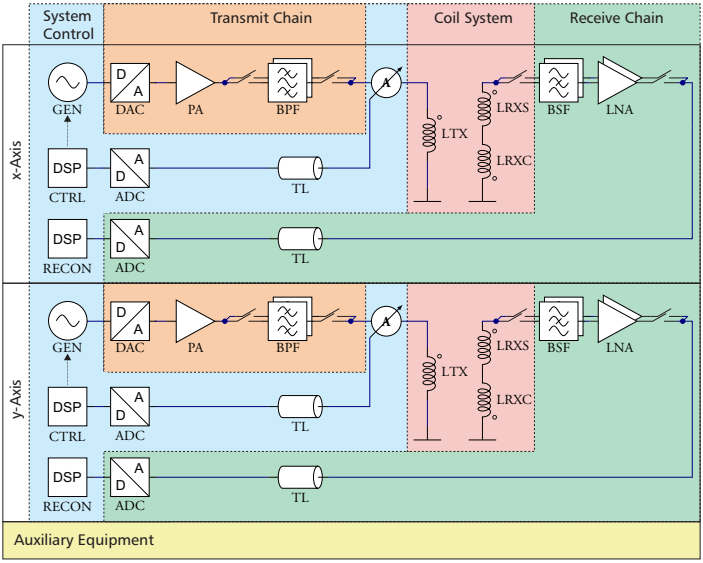

Figure 2.11: Overview of MPIv3 system components.

2.2.2 Scanner Frame & Gradient Field Generators

The choice of gradient strength and extends are key elements for resolution and FOV size of a MPI scanner. Since the gradient field generators are subject to static and dynamic forces, mechanical implementation is also important.

2.2.2.1 Scanner Frame

The scanner frame has merely mechanical purposes, yet it still has to possess some properties which are crucial for the general function of the MPI system:

- It has to be sturdy enough to carry the gradient field generators as well as the coil system.
- Ferromagnetic components should not be used. Where this is not possible, they have to be kept at a considerable distance from the coil system, gradient generators and their cabling or have to be shielded by non-ferromagnetic structures from time varying fields.
- It should not be prone to mechanical vibration. A heavy construction is helpful to that end.
- Optionally, it should also provide a place for the capacitors of drive coil's resonant circuits and space for receive circuitry.

It can also be used to carry or link the system to a calibration robot, allowing repeatable positioning of samples within the bore.

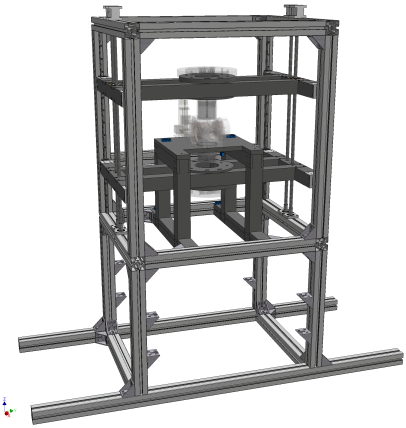

Figure 2.12: MPIv3 system with the scanner frame emphasized.

Figure 2.12 shows the MPI system with the scanner frame emphasized. The support beams for the gradient generators are vertically movable by stepper motors through a trapezoidal threaded spindle. At the center of the system the support table for the central coil system with the drive field generators is visible. Below the field generators, several levels for components of the transmit and receive chain as well as auxiliary equipment are available.

2.2.2.2 Gradient Field Generation

The gradient field generators facilitate the spatial encoding (cf. section 1.2.2 on page 12) of a MPI system. Since the gradient strength directly influences the achievable resolution (1.42), a high gradient is preferable. For this design, a gradient field of $\leq 3\,\mathrm{T/m}$ was targeted for the imaging axes.

Pilot experiments and studies

Several options were evaluated for the gradient field generators. From the experience with an earlier MPI scanner, NdFeB permanent magnets were considered a promising option. However, safe handling of the magnets during installation and maintenance of the system had to be improved compared to the previous design. To this end, the combination of soft magnetic material and permanent magnets was rejected due to accident hazards during assembly. The following remaining options were evaluated:

1. NdFeB permanent magnets only

2. NdFeB permanent magnets with additional coils:
    a. anti-Helmholtz coils constructed of copper pipe
    b. anti-Helmholtz coils constructed of solid enameled wire
3. anti-Helmholtz coils with soft magnetic core material and copper shield against drive field:
    a. constructed of enameled copper pipe
    b. constructed of solid enameled wire

The existing DC current sources (Agilent 6674A) with a maximum current of 35 A as well as the spatial constraints of at least 80 mm of free space between the field generators were used as boundary conditions. Simulation studies revealed that the sole use of air core coils was unfeasible with the equipment at hand. On the other hand, the combination with a soft magnetic material meant additional copper losses for the drive coils due to the required shielding. Therefore the remaining choices were neodymium magnets either with or without additional coils.

Final design

Since neodymium magnets were determined the most suitable option to generate strong gradients, they became the first geometry to be optimized for the final design. Diameter and spacing were chosen to achieve a linear gradient of 6 T/m in the z axis (3 T/m in the imaging plane), while adhering to the maximum size dictated by the manufacturers' capabilities. After the size and the position of the magnets were determined, their casing was constructed in a way that allows the installation of additional coils. These can either act as focus field coils to provide an electrical imaging plane selection in the z axis, or they can serve as anti-Helmholtz coils to adjust the gradient strength. However, as of this writing, these coils have not been installed yet.

An additional aspect of the magnet's enclosure design was the intent to keep a safe distance between the magnet and the operator during installation (cf. figure 2.13). This is required because of the large force of more than 200 N at a distance below 16 mm, should they approach each other.
Since, at the intended configuration, both magnets repel each other, an easy method of keeping the magnets in place during assembly was also desirable. To facilitate this, a bayonet was used as a fast locking mechanism (cf. figure 2.13). After assembly the magnet casing is held in place by additional screws that relieve force from the bayonet and block rotation. The cylindrical casing guides the ring-magnets during installation and prevents accidental flipping.

Since the repelling force of 50 N at a gradient of 6 T/m was still considered to be problematic during assembly, the frame was designed to allow mechanical movement of the gradient magnets. A trapezoidal threaded spindle was chosen as transmission between the stepper motors and the magnet carriers for its self locking property. Therefore the magnets are kept in place without constant force on the stepper motor's gears.

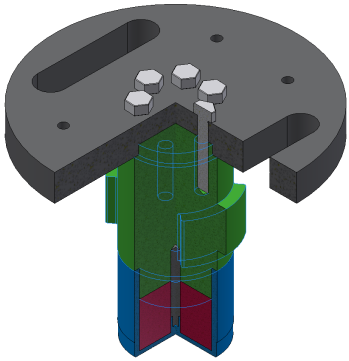

Figure 2.13: One of the NdFeB magnets (red) responsible for the gradient field generation in its compartment (blue). It is held in place by a the cylindrical end of the mounting rod (green), showing the bayonet lock. Handles have been added to the mounting plate (gray) to allow easier insertion of the assembly. The mounting rod is elongated to keep the grips at a safe distance from the magnet.

They also stay in place in case of motor failure or replacement.
A welcome side effect of this construction is the possibility to adjust the gradient strength by choosing the magnet separation. Additionally, when not operating at maximum gradient, a simultaneous vertical shift of both magnets allows the movement of the imaging plane without additional focus fields. Figure 2.14 depicts the field strength in the imaging plane in dependence of the distance to the center for different magnet positions.
The gradient variation with separation distance is shown in more detail in figure 2.15,

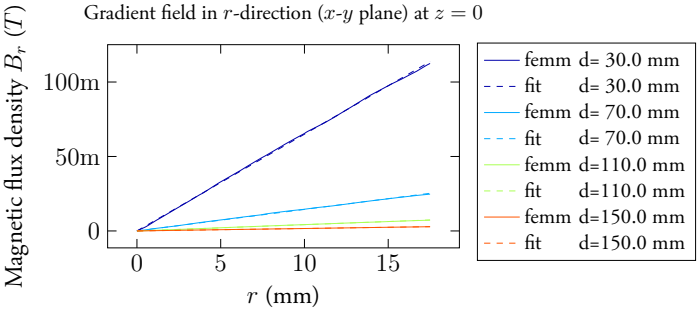

Figure 2.14: Field gradient in the imaging plane at different magnet positions (see legend). A linear regression fit has been added to each plot (dashed). $R^2 > 0.999$ for all fits.

Parameter	Value
Outer diameter	80 mm
Inner diameter	10 mm
Axial height	50 mm
Material	N45H
Coating	Nickel
Minimum spacing	99 mm
Nominal gradient in imaging plane at minimum spacing	3 T/m

Table 2.4: Parameters of the gradient magnets

which depicts the gradient strength along the main gradient axis and within the imaging plane as a function of magnet spacing. A minimum distance of 50 mm is achievable with the coil system in place. The gradient can be approximated by a simple model of two opposing dipoles arranged at the magnets' centers.

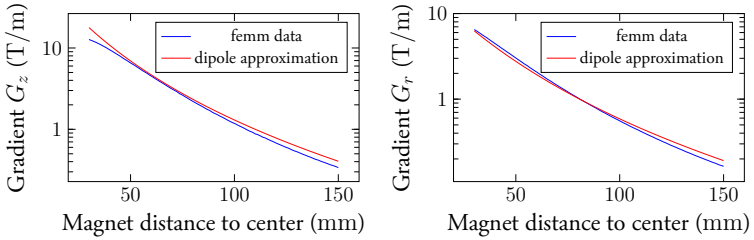

(a) Gradient on z axis

(b) Gradient in imaging plane

Figure 2.15: Gradient strength at the center a) along the z axis, b) in the x and y axes (the imaging plane), in dependence of magnet separation, each plotted along with a dipole approximation, assuming $m = 33\,\mathrm{Am}^2$ and dipole positions in the magnets' center.

2.2.3 Drive Coil System

The drive coil system generates large homogenous AC fields that drive the magnetic nanoparticles within the FOV into saturation. For the presented MPI scanner, a solenoid coil will be used as primary axis (x-direction), with the inner diameter of the coil constituting the scanner's bore.
A second active axis is established with a pair of perpendicular Helmholtz coils, which is designated as y axis.
Because the main direction of the gradient field is in the z axis, the gradient strength in both imaging axes is equal (isotropic imaging plane). As we will see, the imaging

parameters in the x direction are superior to those of the y axis, which is why it is designated as primary.

The requirements for the drive field generators in a MPI system are very similar to those already mentioned for the MPS in section 2.1.3.1 on page 63. Consequently, only the main differences and requirements that are considerably more stringent than in the MPS case will be stated.

A main difference compared to the MPS system is the increased sample area (the FOV) and the presence of a second active axis. Since the generated field strength inside a coil will at least drop with the inverse of its size[6)], this means a significant increase in required winding count or current for the same targeted field strength. Consequently, heat dissipation of the coil becomes so large that passive cooling is rarely sufficient. Different mechanisms have been explored for the cooling of MPI drive coils: Rigid copper tube [111] provides easy guidance of the coolant but exhibits large skin-effect losses and puts large requirements on the driving amplifier. Additionally, it is difficult to handle during manufacturing. Litz wire in direct contact with water shows lower copper losses but suffers from a severely reduced self resonant frequency. Litz wire with mylar serving partially casted in epoxy resin is a viable alternative, which will be used for the system at hand. However, electromechanical distortion can be an issue with this type of construction [111]. Forced airflow over epoxy reinforced litz wire is also reported [109], but cooling effectiveness is lower than with liquid coolants.

Two approaches are currently in use for the design of MPI drive systems (cf. section 1.6): Parallel resonant circuits and series resonant circuits formed with the excitation coil. The former require large excitation voltages (and therefore a transformer to drive them) but provide significant current gain, while the latter require larger excitation currents from the amplifier but only low voltages. For the first type, coils with only a few windings are optimal, while for the latter, a moderate-to-high winding count is better. Based on the experience with a previous system and the available infrastructure, the latter design has been chosen. In contrast to the few windings of the first case, where an optimization procedure of sparse wound coils can be used to produce the required field [116], our approach is closer to the design procedure already outlined in the MPS section, where the shape and winding count of a multi-layered coil is optimized.

Common for all designs is the requirement for high linearity, prohibiting the use of ferromagnetic materials or soft magnetic cores. Heat management and cooling will be discussed in later sections, after the optimized coil shapes have been presented.

2.2.3.1 Liquid coolants and Influence on Coil Self-Resonant Frequency

Pilot experiments and studies

In order to handle the losses produced in the coils, several coolants were evaluated. The requirement on the coolant was that it should be easy to handle, be non-toxic and provide efficient heat transfer. Additionally it had to work with the existing impeller

[6)] I.e., the radius of the coil in the case of a solenoid or the separation in case of a Helmholtz pair.

pumps, limiting its viscosity range and excluding chemically aggressive coolants. Test-coils were used to evaluate the influence of the coolant on the coil's self resonant frequency as well as the cooling capability.

Mineral oil (*Shell Diala*) was found to provide acceptable cooling and to have low influence on the self-resonance. However, mineral oils are toxic and difficult to handle. Especially removal of the oil after leakage and reliable seals were found to be an issue. Compared to machinery parts, where metal structures with high quality surfaces can be used, the requirement to have non-magnetic and non-conducting materials used for the coil system hinders the construction of reliable seals.
Silicone oil was evaluated as a substitute. It has comparable influence on the self-resonant frequency and is non-toxic. However, it is even more prone to creep through seals than mineral oil. Additionally, it cannot be removed without residue from surfaces that cannot tolerate acetone, as is the case with many polymers. It also has a higher viscosity compared to water, leading to a much more laminar flow profile. As a side effect, areas that are not directly in the flow profile show much less heat exchange. This can lead to hot-spots at corners with obtuse angles, which overheat even though they are surrounded by coolant.

Due to these considerations, de-ionized water has been chosen as a coolant. Since it can be removed without residue, the option to use other coolants that are compatible with the PA-6 polymer remains available in the future. The cooling structure has been designed to also work with higher viscosity coolants: by providing many individual cooling channels around hot surfaces, the risk of hot-spots is reduced.

Wire servings and coatings

To counter the negative effects that di-water has on the self resonant frequency of coils, different coatings have been evaluated. As a first measure, it is useful to employ Mylar serving instead of the silk that is commonly used for litz wire. Another benefit of Mylar is the higher tolerable field strength, allowing larger layer-to-layer voltages and removing the need for additional insulating foil between the layers. Since Mylar does not absorb water the way silk does, an insulation area is established around the wires, reducing the parasitic capacitance due to the lower permittivity of the Mylar.
Additional insulation from the coolant can be achieved by sealing layers with epoxy resin. Heat-conducting resin (*Copaltec* ST22, $1.5\,\mathrm{W/(m\,K)}$ thermal conductivity, $34\,\frac{\mathrm{kV}}{\mathrm{mm}}$ dielectric strength, $0.2\,\%$ water take-up) has been used to retain sufficient cooling of the windings. The coil was rotated during the setting process to ensure a homogeneous distribution around the circumference. As a beneficial side effect, the resin also blocks mechanical vibrations of the windings, reducing mechanical distortion.

2.2.3.2 Solenoid Coil Optimization

Since the inner diameter of the solenoid coil's casing constitutes the bore, the coil's size limits the minimum distance to the bore for the second axis. It is therefore advisable to start the design process with the solenoid.

Constraints

Table 2.5 lists the requirements that were used for the design process, along with the parameters as predicted by simulation and measured values from the manufactured coil.

The design was focused on achieving high homogeneity, a 20 mm FOV at a gradient of 3 T/m and compact size, while staying within acceptable limits for required current and thermal losses. The first is given by the used power amplifiers that deliver up to 30 A_{pk} with acceptable distortion (cf. section 2.2.9), while the latter is governed by the cooling system and operating temperature range, as well as the resulting quality factor of the excitation circuit.

Optimization using a genetic algorithm

To optimize the structure of the coil, a genetic algorithm has been used, similar to the approach suggested by *Murgatroyd* and *Man* [140, 141]. The fitness function was chosen to take the achieved homogeneity, the average field strength and the smoothness of the coil former into account.

$$fitness = 0.27 \cdot \frac{B_{\text{avg}}}{B_0} + 0.4 \cdot (1 - k_{\text{inhomogeneity}}) + 0.33 \cdot k_{\text{turn-linearity}} \tag{2.8}$$

Where $k_{\text{inhomogeneity}}$ projects the inhomogeneity result onto the value range of $[0..1]$, whereas $k_{\text{turn-linearity}}$ does the same for the radius step size between adjacent turns. B_0 denotes the maximum achievable field strength for the given winding count using the minimum admissible inner coil radius and B_{avg} is the average achieved field strength in the VOI.

The last criterion, $k_{\text{turn-linearity}}$, was employed to favor coil formers with a manufacturable surface, without discontinuities.

Genetic algorithms are useful for a first design study, since there are only very limited assumptions to be made before the evaluation can start. With sufficiently random mutations during each step, they are also capable of exploring a large portion of the design space, so that local optima do not restrict the evaluated design. However, the fitness function as well as the choice of parameters heavily influence the outcome and should be carefully chosen to reflect the design intent.

Parameter	Requirement	Simulation	Measurement
Bore diameter d	$> 30\,\mathrm{mm}$	39 mm	39 mm
FOV size x axis	$> 20\,\mathrm{mm}$	20 mm	20 mm
Inhomogeneity (1.53)	$< 4\,\%$	$0.676\,\%$	$0.976\,\%$
rms non-uniformity (1.52)	$< 2\,\%$	$0.144\,\%$	$0.242\,\%$
Max. directional Inhomogeneity (1.55)	$< 2\,^\circ$	$0.235\,^\circ$	$< 1.087\,^\circ$
Field per unit current $\cdot\mu_0$		$1.667\,\mathrm{mT/A}$	$1.70\,\mathrm{mT/A}$
Required current for $30\,\mathrm{mT_{pk}}$	$< 20\,\mathrm{A}$	$17.999\,\mathrm{A}$	17.64 A
Resistance (10 kHz, Air)		$338.868\,\mathrm{m\Omega}$	346.2 mΩ
(in Water)			455.8 mΩ
Resistance (25 kHz, Air)		$354.703\,\mathrm{m\Omega}$	400.2 mΩ
(in Water)			1.67 Ω
Thermal losses (10 kHz, $30\,\mathrm{mT_{pk}}$, Air)	$< 300\,\mathrm{W}$	$109.785\,\mathrm{W}$	113.45 W
(in Water)			147.67 W
Thermal losses (25 kHz, $30\,\mathrm{mT_{pk}}$, Air)	$< 300\,\mathrm{W}$	$114.916\,\mathrm{W}$	129.7 W
(in Water)			541.1 W
Inductance		628.199 µH	632.9 µH
Parallel capacitance (Air)		519.89 pF	624.94 pF
(in Water)		1.59 nF	1.65 nF
DC series resistance			344.5 mΩ
Parallel resistance (Air)			41.61 kΩ
(in Water)			2.94 kΩ
Self resonant frequency (Air)	$> 100\,\mathrm{kHz}$	278.494 kHz	258.6 kHz
(in Water)		159.248 kHz	155.5 kHz

Table 2.5: Requirements, simulation results and measurements for MPI x axis transmit coil with 4 layers and 57 turns for layers 1 to 3, 5 re-enforcement windings at each end (layer 4), having an arc radius of 875 mm. 420×0.071 mm strands with 2 layers of Mylar serving were chosen for the litz wire.

The results of this optimization suggested that an arc-shaped coil former was the optimal shape. The resemblance to a *Maxwell* coil[7)] reinforces the notion that curved coil formers produce very homogeneous fields.

Since overall coil size was a strong design criterion, the relatively small radius of the arc was considered an inefficient use of available space. Therefore the optimization was repeated with another layer added to the coil, which only had windings at the

[7)] *Maxwell* coil here means the original arrangement proposed by *Maxwell* to improve the homogeneity of *Helmholtz* coils [77, p.319 $715]. It is not to be confused with gradient generators that use two *Helmholtz* coils with opposing field directions, known as gradient-field *Maxwell* coil.

outer ends of the coil. The arc radius of this barbell shaped coil was then optimized using the genetic algorithm. The result is a coil with higher homogeneity as can be achieved by the rough steps of support winding counts at the end[8)], while keeping an overall compact size. The arc radius became large enough so that the outer diameter of the coil at its mid was lower than at the re-enforced ends, thus no longer dominating the outer coil diameter.

Cooling concept

The cooling system for the x-axis coil has been designed to work with water as well as coolants with higher viscosity. The coolant first enters a distribution chamber, where it is evenly distributed into several cooling channels, that guide it below the perpendicular windings. Due to epoxy resin coating on each layer, the space between the windings is sealed and the coolant can only access the outer winding surface through a chamber at the far end of the coil. After cooling the outer surface, coolant is collected in a third radial chamber, before it exits the coil at the near end.
Figure 2.16 shows the field profile of the coil as well as a cross section of the coil former, revealing the cooling channels on either side of the windings.
The individual coil parts are hermetically sealed at the joints using epoxy glue, with silicone tubes, permanently attached to the inlets and outlets, acting as connects to the cooling system.

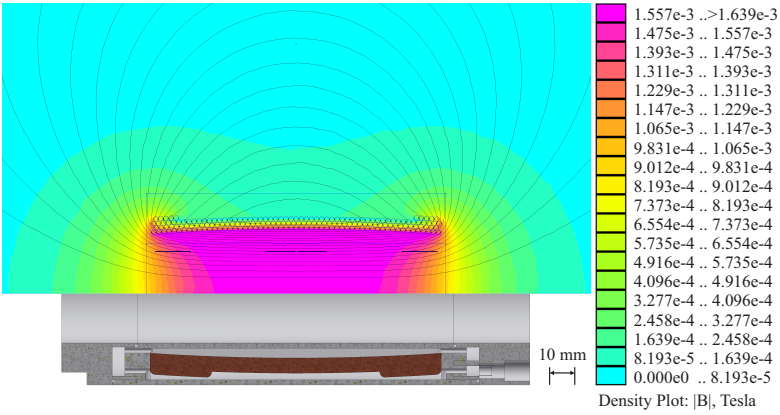

Figure 2.16: Magnetic field simulation and CAD image of MPIv3 x axis drive coil.

As table 2.5 shows, using DI-water as coolant has a large impact on the self resonant frequency. This shift also leads to a large increase in losses at 25 kHz. Since

[8)] This was determined using a simulation study. The homogeneity of the final coil was verified and closely matches simulation results, cf. table 2.5. These measurements were performed using a small test coil.

the coil is operated at a duty cycle, the time average is still tolerable and the cooling capacity is sufficient for continued (cycled) operation. The effect of the coolant on the self resonant frequency led to the development of additional simulation tools (cf. section 2.2.3.5), that allow to examine these variations more closely. Evaluation of test coils that do not reflect the exact winding configuration has proven to be of limited accuracy. Since many geometric properties (like enamel thickness of litz wire strands, serving thickness, etc.) cannot be scaled with reasonable effort, building a scaled coil model also has systemic limitations. Therefore, simulating self-capacitance and mutual winding inductance of multi-layered coils provides additional insights, such as the exact prediction of higher order resonances. Unfortunately, these tools were only available after the drive coils were manufactured. However, since both axes (see below) can be operated at their intended field strengths, there was no need to redesign the coils. To allow future coil designs to benefit from these findings and to compare the results with real world data, the procedure has been outlined in section 2.2.3.5 and selected results have been added after the fact to table 2.5 on page 86 and table 2.6.

2.2.3.3 Helmholtz Coil Optimization

Constraints

The parameter constraints imposed upon the Helmholtz coil design for the y axis are listed in table 2.6. Besides these values, a major constraint for the design are the sizes of the x axis coil, as well as the gradient generators. For all field generators, keeping the size as compact as possible and minimizing the distance to the bore is of great importance.
In contrast to the x coil, where most requirements could be met with a rather large margin, the y axis required several trade-offs. Due to cooling requirements and the already compact size of the x coil, there was little room for further optimization to meet all design goals of the y axis. This is for a large part the result of the inferior coil constant of a Helmholtz configuration and the limitations imposed by the available power amplifier.
Two areas were accepted to fall short of the initially desired values: field homogeneity for the full FOV, and FOV size. To meet these constraints would require larger currents from the power amplifiers than were available for this design. The choice of a parallel resonant structure could prove beneficial in this case, but was rejected for the initial design. The project time-line precluded the prototype experiments that would have been required for a parallel resonant excitation. Due to the modular nature of the MPI system, the y axis coils can be exchanged without the need to disassemble the x axis or gradient field generators, once such a solution becomes available. Another possible improvement would be the usage of bended (saddle) coils [142], which on the other hand would place great demands on the manufacturing when combined with a liquid cooling system. They would also require to modify the coil system case.

Parameter	Requirement	Simulation	Measurement
Bore diameter d	$> 30\,\mathrm{mm}$	39 mm	39 mm
FOV size y axis	$> 10\,\mathrm{mm}$	10 mm	10 mm
Inhomogeneity (1.53)			
(20 mm × 20 mm)	$< 5\,\%$	16.0 %	20.15 %
(20 mm × 10 mm)	$< 4\,\%$	7.34 %	10.75 %
rms non-uniformity (1.52)			
(20 mm × 20 mm)	$< 3.5\,\%$	3.34 %	5.51 %
(20 mm × 10 mm)	$< 2.8\,\%$	1.65 %	2.47 %
Max. directional Inh. (1.55)			
(20 mm × 20 mm)	$< 2°$	5.26 °	$< 8.52°$
(20 mm × 10 mm)	$< 2°$	2.82 °	$< 6.19°$
Field per unit current $\cdot\mu_0$		505.04 µT/A	510 µT/A
Required current for $15\,\mathrm{mT_{pk}}$	$< 35\,\mathrm{A}$	29.7 A	29.4 A
Resistance (10 kHz, Air)		276.45 mΩ	267.4 mΩ
(in Water)			271.0 mΩ
Resistance (25 kHz, Air)		328.95 mΩ	329.0 mΩ
(in Water)			374.6 mΩ
Thermal losses (10 kHz, $15\,\mathrm{mT_{pk}}$, Air)	$< 300\,\mathrm{W}$	243.85 W	231.13 W
(in Water)			234.2 W
Thermal losses (25 kHz, $15\,\mathrm{mT_{pk}}$, Air)	$< 300\,\mathrm{W}$	290.16 W	284.37 W
(in Water)			323.8 W
Inductance		683.8 µH	535.9 µH
Parallel capacitance (in Air)		5.32 pF	42.87 pF
(in Water)		72.3 pF	66.65 pF
DC series resistance			256.56 mΩ
Parallel resistance (Air)			96.4 kΩ
(in Water)			33.9 kΩ
Self resonant frequency (Air)	$> 100\,\mathrm{kHz}$	2.64 MHz	1.05 MHz
(in Water)		715.79 kHz	823.4 kHz

Table 2.6: Requirements, simulation results and measurements for MPI y axis transmit coils: Two Helmholtz coils in a $10 \times 4 + 12 \times 4$ configuration made of litz wire with 280×0.1 mm strands and 2 layers of Mylar serving.

Choice of winding configuration

Considering the demanding space requirements for the y-axis coil, the choice of winding configuration is important for the achievable field strength, homogeneity and self resonant frequency.

Since access to the bore is required, solenoid coils do not work for the y direction and a Helmholtz coil pair is used instead. Due to the dimensions of the gradient magnets, the outer y coil diameter, especially in close proximity to the FOV, is limited. This poses a problem for homogeneity, since for an ideal[9] Helmholz coil

$$d_{\text{sep}} = R_{\text{Helmholtz}} \tag{2.9}$$

the separation d_{sep} should equal the coil radius $R_{\text{Helmholtz}}$ to achieve a field with maximum homogeneity at the center. Due to the presence of the x axis solenoid, the spacing between the coils cannot be reduced enough to account for the limited diameter. To mitigate this issue, each coil is divided into two disks of windings, with the outer disk (not obstructed by the magnets) having a larger diameter.
Concerns regarding self-resonant frequency, coil inductance and coil factor however limit the upscaling of the outer winding radius, leading to a high inhomogeneity compared to the x axis. This is acceptable for the frequency domain reconstruction (cf. section 1.2.3.1 on page 16), where the system matrix takes care of the resulting distortion. For x-space reconstruction (cf. section 1.2.3.2) however, this might limit the usable FOV in the y direction. Since x-space reconstruction is currently not available on a lissajous trajectory anyway, this is an acceptable limitation.

Achievable field strength is another concern with the y axis coil: Due to the limited output power[10] of the employed power amplifier, the FOV-size in the y direction had to be reduced to 10 mm. This however can be solved without additional construction effort by paralleling two power amplifiers. Thanks to the available space at the outer sides of the coil, the cooling system of the y axis coils could be designed to handle enough current so that the originally desired FOV size can be obtained.

Another benefit of the division of the coil into two separate disks is a reduced self-capacitance of the coil. Due to the separation of both coils by a septum, the capacitive coupling between them is lowered. Both act more closely to a series circuit of two individual coils, therefore the inductance adds but the self-capacitance does not. Therefore this technique might be worth adapting for the x axis coil as well in a future revision. A similar technique is known as *disk winding method* [143], but its effect on self-resonance is not well documented in the literature.

Optimization

The geometrical constraints imposed upon the y axis drive coil design make the available optimization options more subtle. In addition to variations in the layer- and winding counts, the choice of septum thickness and the outer diameter of the outer coil are available for optimization. To support larger currents for future improvements, a 280×0.1 mm stranded litz wire has been chosen. Similar to the x axis, Mylar serving is chosen to reduce the self-capacitance increase with liquid coolants. Likewise, epoxy resin has been used to coat individual layers and avoid vibrations. Optimization of the

[9] I.e. a coil made of a wire with infinitesimal radius.
[10] Or more precisely: the output power range with acceptable distortion values

available parameters resulted in a configuration with 10 layers × 4 windings for the inner coil pair and 12 × 4 for the outer coils. Figure 2.17 shows a field simulation of the coil along with a CAD image. The x axis coil is also included as semi-transparent overlay, revealing why the coils could not be spaced closer together, whereas figure 2.18 shows the gradient magnets limiting the outer coil diameter of the inner disk.

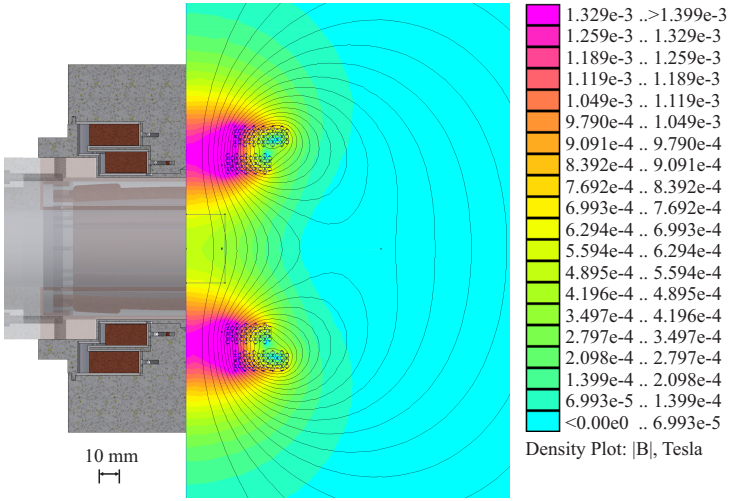

Figure 2.17: Magnetic field simulation and CAD image of MPIv3 y axis drive coil. The x coil is shown as semitransparent in the CAD drawing to show the bore size.

Cooling concept

Another virtue of the disk winding method is extra available space between the disks that can be used for coolant channels. With the help of a 3d-printed septum, coolant supplied from the center axis of the coil is distributed radially along either sides of both disks. At the outer radii, the coolant is collected and drained from the casing. This leads to a much better cooling rate than is available for the x coil. However, this is only possible because generous space is available at the outer faces of the coils. Again, the casing has been sealed with epoxy glue, which has proven to be a a better option than sealing gaskets. This is due to elasticity and the achievable surface roughness of the PA-6 polymer, which is used for the cases.

2.2.3.4 Coil system case

The coils of both active axes are held in place by a case structure that fixes them to the coil system table of the scanner frame. The shape of the case is designed to al-

low minimal spacing between all components, while providing a mechanically sturdy structure.
Figure 2.18 shows the coil system with both axes present with a quarter section removed to reveal coil windings and cooling channels.

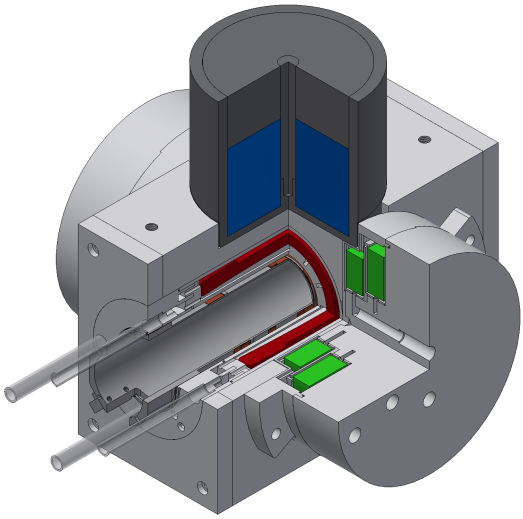

Figure 2.18: CAD image of the MPIv3 coil system assembly, with a quarter section cut open to reveal the coils. The windings of the x axis drive coil have been colored in red, the y axis is depicted in green and the gradient magnets are shown as blue.

2.2.3.5 Predicting self resonance through simulation methods

In the previous sections, the self resonant frequency (SRF) of coil structures has been a constant concern. To properly determine the SRF requires either the solution of the quasi-magnetostatic and quasi-electrostatic problems or the quasi-stationary electromagnetic problem of the coil.
As mentioned before, the following approach was developed after the MPI coils had been constructed. Since the results agree well with measured data, the methods are documented here. Notably, the results fit measured data beyond the first resonance, a range which is rarely discussed in the literature outside RF-applications. It is, however, useful information when designing resonant filters, as it may limit the range over which the filter elements retain their designated functions[11)]. As explained in section 1.3.2.7,

[11)] In some cases, as we will see in section 2.2.7.2 on page 114, the parasitic series resonance of the coil is more important. E.g., the parasitic parallel resonance of a series resonant shunt circuit in a bandstop filter does not harm the filter's function, while the parasitic (second) series resonance does.

the developed method is based on prior works by *Grandi* et al. [72], *Massarini* et al. [69] and *Hole* et al. [73], which have been adapted and expanded to include coolants and additional loss mechanisms [74].

Calculating the self-capacitance of a coil

For solving the electric problem separately, several methods are available. Based on the derivation of (1.56) the turn-to-turn capacitance between two adjacent windings can be calculated. Contrary to the original geometry, which assumed tightly spaced turns [69], the formula presented here assumes that adjacent windings are separated by a small space $2\ s_\mathrm{g}$ between the outer edges of their insulation. It is further assumed that this space is filled with a medium that has a dielectric constant ε_g. For this geometry, we have [74]

$$C_\mathrm{tt} = 2\,[C_\mathrm{ser}]_{\theta=0}^{\theta=\frac{\pi}{6}} = \frac{2\,\varepsilon_\mathrm{in}\,\varepsilon_\mathrm{g}\,l_\mathrm{t}\,r_\mathrm{in}\,\arctan\left(\frac{\varepsilon_\mathrm{in}\,s_\mathrm{g}+2\,\varepsilon_\mathrm{in}\,r_\mathrm{in}+D}{(\sqrt{3}+2)\,S}\right)}{S}. \tag{2.10}$$

$$S = \sqrt{(s_\mathrm{g}+2r_\mathrm{in})\,s_\mathrm{g}\,\varepsilon_\mathrm{in}{}^2 + (s_\mathrm{g}+r_\mathrm{in})\,2\varepsilon_\mathrm{in}D + D^2} \tag{2.11}$$

$$D = \varepsilon_\mathrm{g} r_\mathrm{in} \ln\left(\frac{r_\mathrm{in}}{r_\mathrm{cu}}\right) \tag{2.12}$$

where C_{tt} is the turn-to-turn capacitance, ϵ_g is the permittivity of the coolant and ϵ_{in} that of the insulator. $2\,r_{in}$ and $2\,r_{cu}$ are the outer insulation diameter and the copper diameter respectively. The winding length is designated as l_t (cf. [69]).

A similar approach can be pursued using numerical methods. This has the benefit that complex geometries become easier to model during optimization. Handling of boundary conditions and geometrical dependencies become increasingly difficult for the analytical case, especially when the geometry to be examined doesn't conform to a Cartesian or polar grid, or contains a mixture of both. These issues are addressed by the meshing algorithm when using numerical methods. However, the different orders of magnitude encountered in the dimensions of MPI coils can be problematic: The inter-winding distance is usually in the range of $50\,\mu\mathrm{m} \ldots 200\,\mu\mathrm{m}$, while the overall coil dimensions regularly exceed $100\,\mathrm{mm}$. This creates issues when trying to model three-dimensional structures due to the amount of cells required. For two-dimensional simulations and axisymmetric three-dimensional problems the available memory and computing power of current workstations is more than sufficient, leaving this route as a promising option for a practical approach.

Two approaches are available when trying to determine the self-capacitance numerically: The coil structure can be handled in total, i.e. the total electric energy within the coil is calculated and the capacitance is derived via

$$C = 2 \int\limits_{V_\mathrm{Coil}} \varepsilon \boldsymbol{E}^2 d^3\boldsymbol{r}. \tag{2.13}$$

The potential of the individual windings has to be determined from the total voltage drop over the coil, the winding pattern and impedance of each turn. Comparison of capacitance values with measured data suggests that the assumption of a constant voltage drop per winding leads to acceptable results even in the presence of slightly varying winding radii [74].
Alternatively, the capacitance of adjacent wires can be calculated separately. The behavior of the total structure is then handled by inserting these values into a network that represents the winding pattern of the structure. This can be accomplished numerically by slightly varying the potential of one winding and observing the corresponding change of the charge for each other wire, while keeping their potentials. The capacitance can then be calculated by [12)]

$$C_{m,n} = -\frac{\partial Q_m}{\partial U_n}. \tag{2.14}$$

While the first method is more straight forward and less error-prone, the second method offers deeper insight into the source of self-capacitance, at the expense of additional complexity and computational effort. It also scales not as well as the first approach when second order effects (e.g. not directly adjacent wires) are to be included (although they can often safely be neglected).

Both methods have been implemented in the femm simulation framework that was also used for magnetic simulations. This ensures that both magnetic and electric simulation are performed on the same geometry. Not surprisingly, the results show that for multi-layer coils the inter-layer capacitance is much more important than the inter-winding capacitance within a layer, to the point where the latter can be neglected. Although the capacitance values are almost identical, inter-layer capacitances have a much higher voltage drop between them and therefore lead to considerably more displacement current. This can be addressed by using special winding patterns, e.g. the disk-winding technique. However, manufacturing becomes more involved when using these methods and capacitance reduction is often traded for increased overall coil size.

Inductance calculations

The total coil inductance can be calculated by using the methods outlined before during coil optimization (cf. section 2.1.3.2). Similar to the electric problem, a second numerical method exists, where the current in a single winding is changed and the effect on the other windings (and itself) is observed. This allows to extract the

[12)] The negative sign is due to the fact that the potential of the m winding is being held constant. Therefore additional negative charge is required there to satisfy the field equations if ∂U_n is positive.

(mutual) inductance matrix for the coil:

$$\boldsymbol{L} = \begin{pmatrix} L_{1,1} & M_{1,2} & \dots & M_{1,n} \\ M_{2,1} & L_{2,2} & \dots & M_{2,n} \\ \vdots & \vdots & \ddots & \vdots \\ M_{m,1} & M_{m,2} & \dots & L_{m,n} \end{pmatrix} \tag{2.15}$$

with the individual elements calculated by $M_{m,n} = \frac{\partial \Phi_m}{\partial i_n}$ and $L_k = L_{k,k} = M_{k,k}$.

Again, the results can be put into context by the equivalent network. Due to the character of the magnetic field, the relevant mutual inductances cannot be determined by only considering the distance between the windings. Since the data from the numerical solution contains the information on all mutual inductances for each individual wire, it is easy to extract all coupling factors and drop negligible ones as a post-processing step.

The desired values for the (mutual) inductances of the individual windings can also be determined analytically using the formulas (1.57), (1.58) on page 36. For solenoid coils, even in the presence of a slightly bent coil former, the results agree very well with measured data and show a difference of less than 2%.

Equivalent network

The equivalent network of the coil is constructed through the combination of the (parasitic) elements determined from the electrical and magnetic simulations. It is based on the model shown in figure 1.11, but is used here in an expanded form, which includes additional loss mechanisms (cf. figure 2.19).
For coils with large winding counts and turn lengths well below the wavelength, the lumped elements of the network can be formed directly from the data of the individual windings. For coils with fewer windings or at high frequencies it is necessary to divide every winding into several sections, to adequately describe the distributed nature of the studied parasitics. At even higher frequencies, field retardation has to be included and a full scale PEEC simulation [81] can be used, which is beyond the scope of this work.

Every cell m contains a self-inductance L_m of the cell, derived from the self inductance of the corresponding winding $L_{m,m}$. It is coupled to the self-inductance of other windings by specifying the coupling factor from the relation

$$k_{m,n} = \frac{M_{m,n}}{\sqrt{L_{m,m} \cdot L_{n,n}}}, \tag{2.16}$$

where all variables on the right hand side are readily available from the inductance matrix (2.15). The inductance branches also include the AC losses through skin- and proximity effect, modeled by $R_{ac,m}$.

The nodes N_m, N_{m+1} of the inductance L_m (cf. figure 2.19) are then coupled to the nodes of the neighboring windings $m-1$, $m+2$ by the coupling capacitances $C_{\mathrm{tt}_{(m-1,m)}}$, $C_{\mathrm{tt}_{(m+1,m+2)}}$. Additionally, there exists a parallel capacitance $C_{\mathrm{tt}_{(m,m+1)}}$ across the winding m from N_m to N_{m+1}. There are also inter-layer capacitances $C_{\mathrm{i}_{(m,n+2)}}$, $C_{\mathrm{i}_{(m+1,n+1)}}$, $C_{\mathrm{i}_{(m,n+1)}}$, ... Their value, similar to all coupling capacitances, is available from the electric simulation (2.14). All capacitances are modeled with parallel conductances present, to account for the loss mechanisms mentioned in section 1.3.2.4.

Spice simulation results and comparison with measured data

The equivalent network of the coil, which is formed by connecting the previously described basic cells depicted in figure 2.19, can be solved using either a modified nodal approach [144], or it can be translated into a netlist and solved by a SPICE circuit solver [145, 146]. Connecting the coil network at both ends with a voltage source, the impedance of the network can be determined by performing an AC simulation and evaluating the resulting current and voltage of the voltage source branch

$$Z_{\mathrm{coil}} = \frac{V(\mathrm{ACVS})}{I(\mathrm{ACVS})}. \tag{2.17}$$

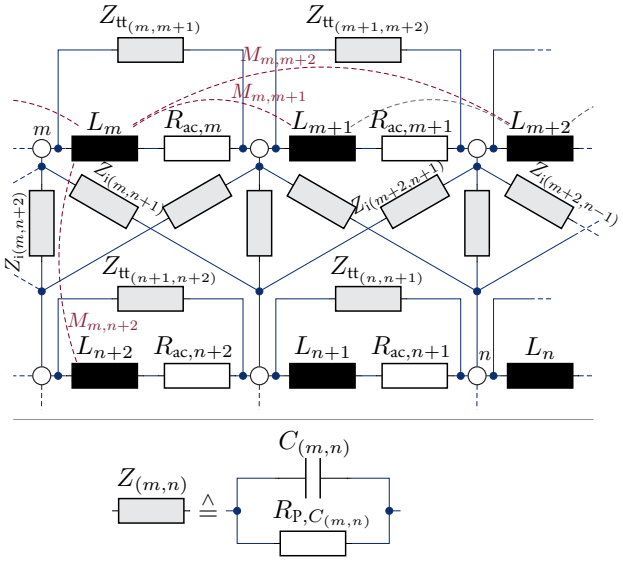

Figure 2.19: Lumped component network of a coil based on the suggestion by *Grandi* et al. [72], expanded to include additional loss mechanisms.

The result is plotted in figure 2.20 and figure 2.21, in comparison with measured data and a simple fit of an RLC model (cf. figure 1.8 on page 29). The lumped component values were determined using either analytical formulas ($Z_{\text{Analyt.}}$) or numerical simulations (Z_{FEM}). To evaluate the influence of the model elements, another simulation result has been added, where only the capacitive coupling of the L_m elements is considered (Z_{CC}): The inductance value has been adjusted there to use the total flux linkage of the winding $L_m = \frac{\Phi_{\text{total},m}}{I_m}$, to account for the mutual inductance with other windings, which is no longer modeled individually. The cell size was chosen to be identical with a single winding. A S-parameter skin effect model based on a femm frequency sweep of the magnetic simulation or analytical expression (1.60) was used in place of $R_{\text{ac},m}$ and remaining loss elements were given a constant value that was fitted to measured data at the first resonance to focus on the frequency dependency and resonances.

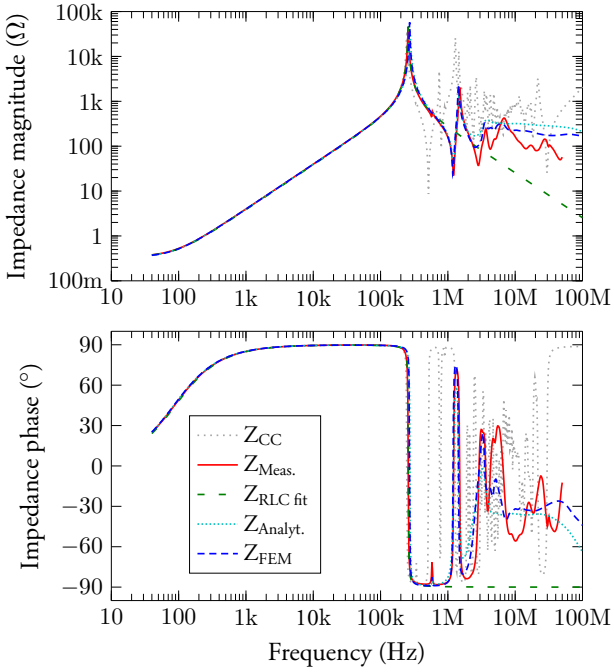

Figure 2.20: Comparison of the analytically ($Z_{\text{Analyt.}}$) and numerically (Z_{FEM}) predicted impedance of the dry x axis drive coil with measured data ($Z_{\text{Meas.}}$) and an RLC model fit ($Z_{\text{RLC fit}}$). The calculation was also performed without individual mutual inductive coupling and only the capacitive coupling in place (Z_{CC}).

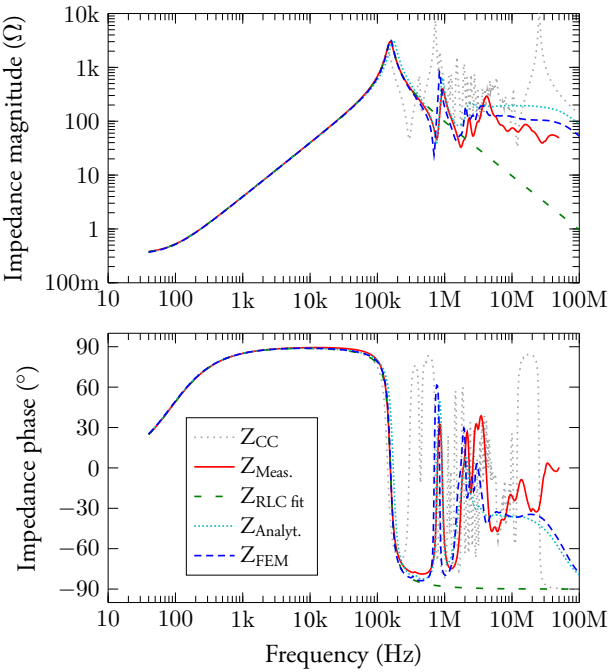

Figure 2.21: Comparison of the analytically ($Z_{\text{Analyt.}}$) and numerically (Z_{FEM}) predicted impedance of the water cooled x axis drive coil with measured data ($Z_{\text{Meas.}}$) and an RLC model fit ($Z_{\text{RLC fit}}$). The calculation was also performed without individual mutual inductive coupling and only the capacitive coupling in place (Z_{CC}).

As can be seen from figure 2.20 and figure 2.21, the lumped cell networks with analytically and numerically determined elements accurately predict the first parallel resonance of the coil, to the point where no difference to the measured data or fitted RLC model can be spotted. More interestingly, the models also predict the frequency of the first series resonance and the second parallel resonance with adequate precision. Arguably, the second series resonance is also in accordance with measured data.
From this point upwards, it becomes obvious that additional frequency dependent loss mechanisms have not been modeled accurately in the model. Therefore the quality factor of higher order resonances is underestimated, leading to increasing deviations between the model and the measured data. This is especially the case for the analytical calculation of AC losses that calculated to be even higher than the numerically determined values. Despite these deviations, the geometric mean value continues to match the measured data up to 10 MHz.

Comparing this result to the reduced model, where only capacitive coupling between the windings has been incorporated (Z_{CC}), it becomes obvious that the inclusion of mutual-inductance effects is mandatory if reasonable accuracy is required beyond the first resonance. Therefore, the extraction of the inductance matrix, while computationally expensive, is beneficial for the overall result. Since the analytical values of the (mutual) inductance are also in very good agreement with numerical results and measured data, they can be used to further decrease the simulation time.

The computing time for the above modeling approach using the finite element method on a Core2Duo E8500 3.1 GHz processor with 8 GB RAM was less than 12 h for all required magnetic and electrostatic simulations. Netlist generation and Spice simulation can be performed on the same hardware in less than five minutes. Since each winding is investigated independently, the problem can be parallelized without additional effort. With the same single-thread performance, computing the simulations for all windings in parallel would reduce simulation time to under eight minutes. The simulation time for the analytical approach (not parallelized) is fifteen minutes.
This is in stark contrast to the estimated computation time for a three-dimensional quasi-stationary electromagnetic simulation using a commercial field solver, which was over a week on the same hardware.

The outlined approach therefore lends itself well for the final design verification before coil production is started. To guide the design process, the analytical formulas for the mutual inductances can be used and a reasonable estimate of the first resonance can be achieved, while drastically reducing the computational effort.

Since a SPICE netlist is generated from the simulation results, this method also lends itself well for the modeling of filter structures. To reduce simulation time, S-parameter extraction can be performed for filters with many coils modeled this way.

As figure 2.21 shows, above results also match measured values well for the water cooled coil. Consequently the simulation method is able to predict the effect of coolants on the self-resonant-frequency. The analytical capacitance values, however, show some deviation compared to numerical results which leads to the first resonance being predicted slightly higher than measured. Examining the model values it becomes apparent that these deviations are most pronounced between windings at the edges of the coil [74]. To further improve the results (2.12) needs to be adjusted. But since the numerical values show very good agreement with the measurements and the electrical FEM simulation is relatively fast, analytical capacitance calculation is not required to obtain accurate results in a reasonable time-frame.

When comparing the results without coolant as shown in figure 2.20 on page 97 more closely, it becomes apparent that there is a 4.6% error for the first parallel resonance. However, the first series resonance and the second parallel resonance fit well with measured data and overall prediction is more accurate than for the water-cooled coil. If the skin effect losses extracted from the magnetic simulation are excluded (cf. figure 2.22), it can be seen that the higher resonances that are overdamped by the simulated AC losses are present in the network structure. However, the non-uniform dampening of individual resonances that is apparent in measured data from the sec-

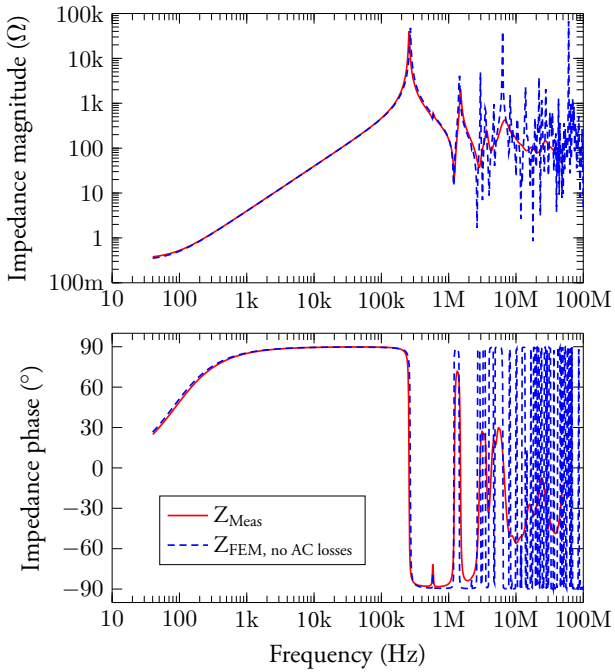

Figure 2.22: Comparison of the numerically predicted impedance without AC loss modeling of the dry x drive coil and measured data ($Z_{\text{Meas.}}$).

ond series resonance onward suggest that more complex loss mechanisms need to be incorporated to extend the model beyond that.

Limitations

From the comparison, good agreement between the coil model and measured data can be found up to the second series resonance which is at 4 MHz in the dry case and at 2.5 MHz for the water cooled coil. For frequencies above that point, losses are overestimated, resulting in higher dampening than is seen in measurements. Whether this is a general limitation of the simulation method or specific to this coil has not been examined further, since that frequency range lies well beyond the bandwidth of interest for MPI. It is, however, safe to assume that the coupling of electric and magnetic parameters *a posteriori* will break down somewhere in the RF regime, once the magnetic fields generated by displacement currents can no longer be neglected. A quasi-stationary EM field solver would be required in that regime to extract meaningful data for a lumped circuit model. Field retardation is another concern that is not

included and will become relevant at higher frequencies. On the other hand, usage of a coil like the presented one in the RF regime has few applications and structures with fewer windings are more common there, making the application of full-wave field solvers practical because of the simpler geometries.
Coolant losses are also a point that requires additional consideration. Taking a look at the real part of the coil in water, slight discrepancies between measured data and the model (including losses) are apparent in the range from the first parallel resonance up to the second series resonance. By adding another frequency dependent resistor to the basic cell, it should be possible to include these mechanisms as well. However, electrochemical theory suggests that the frequency dependency is more sophisticated and their parameters are harder to predict (cf. section 1.3.2.4). These efforts are beyond the scope of this work.

2.2.4 Drive frequencies

In the previous section on drive coil design, we already assumed two drive frequencies at 10 kHz and 25 kHz. The remaining design decision is the determination of the exact frequency for each axis, which also determines the FFP trajectory and influences resolution (cf. section 1.2.4.2 on page 19). For the 10 kHz drive frequency, values have been chosen to match those of the preceding system to allow both systems to share components and ease comparison of results.

At the 25 kHz drive frequency, the base frequency was chosen as the sampling rate of the slowest ADC or DAC converter sampling rate[13)], which happens to be that of the *NI PCI-6733* with 1 MSPS.
The choice of dividers was based on the achievable resolution, which should be in the sub-mm range, and the repetition frequency, which should be in the tens of ms.

Two sets were developed, which share a common frequency for the x axis, but differ in their values for the y axis. The second set was developed as a possible upgrade path for the system. It would require a faster DAC card to faithfully produce these frequencies and offers approximately doubled trajectory density. The y axis frequencies of the both sets are close enough so that they can be used with the same set of filters, since the filters' passband bandwidth is large enough (cf. next section). Table 2.7 lists the values of several parameters such as dividers and repetition frequencies for both sets.

[13)] I.e. the slowest conversion rate directly contributing to the imaging process. Another ADC card with slower sampling rate is available in the system, but is not used for imaging data.

Parameter	10 kHz		25 kHz, coarse set		25 kHz, dense set	
Base frequency	1	MHz	1	MHz	2	MHz
N_x	100		40		80	
N_y	96		39		79	
N_z	104		41		81	
f_x	10	kHz	25	kHz	25	kHz
f_y	10.417	kHz	25.641	kHz	25.316	kHz
f_z	9.615	kHz	24.390	kHz	24.691	kHz
T_x	100	µs	40	µs	40	µs
T_y	96	µs	39	µs	39.5	µs
T_z	104	µs	41	µs	40.5	µs
$T_{\text{Rep}}(x, y, z)$	31.200	ms	63.960	ms	255.96	ms
$T_{\text{Rep}}(x, y)$	2.400	ms	1.560	ms	3.1600	ms
$T_{\text{Rep}}(y, z)$	1.248	ms	1.599	ms	3.1995	ms
$T_{\text{Rep}}(z, x)$	2.600	ms	1.640	ms	3.2400	ms
x-density(x, y)	1.253	mm	784.59	µm	392.60	µm
y-density(x, y)	1.305	mm	804.67	µm	397.57	µm

Table 2.7: MPIv3 drive frequencies.

2.2.5 Transmit Filters

Filtering in the transmit chain is necessary since power amplifiers capable of delivering the required power to supply the MPI drive coils are not available with THD levels below 0.1% (-60 dBc). Achievable values under heavy load are often not better than (-50 dBc). Since spectral purity of (-80 dBc) or better is desired for MPI imaging, filtering is inevitable. For the very same reasons, only passive filters can be used.

Requirements for the transmit filters are as follows:

1. High linearity of (-90 dBc) or better
2. Low losses in the passband
3. Impedance suitable for integration into the transmit chain. Either directly or through a matching transformer.
4. Low susceptibility to electromagnetic interferences, especially in the kHz regime.
5. High stop-band attenuation up to 1.25 MHz
6. Easy to manufacture
7. Low-pass or band-pass characteristic

Due to the linearity requirement, the inductors in the filters can only be constructed as air-cored coils. This, however, makes cross-coupling between filter elements a major concern: Unlike coils with soft magnetic core and anchor structures, fringing fields are much more pronounced with air-core coils. Toroidal coils can to

some extent mitigate cross coupling but require additional manufacturing effort. Careful positioning is still necessary in addition.
Capacitor choice is also very important for the overall linearity. As discussed in section 1.3.1.3 on page 28, dielectric material and power rating are key parameters for capacitor selection. Since capacitors are routinely used (in parallel) for trimming purposes in passive filter circuits, trimming capacitors should satisfy the same criteria, with the exception of current ratings, which can be reduced according to the admittance ratio with the main capacitor.

To achieve high stop band attenuation up to the MHz regime, capacitor and especially inductor parasitics are important, as will be discussed later on the basis of the network implementing the filter (cf. section 2.2.5.2).
Selecting a suitable impedance for the filter is not only a matter of matching the filter to the amplifier and the transmit coil, but also influences the effect parasitics have on the filter response. More precisely, the effect of impedance scaling on the filter elements and the resulting minimum component values are important. Once they are in the same order of magnitude as the parasitics of filter elements and cabling, the implemented filter network significantly differs from the intended one, since parasitics can no longer be neglected. The result is a drastically altered frequency response, that may not even show the intended characteristic at all.

Considering the special case of a mMPI system, the major difference to a conventional MPI system is the presence of two drive frequencies per axis. As shown in the block diagram in figure 2.11 on page 78, each drive frequency has its own transmit filter. This limits the complexity (i.e. the order) of the filters, once overall space requirements and manufacturing costs are taken into account.

2.2.5.1 Choosing a Filter Response

The next step towards transmit filter implementation is the choice of filter characteristic and response type.

Requirements

Considering the general transmit filter requirements from the previous section with respect to the filter characteristic and response type, the aspects of impedance matching and integration into the transmit chain constitute the main points that influence filter design. They also rule out simple low-pass filters, since their insertion impedance increases with the filter order, which either leads to excessively small element values or undesirably high values of insertion impedance.

Since the drive signal is a continuous wave signal, the response type has only influence on the spurious signals to be filtered out and should not matter in the ideal case. Since most response types[14)] share a similar frequency dependency far in the stop-band region, the choice is mostly unrestricted from a functional point of view.

[14)] With the exception of elliptic filters, which trade steep transition into the stop-band for stop-band attenuation.

System integration

As outlined before, the filter impedance (i.e. its input, insertion and output impedance) should integrate well with the power amplifier and the drive coil circuitry.
This is where differences between the different response types are most pronounced. To keep the discussion concise, our comparison will be restricted to *Butterworth* and *Bessel* type filters. However, the same comparison can be applied to any other type.

In section 2.2.3 we have determined the inductances of our drive coils which we want to integrate into the transmit chain. For both axes, the values are rather large for air-core coils. The best way to integrate drive coils and transmit filters into the system, is to make the drive coils a part of the filter network. This completely eliminates the need for additional matching networks, avoiding losses through insertion impedances and stray fields from such arrangements.
However, this also means that the drive coils' inductance has a large influence on the values of all other filter elements.

Dimensioning procedure

Before choosing a filter type, it is beneficial to consider a general dimensioning procedure. Since we want to arrive at a certain inductance value at the end of the filter, the procedure is started "backwards" compared to the treatment in section 1.4, by discussing impedance and frequency scaling first. We then take a look at actual filter coefficients and choose the response type.

Table 1.1 on page 52 shows the element transformations for the conversion from a prototype low-pass to the band-pass filter we desire. Conversely, if we start at the last inductance value, we get an equation for the bandwidth and filter impedance.
Since we want high current in our drive coils, which have relatively large inductance values, it is suitable to choose a series element as the last filter block, which is shunted to the return path at the end by the termination resistor. We therefore get the equation

$$L_{\text{drive}} = k_R \cdot \frac{L_S}{b} \tag{2.18}$$

where k_R is the impedance scaling factor, b is the bandwidth (factor) of the filter and L_S is the prototype value of the series element.

The impedance factor directly determines the termination resistor values and scales all filter element values according to the relations given in table 1.1. Suitable values are bounded at the lower end by the smallest element values in the filter in comparison to expected parasitics, and at the upper boundary by the insertion impedance of the filter, i.e. the value of the termination resistors. Additionally, there is a practical limit for the maximum element size, so that excessively large impedances lead to bulky filter elements which tend to exhibit increased losses. For this design, an impedance of $4\,\Omega$ was chosen. This also ensures sufficient impedance matching with the driving power amplifier's output impedance.
This leaves the filter bandwidth b as the only remaining parameter (since the center

frequency is given by the desired drive frequency and the prototype value is calculated from the filter order and the response type).

To proceed, we should now pick a filter order. Since we want to limit the complexity and construction effort as much as possible, a filter order of $n = 3$ has been chosen. An order $n = 5$ will be evaluated as well. This leaves us with a series-shunt-series filter structure, which is very desirable. The series element at the input is beneficial, since it decouples the amplifier from the shunt element at all stop-band frequencies. This avoids excessive loads on the amplifier outside the passband, which might be detrimental to the linearity of its output stage. Therefore, if we were to add more filter stages, odd filter orders should be chosen.

To determine the filter bandwidth and calculate all remaining element values, we now need the values of the prototype low-pass filter. To do so, we apply the procedure summarized in section 1.4.3.5 on page 50 to the *Butterworth* and *Bessel* transfer functions, determined by (1.78) and (1.84).

For the Butterworth response, we get the well known transfer functions

$$H_{\text{Butter},3}(s) = \frac{1}{s^3 + 2s^2 + 2s + 1} \tag{2.19}$$

$$H_{\text{Butter},5}(s) = \frac{1}{s^5 + 3.236068s^4 + 5.236068s^3 + 5.236068s^2 + 3.236068s + 1} \tag{2.20}$$

from which we derive the element prototype values

n	3	5
R	1	1
$L_{S,1}$	1	0.618 033 988 749 894 1
$C_{P,2}$	2	1.618 033 988 749 89
$L_{S,3}$	1	1.999 999 999 999 991
$C_{P,4}$		1.618 033 988 749 874
$L_{S,5}$		0.618 033 988 749 908 6

Table 2.8: Butterworth LC element values for the prototype low-pass, orders 3 and 5 for a doubly terminated ladder.

These values agree well with tabulated values from the literature [147].

We compare this with the results for the Bessel transfer functions

$$H_{\text{Bessel},3}(s) = \frac{15}{s^3 + 6s^2 + 15s + 15} \tag{2.21}$$

$$H_{\text{Bessel},5}(s) = \frac{945}{s^5 + 15s^4 + 105s^3 + 420s^2 + 945s + 945} \tag{2.22}$$

with the corresponding low-pass prototype element values,

n	3	5
R	1	1
scale	1.755 672 368 681 211	2.427 410 702 152 628
$L_{S,1}$	1.255 024 271 901 255	0.930 298 712 544 450 7
$C_{P,2}$	0.552 786 404 500 052 2	0.457 703 004 075 216 5
$L_{S,3}$	0.192 189 323 598 702	0.331 221 729 561 598 5
$C_{P,4}$		0.208 963 662 587 665 4
$L_{S,5}$		0.071 812 891 227 286 96

Table 2.9: Bessel LC element values for the prototype low-pass, orders 3 and 5.

which are also in good agreement with literature values [89]. As has been remarked before, the $-3\,\mathrm{dB}$ point of the Bessel transfer function does not lie at $|s| = 1$. The corresponding scaling factor has therefore been included in the table. It can be used to multiply all element values by it to arrive with a frequency scaled response that does have this property, as often found in the literature [147].

Comparing the tables we find that the element values of the *Bessel* characteristic are asymmetric, while the *Butterworth* elements are symmetric around the center. This property of the *Bessel* filter types comes in handy for our design. Since we need to incorporate the relatively large drive coils into the filter, it is useful to put them at the "large" end of the ladder. Because we are dealing with linear passive time-invariant lossless networks, the principle of reciprocity applies and the transfer function is the same if the filter is to be used in reverse. The choice of using the largest prototype value for the transmit coils ensures that all other coils in the filter are smaller than the drive coils, reducing insertion impedances and losses in the filters. Other benefits are reduced construction effort and space requirements of the filter.

Having determined the prototype element values and having chosen the *Bessel* response, we can proceed to calculate the bandwidth according to (2.18). With no unknowns left, the remaining filter elements can be found by frequency transforming and impedance scaling the values of table 2.9 according to table 1.1.

Figure 2.23 shows the filter network for the x and y axis transmit filters. The element values are given in table 2.10.

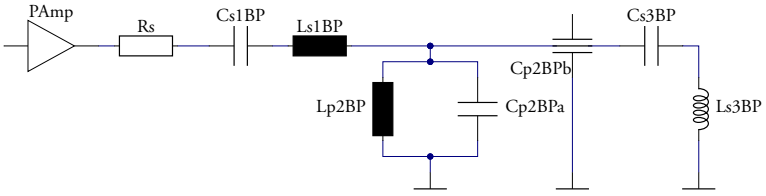

Figure 2.23: MPI 25 kHz transmit filter circuit. The second termination resistor has been omitted, since it is formed by the parasitic resistance of the transmit coil Ls3BP.

	Ls1BP	Cs1BP	Lp2BP	Cp2BP	Ls3BP	Cs3BP
x	96.325 µH	420.749 nF	2.340 µH	17.317 µF	629.050 µH	64.428 nF
y	82.094 µH	474.511 nF	2.639 µH	14.759 µF	536.120 µH	72.660 nF

Table 2.10: Element values of the transmit filters at 25 kHz

Figure 2.24 shows the ideal responses of the filter elements resulting from the values of table 2.10. The clean responses will later be traded for lower passband attenuation by reducing the dampening through lowered termination resistances consisting solely of parasitics. Measured responses will be given in section 2.3.1.2.

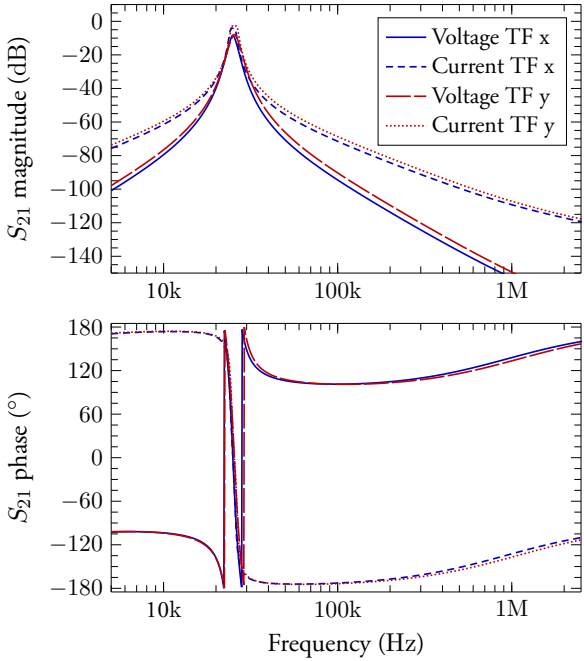

Figure 2.24: Ideal voltage and current transfer functions of the x and y transmit filters with values according to table 2.10, doubly terminated with no parasitics included.

With this information, we can now continue with the implementation.

2.2.5.2 Filter Implementation

The next step is to implement the filter elements. This is essentially the construction of suitable coils. Since air-core inductors are needed, commercial stock parts are not suitable, as they are not available as core-less variants in the required inductance range.

General consideration on the effects of parasitics

Parasitics are a major concern for the transmit filters. As can be deduced from figure 2.23 on page 106, in case of the series resonant circuit Cs1BP, Ls1BP, the parasitic parallel resonance of the coil (which happens to be the first parasitic resonance) will limit the impedance range over which the coil appears inductive. After the first parallel resonance the input impedance will therefore drop and the ability of the filter to prevent current flow in that frequency range will suffer. For the parallel circuit Lp2BP, Cp2BP, it is the first series resonance of the capacitor after which the circuit will appear inductive again and fail to short its node to ground, letting the current from the previous stage pass to the filter output. It is therefore advisable to design a filter with a large bandwidth, as this will lead to small values for the series inductors and parallel capacitors (cf. table 1.1). This is, however, limited by the desired attenuation at the low-ordered harmonics. Unfortunately, those harmonics are the ones with the most spectral energy in the transmit signal, so that a trade-off is required. For the design procedure outlined before the bandwidth was given by the drive coil inductance and the filter impedance scaling. With the chosen values, the resulting filter bandwidths are large enough to arrive at a good compromise. Apart from the choice of values, all elements should be selected, constructed and connected in a way that reduces parasitics.

Approximation of optimal multi-layer toroid coils

One major disadvantage of air-cored inductors are their large fringing fields, since there is no core that concentrates the flux. To keep susceptibility to external fields at a minimum and reduce losses in nearby metallic surfaces, such as enclosures, toroidal coils are built.

Optimizing the inductance per unit wire length leads to toroidal coils that have a D-shaped cross section [140]. This design has also been evaluated for the use as MPI filter coils before [148].

To properly dimension the coils, a MATLAB class was written that calculates the inductance of such an arrangement, similar as reported by *Murgatroyd* et al. [140]. However, extending upon the original suggestion, the calculations have been expanded to take the non-constant flux density inside a winding layer segment into account: The flux increases according to *Ampere*'s law when moving radially "into" the winding area and decreases accordingly as the outer winding area is passed. The corresponding integrals for the energy inside these cells have been solved analytically and incorporated into the result. This allows to increase the accuracy of calculations without resorting to larger cell counts, with minimal increase in computational effort.

Figure 2.25 shows a quarter of the cross section of a toroidal coil as it is evaluated in the script. Due to symmetry considerations, only the upper part of the cross section needs to be evaluated. The class tends to underestimate the inductance by a small amount of $< 5\%$, which gives a safety margin for estimating wire lengths. To simplify manufacturing, the coil formers are made of radii instead of the free-form curves that

result from the optimization. The influence of this change on the inductance-to-wire-length ratio is small, as was confirmed using the inductance calculation class.

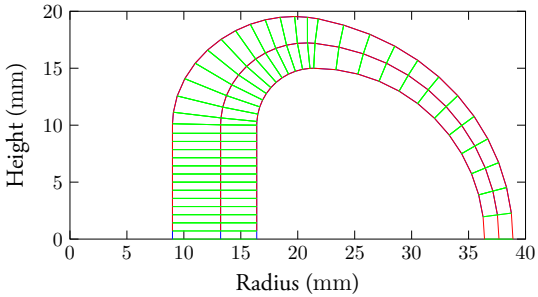

Figure 2.25: Quarter cross section of the Lp2BP toroid coil with the gridding, used by the dimensioning MATLAB class, visible. The center of the toroid is at 0; 0.

Manufacturing of coil formers was done using 3-d printing, using the fused deposition modeling method to produce the coil formers from polylactide filament. Litz wire with $630 \times 0.1\,\mathrm{mm}$ strands was used for the windings.

Choice of capacitors

As discussed in section 1.3.1 on page 27, capacitors can have a major impact on the linearity of a filter circuit. This is especially true in the transmit filters, where capacitors must handle high currents and voltages. *Celem* C500T and *Celem* CSP150 type capacitors have been used to implement the values according to table 2.10, with *Cornell Dubilier* series 942C20 capacitors used for trimming.

One notable exception are the Cp2BP capacitors, which are split (Cp2BPa, Cp2BPb in figure 2.23). A value of 4.7 µF is contributed by a *Schaffner* FN 7563 feed-through capacitor that passes the drive signal into the shielding chamber (cf. section 2.2.10 on page 126). The remaining capacitance is provided by *Celem* and *Cornell Dubilier* capacitors similar to the other elements. The feedthrough capacitor is used to provide a low impedance path at all relevant frequencies to the connector panel (see section 2.2.10 on page 126).

For the drive coils, as a consequence of the large self-induced voltages, arrays of *Cornell Dubilier* 942C20 have been used.

Parasitics of interconnects

Owing to the air-core-inductors and the large current requirements, filter elements for MPI drive chains tend to be somewhat bulky. In addition, some amount of space (especially between coils) is required to avoid undesired coupling. This leads to interconnect

lengths with parasitic inductance values that can no longer be neglected. Trimming of LC circuit's capacitor values must therefore be performed with the connecting wires in place. To reduce inductances, twisting of interconnect wires is mandatory. The current loop technique [92] should also be observed for all wires and interconnects in the transmit chain. Similar to the inductors, connecting wires should also be kept at considerable distance from ferromagnetic materials, to prevent nonlinearities.

Termination resistors

The termination resistors from the doubly terminated ladder filter have not been added explicitly to the filter structure to reduce passband attenuation and power losses. There is, however, to some degree a termination present that is formed by the parasitics on either side of the filter, i.e. the output impedance of the power amplifier and the resistance of the transmit coils. To this end, it is again beneficial that the largest valued inductors in the filters are the transmit coils. The achieved termination is not complete and some amount of undamped resonances are accepted (cf. section 2.3.1.2) in exchange for low losses. Since the excitation signal is a single sine, the shape of the filter's response is not important as long as it achieves low pass-band losses and sufficient stop-band attenuation.

Contact surface resistances

Another important aspect of the cabling is the contact resistance between components. It has been observed that contact degradation can lead to amplitude dependent transient phenomenons that create wideband harmonic content of the fundamental frequency up to the MHz range. Most probably, this is the result of arcing through thin oxide layers on the contacts carrying high currents, which happens beyond a certain amplitude. Contact materials should therefore be carefully chosen and should have firm mechanical contact.

Frequencies of y axis filters

To allow both sets of drive frequencies (cf. section 2.2.4) to be used, the y axis filters are trimmed to 25.5 kHz. Because of the finite bandwidth of the filters, this configuration allows the usage of both sets with negligible attenuation at the fundamental.

2.2.5.3 10 kHz Filters

For the 10 kHz drive frequencies, similar filter structures as for 25 kHz have been used, with the exception that an additional series element was used before the feed-through capacitor, which was used as a non-resonant shunt element. Figure 2.26 shows the filter circuit. The filter elements were re-used from the previous generation

MPI scanner [17, 149], where they had been introduced as an upgrade to the original, non-resonant design.

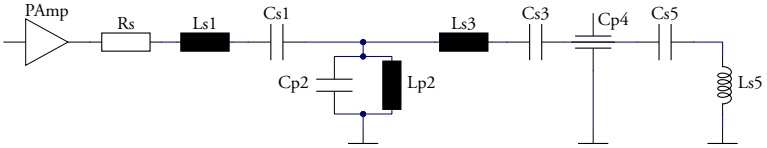

Figure 2.26: MPI 10 kHz transmit filter circuit.

2.2.6 Additional Bandstops and Postfiltering

In addition to the bandpass filters, the 25 kHz transmit chain possesses additional bandstop filters for the third and fifth harmonic. Since these harmonics are dominating the amplifier spurs, it is useful to apply additional attenuation for them. Another reason to add dedicated bandstops for them is the fact that they lie nearest to the fundamental, so that attenuation of the bandpass filters is comparably low.

Inside the shielded room (cf.section 2.2.10), an additional second order bandpass has been found to be beneficial to the drive field THD. Its characteristic impedance was chosen to be 6 Ω and was designed with a bandwidth $b = 19.9$ kHz using a *Bessel* characteristic.

2.2.7 Receive System

As outlined in figure 2.11, the receive system consists of the receive coil, bandstop filters and a low-noise amplifier. During the design process, the receive chain should be evaluated as a whole. Because the receive coil impedance interacts with the input impedance of the receive filter, it is necessary to account for this relationship during optimization. The same is true for the achievable input referred noise level.

2.2.7.1 Fully Differential Receive Coil

A major task of the receive chain is the suppression of fundamental feed-through from the transmit chain. Since the receive signal fundamental is dominated by the drive signal, the useful amount of information in this frequency component is very low.

Drive field feed-through suppression: Differences to MPS receive coil design

As we have learned before from the MPS setup, a differential receive coil (cf. section 2.1.5 on page 69) can be used to suppress fundamental feed-through. Unfortunately, due to the large FOV volume compared to the MPS sample volume, achieving sufficient suppression of the fundamental to reveal the particle signal is difficult in

a MPI system. While mechanical trimming can reproducibly achieve up to 70 dB of fundamental suppression [150], this is not enough to reveal the $1f$ particle signal without additional subtraction, which can either be done electronically or by using digital signal processing. Since the fundamental of the MPI signal is not required for successful reconstruction [151], the construction effort of a tunable differential coil is not justified. The construction of a trimming capability with two independent axes would be even more involved.

Even though complete rejection of the fundamental is not feasible, a differential coil design is still highly desirable, even though additional construction effort is required. Using winding counts and winding positions to fine-tune $1f$-rejection, 25 – 35 dB of suppression are achievable with reasonable effort. This reduces the amplitude that appears at the input of the receive filter, reducing the requirement for its input impedance and component ratings. Filter component ratings can therefore be selected with a large margin to the actual signal levels, which avoids non-linear effects.

Fully differential coil design

Another major concern of the receive signal is immunity to spurious signals, which may either come from the drive signal or other sources like switched-mode power supplies (SMPS).
A common technique to improve this immunity is differential signaling. It relies on the fact that two complementary signals which are propagated on adjacent wires will pick up almost identical signals from sources of disturbance, provided their distance to these sources is much larger than the wire spacing[15]. By subtracting both signals, the amplitude of the picked up signals can be reduced, while the payload signal amplitude is doubled. For maximum effect, a differential signal source should be used, so that the protective effect of differential signaling is available as early as possible in the transmission path.

Applying these considerations to the MPI receive chain, this means that a receive coil with differential outputs should be constructed. Any easy way to achieve this is to split the coil into two sections that are read out independently. To arrive at a complementary signal, the winding directions of both sections are opposite to each other. Each section consists of a differential coil arrangement which suppresses fundamental feed-through.
While this design does not help against spurs from the magnetic drive signal, it is capable of reducing spurs that couple capacitively onto the receive coil or its connections. Two identical receive filters and low-noise amplifiers should then be used to condition the signal. To transmit the signal to the ADC card, a fully differential amplifier (FDA) can be used, which will reduce any common-mode signals that have coupled onto the receive signal up to this point. The same effect is repeated for spurs that couple in after the FDA, when the signal is fed into a differential ADC input.

[15] Also, their properties (e.g. transmission line impedance and termination) should be similar to achieve this.

In addition to the gained immunity, the split coil design also helps to reduce the self resonant frequency: The reduced inductance compared to a coil with the same total winding count and just one section results in a factor $\sqrt{2}$ increase in the resonance frequency formed with the cable's capacitance. However, this is partially offset by the smaller signal levels in case that the receive signal amplitude is limited by receive amplifier noise. As long as spurs limit the lowest receivable signal level, this disadvantage does not apply.
Since the two coil sections can always be added together electrically by a series connection, a fully differential receive coil can always be converted into a conventional receive coil. This leaves the additional construction effort for coil and filters as remaining consideration that must be traded against the increased EMI immunity.

Receive coil implementation

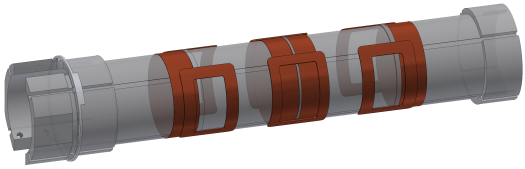

Figure 2.27: Fully differential receive coil of the MPIv3 system. The coil former is shown as semi-translucent to reveal the second pair of saddle coils for the y detection. The solenoid coils (made from $12 \times 0.04\,\mathrm{mm}$ silk served litz wire) constitute the x axis receive coils. Compensation coils are placed to either side of the sensing coils at the center. The extension on the left serves as a strain relieve for the cables. The ring on the left locks to the coil system case and prevents axial rotation.

Figure 2.27 shows the fully differential receive coil of the MPIv3 system. The y axis receive coils, which are constructed as saddle coils and positioned to either side of the coil, lend themselves naturally to the fully differential design by connecting each side individually. For the x axis solenoid receive coils, the center plane was used for splitting the axis into sections. All sections come with their individual compensation coils that have been axially moved outwards along the bore. At this position the winding counts have been adjusted so that the picked up signals from the drive field are identical to that of the sensing sections in the middle. Due to the rapid decay of the particle signal with distance, the compensation coils are only receiving very low MNP signal levels as compared to the sensing sections. As a result of the different winding directions, the voltage sum (by a series connection) has vastly reduced fundamental levels while the particle signal amplitude remains almost unaffected.

The sensitivity profile of the x axis coils is shown in figure 2.28. The vertical lines mark the ends of the FOV. While the graphic shows arbitrary units, later experiments

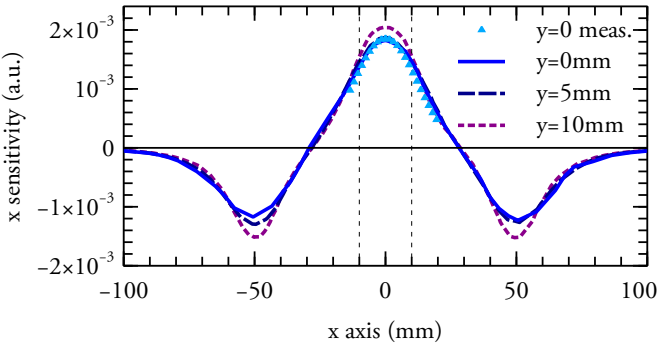

Figure 2.28: Sensitivity profile of the x axis receive coils (differentially after subtraction or wired for single ended readout) at different y distances from the center axis.

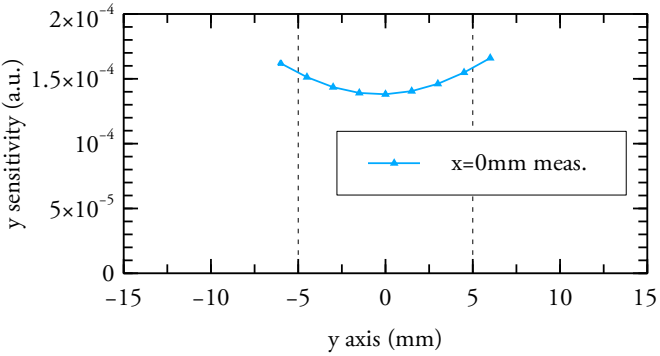

Figure 2.29: Sensitivity profile of the y axis receive coils.

during characterization determined the sensitivity at the center as $2 \cdot 624.08 \frac{\mathrm{V}}{\mathrm{Am}^2}$ (cf. section 2.3.1.6). The sensitivity profile of the y axis is depicted in figure 2.29.

2.2.7.2 Receive Filters

The receive filters possess a bandstop characteristic at the drive field fundamental to suppress the remaining $1f$ signal that exists due to sense- and compensation coil mismatch.
Since we are building a multi-frequency MPI system, four receive filters are required: One for each axis and frequency. For the 25 kHz drive frequency, which suffers the most from power amplifier spurs and SMPS switching noise, a differential receive filter is implemented by duplicating the design. To reduce magnetic and electric coupling into the receive filter coils, a solid copper enclosure is used for shielding.

Filter Response and Input Impedance Considerations

Similar to the transmit filter design, we need to choose a filter response that fulfills the requirements of the receive filters:

1. Good suppression $> 60\,\mathrm{dB}$ of the fundamental frequency
2. High input impedance at the fundamental to avoid excessive current in the receive coil
3. High linearity
4. Low pass-band attenuation from the second harmonic over the complete receive bandwidth up to $1.25\,\mathrm{MHz}$[16)]

Again, the *Bessel* response with its asymmetric element values is suitable for that task.

At this point we should elaborate a bit on the input impedance of the filter. Since we must avoid loading of the receive coil at the fundamental frequency to prevent excessive current flow and destruction of the receive coil windings, it is worth taking a closer look at this property. When designing a bandstop filter, according to table 1.1 on page 52, we can either get a parallel resonant circuit as a series element or a series resonant circuit as a shunt element at the filter input. It is obvious that the parallel resonant circuit will offer a high impedance at the fundamental, raising the total input impedance of the filter. The shunt element on the other hand would create a zero at the fundamental for the input impedance, which we must avoid.
A more subtle matter is the question, which element value of the prototype filter will lead to a high input impedance. If we assume the coil model of section 1.3.2.1 on page 29 with a parallel capacitor as well as a series and parallel resistance as parasitic elements, calculating the value of the impedance at the resonant point, we arrive at

$$Z_{\text{series element},L\|C}\Big|_{\omega_{\text{res}}} = \frac{C\,R_p\,R_{s,C}\,R_{s,L} + L\,R_p}{(R_{s,C} + R_{s,L})\,C\,R_p + C\,R_{s,L}\,R_{s,C} + L}\,, \tag{2.23}$$

$$\omega_{\text{res}} = \sqrt{\frac{C{R_{s,L}}^2 - L}{C{R_{s,C}}^2 - L}\frac{1}{LC}} \tag{2.24}$$

where L and C are the elements of the parallel resonant circuit and $R_{s,L}$, $R_{s,C}$ are the parasitic series resistances of the inductor and the capacitor respectively. R_p is the parasitic parallel resistance, which can be derived from the element values by $R_{p,L} \parallel R_{p,C}$, similar to the way C is calculated from $C_{p,L} \parallel C_{p,C}$. The latter can often be approximated by $C \approx C_{p,C}$.

Since the series resistances tend to be much smaller than $1\,\Omega$ and the parallel resistances, we can neglect terms where a product of series resistances appears in a sum with parallel resistances present. Thus we obtain

$$Z_{\text{series element},L\|C}\Big|_{\omega_{\text{res}}} \approx \frac{C R_p R_{s,C} R_{s,L} + L R_p}{C R_p (R_{s,L} + R_{s,C}) + L} \approx \frac{L R_p}{C R_p (R_{s,L} + R_{s,C}) + L}. \tag{2.25}$$

[16)] Determined by the sampling rate / bandwidth of the acquisition system

Considering the dimensioned value for C obtained from (2.24) to achieve resonance at the angular frequency ω_{res} (and using L'Hospital's rule)

$$C_{\text{dim.}} = \frac{L^2{\omega_{\text{res}}}^2 + {R_{\text{s,L}}}^2 - \sqrt{L^4{\omega_{\text{res}}}^4 + \left(2L^2{R_{\text{s,L}}}^2 - 4L^2{R_{\text{s,C}}}^2\right){\omega_{\text{res}}}^2 + {R_{\text{s,L}}}^4}}{2L{R_{\text{s,C}}}^2{\omega_{\text{res}}}^2} \tag{2.26}$$

$$\overset{R_{\text{s,L}},R_{\text{s,C}}\to 0}{=} \frac{1}{L\,{\omega_{\text{res}}}^2}, \tag{2.27}$$

we can therefore conclude that in addition to high values of R_p, large values for L and small values for C, as well as small series elements for L and/or C are beneficial to our goal. The relationship (2.27) between L and C ensures small values of C once L is increased. We should note however, that increasing L also tends to increase $R_{s,L}$ with $\sqrt{L}$ while R_p decreases with the layer count[17]. This, together with practical considerations, limits the maximum value of L.
Coming back to the matter of the prototype values, table 1.1 tells us that

$$L = \frac{b\,L_S}{{\omega_0}^2} \tag{2.28}$$

$$C = \frac{1}{b\,L_S}. \tag{2.29}$$

It follows that large prototype values L_S should be preferred to achieve a high input impedance. In addition, choosing a large bandwidth b also helps in this regard, but also affects the filter response.

Since we want to terminate the filter at the output to get a well defined input impedance for the low-noise amplifier, but do not want to increase the noise at the receive coil by a series resistor, we choose a singly terminated ladder (cf. section 1.4.3.4 on page 48).
For every ladder filter, there exists a dual implementation that uses the element values "in reverse". This is similar to (1.107), where the choice of signs determined whether we arrived at a minimum inductor or minimum capacitor implementation. One difference (since we are dealing with singly terminated ladders) is, that for the switch from minimum inductor to minimum capacitor we need to invert the termination. However, while dealing with prototype filters with $1\,\Omega$ terminations, this difference does not show.
The filter order was chosen according to the required stop-band attenuation as $n = 4$ for the prototype, which translates to a 8^{th} order bandstop.

The characteristic impedance of the filter is another design parameter. The receive coil impedance forms a voltage divider with the receive filter that can attenuate the receive signal. The rising source impedance over frequency of the receive coil makes this effect even more pronounced. It is therefore advantageous to have a high

[17] The decrease of R_p strongly depends on the winding technique, therefore no universally valid relationship can be given.

filter impedance to reduce this effect. It also increases the inductor value at the input even further, again helping to achieve high input impedance. A characteristic filter impedance of 50 Ω has been chosen, since it works well with impedance controlled cabling at the filter output, for which it achieves proper termination. In addition, higher impedance values would require very large filter coils that are hard to manufacture with air-core inductors.

The filter bandwidth, our last remaining parameter, was chosen as a compromise between high input impedance and low attenuation of the second harmonic. Increasing the bandwidth further would reduce the signal level of the $2f$ signal. With the chosen value of $b = 25 \cdot 1f$ we get a reduction of 4 dB for the second harmonic, which is acceptable.

The implemented transfer function of the prototype filter, calculated from (1.83), is

$$H_{\text{Bessel},4}(s) = \frac{105}{s^4 + 10s^3 + 45s^2 + 105s + 105}. \tag{2.30}$$

Table 2.11 lists the prototype values (according to the procedure from section 1.4.3.4) and table 2.12 shows the scaled element values resulting from the design decisions for the 25 kHz receive filters. Measured results of the achieved transfer function in comparison with the theoretical values are shown in figure 2.44 and figure 2.45 on page 138 for the x and y axis respectively.

As with the transmit filters, the 10 kHz receive filters were re-used from the previous MPI system. In contrast to the new design, they do not implement a specific response type. To achieve a high enough input impedance at 10 kHz, they resort to two parallel circuits in series at the input, which achieves partial pole removal and does not increase the order of the realized transfer function. This approach is necessary as the implementation of a filter with 50 Ω impedance at 10 kHz is not an option, as it leads to inductor values that are impractical to achieve with air-core coils.

n	4
R	1
scale	2.113 917 674 904 216
$L_{\text{series},1}$, $C_{\text{shunt},1}$	0.710 144 927 536 231 9
$C_{\text{shunt},2}$, $L_{\text{series},2}$	0.462 682 215 743 440 2
$L_{\text{series},3}$, $C_{\text{shunt},3}$	0.289 855 072 463 768 1
$C_{\text{shunt},4}$, $L_{\text{series},4}$	0.10

Table 2.11: Bessel LC element values for the 4th order prototype low-pass implemented by a singly terminated ladder structure, synthesized using the procedure outlined in section 1.4.3.4. The values agree well with those found in the literature [152].

LC	**Lp1BS**	**Cp1BS**	**Ls2BS**	**Cs2BS**	**Lp3BS**	**Cp3BS**	**Ls4BS**	**Cs4BS**
x	899.4 µH	45.1 nF	172.9 µH	234.4 nF	367.1 µH	110.4 nF	800.0 µH	50.7 nF
y	881.7 µH	44.2 nF	169.5 µH	229.8 nF	360.0 µH	108.2 nF	784.3 µH	49.7 nF

Table 2.12: Element values of the receive bandstop filters at 25 kHz and 25.5 kHz with a bandwidth of 47.14 kHz and 48.09 kHz respectively.

Receive filter implementation

The receive filter coils have been implemented using the same toroidal shape and dimensioning procedure that was used for the transmit filter coils (cf. section 2.2.5.2 on page 107). Litz wire with 25×0.07 mm strands was used for the larger coils, while the smaller coils were produced using 0.5 mm enameled copper wire. Capacitors for each coil were mounted on a PCB atop of it. Each LC-circuit was put in a separate compartment of the shielding enclosure to avoid coupling between the coils while allowing a compact design.

2.2.7.3 Low-Noise Receive Amplifier

The low-noise amplifiers are incorporated into the receive filter shielding enclosure to avoid coupling of spurs into the sensitive receive signal. A modular concept is used to allow easy adaptation to different input or output configurations. Two amplifier modules can be plugged into a base PCB board that provides power supply and connects to the receive filters. At the input and output of each amplifier module, passive modules can be used, e.g. to AC couple signals or provide input protection. The base board and the amplifier module pin-out have differential inputs and outputs. By using different modules, all combinations of either single-ended or differential inputs to single-ended or differential outputs are possible.

Amplifier modules for single-ended as well as for fully-differential configurations, based on commercially available operational amplifiers, have been built. As with other components, linearity is a central requirement, although the suppression of the fundamental by the differential receive coil design and the receive filter relaxes this requirement compared to the components earlier in the signal chain.
Low input referred noise is another important factor for receive amplifier design. Due to the inductive signal source, voltage noise tends to dominate lower harmonics, while high harmonics are more likely to be affected by the amplifiers' current noise. Since the harmonic amplitude drops with frequency, the current noise of the amplifier is important for the achievable resolution, once the noise-floor becomes the limit. Spurious signals from the excitation, however, can easily mask higher harmonics as well. Unless these spurious signals are very stable over time, they also limit the sensitivity and resolution of the scanner.

Implementing an amplifier module requires several trade-offs. One important compromise has to be made between best noise performance and optimum linearity. Due to the use of negative feedback, all operational amplifiers perform best in terms

of distortion at their minimum stable closed loop gain, where the feedback factor is highest. The decreasing bandwidth of voltage-feedback amplifiers with increasing closed-loop gain is another factor that reduces linearity at higher gains.
Noise performance on the other hand is frequently worst under low-gain conditions, as the payload signal gets subjected to the noise of the output stage without much prior amplification. Obviously, a moderate gain value has to be chosen to achieve good noise performance without sacrificing too much linearity. The exact value differs between amplifier models.

The positive effect of negative feedback on linearity is the reason why low-distortion amplifiers are very often wide-band types. The operational amplifiers used for the modules have $-3\,\mathrm{dB}$ small-signal bandwidths in the $500\,\mathrm{MHz}$ range. Proper circuit and layout techniques need to be in place to avoid oscillations of such wide-band devices. The schematic diagram of the receive amplifier is depicted in figure 2.30.

2.2.7.4 Receive system optimization

The winding counts of the receive coils, as well as the SNR of the receive system were optimized. To this end, the magnetic simulation of the drive coils was extended to include the receive coils. This was used to arrive at a starting point for balancing sensing and compensation coils. It also served to predict the receive coil impedance and study its effect in conjunction with the receive filters. The results from the magnetic simulation where fed into a SPICE network and analyzed in an AC simulation of the receive chain. The receive coil was represented by its equivalent circuit [67, Fig. 6-7]. Since the characteristic impedance of the receive filters is limited by manufacturing constraints, there exists an upper limit for the receive coil winding counts after which the increase in sense signal is fully canceled by the voltage divider action formed with the receive filters. The receive coil winding count should be chosen just below that point. For the y axis, the limited homogeneous drive field volume presents a problem, as it leads to large winding counts and inductance values for the compensation coils. In conjunction with the finite receive filter impedance, this reduces the sensitivity compared to the x axis.
To achieve high overall SNR, it is necessary to have receive amplifiers with low input referred noise values. For the first harmonics, the receive amplifiers voltage noise tends to limit the SNR, while the inductive source impedance makes the current noise important for higher harmonics.

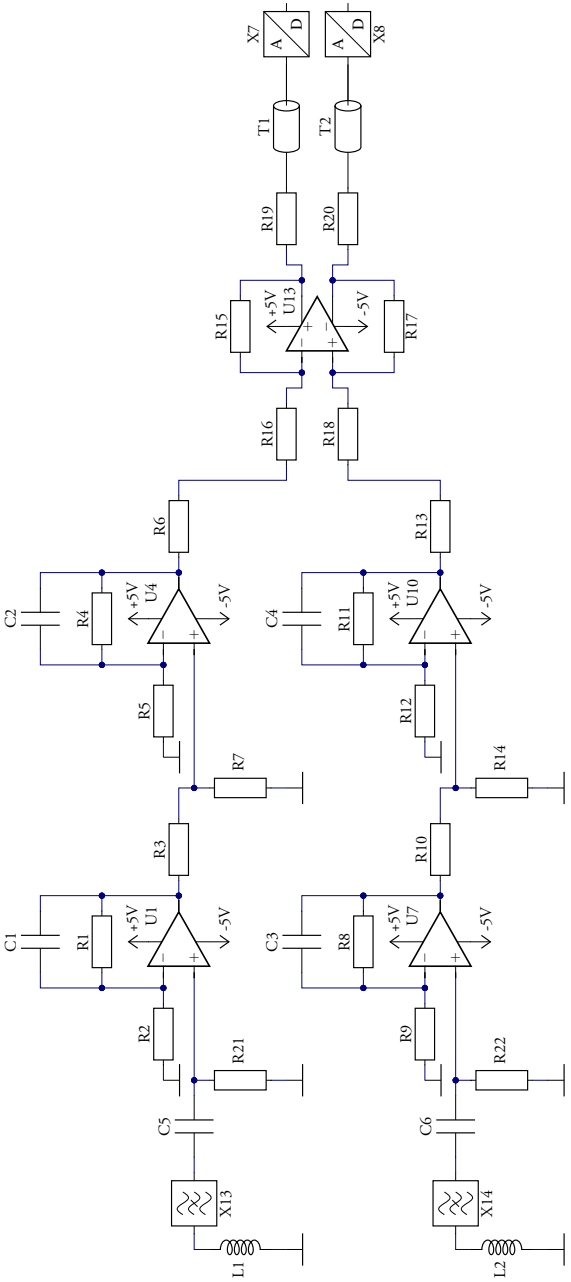

Figure 2.30: Receive amplifier circuit for the fully differential receive coil of the x-axis. Receive coil halfs L1 and L2 are each constructed as differential (gradiometric) coils. *Analog Devices* ADA4817 are used for U1, U4, U7, U10 and an ADA4938 for U13.

2.2.8 Data Acquisition and System Control

Data acquisition and signal generation is handled by commercially available DAC and ADC cards. This section briefly summarizes their key performance parameters for reference. It also describes how system control is handled.

2.2.8.1 Data acquisition

Data acquisition is performed using a *National Instruments* PCI-6133 [153] ADC card. It supports 2.5 MSPS simultaneous conversion rates of up to eight analog input channels with 14 bit resolution. The THD is specified as 100 dB at 10 kHz with a SFDR of 95 dB. The master clock is shared with the *NI* PCI-6733 DAC card to ensure synchronous sampling clocks of the output and input converters.

2.2.8.2 Amplitude and Phase control for drive field

As mentioned in section 2.2.1 on page 77 and similar to the MPS setup, the drive coil current of each axis is measured to ensure stable amplitude and phase in the presence of several filters in the transmit chain. *Sensitec* CMS3025 magnetoresistive current sensors and custom built *Rogowski* coils are used to measure the drive current. The former are used for their absolute accuracy and flat frequency response, while the latter excel at low distortion values, allowing in-system measurement of drive current THD (cf. section 2.3.1.3).

To keep the drive current at the specified amplitude and phase, a simple integral controller is used that ensures the system has no stationary control error. Amplitude and phase are measured using a digital lock-in algorithm. Although computationally more expensive than a FFT, it allows accurate phase measurement even if the frequency to be measured is not a multiple of the inverse of the measurement duration as required with the FFT. Since all variations have very large time constants (e.g. because they are based on thermal drift), this simple controller structure is sufficient to ensure accurate phase relationships between both active axes. The simultaneous sampling of the ADC card as well as the synchronization with the DAC is essential for this to work.

2.2.8.3 Control software

The low-level system control software is implemented in *NI LabVIEW*, since it provides good support for the utilized converter cards. It also provides a graphical front panel that allows the user to specify measurement parameters and supervise data acquisition. Additionally, the calibration procedure has been automated so that repeated measurement sequences and repositioning of the calibration robot are performed automatically.
A more abstracted high-level interface has been written in C# to provide an easy accessible GUI for the user [17]. This also allows tighter integration of the reconstruction framework with the data acquisition and is the first step towards online reconstruction. At the same time, the LabVIEW and C# parts communicate in real time, making the separation transparent to the user.

2.2.8.4 Active suppression of spurious signals

Beside the use of passive filters to increase the harmonic drive field purity, active compensation schemes to suppress power amplifier non-linearities can be used. They assume that amplifier distortion is constant over time and can be compensated with a suitable complementary signal.

Active compensation

Based on the results of other groups [118, 119], an active compensation setup to reduce spurious signals in the drive current has been evaluated. The idea is to cancel the harmonic content introduced by the power amplifier (PAmp) into the transmit chain by means of a second, more wideband, amplifier. This second amplifier needs significantly lower output power, since the harmonic content of suitable power amplifiers is already about 60 dB below the fundamental amplitude. The distortion performance of the wideband compensating amplifier (CAmp) can be in the same order of magnitude. Since its signal level is already 60 dB below the fundamental, even a THD of -40 dBc will only introduce spurs at -100 dB relative to the fundamental, which can often be neglected. However, since the bandwidth of the amplifier has to be larger than that of the power amplifier to achieve good compensation, it is useful to keep the transmit bandstop filters in place to reduce high frequency disturbances introduced by the CAmp.

Two concerns need to be addressed in order for this compensation scheme to work:

1. The output of the CAmp needs to be coupled into the transmit chain without interfering with the impedance matching of the transmit filters and without loading the PAmp.

2. The CAmp needs to be decoupled from the PAmp at the fundamental to prevent destruction of its output stage by the external voltage coming from the PAmp which significantly exceeds the power rating of the CAmp.

A possible solution for these issues is the inductive coupling into the transmit chain using a transformer. Figure 2.31 shows the principal schematic of such a scheme with L1, L2 constituting the coupling transformer and bandstop filter BSF1 providing adequate decoupling of the compensating and power amplifier at the fundamental. BSF2 is often necessary to reduce the required dynamic range before measuring the harmonic spurs in the drive signal. Although drawn separately in figure 2.31 to make the general setup more clear, L2 needs to be integrated into the BPF1 bandpass filter network to maintain impedance matching. A possible solution is to make L2 part of the first series element of BPF1 (usually a series resonant circuit). Despite the beneficial results reported by other groups [118] and reproduced at our own setup, the active compensation technique comes with considerable additional hardware effort. Additionally, it is most useful for low-order harmonics and low-frequency spurs, where the transmit filters provide limited attenuation. At higher frequencies the compensation

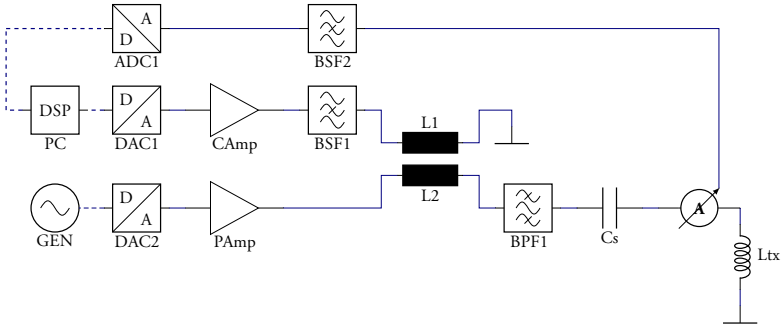

Figure 2.31: Setup for active compensation with a second (wideband) power amplifier and required (de-)coupling network.

becomes increasingly difficult, both because the stability of such spurs is usually not as good as for lower frequencies, and because accurate acquisition requires fast ADCs with good linearity.

Due to these limitations, the concept of active compensation has not been implemented in the final scanner design. A somewhat similar technique that uses predistortion to compensate low order harmonics, however, has been introduced into the scanner design.

Active predistortion

Predistortion is a well known technique in wireless communication systems [154] to reduce the significant nonlinearities inherent for most devices in the HF range. Owing to the CW character of the MPI drive signal, a simplified version of these schemes is sufficient to provide adequate suppression of harmonic content in the MPI drive signal. Contrary to the active compensation, no additional hardware is necessary if a highly linear current sensor (e.g. a *Rogowski* coil) with sufficient dynamic range is present in the system. Otherwise, only additional measurement capabilities are required and no changes in the transmit circuitry are necessary. This is a significant advantage over the active compensation principle, since the construction effort to modify the transmit chain can be avoided. Active predistortion is, however, limited to harmonic content well below the -3 dB bandwidth of the power amplifier, because it uses the amplifier to compensate its own nonlinearity. Once the gain of the amplifier has dropped below a certain level, this compensation effort will not be successful and might even lead to additional distortion through the increased output power.

The predistortion concept used for the MPI system at hand consists of the three step process, which is illustrated in figure 2.32. The drive (current) signal is measured at the drive coil, similarly to the setup of figure 2.31.

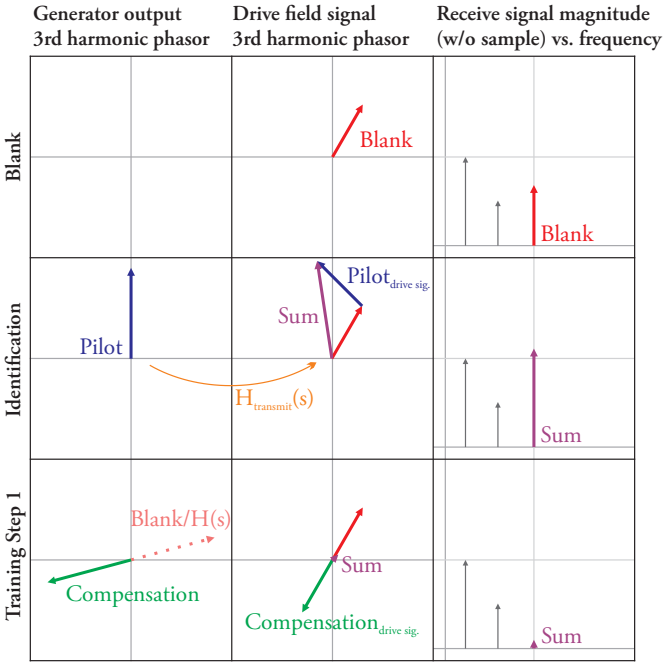

Figure 2.32: Predistortion principle and algorithm, demonstrated for the 3rd harmonic: The distortions in the Blank signal are reduced by identifying the transmit chain transfer function and generating a suitable compensation signal. Owing to the nonlinear nature of the distortion process, the identification and training steps are repeated to re-estimate the transfer function at the operating point of interest, until adequate suppression is achieved.

1. **Blank measurement:** Acquire the complex spectrum of the drive field (current) signal during a Blank measurement. To increase accuracy, averaging is often required.

2. **Transmit chain identification:** Generate a pilot signal at the frequency components in the drive signal that should be compensated. Measure the resulting drive signal. The phase of the pilot signal is arbitrary but should be well defined. The amplitude should provide good SNR when measured in the drive signal, but should not cause significant additional load on the power amplifier. It should be of the same order of magnitude as the amplifier distortions when examined in the drive signal. From the known signal generator output and the measured effect on the drive signal (with the blank signal substracted), the transfer function $H_{\text{transmit}}(s)$ can be obtained: $H_{\text{transmit}}(s) = \frac{Sum - Blank}{Pilot}$

3. **Training phase:** Using the identified $H_{\text{transmit}}(s)$ the required compensation signal $Compensation = \frac{-Blank}{H_{\text{transmit}}(s)}$ can be calculated. Ideally, this should fully compensate the targeted harmonic. Since the distortion is a non-linear process, this is not the case and a residual signal remains in the drive field. By repeating the identification process using the residual signal, a better estimation of $H_{\text{transmit}}(s)$ (or, more precisely, an estimation at the operating point of the compensation) can be obtained and the quality of the compensation can be iteratively improved. Ten iterations are usually sufficient to achieve a compensation that is limited by the system stability.

Once sufficient compensation is achieved using this scheme, the predistortion settings can be held constant to avoid compensation of the receive signal during sample measurements. Experimental results demonstrating the active predistortion are given in section 2.3.1.4 on page 135.

2.2.9 Power amplifiers

The power amplifiers used for the MPIv3 system are commercially available *AE Techron* 7548 DC enabled industrial amplifiers [155]. Compared to the type used for the MPS setup, these units have a fixed gain setting of $\frac{20\,\text{V}}{\text{V}}$. The amplifiers have a large-signal bandwidth of 30 kHz at rated power. The THD is specified as $< 0.1\%$ (-60 dBc) for the frequency range from DC to 30 kHz [156]. Measurements show that the specified THD can be obtained under the load conditions of the MPIv3 system (cf. section 2.3.1.3 on page 134). Additional THD and HD3 measurements are summarized in table 2.13. Unfortunately, the produced signal also contains wideband harmonic components that drop off only slightly within the receive bandwidth, requiring good attenuation of the transmit filter up to 1 MHz. Section 2.3.1.4 shows that the lower harmonics can be further reduced through signal predistortion.

U_{Gen}	I_{L}	THD+N	HD3
0.5 V_{pk}	7.4 A_{pk}	-61.0 dBc	-63.6 dBc
1.0 V_{pk}	14.8 A_{pk}	-64.3 dBc	-66.2 dBc
1.5 V_{pk}	22.1 A_{pk}	-66.2 dBc	-69.0 dBc
2.0 V_{pk}	29.5 A_{pk}	-56.3 dBc	-64.9 dBc
2.5 V_{pk}	37.0 A_{pk}	-57.1 dBc	-67.2 dBc

Table 2.13: THD and HD3 values of the AE 7548 power amplifiers at 25 kHz driving I_{L} into a 1 Ω resistive load. Measurements were performed using a resistive divider to adjust the voltage drop over the load to the input range of the ADC card, keeping the fundamental level approximately constant at the ADC input.

2.2.10 Shielding and "Ground" structure

2.2.10.1 Shielded Room

Floor plan

The general layout of the setup in the lab is presented in figure 2.33. Especially the position of high-power components, such as the power amplifiers, is important. Also, equipment with SMPS such as motor controllers should be placed away from sensitive parts of the system, such as the cables that carry the receive signal.

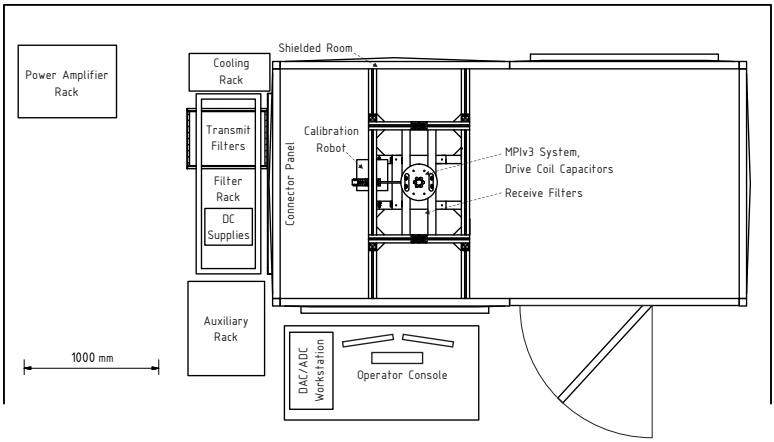

Figure 2.33: Floor plan of the MPI system components inside and outside of the shielded room, as well as of auxiliary equipment.

Connector panel

The connector panel serves as central interface for all signals that enter or leave the shielded room. It is manufactured from a solid copper plate. This allows it to serve as signal reference, because voltage drops between individual connectors are minimized. To ensure good connection to the shielded room, the panel is mounted on a flat steel frame. 44 screws ensure good contact with the frame and the connector panel. The frame itself is welded to the wall of the shielded room to ensure good and permanent electrical contact. Figure 2.34 shows the outline of the connector panel. Connectors are arranged to achieve good separation (within practical limits) between high current drive signals and the sensitive receive cables. Cooling water is fed through with plugs that are electrically connected to the panel. DC signals are passed through feed-through capacitors (*Tesch EMC / Pikatron* 02100204 1.2 µF) and feed-through filters (*Schaffner* FN 7661) to ensure no RF signals couple into the shielded room.

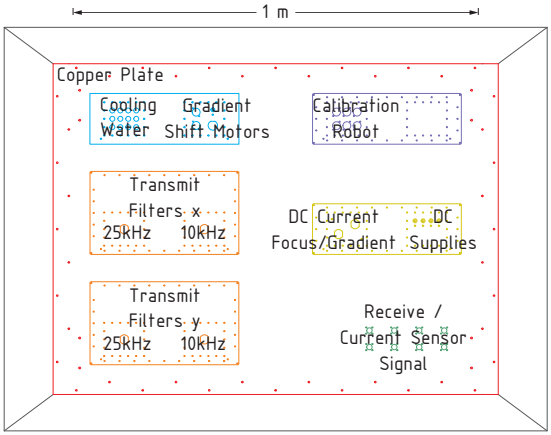

Figure 2.34: Outline of the connector panel.

In the same manner, feed-through capacitors are used at the shunt elements of the transmit filters (cf. section 2.2.5.2 on page 107).

Interconnects for stepper motors (e.g. for the calibration robot, see section 2.2.11.1) are more difficult to handle. Because filtering would interfere with the motor controllers and would lead to step losses at faster turn rates, their cabling is handled differently. Signals for them are fully shielded inside the shielded room and have shielded connectors at the connector panel. This way, their signals are effectively kept “outside” of the shielded room. While very effective, unavoidable inductances and resistances in the cabling still allow a small fraction of the stepper signal to couple to the receive cabling. Separation of these cables inside the shielded room is therefore essential.

A similar technique is employed for the receive cables, which cannot be filtered due to the wide-band nature of the receive signal (50 kHz to 1.25 MHz).

Receive Filter Enclosure

As discussed in section 2.2.7.2, the receive filter sections are shielded against each other and external interference by means of a copper enclosure. Figure 2.35 shows an image with the filter coils and receive electronics present. To make manufacturing more economical, the same base structure is used for the electronics housing and a pair of filter segments. The sheet metal enclosures have brazed seams to ensure good conductivity between all parts of the enclosure. Connection between sections are made through disk fittings to ensure radial contact at the interconnection holes. BNC connectors are used for signal input and output. DC supplies are connected through a shielded six pin DIN connector.

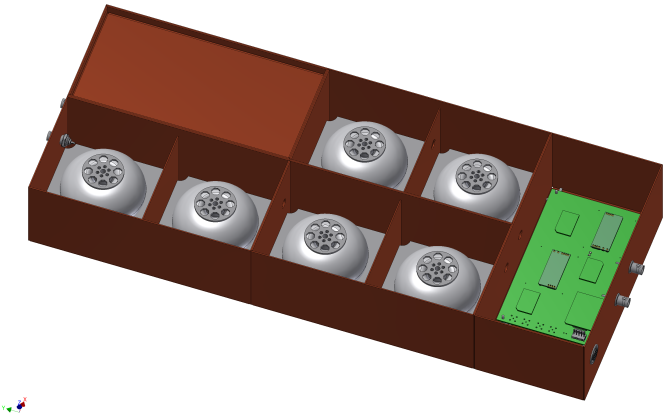

Figure 2.35: Receive filter enclosure with the lids of three filter compartments and the amplifier section removed (CAD image).

2.2.10.2 "Ground" structure

Since MPI uses high power signals for the drive fields (and focus fields if applicable) and requires a wide-band receive signal to be detected, decoupling the two is very important. This is especially true for harmonic content and spurious signals in the drive current before filtering is applied. If these signals couple into the receive chain they can mask the harmonics in the receive signal.

The "ground" (or better: signal return) system can be a major source of crosstalk from the transmit into the receive chain. Low impedance connections are necessary to minimize voltage drops in the drive circuitry. For the MPIv3 system the connector panel serves as a signal reference for both the transmit and receive chain. Due to its material and geometric shape, it ensures low impedance paths between all components.

Separation of high power and receive signal current paths

Even though the connector panel itself can be considered a low impedance connection far beyond the receive bandwidth, it is useful to physically separate drive and receive signals as much as possible. This reduces capacitive and inductive coupling, that can be observed between cables or filter inductors. Shielding is used in addition for both sides. Also, signal returns are routed as close as possible to the corresponding signals to reduce inductive coupling.

Star reference points

For the receive signal, where currents are almost negligible, the connector panel serves mainly as signal reference. The receive filters as well as the data acquisition hardware derive their reference potential from there.
In case of the transmit filters it is important that all filtering action is performed against that potential as well. Doing so prevents common mode signals on the ground and signal lines of the transmit chain to enter the shielded room. More precisely, the common mode signal is canceled because the shielded room and acquisition system use it as reference. Naturally, the maximum amplitude of the common mode signal has to remain small to prevent damage to those parts of the receive circuitry that are connected to another reference level, e.g. through protective earth circuity. Careful cabling and bypassing to the connector panel is helpful to that end.
For circuitry that has to be positioned at some distance from the connector panel (like receive filters and receive amplifiers), individual reference star nodes are used. Where possible, only one connection to the connector panel exits. In all other cases, the individual cables are kept close to each other.

2.2.11 Auxiliary equipment

2.2.11.1 Calibration robot

A calibration robot is used to shift a point like sample through the FOV to acquire the system matrix of the scanner. Figure 2.36 shows a CAD image of the robot which was also used for the previous generation MPI scanner [17]. It is driven by stepper motors that operate a three axis linear stage. Since the SMPS on the motor controller board generate spurs in the kHz range that interfere with the receive signal acquisition during the calibration procedure, the stepper motors have been upgraded with shielding enclosures. Additionally, shielded cabling is now used to connect the motors to the connector panel of the shielded room. Cabling to the limit switches has also been replaced with shielded wires.
A commercial motor controller unit [157] that receives commands from the acquisition computer is used to drive the stepper motors.

2.2.11.2 Power supplies

As stated before, SMPS supplies are unsuitable for MPI applications, since their switching frequencies are in the same frequency range as the receive signal. High quality supplies with linear output stages are an exception, provided the supply lines are filtered. To ensure good attenuation and prevent other signals from coupling onto the DC supply cables after filtering, feed-through components (cf. section 2.2.10.1) have been used to ensure low impedance connections to the connector frame, which serves as signal reference.

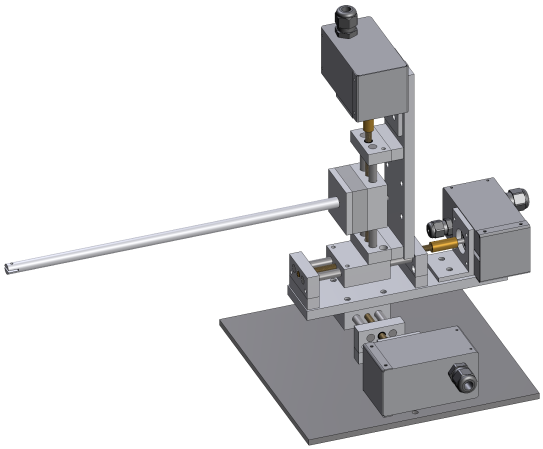

Figure 2.36: CAD image of the calibration robot with shielded stepper motors.

2.3 Characterization

2.3.1 System Component Characterization

In this section, the individual components of the MPI system are verified against their design parameters or requirements.

2.3.1.1 Transmit Coils

Characterization of the transmit coils included verification of the produced field per unit current, coil impedances and homogeneity. To allow better comparison, most of these parameters have already been given in addition to theoretical values in the design section (cf. table 2.6 and table 2.5). The field plots used to derive the homogeneity are presented in figure D.17 and figure D.18 on page 184 in the appendix, along with the results of impedance measurements (cf. section B.2 on page 178).

Many properties of the transmit coils are also implicitly included in the characterization of the complete system (e.g. distortion performance in section 2.3.1.3).

2.3.1.2 Transmit Filters

Due to the low impedance of the drive chain, transmit filter characterization has to be performed using a power amplifier to drive the filters. Otherwise, the voltage drop at the series impedance of the source in connection with the large dynamic range would preclude accurate measurements.

Using the setup shown in figure 2.37 the voltage and current transfer functions of the transmit filters have been measured. A *Rohde & Schwarz* ZVL 3 vector network analyzer (VNA) [158] was used to acquire the necessary transfer functions between the nodes shown in the diagram.

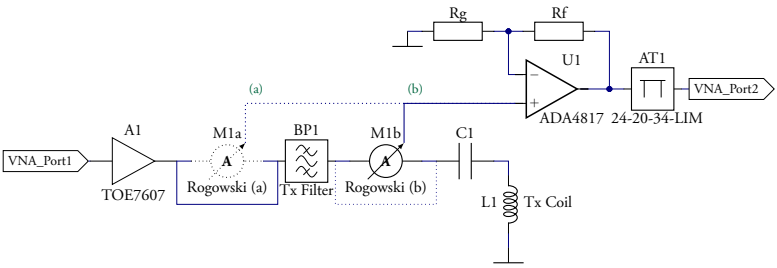

Figure 2.37: Simplified schematic of the measurement setup used to determine the transmit filter attenuation. The same *Rogowski* coil (M1a, M1b) was used to determine the input (a) and output current (b). U1 acts as cable driver, AT1 protects the VNA input. For the voltage-to-current transfer function, the input of AT1 was connected to the output of A1 instead of U1 during configuration (a).

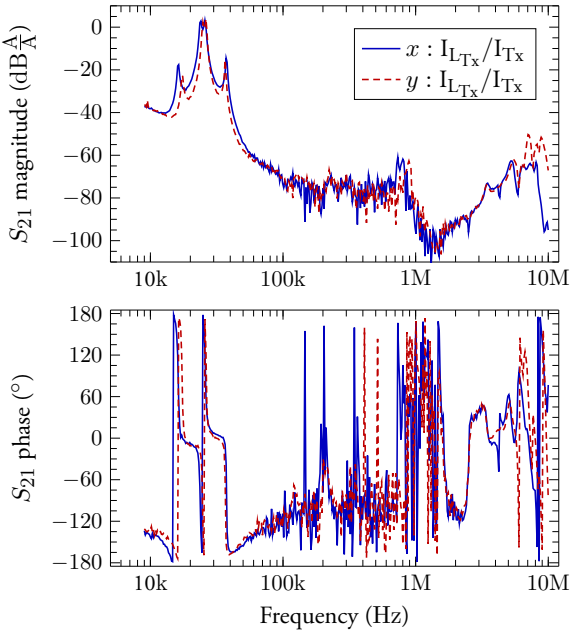

Figure 2.38: Current transfer functions of the x and y axis transmit filters. The current through the transmit coil was measured and referred to the amplifier output current.

Figure 2.38 shows the results for the x and y axis in terms of the current transfer function. As can be seen from figure 2.39, the plateau above 200 kHz and the reduced attenuation at 700 kHz are due to the inability of the power amplifier to deliver constant current to the filter input. Since this means that the filter shows high input impedance in that frequency range, this is a desirable property since it reduces loading of the amplifier's output stage, preventing large power draw at the amplifier spurs and consequently preventing additional non-linearities. The filters attenuate the second harmonic by 54 dB and the third by 65 dB. Attenuation is better than 70 dB from 100 kHz to 700 kHz and better than 60 dB up to 4 MHz. It should be noted that these values are most likely limited by the dynamic range and noise floor of the measurement equipment as well as the current output of the power amplifier used to acquire the responses.

From the voltage-to-current transfer function a wideband attenuation of better than 77 dB is observed for both axes (cf. figure 2.39). Second harmonic attenuation is 61 dB and the third harmonic shows 73 dB of attenuation.

Passband attenuation in the current transfer function is pleasingly low with only 0.67 dB for the x axis and 0.46 dB for the y axis in figure 2.38[18].

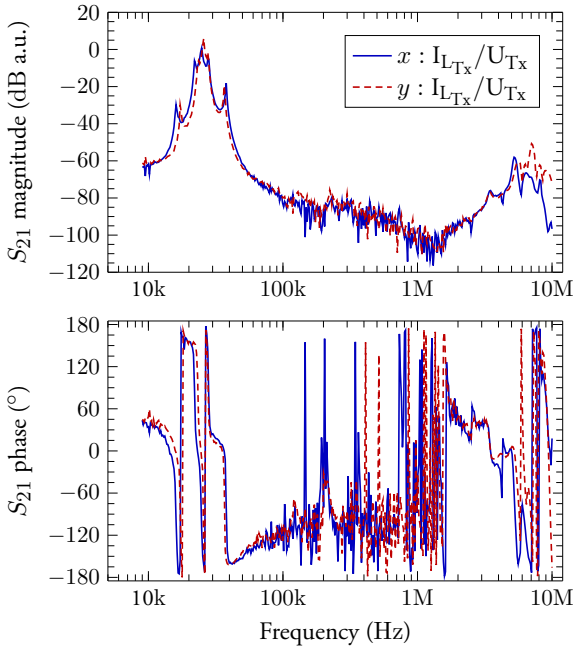

Figure 2.39: Voltage-to-current transfer functions of the x and y axis transmit filters. The current through the transmit coil was measured and referred to the voltage at the amplifier output.

Comparison with a circuit simulation shows deviations regarding the stop-band attenuation and the exact response shape (cf. appendix section C.1). The first can be attributed to the dynamic limitations of the measurement equipment as well as parasitic coupling between the filter elements (and therefore the filter output with the input). The variations between the measured transfer function and the expected results (even if parasitics are included in the simulation) are due to the coupling between the filter elements not being present in the simulation and the parasitics of interconnects that change once a filter element is examined during individual impedance measurements. However, the basic shape of the response as well as attenuation values close to the passband are reasonably well predicted and stop-band attenuation is sufficient.

[18] Although not clearly visible at the graphs chosen frequency scale, the transfer function's magnitude is flat at the passband center.

Consequently, the transmit filters pass all their design requirements and deliver good wideband attenuation. The slightly lower attenuation at the first harmonics can be improved through active compensation techniques, as outlined in section 2.2.8.4 and shown in section 2.3.1.4.

2.3.1.3 Transmit THD

Characterization of the transmit THD is best done for the current signal, since the current is ultimately responsible for the drive field generation and therefore the drive field THD.

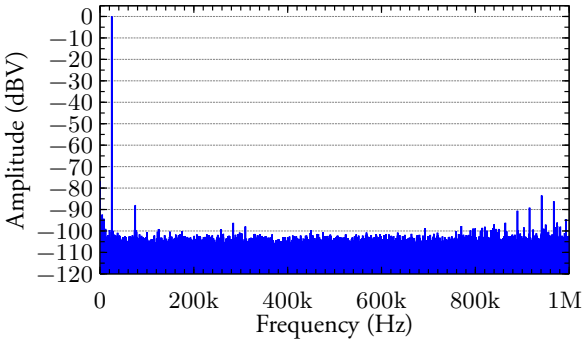

Figure 2.40: Amplitude spectrum of x axis drive coil current at 17 A_{pk} (nominal FOV size), normalized to the level of the fundamental.

Figure 2.40 shows the drive coil current amplitude spectrum of the x axis for the nominal current (nominal FOV), acquired with a *Rogowski* coil and normalized to the fundamental to allow easy determination of spurious signal levels. A HFT95 flattop window [159] and 97.7234 Hz ENBW were used. The 3rd harmonic dominates the THD in the frequency range up to 850 kHz[19] and shows a value of −87 dBc. This can be compared to the normalized current amplitude spectrum at the output of the power amplifier depicted in figure 2.41, which shows −66 dBc for the third harmonic. While this is only a moderate improvement, looking at the harmonic amplitudes for higher order harmonics shows improvements larger than 40 dBc. Consequently, the transmit filters clearly show a considerable effect[20].

Figure 2.42 depicts the normalized drive coil current amplitude spectrum for the y axis. The 5th harmonic shows a level of −90.5 dBc, dominating the rest of the

[19] Spurious signals above 850 kHz are the result of the SMPS of the robot motor control board.

[20] The seemingly different values of attenuation determined from transfer function and THD measurements can be explained through the excitation current strength: While the transfer functions are small-signal measurements, the THD results are measured at nominal drive field amplitudes. They therefore include nonlinearities generated by the transmit chain. Also, the observable attenuation when examining the THD is limited by the dynamic range, linearity and noise floor of the measurement equipment.

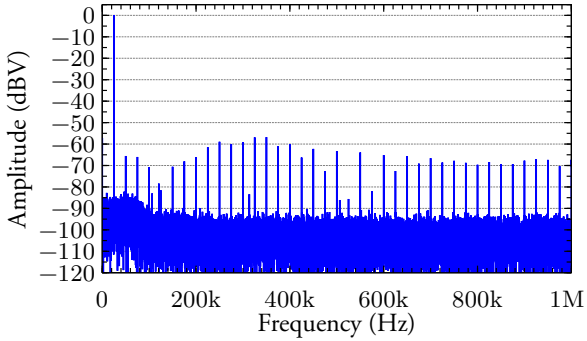

Figure 2.41: Amplitude spectrum of the x axis drive current at the power amplifier output, normalized to the fundamental's level. Drive coil current at 17 A_{pk}.

spectrum. The level of the third harmonic was measured as -104 dBc after multiple averages (not shown).

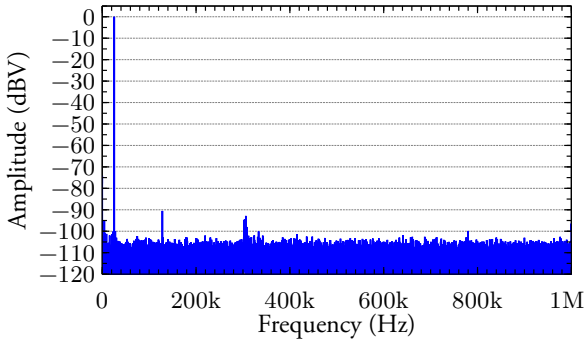

Figure 2.42: Amplitude spectrum of y axis drive coil current at 20 A_{pk} (nominal FOV size), normalized to the fundamental's level.

2.3.1.4 Transmit THD improvement through predistortion

As outlined before, predistortion can be used to compensate the low ordered harmonics caused by the power amplifier in the frequency range close to the fundamental, where the transmit filters provide low attenuation. Figure 2.43 shows the effect of predistortion on the third harmonic, reducing it by 13.5 dB from -86 dBc to -99.7 dBc. This, however, comes at the cost of increased amplifier power output, therefore increasing harmonic content in the range around 500 kHz slightly.

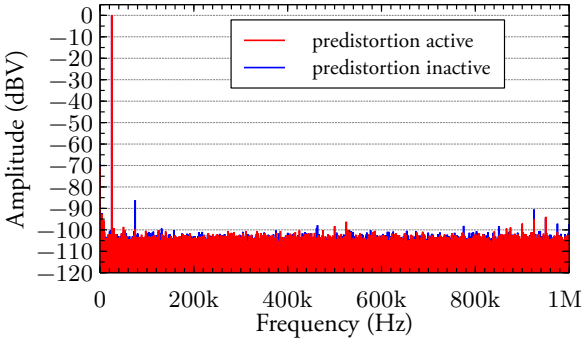

Figure 2.43: Effect of predistortion on the amplitude spectrum of x axis drive coil current at 17 A_{pk} (nominal FOV size), normalized to the level of the fundamental. The third harmonic was compensated (red graph) and compared to normal operation (blue).

2.3.1.5 Receive Filters

Transfer function

The receive filters were characterized using a *Rohde & Schwarz* ZVL 3 vector network analyzer (VNA) [158]. The reference plane for the two-port TOSM calibration was at the end of the cables that were connected to the filter inputs and outputs. For measurements in the enclosure, the receive amplifiers were bypassed. Since the filters are designed for a termination impedance of 50 Ω, they are matched to the ports of the network analyzer, allowing wide-band measurements. However, since the receive filters are designed as singly terminated ladders, the transfer function is slightly changed through the 50 Ω termination at the filter input. This has been addressed in the comparison with measured data, by performing a simulation with a filter terminated at both sides. That way, the simulated network matches the measurement setup[21]. Figure 2.44 depicts the results, which show good agreement between measured data and expected values. The filter has a flat passband attenuation up to 2.56 MHz (2.5 dB), which exceeds the measurement bandwidth of 1.25 MHz by a factor of two. At the second harmonic, the filter has −2.74 dB of attenuation, which is acceptable. The third harmonic receives only slight attenuation of −0.72 dB at 75 kHz. In the middle of the passband region, −0.19 dB (at 150 kHz) are observed.
Stop-band attenuation is at least 88 dB. It should be noted that this value is limited by the noise floor of the VNA. The exact value is not important for MPI experiments, so the determination of a lower bound for the attenuation is sufficient.

[21] Alternatively, de-embedding could have been employed to reconstruct the unterminated transfer function. The chosen approach ensures that the measured data can be shown without the need for manipulation.

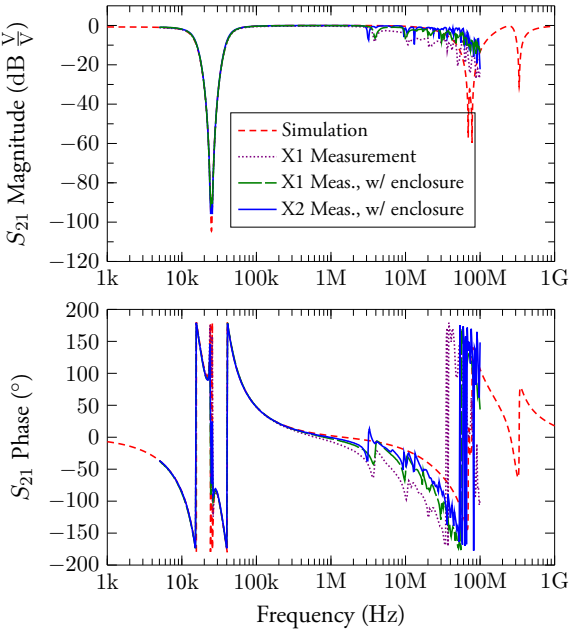

Figure 2.44: Measured transfer function of the x axis receive filters in comparison with simulated data.

Figure 2.45 shows the same measurements of the y axis receive filter, which achieves at least 89 dB stop band attenuation. The attenuation at 50 kHz is 4 dB. Additional 0.9 dB of attenuation are observed inside the enclosure due to the installation of a fuse that adds 12 Ω resistance at the filter input.

Input impedance

Figures 2.46 and 2.47 show the input impedance of the x axis receive filter with 50 Ω output termination and open output respectively. In both cases, the input impedance at 25 kHz is 2.4 kΩ. It is interesting to note that for the range between 98 kHz and 3 MHz the input impedance increases when the termination is dropped while the range between 55 kHz and 98 kHz shows lower impedance due to under damped resonances. It can therefore be beneficial to increase the termination resistor to trade some degree of resonances in the input impedance (and frequency response) for high input impedance in the detection bandwidth.

Since the impedances for the y axis are very similar and allow no additional insight, these graphs have been omitted.

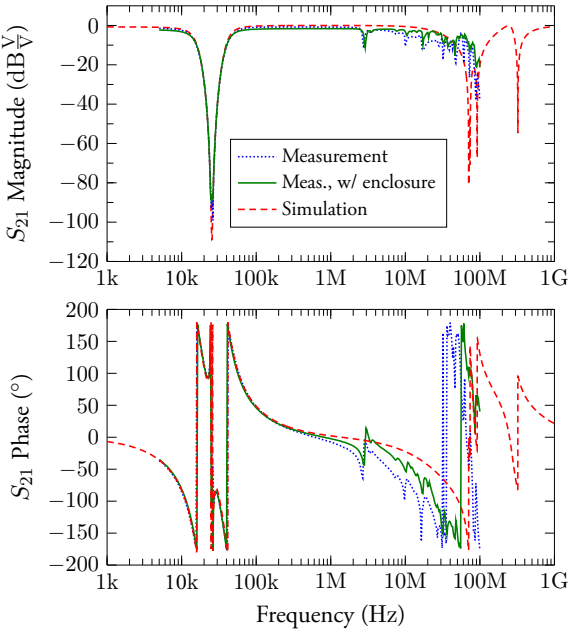

Figure 2.45: Measured transfer function of the y axis receive filter in comparison with simulated data.

Common Mode Rejection Ratio

The common mode rejection ratio (CMRR) of the x axis filter has been examined with and without 50 Ω termination at the input of the preamplifiers. The CMRR is defined as

$$CMRR = 20 \log \frac{|G_{\mathrm{D}}|}{|G_{\mathrm{CM}}|} \tag{2.31}$$

where G_{D} is the differential gain and G_{CM} denotes the common mode gain. The preamplifier voltage gain was set to 30 dB with an additional gain of 6 dB for the fully differential amplifier module, which was used as a second stage. The results are visualized in figure 2.48 on page 140.

It becomes apparent that the CMRR for frequencies around 75 kHz suffers if the termination value is increased, while frequencies above 100 kHz continue to show good CMRR up to 2 MHz. Since the frequency range above 100 kHz is especially important, as it contains low leveled harmonics, decreasing the filter dampening is a valid option.

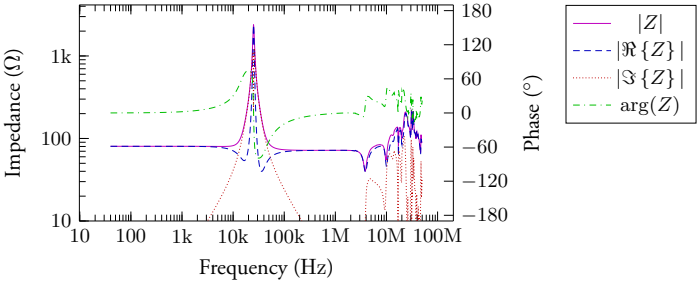

Figure 2.46: Input impedance of the x axis receive filter with the output terminated at $50\,\Omega$.

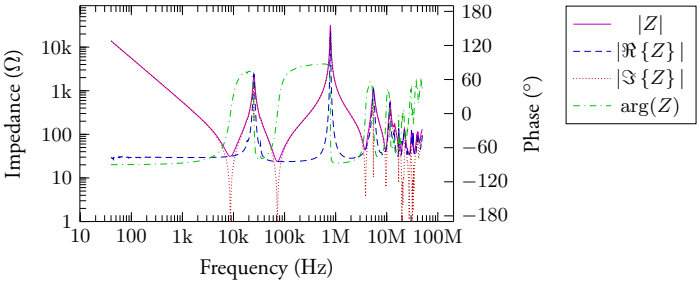

Figure 2.47: Input impedance of the x axis receive filter with the output open.

2.3.1.6 Receive Amplifier

Apart from the CMRR that was already measured before (including the receive filters, s. section 2.3.1.5), the noise performance of the receive amplifier is another important property.

Noise performance

To achieve realistic values, the noise floor of the receive amplifier was measured with the complete receive chain connected. At the input of the ADC, the noise floor is determined as $1.1\,\mu V/\sqrt{Hz}$. Figure 2.49 shows a plot of the measured output noise at the ADC. With a single ended gain of 118.9 this amounts to $9.251\,nV/\sqrt{Hz}$ input referred voltage noise ($\geq 10\,kHz$) for the receive amplifier. For a differential configuration, due to the amplifier dominated noise and therefore uncorrelated noise processes for the positive and negative channel, the input referred differential mode noise is $1/\sqrt{2}$ lower, resulting in $6.542\,nV/\sqrt{Hz}$.

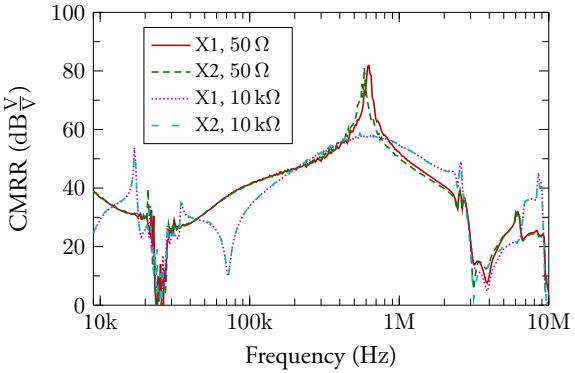

Figure 2.48: CMRR of the x axis receive chain, measured at the filter inputs. $X1$ and $X2$ denote which output was used for the differential gain, since the network analyzer only has a single ended input. The unused output was terminated with a match to keep the outputs balanced.

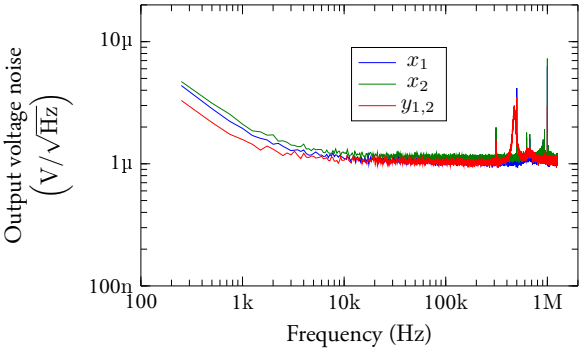

Figure 2.49: Output voltage noise of the x-axis receive channel, measured single ended, with the full receive chain in place. Amplifier (single ended) gain was 118.9 V/V. Discrete spurs above 900 kHz are neglected in the calculations since they are outside the usual receive bandwidth. The noise peak around 470 kHz and 650 kHz is the result of the resonant frequency of the x and y coils (with the cables).

These values can be related to field units through the sensitivity of the receive coil: Since this is a long baseline gradiometer, two approaches are valid:

1. For the sample measurement within the area of the FOV, the sensitivity can be approximated as constant. The noise can therefore be related to field values by the coil sensitivity to homogenous fields (within that area): A conservative

approach using the minimum sensitivity within the FOV leads to a sensitivity of 19.733 $\frac{\mathrm{V}}{\mathrm{mT}}$ for the x axis receive coils at 100 kHz. Consequently the field referred noise amounts to 468 $\mathrm{fT}/\sqrt{\mathrm{Hz}}$ for a single output of the fully differential detection. Figure 2.50 shows the results as obtained by using an experimentally determined field-to-voltage transfer function over the full detection bandwidth.

2. If the long baseline gradiometer is seen as a sensor only sensitive to gradient fields, the noise can also be related to the measured magnetic (dipole) moment for a dipole positioned at the center of the FOV: For a testcoil with 1 mm radius and 0.2 mm wire diameter, the sensitivity (of a single differential input) can be determined as 624.08 $\frac{\mathrm{V}}{\mathrm{Am}^2}$ at 100 kHz. Therefore, for fully differential measurements, the magnetic moment referred noise is 5.241 $\mathrm{pAm}^2/\sqrt{\mathrm{Hz}}$ at 100 kHz. This includes a 5.3% signal reduction because of the compensation coils.

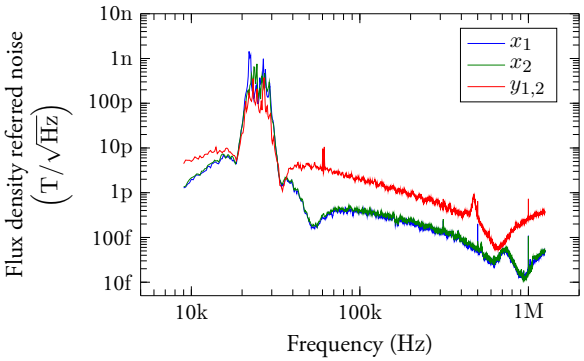

Figure 2.50: Flux density referred noise of the 25 kHz receive chains, determined by using a test-coil to measure the receive chain transfer function.

THD

The THD of the receive amplifiers was verified to be below −85 dBc at 75 kHz for 2 $\mathrm{V_{pp}}$ output voltage and 118.9 V/V single ended gain with the amplifier loaded by the acquisition hardware and its cabling. The THD is also evaluated for the complete receive chain in section 2.3.2.3 on page 144.

2.3.2 System Characterization

2.3.2.1 Drive coil decoupling

Using the procedure outlined in [160], the voltage and current transfer functions between the drive coils were determined using a vector network analyzer. Figure 2.51 shows the measurement setup. The data was acquired for all permutations of coil polarities. This is important, since both coils share a common voltage potential for their signal return connectors, both during the measurement and when operating as MPI drive coils. Because the coils are not symmetric about their connections, the polarity influences the effect of the capacitive cross coupling and the sign of the magnetic interaction.
Using an adequate polarity arrangement, the coupling coefficient can be reduced. Further reduction is possible by means of a capacitor C_{comp} placed between the hot ends of the drive coils to inject a compensation current [160]. Since both axes already possess good orthogonality, only small compensation currents are required. At 25 kHz the optimal decoupling capacitor value was determined to be 23 pF.

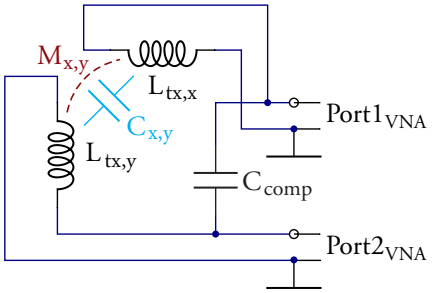

Figure 2.51: Measurement setup of the cross coupling measurement. All possible permutations of coil polarity were measured (not shown).

2.3.2.2 Thermal management

The thermal behavior was investigated during the acquisition of system matrices, which is the most stressful situation for the system as they require the consecutive acquisition of all sample positions in the FOV with a high number of averages.

The system heat-up was measured using an *Infratec* M8 infrared (IR) camera and was evaluated with the IRBIS 3 software provided by the manufacturer. A correction for ambient temperature (24 °C) and the emissivity of the PA-6 Nylon (0.85, according to *Okada* et al. [161]) were used to reduce systematic errors. Results were acquired after three hours (621 measurements) of data acquisition using a $1.5 : 10$ duty cycle with 1.5 s at nominal output power during controller activity and acquisition.

Figure 2.52a depicts the thermal image acquired after a long system matrix scan using the 25 kHz transmit path. As is apparent from the image, the highest temperature of 28.42 °C is measured at the cooling tubes of the x axis drive coil and their immediate surroundings. The y axis coils remain effectively at ambient temperature (23.1 °C) with only the tubing showing a slight temperature rise, reading a temperature of 24.96 °C.

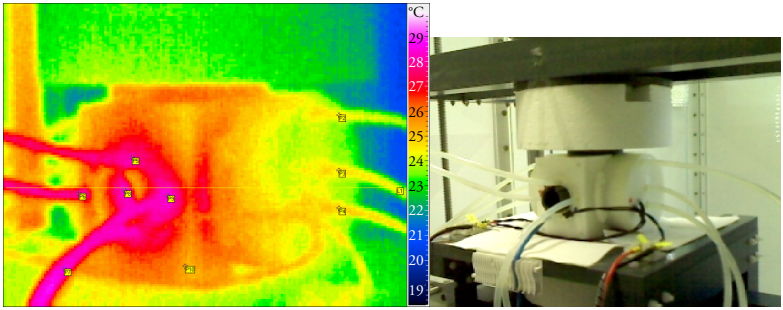

(a) Thermographic IR image (b) Visible light image

Figure 2.52: Heat-up at 25 kHz: Thermal image (a) and visible light image (b) of the MPI system 10 s after the end of a three hour system matrix acquisition session using the 25 kHz drive frequencies and both axes. Sampled measurement points (values in the text) are shown in yellow.

As expected from the data of table 2.5, the thermal losses at 10 kHz are significantly lower, leading to only a marginal rise above ambient temperature (24.67 °C) after a similar calibration session when using the 10 kHz transmit chain, as shown in figure 2.53. The coil system shows an almost homogeneous temperature distribution with a maximum temperature of 26.21 °C.

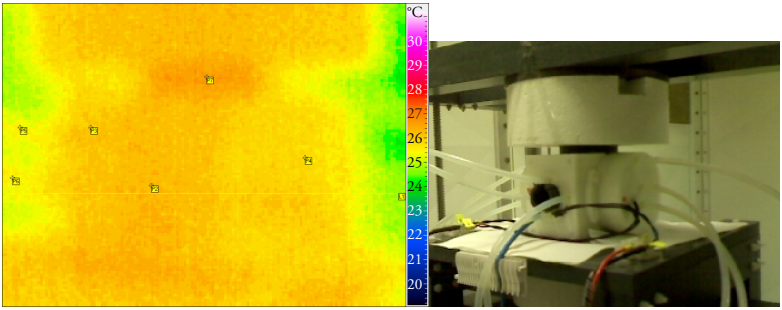

(a) Thermographic IR image (b) Visible light image

Figure 2.53: Heat-up at 10 kHz: Thermal image (a) and visible light image (b) of the MPI system 10 s after the end of a three hour system matrix acquisition session using the 10 kHz drive frequencies and both axes. Sampled measurement points (values in the text) are shown in yellow.

Correct measurement of the temperature was verified with measurements of the coil system at ambient temperature (not shown) which confirmed the selected value for the emissivity of the PA-6.

Summing up these results, the cooling system proves to be adequate for the intended measurement intervals. Due to the large overall power losses and the sturdy system design, the existence of local hotspots, although unlikely, is still possible even though IR images show a rather homogeneous temperature rise. Small, thermally isolated areas, can build up significant temperature differences compared to their surroundings, while the trapped heat is still a fraction of the total power losses (and therefore hidden in systematic errors when trying calorimetric measurements). But since the temperature of the cooling tubes is at the same or higher temperatures as the coil system, good thermal coupling between the coolant and the coils can be deduced. The thermal conductivity of the wire also reduces the risk of hotspots being present. However, only (potentially destructive) extended tests with reduced duty cycles would provide definite results about duty cycle and thermal limits.

2.3.2.3 Receive System

Receive Spectra

Verification of the receive system was performed using a calibration sample that was also used for system matrix acquisition. Figure 2.54 shows the receive signal for the x axis at two different sample positions in comparison to a residual blank spectrum and figure 2.55 depicts the corresponding spectra for the y axis.

As can be seen from the graphs, the calibration sample shows a rich harmonic spectrum and corresponding intermodulation products. It is also apparent that the lower drive field in the y direction leads to a spectrum with a steeper drop per har-

monic order. As will be shown in section 2.3.3, the spectra of both axes allowed the extraction of corresponding system matrices which were successfully used for image reconstruction.

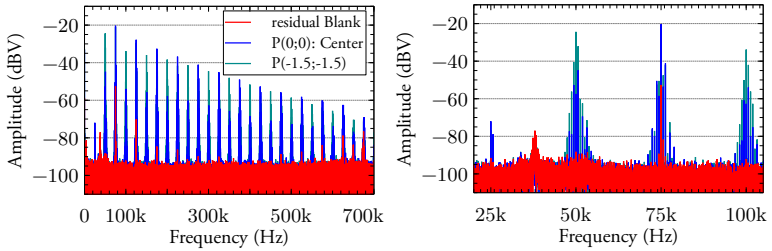

(a) Receive spectrum x

(b) x spectrum detail

Figure 2.54: Receive spectrum of the x axis for calibration sample #sp, which consisted of 22 µL FeraSpin XL at a concentration of 45 mmol/L. The graphic shows (a) a wideband view and (b) a detail of the receive spectrum at the center point and a point 1.5 mm on each axis from it. The residual blank spectrum is also shown.

Some non-ideal properties of these spectra are worth discussing: The rise of the noise floor at 37.8 kHz originates from the transfer function of the transmit filters (cf. section 2.3.1.2 on page 131). Some remaining spurious signals that rise slightly above the noise floor at 300 kHz originate from the SMPS of the robot's motor controller and the DC power supplies. Since their amplitude is already significantly reduced by the shielding / filtering and since they are not coinciding with harmonics of the 10 kHz and 25 kHz configurations, the remaining spurs from them are tolerable.

The residual blank signal at the third harmonic of the x axis is another concern. While it limits the sensitivity for small sample concentrations at the 75 kHz point, it shows few to no residual intermodulation products, which renders it acceptable. Raw spectra are given in the appendix in section E.

The increase in the noise floor of the y channel at 470 kHz is due to the self-resonant frequency that is formed by the y axis receive coil with the shielded receive cabling. Raising it would either require less capacitive load or a reduced coil inductance. The first is not easy to achieve as it would mean shorter cabling that would bring the sensitive coils of the receive filters closer to the transmit cabling. The latter would also reduce the overall sensitivity of the coil which is also undesirable. Optimized receive coil shapes in the y axis could be a solution that might improve the sensitivity-to-inductance ratio of the coil. This option has not been fully explored and remains for future revisions.

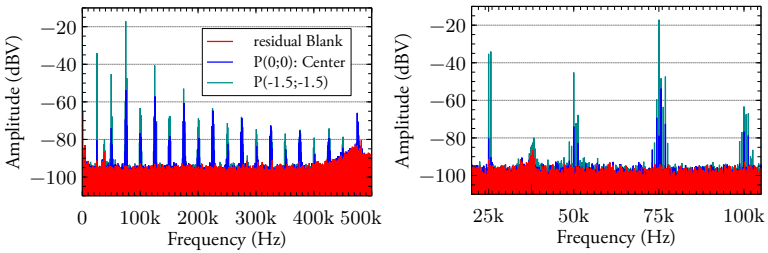

(a) Receive spectrum y (b) y spectrum detail

Figure 2.55: Receive spectrum of the y axis for calibration sample #sp, which consisted of 22 µL FeraSpin XL at a concentration of 45 mmol/L. The graphic shows (a) a wideband view and (b) a detail of the receive spectrum at the center point and a point 1.5 mm on each axis from it. The residual blank spectrum is also shown.

THD

Similar to the evaluation of the receive amplifier THD in section 2.3.1.6, distortion measurements were carried out for the complete receive chains. A 75 kHz test signal was used to represent the largest frequency component in the receive spectrum (cf. figure 2.54 and figure 2.55).

The results are shown in fig. 2.56a and fig. 2.56b for the x and y axis respectively. To allow low output voltages and low load on the *Stanford Instruments* DS360 function generator (and thus good generator THD), a relatively large test coil (30 mm diameter) had to be used. For the y axis, this resulted in partial reduction of the test coil signal through the compensation coils. Since this compensation is frequency dependent, the THD is measured higher than actually present. Connecting the generator directly to the receive filters (and bypassing only passive, linear components), the same level of distortion as for the x axis is determined. This correction is not necessary for the x axis since its compensation coils are placed farther from the center as it has a larger homogeneous field volume.

The THD is dominated by the third harmonic of the 75 kHz test signal at 225 kHz, showing −87.156 dBc for the x axis and −81.654 dBc (−86.28 dBc at the filter input) for the y axis (HD3). The second harmonic is much lower at −94.537 dBc for the x and −93.832 dBc for the y axis (HD2). The data was evaluated using a HFT95 window [159] resulting in 3.9725 Hz ENBW.

2.3.2.4 Random measurement error

The random errors in the mMPI scanner were evaluated in a similar manner as for the MPS system in section 2.1.9.2 by placing a nanoparticle sample with typical concentration in the system and evaluating the stability of the measured spectrum. The presence of a multitude of intermodulation products, however, complicates a concise

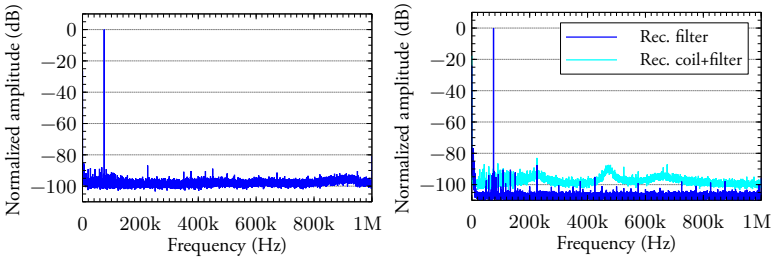

(a) Receive THD x (b) Receive THD y

Figure 2.56: Receive THD spectrum of the (a) x and (b) y axis when driven to 1 V_{pp} by a 75 kHz sine wave using a test coil inside the bore. Since part of the apparent y axis THD stems from the compensation frequency characteristic of the y axis gradiometer and the large size of the test coil, the y axis receive chain has been evaluated also directly at the detection filter input. All spectra are normalized to the amplitude of the fundamental. A peak detector was used to decimate the data by a factor of 100.

and meaningful analysis for the MPI system (cf. figures 2.54 and 2.55). To evaluate the signal properties, the relative random magnitude errors and the random phase errors of the spectral components were evaluated within a typical detection bandwidth under 2D drive field excitation at nominal drive field strengths using a 22 µl Feraspin XL sample at a concentration of 45 mmol/L, that was also used later on to acquire system matrices for mMPI experiments. To avoid interference from the noise floor of the system, only components with a SNR above 6 dB were chosen. Since the plot of these random errors over frequency is still difficult to evaluate due to the tight spacing of the frequency components (cf. right sides of figure 2.57 and figure 2.58), histograms of the error distribution are also given.

As can be seen from the histograms on the left side of figure 2.57 and figure 2.58, the majority (i.e. $> 50\%$) of the 243 evaluated frequency components in the receive signal of the x (and y) axis show standard deviations below 0.67 % (0.32 %) and 0.88° (0.56°) for the magnitude and phase respectively. 90 % of the frequency points lie within the range below 2.3 % (2.4 %) magnitude deviation and 1.71° (1.52°) phase deviation. The larger phase deviations for the x axis are because of the multiplicative effect at higher harmonics and the richer (more wideband) received spectrum in the x channel. The lower apparent count of frequency components in the y channel compared to figure 2.55 are due to the fact that sidebands around the "pure" harmonics of the channels were chosen, which leaves most projections of x components into the y channel unconsidered. These components are included in the x channel and are thus already part of the random error evaluations, thus this effect is intended. The standard deviation values were calculated based on 15 repetitions with 15 frames.

These results are agreeable since they allow differentiation between different mobility states of the particles, with typical effects (determined by MPS measurements, cf.

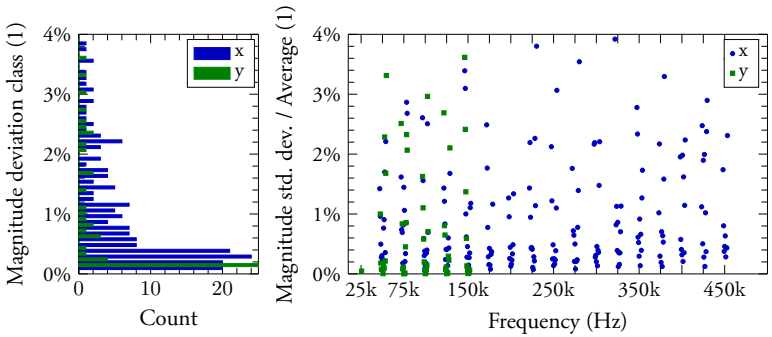

Figure 2.57: Random magnitude errors for the x and y axis of the MPI at 25 kHz under nominal drive field parameters for a typical 22 µl 45 mmol/L Feraspin XL calibration sample.

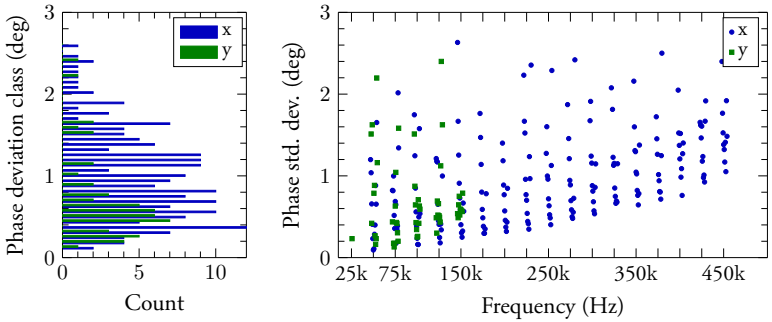

Figure 2.58: Random phase errors for the x and y axis of the MPI at 25 kHz under nominal drive field parameters for a typical 22 µl 45 mmol/L Feraspin XL calibration sample.

section 3.1.3) in the range of 8.5 % . . . 10.1 % magnitude and −0.85° . . . −1.4° phase for the 7$^{\text{th}}$ harmonic and 9.8 % . . . 10.4 % magnitude and −1.68° . . . −2.97° phase for the 15$^{\text{th}}$ harmonic at 25 kHz (cf. table 3.3 on page 158). As the effects at 10 kHz are approximately twice as large (cf. table 3.2) and since the stability at the 10 kHz drive fields is even better (not shown), MPI should be possible considering the signal quality of the constructed scanner. MPI measurements under two-dimensional drive field excitation (cf. section 3.5.3.1 on page 164) suggest that dynamic effects are even larger once more than one active axis is used.

2.3.3 System Calibration

System matrix acquisitions are necessary for f-space reconstruction for every sample type. More precisely, an individual system matrix is required for quantitative imaging for every type of nanoparticle and possibly every particle environment if the viscosity or hydrodynamic parameters differ significantly and cannot be interpolated.

In this section, only the general ability of the system to acquire such matrices and exemplary results thereof are shown. Because the matrices are intimately related to the scans, the applications chapter also contains the corresponding system matrices where they provide insight.

2.3.3.1 One-d Calibration Matrices

One-dimensional system matrices are acquired by moving a point sample along the desired axis and acquiring the harmonic content at each position. The harmonic content over the axis coordinate constitutes the system matrix (cf. section 1.2.3.1).

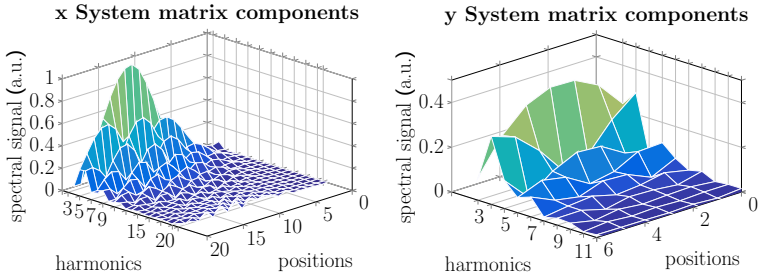

(a) One-d x axis system matrix, $f = 25\,\mathrm{kHz}$, $\hat{B} = 22\,\mathrm{mT_{pk}}$

(b) One-d y axis system matrix, $f = 25.64\,\mathrm{kHz}$, $\hat{B} = 12.5\,\mathrm{mT_{pk}}$

Figure 2.59: First one-d system matrices acquired with the MPIv3 scanner at 25 kHz for (a): the x and (b): the y axis with a 2 mm Resovist calibration sample at $G_{x,y} = 1\,\mathrm{T/m}$, using a 2 mm grid.

Figure 2.59 depicts the first one-dimensional system matrices acquired with the scanner at 25 kHz. As discussed in section 2.2.9, the drive frequency of 25 kHz is more critical than 10 kHz, which suffers less from amplifier spurs and component non-linearities. Both axes show the expected structure of harmonics and allowed one-dimensional reconstruction. However, the y axis is showing much weaker signals, owing to the saddle coil detection as opposed to the solenoid coil in the x direction, as well as the reduced drive field amplitude due to power amplifier limits. Nevertheless, one-dimensional images could be reconstructed for both axes at every point of the axis. The results thereof are shown in figure 3.5 on page 159.

2.3.3.2 Two-d System Matrix Calibration

Similar to the one-dimensional case, a two-dimensional system matrix can be acquired with both axes concurrently generating drive fields while moving a point sample on a two-dimensional grid. The large number of harmonics and intermodulation products, however, makes it difficult to visualize the complete content of such a matrix. Therefore only selected components are shown and compared to their expected structure according to theoretical considerations (cf. figure 2.60). Reconstructed two-dimensional data is shown in section 3.3. As is apparent from fig. 2.60a, especially for the higher order matrix components on the right, the measured matrix is slightly distorted. These distortions arise from non-idealities (amplitude and phase transfer functions, non-constant sensitivity over the imaging volume, etc.) in the system and are one of the reasons why a system matrix needs to be acquired to account for these effects. To some degree particle effects (e.g. dynamics) are also responsible, which can be used to acquire mobility information.

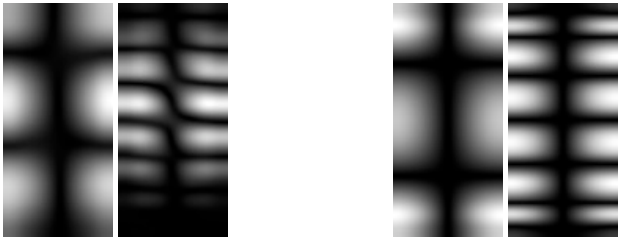

(a) Measured components (b) Simulated results

Figure 2.60: Two components of the first acquired two-d system matrix with the x-axis configured as $f = 25\,\mathrm{kHz}, \hat{B} = 22\,\mathrm{mT_{pk}}$ and the y axis adjusted to $f = 25.64\,\mathrm{kHz}, \hat{B} = 12.5\,\mathrm{mT_{pk}}$ in a $G_{x,y} = 1\,\mathrm{T/m}$ gradient (a). The utilized point sample was a 2 mm Resovist sample moved on a 2 mm grid. Both components are compared to theoretical data (b).

CHAPTER 3

Application

3.1 MPS Measurements

This section shows several experiments in which the MPS system (cf. section 2.1) was used to investigate tracer behavior for MPI applications.

3.1.1 Tracer characterization for MPI

The first application of the MPS system was the characterization of new tracer systems developed by nanoPET Pharma GmbH (Berlin, Germany) in comparison to their established Feraspin R series with regard to MPI performance.

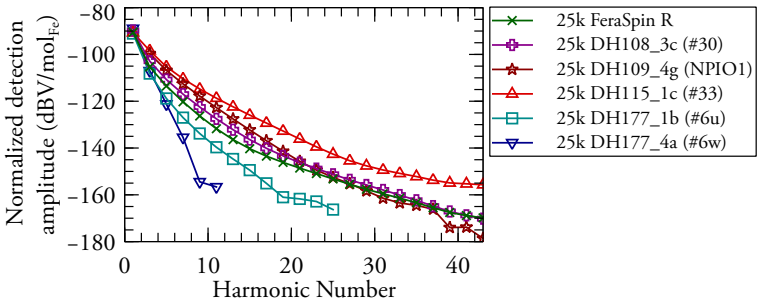

Figure 3.1: Comparison of the harmonic spectra of several new tracer systems prepared at nanoPET to the Feraspin R tracer. All spectra were normalized to the amount of iron.

Figure 3.1 shows the results of several particle series developed during the course of a ZIM project. Similar to the evaluation in the following section, there are particle systems that out-perform the FeraSpin R series (which produces a signal identical to Resovist). Samples #30 and #33 surpass FeraSpin R with regard to harmonic content by 4.25 dB and 14.04 dB (a factor of 5) respectively at the 13$^{\text{th}}$ harmonic. The NPIO1 sample has a 8.05 dB signal gain at the 13$^{\text{th}}$ harmonic compared to FeraSpin R. $M(H)$ measurements on this sample suggested a bimodal effective core size distribution [162]. Samples #6u and #6w show lower signals than FeraSpin R and are included for completeness. Sample properties, where available, are given in table 3.1.

Name	Serial	Core	d_{core}	d_{hyd}	Concentration	Remarks
FS-R	#49	multi	5 nm	60 nm	50 mmol/l	D
DH108_3c	#30	multi	-	-	27.1 mmol/l	
DH109_4g	NPIO1	multi	5 nm	196 nm	11.3 mmol/l	P
DH115_1c	#33	multi	-	-	6.5 mmol/l	
DH177_1b	#6u	multi	10 nm	188 nm	17.5 mmol/l	
DH177_4a	#6w	multi	15 nm	136 nm	9.9 mmol/l	

Table 3.1: Properties of selected nanoparticles characterized during the ZIM project. P denotes polymer coating, M monomer coating, D carboxydextran coating.

3.1.2 Evaluation of particle systems for high MPI drive frequencies

While investigating possible applications of MPI in human medicine, the problem of peripheral nerve stimulation was identified and investigated by several groups [120, 121]. At frequencies in the MHz range, safety limits concerning magnetic fields are governed by the heating of tissue, which is evaluated using the specific absorption rate (SAR). For lower frequencies the heating effect is much less pronounced and peripheral nerve stimulation (PNS) is observed before reaching SAR limits [120, 121]. Because PNS results in an unpleasant sensation for the patient and is dependent on the size of the subject, it is a major concern for human sized MPI scanners. Since PNS limits rise with increasing frequency [163], increasing the MPI drive frequency provides a way to avoid PNS in patients. The increased drive field frequency, however, also affects tracer behavior through particle dynamics. To evaluate the consequences of a drive frequency in the 100 kHz range, the behavior of two particle tracers with good MPI performance has been evaluated. Figure 3.2 depicts the results for UW-A and Resovist tracers. UW-A is a tracer produced by the University of Washington (Seattle, WA, USA) that was specifically tailored for MPI applications [164]. It is a single core particle system with 25 nm core size and a hydrodynamic diameter of 77 nm, showing a mono-modal distribution with a polydispersity index of 0.065 [134, 165]. The particles were measured at concentrations of 25 mmol/l and 5 mmol/l, which showed the same result after normalization to the iron mass. Resovist on the other hand is an established MPI tracer that was also used as contrast enhancer in MRI

in humans. It is a multi-core system with 4 – 7 nm crystallites forming magnetic cores. The hydrodynamic size of the coated particles is in the range of 50 – 70 nm [137]. As is apparent from figure 3.2, both particle systems show good performance at all

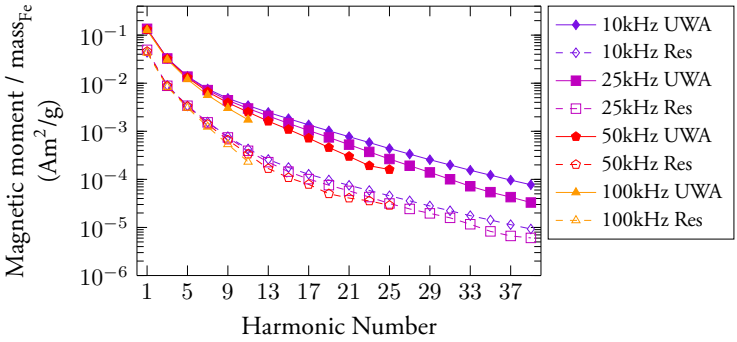

Figure 3.2: Comparison of the harmonic spectra of Resovist with the UW-A tracer at all available drive frequencies of the MPS setup (cf. [134]). System calibration was performed and applied as outlined in section 2.1.9.1. The concentration of the UW-A sample was 25 mmol/l and that of the Resovist sample 50 mmol/l.

drive frequencies with the UW-A tracer generally showing spectra with amplitudes about five to sevenfold larger than that of Resovist. However, the harmonic spectra of both tracers drop off more quickly as the drive frequency is increased. This effect is related to particle dynamics, which also manifest themselves in the observed phase lag apparent in the time domain, when considering the dynamic $M(H)$ curve of the particles (see figure 3.3). Since MPI systems generally use coils as field sensors, this steeper slope of the harmonics in figure 3.2 is offset by the fact that the receive voltage amplitude increases (for equal drive field strengths) as the frequency is increased. Due to the slope increase there exists a crossing point at a certain harmonic number above which the increased receive signal is fully consumed by the harmonic slope. Above this point the resulting signal falls below that at lower drive fields, possibly diminishing the spatial resolution of MPI scanner because of the reduced number of detected harmonics. Judging from the MPS measurements and the moderate change in the slope, it can be expected that this effect is not a major concern. It can, however become important if the spurious background signal generated by the MPI system at higher drive frequencies also increases. As a conclusion, a clean drive signal becomes increasingly important as the drive frequency is increased, but also increasingly difficult to achieve due to power amplifier and component behavior.

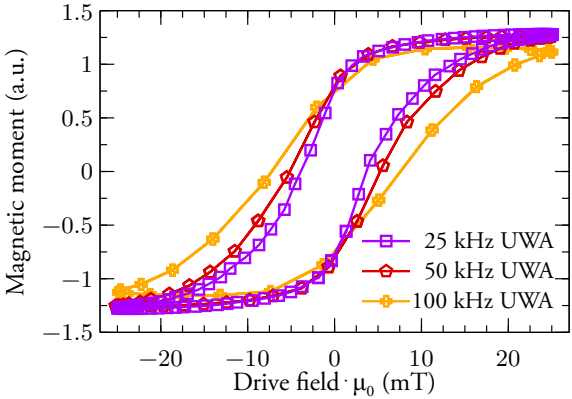

Figure 3.3: M(H) plot of the particle response of the UW-A particles at different excitation frequencies [134]. The effect of the particles dynamics is visible as (dynamic) hysteresis. © IEEE 2015.

3.1.3 Effects of viscous media on the particle signal as pre-experiment for mMPI

In preparation of mMPI scans, viscous samples with water glycerin mixtures were examined in the MPS system. The viscosity was calculated according to *Cheng* [166] and simulates an equivalent change in the hydrodynamic size according to the *Brownian* time constant (1.5) on page 6. Three viscosity values (`#sm`: 84.85 mPa s, `#sn`: 18.88 mPa s, `#so`: 4.20 mPa s) and a purely aqueous sample (`#sp`: 1 mPa s) as well as a freeze-dried sample (`#t2`: FD) were prepared. The Feraspin XL particle system (*nanoPET Pharma GmbH*, Berlin, Germany) was selected for its long term stability in water-glycerin solutions and its suitability for preclinical applications.

As before, the measured spectra were converted to absolute units and normalized to the iron mass. Figure 3.4 depicts the results at 10 kHz and 25 kHz excitation frequencies and 25 mT field amplitude. These conditions match the MPI drive field conditions at the respective frequency and are therefore representative for the center point in the FOV.

Figure 3.4 makes it clear that the effect on the amplitude and phase response is rather small. Table 3.2 and table 3.3 on page 158 show the same data in tabular form with the deviations from the liquid sample calculated, to better compare the amplitude variations as is possible on a logarithmic scale. In the tables, $|H_n|$ denotes the linear magnitude of the n^{th} harmonic and $\Delta|H_n|$ its difference to the value of the liquid sample. Similarly, $\measuredangle H_n$ is the phase angle of the n^{th} harmonic and $\Delta\measuredangle H_n$ its deviation from the phase of the liquid sample. It becomes apparent that while the amplitude variation reaches a large portion of their effect at lower harmonic orders (half at the third harmonic), the phase deviations scale approximately with the

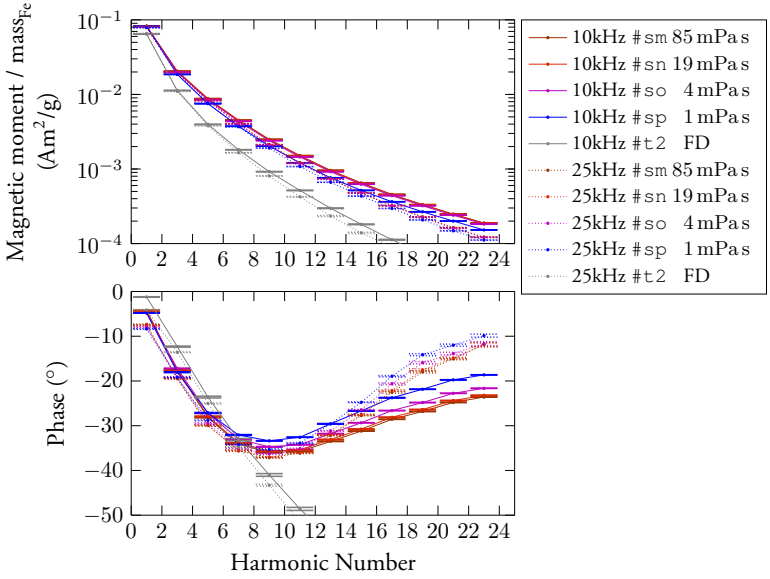

Figure 3.4: Results of the glycerin viscosity series for the Feraspin XL tracer ranging from 84.8 mPa s to 1 mPa s at 10 kHz and 25 kHz. Empirical standard deviations were added as error bars to show the relation between the stability of the receive signal and the variations caused by the viscous environment.

order, making them ideal for higher harmonics. However, the overall effect for both quantities, being in the range of 20 % and 4° at 10 kHz, is small considering the value range occupied by the spectra. At 25 kHz the effects approximately halve to 10 % and 2.5°. It should also be noted that the limited availability of higher harmonics in an imaging system restricts the degree to which the scaling effect of the phase response can be harnessed in mMPI.

Comparing the individual samples shows that samples #sn and #so can be well distinguished between each other and the sample in pure water #sp. The difference between #sm and #sn, however, is very small. Although all data points show larger deviations for #sm than for #sn, as is expected from their viscosity values, it is doubtful whether a clear differentiation between those two samples would be possible for the weaker signal in an imaging system.

Another noteworthy observation is the response of the freeze-dried sample. Besides its much reduced amplitude, due to the missing *Brownian* contribution, the phase shows a behavior that is distinctively different from that of the mobile samples. At both 10 kHz and 25 kHz it shows almost a linear phase dependency over the harmonic number (which is proportional to frequency). This is most likely due to the

high value of the *Néel* relaxation time constant's inverse compared to the excitation's angular frequency.
It is also remarkable that the magnitude of the response rises as the viscosity of the sample is increased. Both observations are consistent with the results found from comparing the responses of FeraSpin R particles at 1 kHz and 10 kHz [167], that showed the same relationship and revealed even larger effects at 1 kHz. However, imaging at 1 kHz drive frequencies would be a lot more challenging due to the reduced sensitivity of the receive coils, which is why 10 kHz was chosen instead.

Freq.	10kHz	10kHz	10kHz	10kHz	10kHz
Sample	#sm	#sn	#so	#sp	#t2
$\lvert H_1\rvert$	82.0 m	82.0 m	82.0 m	81.999 m	64.328 m
$\Delta\lvert H_1\rvert$	975.466 µ%	1.030 m%	342.929 µ%	0.0 %	−21.551 %
$\measuredangle H_1$	−4.225 °	−4.349 °	−4.805 °	−4.776 °	−1.226 °
$\Delta\measuredangle H_1$	551.929 m°	427.813 m°	−28.931 m°	0.0 °	3.551 °
$\lvert H_3\rvert$	20.510 m	20.346 m	20.020 m	18.596 m	11.314 m
$\Delta\lvert H_3\rvert$	10.291 %	9.411 %	7.657 %	0.0 %	−39.159 %
$\measuredangle H_3$	−17.684 °	−17.516 °	−17.195 °	−18.043 °	−12.319 °
$\Delta\measuredangle H_3$	358.798 m°	526.935 m°	847.725 m°	0.0 °	5.724 °
$\lvert H_5\rvert$	8.789 m	8.710 m	8.521 m	7.510 m	3.970 m
$\Delta\lvert H_5\rvert$	17.024 %	15.973 %	13.461 %	0.0 %	−47.144 %
$\measuredangle H_5$	−28.142 °	−27.921 °	−27.184 °	−27.139 °	−23.604 °
$\Delta\measuredangle H_5$	−1.003 °	−782.153 m°	−45.244 m°	0.0 °	3.536 °
$\lvert H_7\rvert$	4.517 m	4.472 m	4.358 m	3.745 m	1.813 m
$\Delta\lvert H_7\rvert$	20.616 %	19.409 %	16.383 %	0.0 %	−51.595 %
$\measuredangle H_7$	−34.102 °	−33.850 °	−33.007 °	−32.071 °	−33.113 °
$\Delta\measuredangle H_7$	−2.030 °	−1.778 °	−936.083 m°	0.0 °	−1.041 °
$\lvert H_9\rvert$	2.497 m	2.471 m	2.400 m	2.030 m	920.988 µ
$\Delta\lvert H_9\rvert$	22.993 %	21.692 %	18.182 %	0.0 %	−54.640 %
$\measuredangle H_9$	−35.997 °	−35.691 °	−34.717 °	−33.380 °	−41.008 °
$\Delta\measuredangle H_9$	−2.618 °	−2.312 °	−1.338 °	0.0 °	−7.628 °
$\lvert H_{11}\rvert$	1.511 m	1.496 m	1.449 m	1.211 m	515.938 µ
$\Delta\lvert H_{11}\rvert$	24.816 %	23.501 %	19.689 %	0.0 %	−57.393 %
$\measuredangle H_{11}$	−35.759 °	−35.399 °	−34.239 °	−32.575 °	−48.594 °
$\Delta\measuredangle H_{11}$	−3.184 °	−2.824 °	−1.664 °	0.0 °	−16.019 °
$\lvert H_{13}\rvert$	958.643 µ	949.072 µ	919.660 µ	761.831 µ	297.585 µ
$\Delta\lvert H_{13}\rvert$	25.834 %	24.578 %	20.717 %	0.0 %	−60.938 %
$\measuredangle H_{13}$	−33.500 °	−33.083 °	−31.773 °	−29.583 °	−55.217 °
$\Delta\measuredangle H_{13}$	−3.917 °	−3.500 °	−2.190 °	0.0 °	−25.634 °
$\lvert H_{15}\rvert$	650.071 µ	644.117 µ	624.549 µ	516.691 µ	181.063 µ
$\Delta\lvert H_{15}\rvert$	25.814 %	24.662 %	20.875 %	0.0 %	−64.957 %
$\measuredangle H_{15}$	−31.202 °	−30.748 °	−29.341 °	−26.684 °	−62.197 °
$\Delta\measuredangle H_{15}$	−4.518 °	−4.064 °	−2.657 °	0.0 °	−35.513 °
$\lvert H_{17}\rvert$	456.041 µ	452.272 µ	439.265 µ	363.547 µ	112.566 µ
$\Delta\lvert H_{17}\rvert$	25.442 %	24.406 %	20.828 %	0.0 %	−69.037 %
$\measuredangle H_{17}$	−28.566 °	−28.112 °	−26.616 °	−23.758 °	−68.805 °
$\Delta\measuredangle H_{17}$	−4.807 °	−4.354 °	−2.858 °	0.0 °	−45.046 °
$\lvert H_{19}\rvert$	332.833 µ	330.268 µ	321.323 µ	266.525 µ	72.144 µ
$\Delta\lvert H_{19}\rvert$	24.879 %	23.916 %	20.560 %	0.0 %	−72.932 %
$\measuredangle H_{19}$	−26.813 °	−26.380 °	−24.823 °	−21.852 °	−75.922 °
$\Delta\measuredangle H_{19}$	−4.961 °	−4.528 °	−2.971 °	0.0 °	−54.070 °
$\lvert H_{21}\rvert$	248.367 µ	246.760 µ	240.061 µ	200.201 µ	46.501 µ
$\Delta\lvert H_{21}\rvert$	24.059 %	23.256 %	19.910 %	0.0 %	−76.773 %
$\measuredangle H_{21}$	−24.799 °	−24.368 °	−22.760 °	−19.756 °	−82.420 °
$\Delta\measuredangle H_{21}$	−5.043 °	−4.612 °	−3.004 °	0.0 °	−62.664 °

Table 3.2: Viscosity data at 10 kHz. Amplitude magnitudes are given in Am^2/g (Fe).

Freq.	25kHz	25kHz	25kHz	25kHz	25kHz
Sample	#sm	#sn	#so	#sp	#t2
$\lvert H_1\rvert$	81.952 m	80.442 m	79.284 m	78.490 m	65.693 m
$\Delta\lvert H_1\rvert$	4.410 %	2.486 %	1.011 %	0.0 %	−16.305 %
$\measuredangle H_1$	−7.360 °	−7.553 °	−7.932 °	−8.377 °	−4.149 °
$\Delta\measuredangle H_1$	1.017 °	823.736 m°	444.849 m°	0.0 °	4.228 °
$\lvert H_3\rvert$	19.792 m	19.669 m	19.625 m	18.551 m	11.006 m
$\Delta\lvert H_3\rvert$	6.687 %	6.023 %	5.787 %	0.0 %	−40.675 %
$\measuredangle H_3$	−19.492 °	−19.458 °	−19.136 °	−19.207 °	−13.576 °
$\Delta\measuredangle H_3$	−285.180 m°	−251.651 m°	70.711 m°	0.0 °	5.630 °
$\lvert H_5\rvert$	8.336 m	8.276 m	8.238 m	7.655 m	3.797 m
$\Delta\lvert H_5\rvert$	8.895 %	8.115 %	7.619 %	0.0 %	−50.396 %
$\measuredangle H_5$	−29.946 °	−29.917 °	−29.470 °	−28.802 °	−25.023 °
$\Delta\measuredangle H_5$	−1.144 °	−1.115 °	−668.163 m°	0.0 °	3.779 °
$\lvert H_7\rvert$	4.053 m	4.021 m	3.994 m	3.679 m	1.652 m
$\Delta\lvert H_7\rvert$	10.145 %	9.273 %	8.545 %	0.0 %	−55.102 %
$\measuredangle H_7$	−35.628 °	−35.577 °	−35.031 °	−34.180 °	−34.859 °
$\Delta\measuredangle H_7$	−1.448 °	−1.397 °	−850.890 m°	0.0 °	−678.859 m°
$\lvert H_9\rvert$	2.126 m	2.108 m	2.089 m	1.910 m	806.713 µ
$\Delta\lvert H_9\rvert$	11.341 %	10.382 %	9.402 %	0.0 %	−57.755 %
$\measuredangle H_9$	−37.148 °	−37.041 °	−36.308 °	−35.332 °	−43.296 °
$\Delta\measuredangle H_9$	−1.816 °	−1.709 °	−975.762 m°	0.0 °	−7.964 °
$\lvert H_{11}\rvert$	1.208 m	1.197 m	1.185 m	1.078 m	423.229 µ
$\Delta\lvert H_{11}\rvert$	12.073 %	11.068 %	9.969 %	0.0 %	−60.730 %
$\measuredangle H_{11}$	−36.147 °	−36.003 °	−35.140 °	−33.880 °	−51.440 °
$\Delta\measuredangle H_{11}$	−2.267 °	−2.123 °	−1.260 °	0.0 °	−17.560 °
$\lvert H_{13}\rvert$	741.180 µ	735.567 µ	730.871 µ	663.674 µ	234.198 µ
$\Delta\lvert H_{13}\rvert$	11.678 %	10.833 %	10.125 %	0.0 %	−64.712 %
$\measuredangle H_{13}$	−32.195 °	−32.035 °	−31.147 °	−29.580 °	−59.599 °
$\Delta\measuredangle H_{13}$	−2.615 °	−2.455 °	−1.566 °	0.0 °	−30.018 °
$\lvert H_{15}\rvert$	478.054 µ	475.672 µ	475.825 µ	433.110 µ	139.212 µ
$\Delta\lvert H_{15}\rvert$	10.377 %	9.827 %	9.862 %	0.0 %	−67.858 %
$\measuredangle H_{15}$	−27.736 °	−27.501 °	−26.447 °	−24.767 °	−69.265 °
$\Delta\measuredangle H_{15}$	−2.969 °	−2.734 °	−1.680 °	0.0 °	−44.498 °
$\lvert H_{17}\rvert$	323.524 µ	322.227 µ	323.075 µ	295.516 µ	89.620 µ
$\Delta\lvert H_{17}\rvert$	9.478 %	9.039 %	9.326 %	0.0 %	−69.674 %
$\measuredangle H_{17}$	−22.536 °	−22.132 °	−20.629 °	−18.944 °	−73.618 °
$\Delta\measuredangle H_{17}$	−3.591 °	−3.188 °	−1.685 °	0.0 °	−54.673 °
$\lvert H_{19}\rvert$	227.802 µ	226.273 µ	224.956 µ	207.247 µ	51.690 µ
$\Delta\lvert H_{19}\rvert$	9.918 %	9.180 %	8.545 %	0.0 %	−75.059 %
$\measuredangle H_{19}$	−17.976 °	−17.522 °	−15.917 °	−14.126 °	−70.694 °
$\Delta\measuredangle H_{19}$	−3.850 °	−3.395 °	−1.791 °	0.0 °	−56.568 °
$\lvert H_{21}\rvert$	163.776 µ	162.382 µ	160.304 µ	148.050 µ	21.278 µ
$\Delta\lvert H_{21}\rvert$	10.622 %	9.680 %	8.277 %	0.0 %	−85.628 %
$\measuredangle H_{21}$	−15.070 °	−14.879 °	−13.877 °	−11.996 °	−81.667 °
$\Delta\measuredangle H_{21}$	−3.073 °	−2.883 °	−1.881 °	0.0 °	−69.671 °

Table 3.3: Viscosity data at 25 kHz. Amplitude magnitudes are given in Am^2/g (Fe).

3.2 One-d MPI Results

Figure 3.5 depicts the stacked reconstructed one dimensional images using the matrices described in section 2.3.3.1 on page 149. Reconstruction was performed using the Kaczmarz algorithm with the regularization parameter set to $\lambda = 0.1$ and $N = 15$ iterations.

(a) Reconstructed x axis images

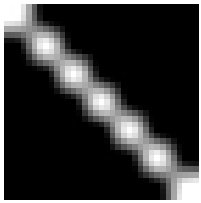

(b) Reconstructed y axis images

Figure 3.5: Stacked reconstructed images using the system matrices shown in figure 2.59 for a point sample at every axis position. The individual images were acquired on a 2 mm grid.

The data was acquired at 25 kHz using 6 repetitions of 5 frames based on a repetition interval of 63.96 ms. The sample was moved on a 2 mm grid on the respective axis at the center of the inactive axis.

All points along the x and y axis could be uniquely identified by the system matrix, leading to a 21 and 7 pixel image corresponding to a theoretical FOV of $42\,\mathrm{mm} \times 14\,\mathrm{mm}$ at a gradient of $1\,\mathrm{T/m}$.

3.3 Two-d MPI Results

Figure 3.6 depicts the first reconstructed two-d images at 10 kHz and 25 kHz.

The 10 kHz data was acquired using 10 frames and 10 repetitions based on a repetition interval of 31.2 ms at 7×17 points on a 2 mm grid. At 25 kHz, 5 frames based on a repetition interval of 63.96 ms were used in conjunction with 7×15 points with 10 repetitions on a 2 mm grid.
A Feraspin R sample with 2 mm diameter was used at both frequencies as a calibration point sample in a $2\,\mathrm{T/m}$ gradient, excited by 16.8 A (x) and 25.02 A (y) drive field currents corresponding to 28.56 mT and 12.76 mT peak drive field amplitude for the x and y axis respectively.

Matrix regularization and image reconstruction was performed using a Kaczmarz algorithm with $N = 12$ iterations. The regularization parameter was chosen as $\lambda = 0.1$.

It is obvious that at 25 kHz the additional amplifier spurs lead to artifacts at the borders of the FOV. Nevertheless, 20 mm of usable imaging range are available in

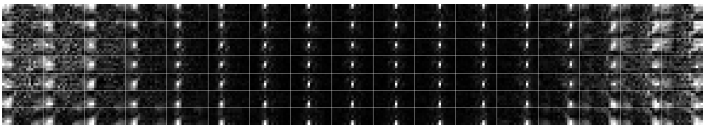

(a) Reconstructed 2d images at 25 kHz

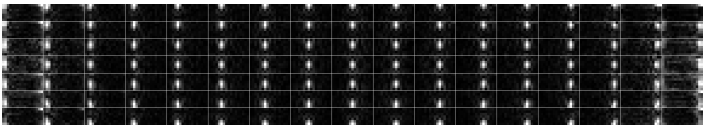

(b) Reconstructed 2d images at 10 kHz

Figure 3.6: Reconstructed images for each point in the FOV using a 2 mm Feraspin R sample on a 2 mm grid (a) at 25 kHz and (b) at 10 kHz, both at a 2 T/m gradient.

the x axis and 12 mm in the y direction. At 10 kHz the x axis performs considerably better, allowing the reconstruction of a 28 mm range (based on the visual quality of the depicted image).

Further measurements were performed at 25 kHz acquiring 15 frames based on a repetition interval of 63.96 ms with 3 repetitions in conjunction with 9×21 1.5 mm spaced grid points.
The system gradient was set to 2 T/m and drive field currents were chosen as 17.1 A (x) and 19.4 A (y), corresponding to 29.1 mT and 9.9 mT peak drive field amplitude for the x and y axis respectively at both frequencies. Feraspin XL point samples were imaged, to verify the ability to differentiate between several samples in the FOV. The reconstructed results are shown in figure 3.7. Reconstruction was performed using the Kaczmarz algorithm with a regularization parameter of $\lambda = 0.5$ and 15 iterations. The image shows a spacing of 4.5 mm which matches the 5 mm spacing between the samples, especially when taking into account that the gray pixel right to the left sample (that is lighter than the gray pixel to the left) indicates that the sample is positioned slightly between grid points. As expected, the resolution in the y direction is inferior to that of the x axis, leading to some blurring of the image in that direction. Nevertheless, the scanner proves to be able of two dimensional imaging.

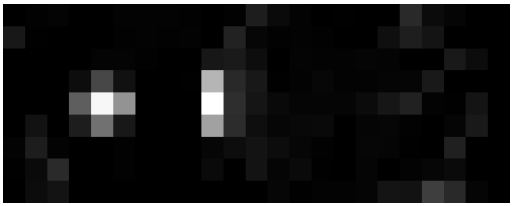

Figure 3.7: Reconstructed image of two 2 mm dot samples spaced 5 mm apart in the x direction, measured at 25 kHz.

3.4 One-d mMPI Results

As a first experiment using multiple frequencies to acquire mMPI data, a one-dimensional experiment was performed where system matrices were acquired at 10 kHz and 25 kHz using both a mobile and a freeze-dried sample. The samples were then shifted together along the x axis at both frequencies. Using the color-MPI method [47] with a stacked system matrix, both samples could be distinguished from each other as is shown in figure 3.8 [48] with a false color overlay. Because of the color-MPI approach, the number of iterations required for the Kaczmarz algorithm to reach convergence increases. The algorithm was used with $N = 150$ iterations and a regularization parameter $\lambda = 0.1$ to arrive at the depicted results.

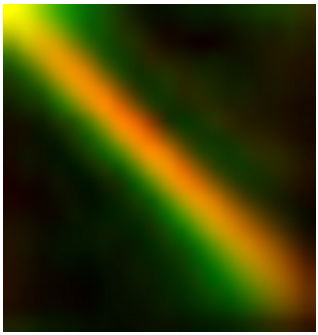

Figure 3.8: Stacked reconstructed mMPI results and false color overlay [48] acquired with a freeze-dried sample exhibiting solely *Néel* relaxation (shown in green) and a sample that includes *Brownian* relaxation (red). Both samples were imaged at the same time at various positions of the x axis and distinguished from each other through the color-MPI method (cf. [47]). Reprinted from JMMM, Vol. 427, *T. Viereck, C. Kuhlmann* et al., "Dual-frequency magnetic particle imaging of the Brownian particle contribution", Pages 156-161, © 2015, with permission from Elsevier

The resolution is comparatively low, since a gradient of only 1 T/m was used for the image acquisition. It is also apparent that the slower relaxation of the freeze-dried sample, as a result of the missing *Brownian* relaxation process, leads to a blurring of that sample's image due to particle dynamics. The mobile sample, however, does not exhibit this effect and indicates therefore the achievable resolution at that gradient.

3.5 Two-d mMPI Results

3.5.1 mMPI (calibration) samples

Figure 3.9 depicts the sample used for calibration and mMPI experiments. During calibration, the samples are used in an upright position, so that they form a point sample at the intersection with the imaging plane.

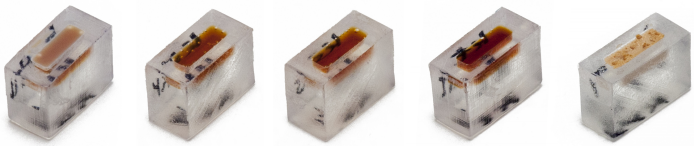

Figure 3.9: Calibration samples with (from left to right) a purely aqueous nanoparticle dilution of 1 mPa s, glycerin-water mixtures with 4.20 mPa s, 18.88 mPa s and 84.85 mPa s, as well as a sample freeze-dried in a mannitol matrix. All samples have a concentration of 45 mmol/L and a volume of 22 µL. The cavity size is 2 mm × 2 mm × 6 mm and the outer dimensions are 7 mm × 5 mm × 10 mm.

The nanoparticle solutions are the same that were measured in the MPS as described in section 3.1.3, except for the freeze dried sample #ky, which had to be prepared directly inside the cavity of the MPI sample vial. It has, however, been prepared from the same batch of FeraSpin XL as the sample #t2, used in the MPS, to ensure it has the same properties.

3.5.2 Influence of viscosity on system matrix components

As a first step, the influence of the viscosity on the system matrix components was investigated. Using the samples shown in figure 3.9, system matrices were acquired using identical parameters for gradient, drive field and grid size. Comparing the results, shown in figure 3.10, it becomes apparent that the imaginary part carries significant information. This is to be expected from the phase dependency observed in section 3.1.3 on page 154.

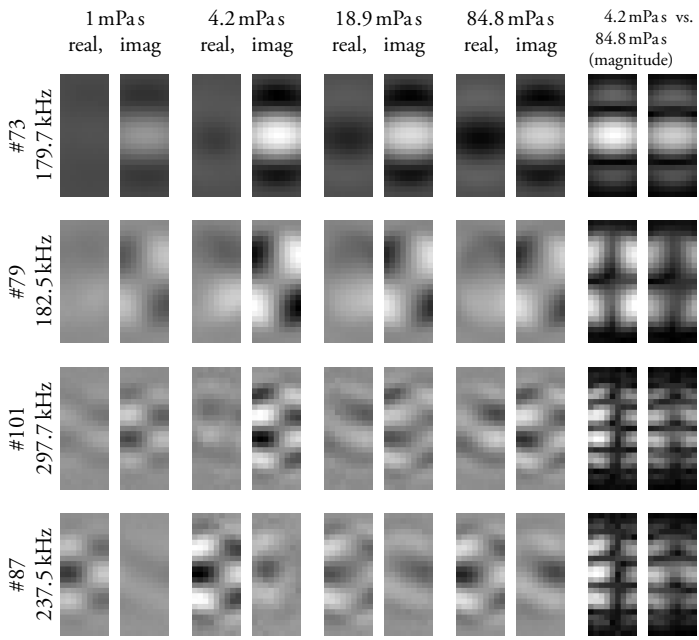

Figure 3.10: Influence of the viscosity on the system matrix components at 10 kHz.

Despite the visible changes, it is obvious that the effect is rather small and that it does not scale linearly with the viscosity value, which is again in agreement with MPS results. It is also interesting to note that the observed changes are more pronounced at higher harmonic orders. E.g. component #87 at 237.5 kHz shows larger differences between the highly viscous and the aqueous sample than the lower ordered component #73 at 179.7 kHz. This is also apparent from the spectra (cf. section 3.5.3.1).

3.5.3 Two-dimensional mMPI results

The calibration samples of figure 3.9 were used to acquire two-d calibration matrices.

The 10 kHz data was acquired using 3 repetitions of 30 frames based on a repetition interval of 31.2 ms at 9×21 points on a 1.5 mm grid. At 25 kHz, 15 frames based on a repetition interval of 63.96 ms were used with 3 repetitions in conjunction with the same 9×21 1.5 mm grid points.
The system gradient was set to 2 T/m and drive field currents were chosen as 17.1 A (x) and 19.4 A (y), corresponding to 29.1 mT and 9.9 mT peak drive field amplitude for the x and y axis respectively at both frequencies.

3.5.3.1 Effects visible in MPI spectra

Taking a look at the raw 25 kHz spectra, as depicted in figure 3.11 and figure 3.12 on page 166 for the x-channel, it can be seen that for the main axis components and low ordered mixing products the amplitude relations between the samples of different viscosities are similar to the MPS result with respect to the general magnitude change. The sample with the highest viscosity (#sm) continues to show the largest amplitude and amplitudes decrease as the viscosity decreases.

The similarity to the MPS results becomes more obvious, once only pure harmonics of the drive frequency of the corresponding axis are shown, as is depicted in figure 3.13 and figure 3.14 for the x axis at two different sample positions. Especially at the center of the FOV (figure 3.13 on page 167) the same relation of harmonic amplitudes and phases as in the MPS measurements (cf. figure 3.4 on page 155) can be identified. Notably, the observed variations show higher relative amplitude and phase changes than in the MPS measurements, most likely owing to the two-dimensional excitation of the particles, which helps to reveal dynamic effects. A reason for this may be the increased available "relaxation" time, because of the longer overall repetition period in the two dimensional drive field case (cf. table 2.7 on page 102).

The amplitude and phase ratio between the different samples reveals another noteworthy effect: Despite the fact that the viscosities of all samples are spaced evenly on a logarithmic scale, all showing approximately a factor of 4 times higher viscosity than the previous sample, the observed changes are most pronounced between the samples with low viscosity. The most viscous samples #sm, #sn on the other hand, show only slight variations in amplitude and phase when compared. As remarked before for the matrix components, there is also the tendency of a larger effect at higher harmonic orders, until the ratios stay approximately constant with frequency from 425 kHz onward.

Results for mixing products (cf. figure 3.11 and figure 3.12) show vast differences to the simple dependency observed in the MPS experiment. This is to be expected, since these components (especially at higher orders) are often the sum of several intermodulation products, involving different combinations of axis harmonics. Consequently, the result is not only dependent on the frequency, but also on the spatial position in the FOV, once again suggesting that capable simulation models are highly beneficial to further advance mMPI.

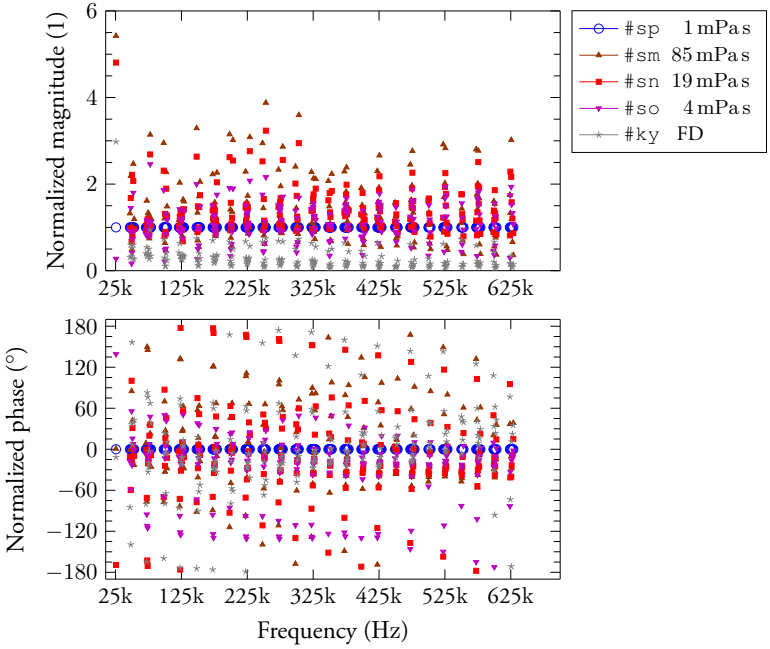

Figure 3.11: Magnitude and phase of the spectral components of samples with different viscosities, normalized to the sample dispersed in pure water. The spectra were acquired at the center of the FOV using the x axis receive channel.

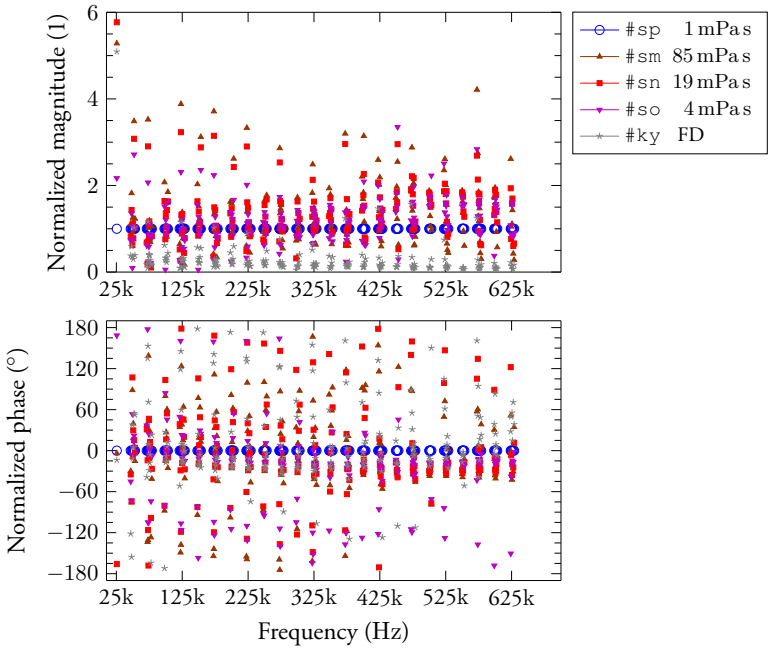

Figure 3.12: Magnitude and phase of the spectral components of samples with different viscosities, normalized to the sample dispersed in pure water. The spectra were acquired at the (−1.5 mm;−1.5 mm) position relative to the center of the FOV using the x axis receive channel.

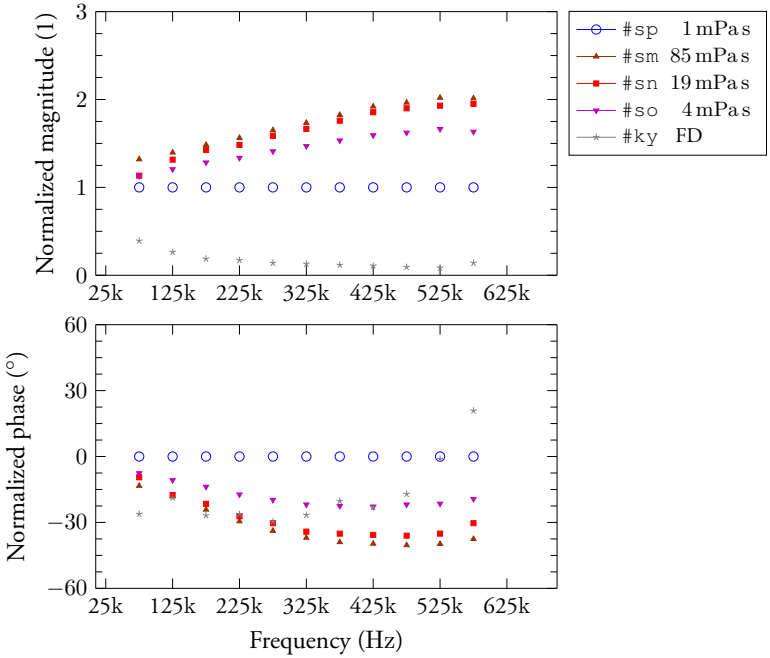

Figure 3.13: Magnitude and phase of the spectral components of samples with different viscosities, normalized to the sample dispersed in pure water #sp. The spectra were acquired at the center of the FOV using the x axis receive channel. Only pure harmonics of the x axis drive frequency are shown.

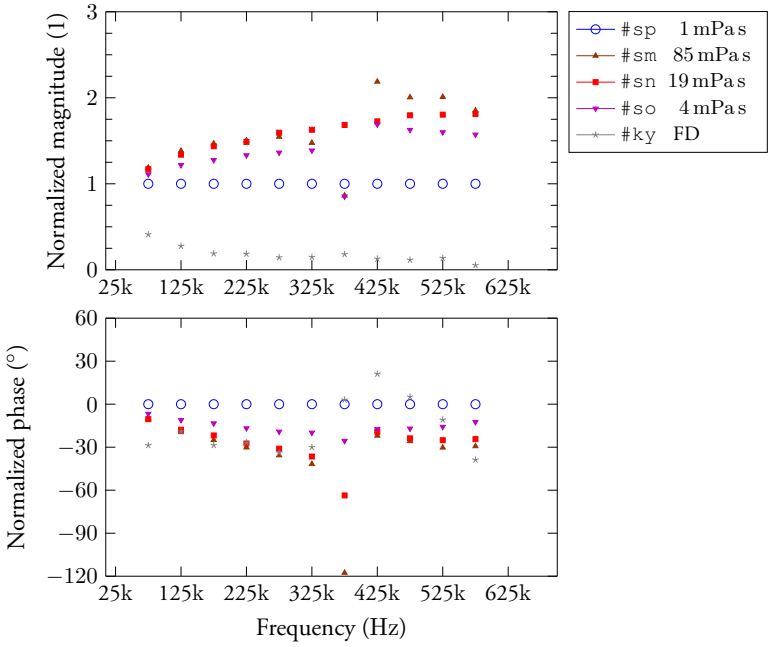

Figure 3.14: Magnitude and phase of the spectral components of samples with different viscosities, normalized to the sample dispersed in pure water #sp. The spectra were acquired at the (−1.5 mm;−1.5 mm) position relative to the center of the FOV using the x axis receive channel. Only pure harmonics of the x axis drive frequency are shown.

3.5.3.2 Two-dimensional mMPI Reconstructions

Figure 3.15 and figure 3.16 depict reconstructed 2-d images of three samples with viscosity values of 1 mPa s, 84.85 mPa s and 18.9 mPa s.

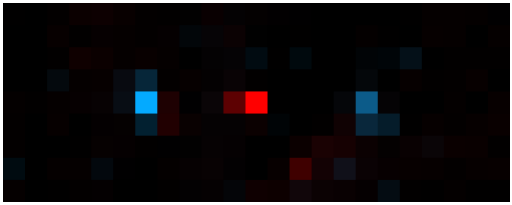

Figure 3.15: 2D color MPI mMPI reconstruction of a 1 mPa s, 84.85 mPa s and 18.9 mPa s sample (left to right) using only the 10 kHz spectra. Although all samples could be resolved and minor differences between 1 mPa s and 18.9 mPa s can be observed, the reconstruction has difficulties identifying the 18.9 mPa s sample.

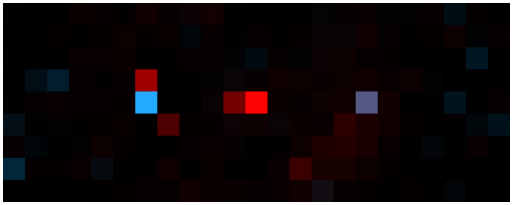

Figure 3.16: 2D color MPI particle mobility reconstruction of a 1 mPa s, 84.85 mPa s and 18.9 mPa s sample (left to right) using the 10 kHz and 25 kHz spectra. All samples could distinguished with regard to their mobility state (shown as false color image). The different value of the 18.9 mPa s sample compared to the sample in water is clearly visible.

The arrangement was deliberately chosen so that the samples with higher viscositiy values are on the outside. Thus, neighboring samples cannot influence the result in a way that would be considered a correct reconstruction of the actual viscosity values. Therefore, the correct representation of the viscosity relations as depicted in the images cannot be the result of neighbor artifacts. The samples were reconstructed using the color MPI approach, using a stacked matrix with all three samples and either 10 kHz or 10 kHz and 25 kHz drive frequencies. Comparing both images, the addition of the second drive frequency in the color MPI approach clearly yields a better contrast between the 1 mPa s and 18.9 mPa s sample, with the latter showing a more realistic tone in figure 3.16. Consequently, the presence of a second drive frequency is highly beneficial for mMPI imaging, making the constructed scanner a valuable asset in the development of better mMPI experiment and reconstruction techniques.

CHAPTER 4

Conclusion and Outlook

Functional imaging capabilities would be a major enhancement for Magnetic Particle Imaging as a clinical or pre-clinical imaging technique. Several methods were suggested [17] to facilitate the extraction of mobility information from the magnetic nanoparticle tracers. To allow a comparison of as many of these approaches as possible with one device, a field-free point MPI scanner with multiple drive frequencies is required.

This work therefore has the objective to construct and put into use a scanner that accomplishes this task and is able to demonstrate mMPI. Starting from a preceding design for a 10 kHz drive frequency, several tasks had to be solved. The experience gathered from a MPS system capable of 10 kHz, 25 kHz, 50 kHz and 100 kHz excitation frequencies showed that amplifier spurs, thermal losses, component linearity and achievable field strength were among the major concerns that needed to be addressed.

The design phase started with several experiments on prototype components during which simulation and modeling techniques were developed and refined. Since the most critical thermal losses are those caused by the real part of the drive coil impedance, prediction of loss mechanisms and self resonant frequency of coils has received some emphasis in this work. Building on prior works, a lumped-component-network coil-model and a procedure to predict its elements were developed, allowing accurate impedance predictions for water-cooled solenoid coils. As expected, coil losses increase with the drive frequency and therefore the 25 kHz drive frequencies are more critical than the 10 kHz set. This is also true with regard to amplifier distortion.

To address amplifier spurs, passive filters were implemented for the transmit chain. To that end, well known synthesis procedures were reviewed. An approach where the drive coil becomes part of the filter network was developed for the transmit filters, which naturally achieves impedance matching to the driving amplifier. Remaining filter components were optimized for low losses and low pass-band attenuation. All

components were selected for maximum linearity to avoid the generation of harmonics in the transmit chain.

For the receive chain, a fully differential gradiometric receive coil was built, along with the necessary differential receive filter arrangement to suppress fundamental feed-through. The arrangement was shielded from interference from the transmit chain and combined with a modular low-noise amplifier.

System component characterization and verification was also a point that received considerable attention throughout the work. Besides performing routine characterizations on every built piece of hardware, such as impedance measurements, all major building blocks of the system were verified against their design parameters.
Although some compromises had to be made in terms of the y axis drive coils due to space and equipment limitations, all important design goals were met. This is also true for the transmit and receive chains that had the transfer functions of their filters compared to the theoretical responses. In case of the receive filters, suppression values exceeding $90\,\mathrm{dB}$ where measured, while a flat pass-band attenuation below $0.75\,\mathrm{dB}$ was achieved from the third harmonic up to $3.2\,\mathrm{MHz}$. Transmit filters showed wide-band attenuation values consistently exceeding $70\,\mathrm{dB}$ in the range $0.06 - 5\,\mathrm{MHz}$. Other parameters that were evaluated include noise performance and common mode rejection ratio of the fully differential receive chain, which proved to be good considering their custom-built nature and showed $> 40\,\mathrm{dB}$ of CMRR above $100\,\mathrm{kHz}$, peaking at $> 60\,\mathrm{dB}$. The effectiveness of the cooling system was evaluated using thermal imaging after prolonged use during system matrix acquisition. No temperature rise of more than $7\,^{\circ}\mathrm{C}$ above ambient temperature was detected at the intended mode of operation.

The completed system was put into use at both its $10\,\mathrm{kHz}$ and $25\,\mathrm{kHz}$ drive frequencies. Both axes were able to generate their nominal field strengths of $30\,\mathrm{mT_{pk}}$ and $15\,\mathrm{mT_{pk}}$. Residual distortion in the drive current was measured to be below $-87\,\mathrm{dBc}$ and $-90.5\,\mathrm{dBc}$ for the x and y axis respectively. This can be improved through a developed active predistortion technique to values below $-99.7\,\mathrm{dBc}$.
As initial measurements, system matrix acquisitions were successfully performed, both under one-dimensional as well as two-dimensional excitation conditions. In both modes, images could be reconstructed from measured data.

Imaging experiments were conducted using phantoms of different viscosity to vary tracer mobility. These experiments were accompanied by MPS measurements that allowed a first evaluation of tracer behavior and the resulting harmonic signals at $10\,\mathrm{kHz}$ and $25\,\mathrm{kHz}$ drive frequencies.

Two dimensional imaging was successfully demonstrated at both $10\,\mathrm{kHz}$ and $25\,\mathrm{kHz}$. Additionally, a similar effect of the viscosity on the harmonic spectra as observed in the MPS could be shown for MPI acquisition, allowing the system to distinguish samples of different viscosity that were imaged simultaneously.

Recommendations for future research and development efforts can be derived from current system limitations. While considerable improvements were made in terms of suppression of amplifier spurs compared to initial measurements and the capabilities of the preceding scanner, the sensitivity at the $25\,\mathrm{kHz}$ drive frequencies

continues to be limited by these signals. A differential transmit filter design of increased filter order would probably allow to overcome these limitations and achieve a noise limited receive signal, allowing further improvements through efforts that lower the receive chain noise floor. A differential filter arrangement would reduce common mode noise and would hopefully also lower coupling outside of the shielded room at the expense of a significantly higher construction effort. Another consequence of differential drive signals would be reduced currents in the ground system, that would make wiring and component placement less critical.
To address the limitations of the y axis drive coil, several approaches seem promising. Using the parallel outputs of two power amplifiers would allow to further increase the drive current of the y channel. To counter the large self-induced voltages across the y axis drive coils, a setup, where the coils are either used in a parallel arrangement or in a parallel resonant circuit, could be evaluated. Additionally, other construction techniques, such as solid copper tubing, could be tested.
For the receive chain, the y channel, which is currently only available single-ended at 25 kHz, as well as both axes at 10 kHz could be enhanced to allow fully differential detection. To reduce the design and construction effort, the Twin-T filter, which has been successfully tested in terms of suppression (55 dB) and linearity at 25 kHz, could be employed. Minor modifications are necessary to allow adequate suppression of both axes' drive frequencies, due to the smaller stop-bandwidth of the Twin-T. Additionally, the sensitivity of the y axis receive coil could be improved, e.g. by using new winding techniques that provide a more homogeneous sensitivity.
Advanced reconstruction techniques and image post processing that are adjusted to the specific properties of the mMPI scanner could also provide better imaging results. Identification of the most limiting properties of the scanner in terms of image quality from the acquired data would also provide additional insight for future improvements. Comparison of different mMPI techniques seems to be the logical next step for experiments concerning scanner application. The results could be widely used to enhance upcoming MPI scanner generations with functional imaging capabilities.

CHAPTER 5

Appendix

A Schematics

Figure A.1 shows the complete schematic of the AC current source that was used to drive the calibration coils during MPS calibration as well as for the determination of the MPI receive transfer function. An additional characterization step of the current source's response (by driving into a load) was employed if no ratio measurements were performed that would cancel this influence.

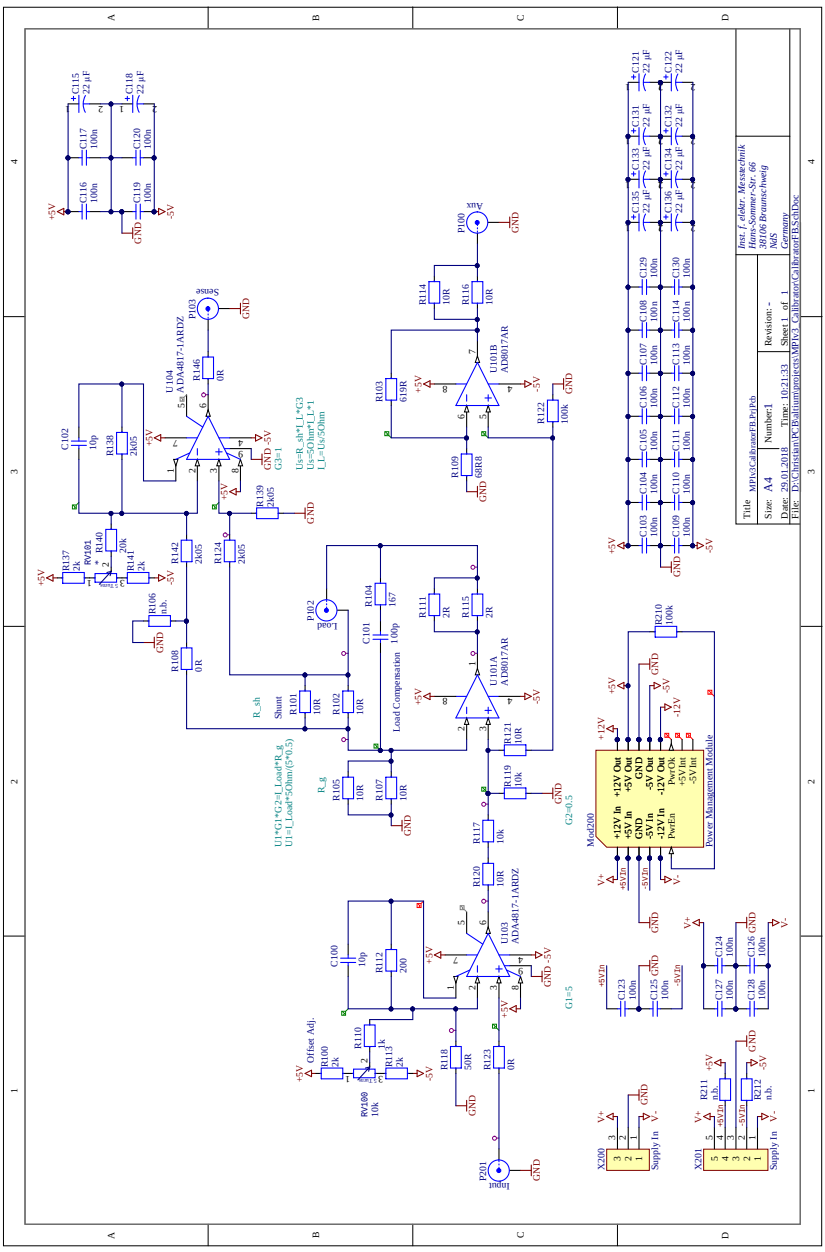

Figure A.1: Schematic of the AC current source used for MPS and MPI receive chain calibration and transfer function measurements.

B Impedance graphs

B.1 MPS Receive coils

Receive coils of axes orthogonal to the excitation

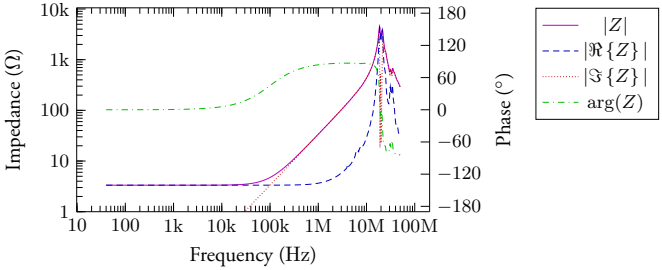

Figure B.2: Impedance of the y axis receive coil of the assembled MPSv2 system.

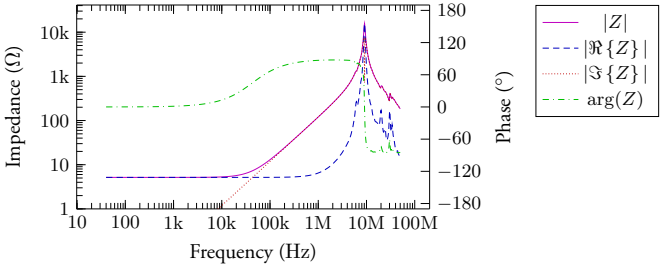

Figure B.3: Impedance of the z axis receive coil of the assembled MPSv2 system.

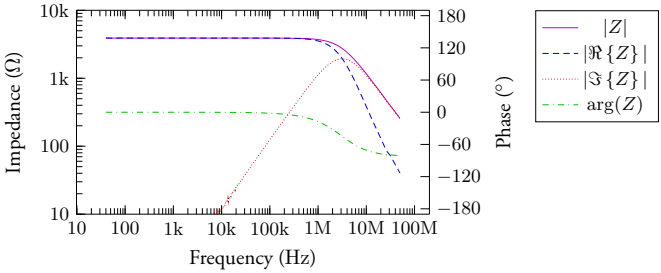

Figure B.4: Input impedance of the preamplifier of the MPSv2 system.
$Z_{\text{in}} = 3.9\,\text{k}\Omega \parallel 12.9\,\text{pF}$.

B.2 MPI Transmit coils

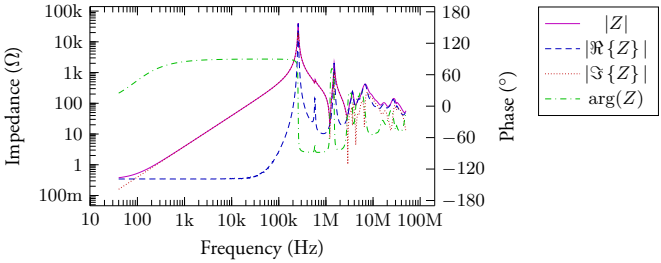

Figure B.5: Impedance of the dry x axis transmit coil of the MPIv3 system.

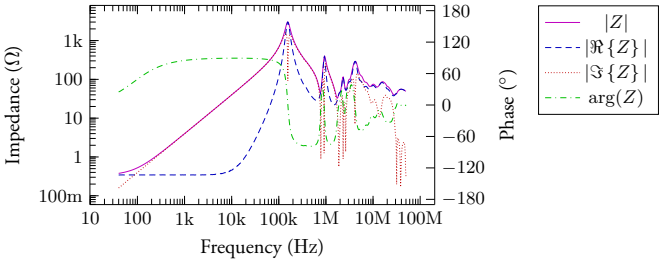

Figure B.6: Impedance of the MPIv3 system's x axis transmit coil submerged in water.

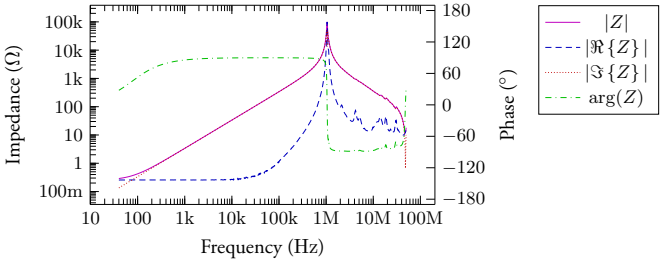

Figure B.7: Impedance of the dry y axis transmit coil of the MPIv3 system.

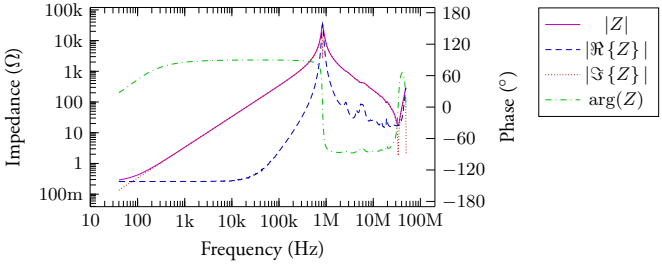

Figure B.8: Impedance of the MPIv3 system's y axis transmit coil submerged in water.

B.3 MPI Receive coils

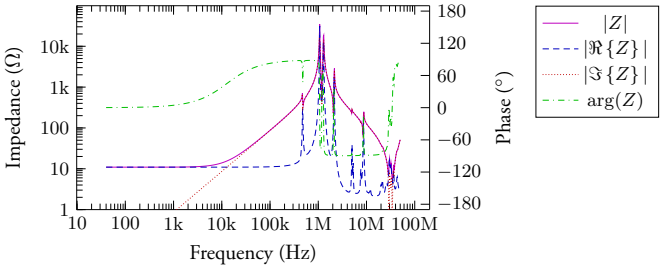

Figure B.9: Impedance of the x axis X1 receive coil (v1.1.1) of the MPIv3 system.

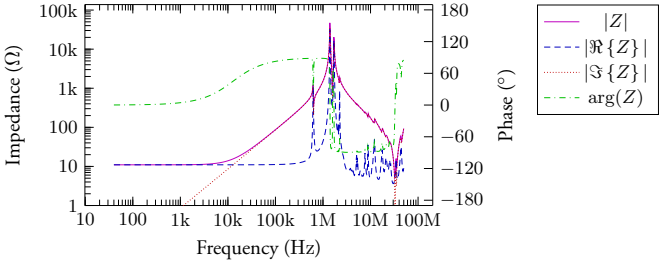

Figure B.10: Impedance of the x axis X2 receive coil (v1.1.1) of the MPIv3 system.

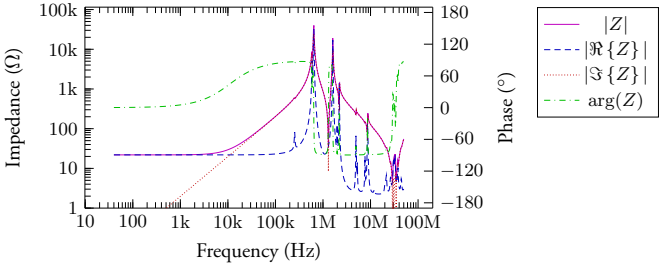

Figure B.11: Impedance of the x axis X1 and X2 receive coils (v1.1.1) wired for single ended detection designated X12.

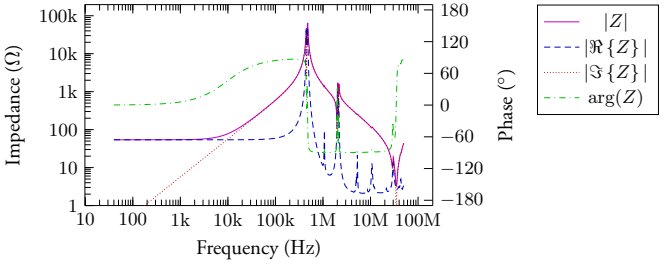

Figure B.12: Impedance of the y axis Y1 receive coil (v1.1.1) of the MPIv3 system.

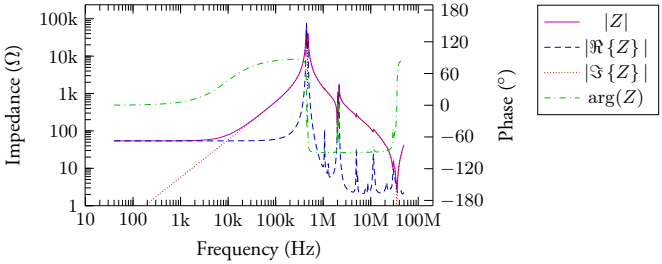

Figure B.13: Impedance of the y axis Y2 receive coil (v1.1.1) of the MPIv3 system.

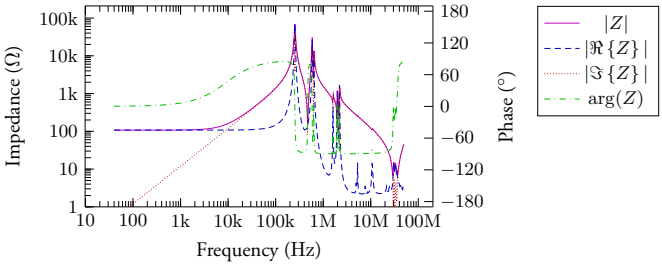

Figure B.14: Impedance of the y axis Y1 and Y2 receive coils (v1.1.1) wired for single ended detection designated Y12.

C Transfer functions

C.1 MPI transmit filters

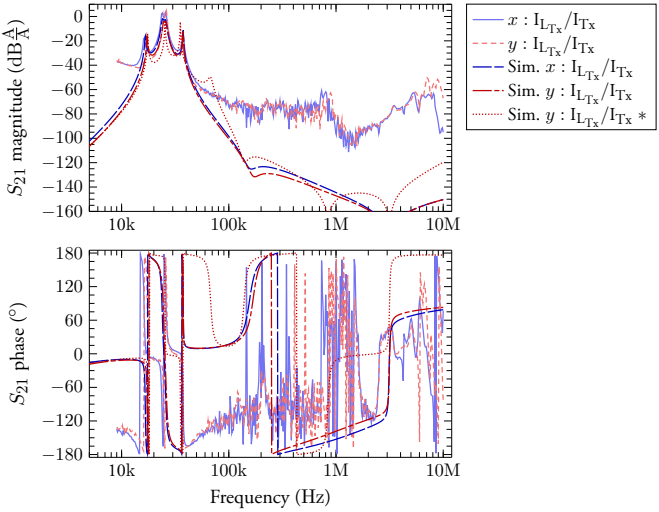

Figure C.15: Current transfer functions of the x and y axis transmit filters in comparison with simulation results. In contrast to the receive filters, deviations are visible because of the non-negligible inter-element coupling. Including additional element parasitics ($*$) without including cross-coupling does not significantly improve the prediction.

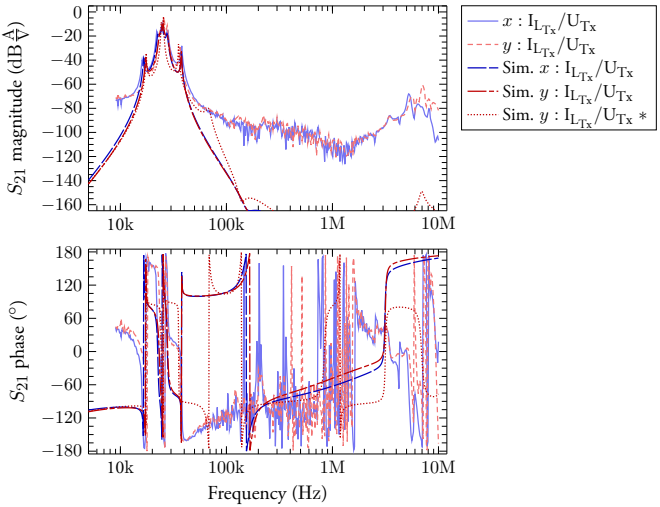

Figure C.16: Voltage-to-current transfer functions of the x and y axis transmit filters in comparison with simulation results. In contrast to the receive filters, deviations are visible because of the non-negligible inter-element coupling. Including additional element parasitics (∗) without including cross-coupling does not significantly improve the prediction.

D Field profiles

The following field profiles have been acquired either by measuring the excitation field strength by means of a small pickup coil with two perpendicular axes (figs. D.17 and D.18) or by driving a signal into the small coil and measuring the resulting receive signal (figs. D.19 and D.20). Only the main components are shown. For the excitation field, the orthogonal components are included in the maximum directional inhomogeneity (cf. tables 2.5 and 2.6).

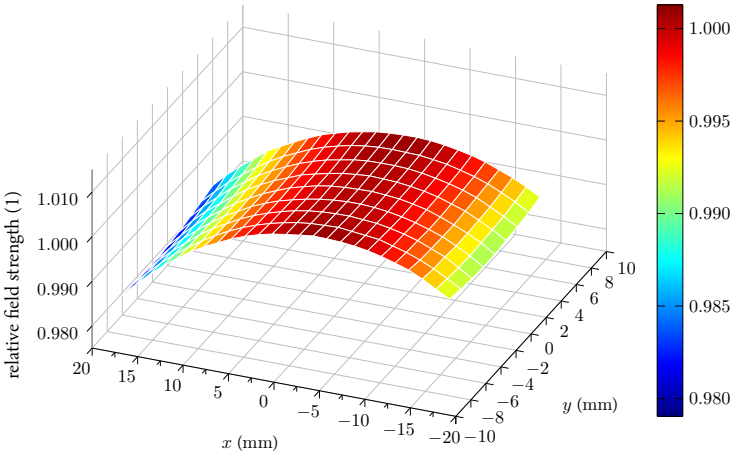

Figure D.17: Relative field strength of the x component of the x axis drive field in the imaging plane referred to the center point, measured at 25 kHz. Measurement range was $-16 \ldots 20$ mm in x and $-6 \ldots 6$ mm in y direction.

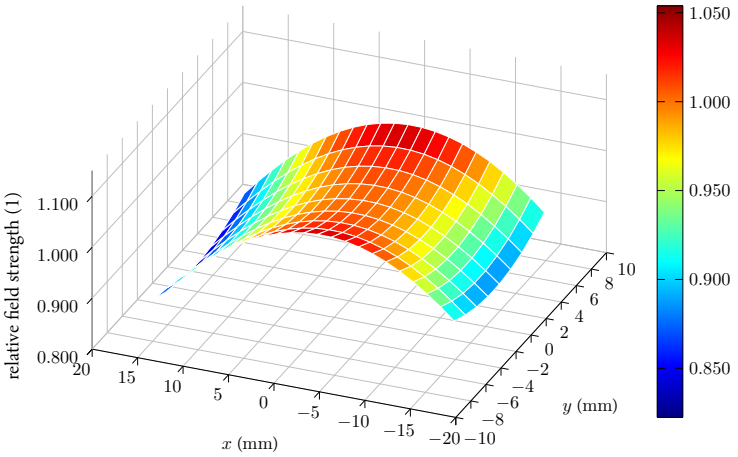

Figure D.18: Relative field strength of the y component of the y axis drive field in the imaging plane referred to the center point, measured at 25.64 kHz. Measurement range was $-16 \ldots 20$ mm in x and $-6 \ldots 6$ mm in y direction.

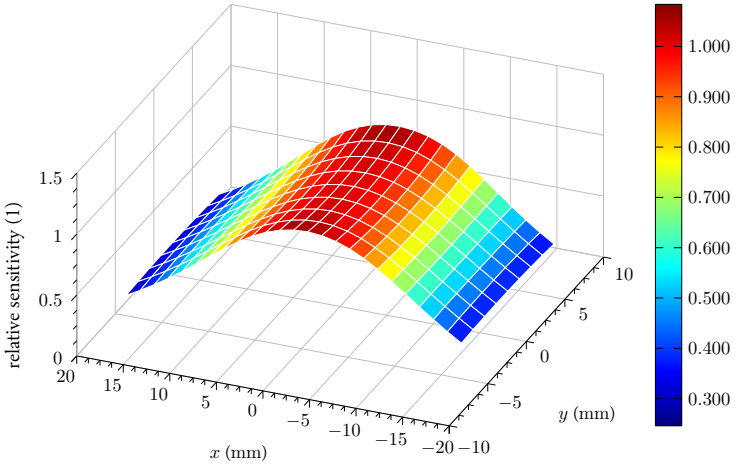

Figure D.19: Relative sensitivity of the x component of the x axis receive coil in the imaging plane referred to the center point, measured at 125 kHz, readout in differential configuration and measured after the fully differential amplifier. Measurement range was $-18 \ldots 18$ mm in x and $-6 \ldots 6$ mm in y direction, thus covering an area larger than the FOV.

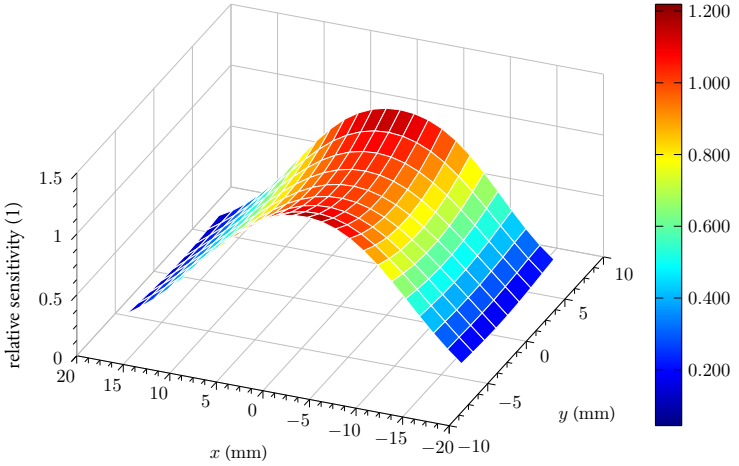

Figure D.20: Relative sensitivity of the y component of the y axis receive coil in the imaging plane referred to the center point, measured at 128.2 kHz, readout in single ended configuration. Measurement range was $-18 \ldots 18$ mm in x and $-6 \ldots 6$ mm in y direction, thus covering an area larger than the FOV.

E Spectra

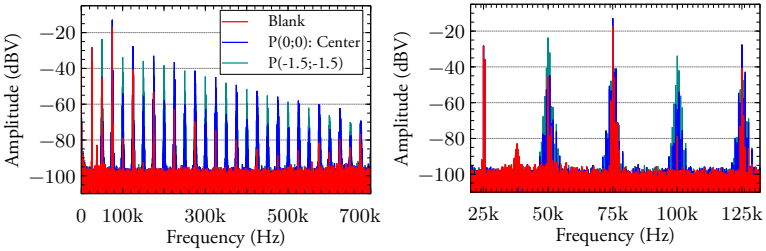

(a) Receive spectrum x (b) x spectrum detail

Figure E.21: Raw receive spectrum of the x axis for calibration sample #sp, which consisted of 22 µL FeraSpin XL at a concentration of 45 mmol/L. The graphic shows (a) a wideband view and (b) a detail of the receive spectrum at the center point and a point 1.5 mm on each axis from it. The raw blank spectrum is also shown.

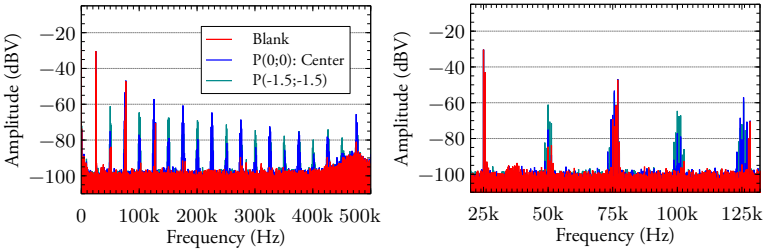

(a) Receive spectrum y (b) y spectrum detail

Figure E.22: Raw receive spectrum of the y axis for calibration sample #sp, which consisted of 22 µL FeraSpin XL at a concentration of 45 mmol/L. The graphic shows (a) a wideband view and (b) a detail of the receive spectrum at the center point and a point 1.5 mm on each axis from it. The raw blank spectrum is also shown.

List of Figures

List of Tables

References

[1] B. Gleich and J. Weizenecker, "Tomographic imaging using the nonlinear response of magnetic particles", *Nature*, vol. 435, p. 1214, Jun. 2005. DOI: 10.1038/nature03808 (pages 1, 58, 60).

[2] B. Gleich, J. Weizenecker, and J. Borgert, "Experimental results on fast 2D-encoded magnetic particle imaging", *Physics in Medicine & Biology*, vol. 53, no. 6, N81, 2008 (page 1).

[3] J. Rahmer, B. Gleich, C. Bontus, I. Schmale, J. Schmidt, J. Kanzenbach, O. Woywode, J. Weizenecker, and J. Borgert, "Rapid 3D in vivo magnetic particle imaging with a large field of view", in *Proc Intl Soc Mag Reson Med*, vol. 19, 2011, p. 3285 (page 1).

[4] B. Zheng, M. P. von See, E. Yu, B. Gunel, K. Lu, T. Vazin, D. V. Schaffer, P. W. Goodwill, and S. M. Conolly, "Quantitative Magnetic Particle Imaging Monitors the Transplantation, Biodistribution, and Clearance of Stem Cells In Vivo", *Theranostics*, vol. 6, no. 3, pp. 291–301, 2016. DOI: 10.7150/thno.13728 (page 1).

[5] J. Wells, H. Paysen, O. Kosch, N. Lowa, F. Schmitzberger, M. Makowksi, J. Franke, L. Trahms, and F. Wiekhorst, "Characterizing a Preclinical Magnetic Particle Imaging System With Separate Pickup Coil", *IEEE Transactions on Magnetics*, vol. 53, no. 11, pp. 1–5, Nov. 2017. DOI: 10.1109/tmag.2017.2708419 (page 1).

[6] J. Weizenecker, B. Gleich, J. Rahmer, H. Dahnke, and J. Borgert, "Three-dimensional real-timein vivomagnetic particle imaging", *Physics in Medicine and Biology*, vol. 54, no. 5, pp. L1–L10, Feb. 2009. DOI: 10.1088/0031-9155/54/5/l01 (page 1).

[7] B. Zheng, T. Vazin, W. Yang, P. W. Goodwill, E. U. Saritas, L. R. Croft, D. V. Schaffer, and S. M. Conolly, "Quantitative stem cell imaging with magnetic particle imaging", in *2013 International Workshop on Magnetic Particle Imaging (IWMPI)*, Mar. 2013, pp. 1–1. DOI: 10.1109/IWMPI.2013.6528323 (page 1).

[8] Q. A. Pankhurst, J. Connolly, S. K. Jones, and J. Dobson, "Applications of magnetic nanoparticles in biomedicine", *Journal of Physics D: Applied Physics*, vol. 36, no. 13, R167, 2003 (page 1).

[9] R. Hao, R. Xing, Z. Xu, Y. Hou, S. Gao, and S. Sun, "Synthesis, Functionalization, and Biomedical Applications of Multifunctional Magnetic Nanoparticles", *Advanced Materials*, vol. 22, no. 25, pp. 2729–2742, May 2010. DOI: 10.1002/adma.201000260 (page 1).

[10] I. Hilger, R. Hiergeist, R. Hergt, K. Winnefeld, H. Schubert, and W. A. Kaiser, "Thermal Ablation of Tumors Using Magnetic Nanoparticles: An In Vivo Feasibility Study", *Investigative Radiology*, vol. 37, no. 10, pp. 580–586, 2002, ISSN: 0020-9996 (page 1).

[11] A. Hofmann, D. Wenzel, U. M. Becher, D. F. Freitag, A. M. Klein, D. Eberbeck, M. Schulte, K. Zimmermann, C. Bergemann, B. Gleich, W. Roell, T. Weyh, L. Trahms, G. Nickenig, B. K. Fleischmann, and A. Pfeifer, "Combined targeting of lentiviral vectors and positioning of transduced cells by magnetic nanoparticles", *Proceedings of the National Academy of Sciences*, vol. 106, no. 1, pp. 44–49, Dec. 2008. DOI: 10.1073/pnas.0803746106 (page 1).

[12] Y.-F. Huang, Y.-F. Wang, and X.-P. Yan, "Amine-Functionalized Magnetic Nanoparticles for Rapid Capture and Removal of Bacterial Pathogens", *Environmental Science & Technology*, vol. 44, no. 20, pp. 7908–7913, 2010, PMID: 20866050. DOI: 10.1021/es102285n (page 1).

[13] M. Koneracka, P. Kopcansky, M. Antalik, M. Timko, C. Ramchand, D. Lobo, R. Mehta, and R. Upadhyay, "Immobilization of proteins and enzymes to fine magnetic particles", *Journal of Magnetism and Magnetic Materials*, vol. 201, no. 1, pp. 427–430, 1999 (page 1).

[14] Y. R. Chemla, H. L. Grossman, Y. Poon, R. McDermott, R. Stevens, M. D. Alper, and J. Clarke, "Ultrasensitive magnetic biosensor for homogeneous immunoassay", *Proceedings of the National Academy of Sciences*, vol. 97, no. 26, pp. 14 268–14 272, 2000. DOI: 10.1073/pnas.97.26.14268 (page 1).

[15] D. M. Bruls, T. H. Evers, J. A. H. Kahlman, P. J. W. van Lankvelt, M. Ovsyanko, E. G. M. Pelssers, J. J. H. B. Schleipen, F. K. de Theije, C. A. Verschuren, T. van der Wijk, J. B. A. van Zon, W. U. Dittmer, A. H. J. Immink, J. H. Nieuwenhuis, and M. W. J. Prins, "Rapid integrated biosensor for multiplexed immunoassays based on actuated magnetic nanoparticles", *Lab on a Chip*, vol. 9, no. 24, p. 3504, 2009. DOI: 10.1039/b913960e (page 1).

[16] J. Dieckhoff, A. Lak, M. Schilling, and F. Ludwig, "Protein detection with magnetic nanoparticles in a rotating magnetic field", *Journal of Applied Physics*, vol. 115, no. 2, p. 024 701, Jan. 2014. DOI: 10.1063/1.4861032 (page 2).

[17] T. Viereck, "Magnetic Particle Imaging - Applications of magnetic nanoparticles for analytics and imaging", PhD thesis, Berlin, Dec. 2016 (pages 2, 21, 23–25, 59, 111, 121, 129, 171).

[18] G. C. Papaefthymiou, "Nanoparticle magnetism", *Nano Today*, vol. 4, no. 5, pp. 438–447, Oct. 2009. DOI: 10.1016/j.nantod.2009.08.006 (pages 3–5).

[19] Y. L. Raĭkher and M. I. Shliomis, "The Effective Field Method in the Orientational Kinetics of Magnetic Fluids and Liquid Crystals", in *Advances in Chemical Physics*. John Wiley & Sons, Inc., 2007, pp. 595–751, ISBN: 9780470141465. DOI: 10.1002/9780470141465.ch8 (pages 3, 7–9).

[20] S. Bedanta and W. Kleemann, "Supermagnetism", *Journal of Physics D: Applied Physics*, vol. 42, no. 1, p. 013 001, Dec. 2008. DOI: 10.1088/0022-3727/42/1/013001 (pages 4, 6–7).

[21] D. Dickson, N. Reid, C. Hunt, H. Williams, M. El-Hilo, and K. O'Grady, "Determination of f0 for fine magnetic particles", *Journal of Magnetism and Magnetic Materials*, vol. 125, no. 3, pp. 345–350, Aug. 1993. DOI: 10.1016/0304-8853(93)90109-f (page 4).

[22] A. Lak, M. Kraken, F. Ludwig, A. Kornowski, D. Eberbeck, S. Sievers, F. J. Litterst, H. Weller, and M. Schilling, "Size dependent structural and magnetic properties of FeO-Fe3O4 nanoparticles", *Nanoscale*, vol. 5, pp. 12 286–12 295, 24 2013. DOI: 10.1039/C3NR04562E (page 5).

[23] C. G. Granqvist and R. A. Buhrman, "Ultrafine metal particles", *Journal of Applied Physics*, vol. 47, no. 5, pp. 2200–2219, 1976. DOI: 10.1063/1.322870 (page 6).

[24] L. B. Kiss, J. Söderlund, G. A. Niklasson, and C. G. Granqvist, "New approach to the origin of lognormal size distributions of nanoparticles", *Nanotechnology*, vol. 10, no. 1, p. 25, 1999 (page 6).

[25] S. Sarangi, I. C. Tan, and A. Brazdeikis, "Brownian Relaxation of Interacting Magnetic Nanoparticles in a Colloid Subjected to a Pulsatile Magnetic Field", *Journal of Nanoscience and Nanotechnology*, vol. 11, no. 5, pp. 4136–4141, May 2011. DOI: 10.1166/jnn.2011.4112 (page 6).

[26] M. A. Leontovich, "Introduction to thermodynamics. Statistical physics", *Nauka, Moscow*, 1983 (1st ed., 1944), Chapter 3 (page 8).

[27] L. R. Croft, P. W. Goodwill, and S. M. Conolly, "Relaxation in X-Space Magnetic Particle Imaging", *IEEE Transactions on Medical Imaging*, vol. 31, no. 12, pp. 2335–2342, Dec. 2012, ISSN: 0278-0062. DOI: 10.1109/TMI.2012.2217979 (pages 10, 17, 19).

[28] J. Rahmer, J. Weizenecker, B. Gleich, and J. Borgert, "Signal encoding in magnetic particle imaging: properties of the system function", *BMC Medical Imaging*, vol. 9, no. 1, p. 4, 2009, ISSN: 1471-2342. DOI: 10.1186/1471-2342-9-4 (pages 12–13, 15).

[29] P. W. Goodwill and S. M. Conolly, "The X-Space Formulation of the Magnetic Particle Imaging Process: 1-D Signal, Resolution, Bandwidth, SNR, SAR, and Magnetostimulation", *IEEE Transactions on Medical Imaging*, vol. 29, no. 11, pp. 1851–1859, Nov. 2010, ISSN: 0278-0062. DOI: 10.1109/TMI.2010.2052284 (pages 14, 17).

[30] M. Storath, C. Brandt, M. Hofmann, T. Knopp, J. Salamon, A. Weber, and A. Weinmann, "Edge Preserving and Noise Reducing Reconstruction for Magnetic Particle Imaging", *IEEE Transactions on Medical Imaging*, vol. 36, no. 1, pp. 74–85, Jan. 2017, ISSN: 0278-0062. DOI: 10.1109/TMI.2016.2593954 (page 16).

[31] W. H. Press, S. A. Teukolsky, W. T. Vetterling, and B. P. Flannery, *Numerical Recipes 3rd Edition: The Art of Scientific Computing*, 3rd ed. Cambridge University Press, 2007, ISBN: 0521880688 (page 16).

[32] R. Bulirsch and J. Stoer, *Introduction to Numerical Analysis*. Springer, Dec. 1, 2010, 764 pp., ISBN: 144193006X (page 16).

[33] A. Zouzias and N. M. Freris, "Randomized Extended Kaczmarz for Solving Least Squares", *SIAM Journal on Matrix Analysis and Applications*, vol. 34, no. 2, pp. 773–793, 2013. DOI: 10.1137/120889897 (page 16).

[34] T. Knopp, S. Biederer, T. F. Sattel, J. Rahmer, J. Weizenecker, B. Gleich, J. Borgert, and T. M. Buzug, "2D model-based reconstruction for magnetic particle imaging", *Medical Physics*, vol. 37, no. 2, pp. 485–491, 2010, ISSN: 2473-4209. DOI: 10.1118/1.3271258 (page 17).

[35] J. Rahmer, J. Weizenecker, B. Gleich, and J. Borgert, "Analysis of a 3-D System Function Measured for Magnetic Particle Imaging", *IEEE Transactions on Medical Imaging*, vol. 31, no. 6, pp. 1289–1299, Jun. 2012, ISSN: 0278-0062. DOI: 10.1109/TMI.2012.2188639 (page 17).

[36] T. Wawrzik, C. Kuhlmann, F. Ludwig, and M. Schilling, *Scanner setup and reconstruction for three-dimensional magnetic particle imaging*, 2013. DOI: 10.1117/12.2006392 (page 17).

[37] T. Knopp, C. Kaethner, M. Ahlborg, and T. M. Buzug, "X-Space and Chebyshev Reconstruction in Magnetic Particle Imaging", in *International Workshop on Magnetic Particle Imaging*, Infinite Science Publishing, 2016, p. 75 (page 17).

[38] P. W. Goodwill and S. M. Conolly, "Multidimensional X-Space Magnetic Particle Imaging", *IEEE Transactions on Medical Imaging*, vol. 30, no. 9, pp. 1581–1590, Sep. 2011, ISSN: 0278-0062. DOI: 10.1109/TMI.2011.2125982 (page 17).

[39] Z. W. Tay, D. W. Hensley, E. C. Vreeland, B. Zheng, and S. M. Conolly, "The relaxation wall: experimental limits to improving MPI spatial resolution by increasing nanoparticle core size", *Biomedical Physics & Engineering Express*, vol. 3, no. 3, p. 035 003, 2017 (page 17).

[40] L. R. Croft, P. W. Goodwill, J. J. Konkle, H. Arami, D. A. Price, A. X. Li, E. U. Saritas, and S. M. Conolly, "Low drive field amplitude for improved image resolution in magnetic particle imaging", *Medical Physics*, vol. 43, no. 1, pp. 424–435, 2016, ISSN: 2473-4209. DOI: 10.1118/1.4938097 (page 19).

[41] E. A. Heim, "Fluxgate-Magnetrelaxometrie magnetischer Nanopartikel in der Bioanalytik", PhD thesis, Berlin, Sep. 2009 (page 22).

[42] J. H. Dieckhoff, "Magnetic Nanoparticles in Rotating Magnetic Fields", PhD thesis, Berlin, Nov. 2015 (page 22).

[43] J. Dieckhoff, D. Eberbeck, M. Schilling, and F. Ludwig, "Magnetic-field dependence of Brownian and Néel relaxation times", *Journal of Applied Physics*, vol. 119, no. 4, p. 043 903, 2016. DOI: 10.1063/1.4940724 (page 22).

[44] T. Yoshida and K. Enpuku, "Simulation and Quantitative Clarification of AC Susceptibility of Magnetic Fluid in Nonlinear Brownian Relaxation Region", *Japanese Journal of Applied Physics*, vol. 48, no. 12R, p. 127 002, 2009 (page 22).

[45] T. Wawrzik, C. Kuhlmann, F. Ludwig, and M. Schilling, "Estimating particle mobility in MPI", in *2013 International Workshop on Magnetic Particle Imaging (IWMPI)*, Mar. 2013, pp. 1–1. DOI: 10.1109/IWMPI.2013.6528372 (page 25).

[46] S. A. Shah, R. M. Ferguson, and K. M. Krishnan, "Slew-rate dependence of tracer magnetization response in magnetic particle imaging", *Journal of Applied Physics*, vol. 116, no. 16, p. 163 910, 2014. DOI: 10.1063/1.4900605 (page 25).

[47] J. Rahmer, A. Halkola, B. Gleich, I. Schmale, and J. Borgert, "First experimental evidence of the feasibility of multi-color magnetic particle imaging", *Physics in Medicine & Biology*, vol. 60, no. 5, p. 1775, 2015 (pages 26, 161).

[48] T. Viereck, C. Kuhlmann, S. Draack, M. Schilling, and F. Ludwig, "Dual-frequency magnetic particle imaging of the Brownian particle contribution", *Journal of Magnetism and Magnetic Materials*, vol. 427, pp. 156–161, 2017, ISSN: 0304-8853. DOI: 10.1016/j.jmmm.2016.11.003 (pages 26, 161).

[49] D. Hensley, P. Goodwill, L. Croft, and S. Conolly, "Preliminary experimental X-space color MPI", in *2015 5th International Workshop on Magnetic Particle Imaging (IWMPI)*, Mar. 2015, pp. 1–1. DOI: 10.1109/IWMPI.2015.7106993 (page 26).

[50] P. Horowitz and W. Hill, *The Art of Electronics*. Cambridge University Pr., Apr. 2, 2015, ISBN: 0521809266 (page 27).

[51] W. Kester, *Data Conversion Handbook*, A. D. Inc, Ed. Newnes, Dec. 11, 2004, 976 pp., ISBN: 0750678410 (page 28).

[52] B. Seguin, J. Gosse, A. Sylvestre, P. Fouassier, and J. Ferrieux, "Calorimetric apparatus for measurement of power losses in capacitors", in *IMTC/98 Conference Proceedings. IEEE Instrumentation and Measurement Technology Conference. Where Instrumentation is Going (Cat. No.98CH36222)*, IEEE. DOI: 10.1109/imtc.1998.679863 (page 28).

[53] K. S. Cole and R. H. Cole, "Dispersion and Absorption in Dielectrics I. Alternating Current Characteristics", *The Journal of Chemical Physics*, vol. 9, no. 4, pp. 341–351, Apr. 1941. DOI: 10.1063/1.1750906 (page 28).

[54] J. F. Gómez-Aguilar, J. E. Escalante-Martínez, C. Calderón-Ramón, L. J. Morales-Mendoza, M. Benavidez-Cruz, and M. Gonzalez-Lee, "Equivalent Circuits Applied in Electrochemical Impedance Spectroscopy and Fractional Derivatives with and without Singular Kernel", *Advances in Mathematical Physics*, vol. 2016, pp. 1–15, 2016. DOI: 10.1155/2016/9720181 (pages 28, 32).

[55] R. A. Pease, "Understand capacitor soakage to optimize analog systems", *Elect. Design News Mag.*, vol. 27 (20), pp. 125–129. 1982 (page 28).

[56] ——, "What's all this soakage stuff, Anyhow?", *Elect. Design News Mag.*, vol. 11, no. 46, pp. 125–128, 1998 (page 28).

[57] J. C. Kuenen and G. C. M. Meijer, "Measurement of dielectric absorption of capacitors and analysis of its effects on VCOs", *IEEE Transactions on Instrumentation and Measurement*, vol. 45, no. 1, pp. 89–97, Feb. 1996, ISSN: 0018-9456. DOI: 10.1109/19.481317 (page 28).

[58] J. Prymak, M. Randall, P. Blais, and B. Long, "Why that 47 uF capacitor drops to 37 uF, 30 uF, or lower", in *Proc. of the CARTS USA Conference*, 2008 (page 28).

[59] B. Zheng, P. Goodwill, W. Yang, and S. Conolly, "Capacitor Distortion in Magnetic Particle Imaging", in *Springer Proceedings in Physics*, Springer Berlin Heidelberg, 2012, pp. 319–324. DOI: 10.1007/978-3-642-24133-8_51 (page 28).

[60] M. Horák and P. Mach, "Study of electrical ageing of polypropylene film capacitors using third harmonics measurement", in *2014 IEEE 20th International Symposium for Design and Technology in Electronic Packaging (SIITME)*, Oct. 2014, pp. 55–59. DOI: 10.1109/SIITME.2014.6966994 (page 28).

[61] M. van der Veen and H. van Maanen, "Non-linear distortions in capacitors", in *Audio Engineering Society Convention 124*, Audio Engineering Society, 2008 (page 28).

[62] H. Haruta, *The impedance measurement handbook: a guide to measurement technology and techniques*. Agilent Technologies, 2000 (page 29).

[63] S. Kim and D. P. Neikirk, "Compact equivalent circuit model for the skin effect", in *1996 IEEE MTT-S International Microwave Symposium Digest*, vol. 3, Jun. 1996, 1815–1818 vol.3. DOI: 10.1109/MWSYM.1996.512297 (pages 30, 38).

[64] X. Nan and C. R. Sullivan, "An Equivalent Complex Permeability Model for Litz-Wire Windings", *IEEE Transactions on Industry Applications*, vol. 45, no. 2, pp. 854–860, Mar. 2009, ISSN: 0093-9994. DOI: 10.1109/TIA.2009.2013594 (page 30).

[65] D. C. Meeker, "Finite Element Method Magnetics, Version 4.2", Tech. Rep., 2012 (page 30).

[66] K. B. Baltzis, "The FEMM Package: A Simple, Fast, and Accurate Open Source Electromagnetic Tool in Science and Engineering", *Journal of Engineering Science and Technology Review*, vol. 1, pp. 83–89, 2008 (pages 30, 64).

[67] G. Dehmel, "Magnetic Field Sensors: Induction Coil (Search Coil) Sensors", in *Sensors Set*. Wiley-VCH Verlag GmbH, 2008, pp. 205–253, ISBN: 9783527619269. DOI: 10.1002/9783527619269.ch6d (pages 32, 119).

[68] Q. Yu and T. W. Holmes, "A study on stray capacitance modeling of inductors by using the finite element method", *IEEE Transactions on Electromagnetic Compatibility*, vol. 43, no. 1, pp. 88–93, Feb. 2001, ISSN: 0018-9375. DOI: 10.1109/15.917948 (pages 33, 35).

[69] A. Massarini and M. K. Kazimierczuk, "Self-capacitance of inductors", *IEEE Transactions on Power Electronics*, vol. 12, no. 4, pp. 671–676, Jul. 1997, ISSN: 0885-8993. DOI: 10.1109/63.602562 (pages 33, 35–36, 93).

[70] C. E. G. Salmon, E. L. G. Vidoto, M. J. Martins, and A. Tannús, "Optimization of saddle coils for magnetic resonance imaging",
Brazilian Journal of Physics, vol. 36, no. 1a, Mar. 2006. DOI: 10.1590/s0103-97332006000100004 (page 34).

[71] I. F. Kovačević, T. Friedli, A. M. Müsing, and J. W. Kolar, "3-D Electromagnetic Modeling of Parasitics and Mutual Coupling in EMI Filters", *IEEE Transactions on Power Electronics*, vol. 29, no. 1, pp. 135–149, Jan. 2014, ISSN: 0885-8993. DOI: 10.1109/TPEL.2013.2254130 (page 35).

[72] G. Grandi, M. K. Kazimierczuk, A. Massarini, and U. Reggiani, "Stray capacitances of single-layer solenoid air-core inductors", *IEEE Transactions on Industry Applications*, vol. 35, no. 5, pp. 1162–1168, Sep. 1999, ISSN: 0093-9994. DOI: 10.1109/28.793378 (pages 35, 37–38, 93, 96).

[73] M. Hole and L. Appel, "Stray capacitance of a two-layer air-cored inductor", *IEE Proceedings - Circuits, Devices and Systems*, vol. 152, no. 6, p. 565, 2005. DOI: 10.1049/ip-cds:20045217 (pages 35–37, 93).

[74] C. Kuhlmann, S. Draack, T. Viereck, M. Schilling, and F. Ludwig, "Modeling the impedance of water-cooled core-less multi-layered solenoid coils for MPI drive field generation", *International Journal on Magnetic Particle Imaging*, vol. 4, no. 1, Apr. 2018, ISSN: 2365-9033. DOI: 10.18416/ijmpi.2018.1804001 (pages 36, 93–94, 99).

[75] E. B. Rosa and F. W. Grover, "Formulas and tables for the calculation of mutual and self inductance.(Revised.)", *Journal of the Washington Academy of Sciences*, vol. 1, no. 1/2, pp. 14–16, 1911 (page 36).

[76] R. Dengler, "Self inductance of a wire loop as a curve integral", *ArXiv e-prints*, Apr. 2012 (page 36).

[77] J. C. Maxwell, "A Treatise on Electricity and Magnetism, third ed. Clarendon Press, Berlin", in. Clarendon Press, 1891, vol. II, ch. XIV. Circular currents (pages 36, 86).

[78] A. Reatti and F. Grasso, "Solid and Litz-wire winding non-linear resistance comparison", in *Proceedings of the 43rd IEEE Midwest Symposium on Circuits and Systems (Cat.No.CH37144)*, vol. 1, 2000, 466–469 vol.1. DOI: 10.1109/MWSCAS.2000.951684 (page 37).

[79] M. Bartoli, N. Noferi, A. Reatti, and M. K. Kazimierczuk, "Modelling Winding Losses in High-Frequency Power Inductors", *Journal of Circuits, Systems and Computers*, vol. 05, no. 04, pp. 607–626, 1995. DOI: 10.1142/S0218126695000370 (page 37).

[80] M. Abramowitz and I. Stegun, *Handbook of Mathematical Functions with Formulas, Graphs, and Mathematical Tables*, ser. A Wiley-Interscience publication. Wiley, 1972, ISBN: 9780471800071 (page 37).

[81] A. E. Ruehli, "Equivalent Circuit Models for Three-Dimensional Multiconductor Systems", *IEEE Transactions on Microwave Theory and Techniques*, vol. 22, no. 3, pp. 216–221, Mar. 1974, ISSN: 0018-9480. DOI: 10.1109/TMTT.1974.1128204 (pages 37, 95).

[82] K. L. Su, *Analog Filters*. Springer, Apr. 30, 2002, 428 pp., ISBN: 1402070330 (pages 41, 44–52).

[83] P. Starič and E. Margan, Eds., *Wideband Amplifiers*. Springer Nature, 2006. DOI: 10.1007/978-0-387-28341-8 (pages 41–42).

[84] S. Butterworth, "On the theory of filter amplifiers", *Experimental wireless & the Wireless Engineer*, vol. 7, no. 6, pp. 536–541, 1930 (page 44).

[85] G. Doetsch, *Introduction to the Theory and Application of the Laplace Transformation*. Springer, Nov. 12, 2011, 340 pp., ISBN: 3642656927 (page 44).

[86] L. Storch, "Synthesis of Constant-Time-Delay Ladder Networks Using Bessel Polynomials", *Proceedings of the IRE*, vol. 42, no. 11, pp. 1666–1675, Nov. 1954. DOI: 10.1109/jrproc.1954.274662 (pages 44–45).

[87] A. Casson and E. Rodriguez-Villegas, "A Review and Modern Approach to LC Ladder Synthesis", *Journal of Low Power Electronics and Applications*, vol. 1, no. 3, pp. 20–44, Jan. 2011. DOI: 10.3390/jlpea1010020 (pages 45, 51, 53).

[88] M. Van Valkenburg, *Analog Filter Design*, ser. HRW series in Electrical and Computer Engineering. Saunders College Publishing, Mar. 1982, ISBN: 9780030592461 (pages 50, 52).

[89] F.-N. Ku, C.-H. Liao, M.-K. Tsay, C.-S. Shyn, and T.-Y. Yang, "Complete LC Ladder Bessel Filter Tabulation", in *MILCOM 2007 - IEEE Military Communications Conference*, IEEE, Oct. 2007. DOI: 10.1109/milcom.2007.4454737 (pages 53, 106).

[90] C. J. Savant, "How to Design Notch Networks", in, e. a. Mac Donald ed., Ed. New York: McGraw-Hill Book Company, Inc, 1953, vol. 7, pp. 242–245, Savant, C. J.: "How to Design Notch Networks," Electronics Engineering Manual, McGraw-Hill Book Company, Inc., vol. 7, pp. 242-245, New York, 1953. (page 53).

[91] C. D. Motchenbacher and J. A. Connelly, *Low-Noise Electronic System Design*. JOHN WILEY & SONS INC, Jun. 11, 1993, 422 pp., ISBN: 0471577421 (page 56).

[92] B. R. Archambeault and J. Drewniak, *PCB Design for Real-World EMI Control (The Springer International Series in Engineering and Computer Science)*. Springer, 2013, ISBN: 978-1-4020-7130-0 (pages 56, 110).

[93] J. Weibler and L. R. Enclosures, "Properties of Metals used for RF shielding", *EMC Test and Design*, p. 100, 1993 (page 57).

[94] J. Weizenecker, B. Gleich, and J. Borgert, "Magnetic particle imaging using a field free line", *Journal of Physics D: Applied Physics*, vol. 41, no. 10, p. 105 009, 2008 (page 58).

[95] T. Knopp, T. F. Sattel, S. Biederer, and T. M. Buzug, "Field-free line formation in a magnetic field", *Journal of Physics A: Mathematical and Theoretical*, vol. 43, no. 1, p. 012 002, Dec. 2009. DOI: 10.1088/1751-8113/43/1/012002 (page 58).

[96] T. Knopp, M. Erbe, T. F. Sattel, S. Biederer, and T. M. Buzug, "Generation of a static magnetic field-free line using two Maxwell coil pairs", *Applied Physics Letters*, vol. 97, no. 9, p. 092 505, Aug. 2010. DOI: 10.1063/1.3486118 (page 58).

[97] T. Knopp, M. Erbe, S. Biederer, T. F. Sattel, and T. M. Buzug, "Efficient generation of a magnetic field-free line", *Medical Physics*, vol. 37, no. 7Part1, pp. 3538–3540, Jun. 2010. DOI: 10.1118/1.3447726 (page 58).

[98] P. Vogel, M. A. Rückert, P. Klauer, W. H. Kullmann, P. M. Jakob, and V. C. Behr, "Traveling Wave Magnetic Particle Imaging", *IEEE Transactions on Medical Imaging*, vol. 33, no. 2, pp. 400–407, Feb. 2014, ISSN: 0278-0062. DOI: 10.1109/TMI.2013.2285472 (page 58).

[99] T. F. Sattel, T. Knopp, S. Biederer, B. Gleich, J. Weizenecker, J. Borgert, and T. M. Buzug, "Single-sided device for magnetic particle imaging", *Journal of Physics D: Applied Physics*, vol. 42, no. 2, p. 022 001, 2009 (pages 58–59).

[100] G. Bringout, K. Gräfe, and T. M. Buzug, "Performance and safety evaluation of a human sized FFL imager concept", in *2015 5th International Workshop on Magnetic Particle Imaging (IWMPI)*, Mar. 2015, pp. 1–1. DOI: 10.1109/IWMPI.2015.7107022 (page 58).

[101] J. Rahmer, B. Gleich, B. David, C. Bontus, I. Schmale, J. Schmidt, J. Weizenecker, O. Mende, O. Woywode, C. Vollertsen, T. Sattel, J. Gressmann, M. Heinrich, and J. Borgert, "3D line imaging on a clinical magnetic particle imaging demonstrator", in *2015 5th International Workshop on Magnetic Particle Imaging (IWMPI)*, Mar. 2015, pp. 1–1. DOI: 10.1109/IWMPI.2015.7107029 (page 58).

[102] J. Franke, U. Heinen, H. Lehr, A. Weber, F. Jaspard, W. Ruhm, M. Heidenreich, and V. Schulz, "First 3D dual modality phantom measurements of a hybrid MPI-MRI system using a resistive 12 channel MPI-MRI magnet design", in *2015 5th International Workshop on Magnetic Particle Imaging (IWMPI)*, Mar. 2015, pp. 1–1. DOI: 10.1109/IWMPI.2015.7106990 (page 58).

[103] ——, "System Characterization of a Highly Integrated Preclinical Hybrid MPI-MRI Scanner", *IEEE Transactions on Medical Imaging*, vol. 35, no. 9, pp. 1993–2004, Sep. 2016, ISSN: 0278-0062. DOI: 10.1109/TMI.2016.2542041 (page 58).

[104] P. Klauer, P. Vogel, M. A. Rückert, and V. C. Behr, "Bimodal TWMPI-MRI hybrid scanner - First NMR results", in *2015 5th International Workshop on Magnetic Particle Imaging (IWMPI)*, Mar. 2015, pp. 1–1. DOI: 10.1109/IWMPI.2015.7106987 (page 58).

[105] T. C. Kranemann, T. Ersepke, and G. Schmitz, "Towards the Integration of an MPI Compatible Ultrasound Transducer", *International Journal on Magnetic Particle Imaging*, vol. 3, no. 1, 2017, ISSN: 2365-9033 (page 58).

[106] C. Bontus, B. Gleich, B. David, O. Mende, and J. Borgert, "Concept of a Generator for the Selection and Focus Field of a Clinical MPI Scanner", *IEEE Transactions on Magnetics*, vol. 51, no. 2, pp. 1–4, Feb. 2015, ISSN: 0018-9464. DOI: 10.1109/TMAG.2014.2326003 (page 59).

[107] E. Y. Yu, P. W. Goodwill, and S. M. Conolly, "Preliminary characterization of a laminated iron-core 6.3 T/m FFL magnet", in *2015 5th International Workshop on Magnetic Particle Imaging (IWMPI)*, Mar. 2015, pp. 1–1. DOI: 10.1109/IWMPI.2015.7107023 (page 59).

[108] P. W. Goodwill, J. J. Konkle, B. Zheng, E. U. Saritas, and S. M. Conolly, "Projection X-Space Magnetic Particle Imaging", *IEEE Transactions on Medical Imaging*, vol. 31, no. 5, pp. 1076–1085, May 2012, ISSN: 0278-0062. DOI: 10.1109/TMI.2012.2185247 (page 59).

[109] M. Weber, M. Erbe, K. Bente, T. F. Sattel, and T. M. Buzug, "Power loss optimized field free line generation for magnetic particle imaging", in *2013 International Workshop on Magnetic Particle Imaging (IWMPI)*, Mar. 2013, pp. 1–1. DOI: 10.1109/IWMPI.2013.6528354 (pages 59, 83).

[110] C. Kuhlmann, T. Wawrzik, F. Ludwig, and M. Schilling, "A 3D MPI system for biological studies on mice", in *2013 International Workshop on Magnetic Particle Imaging (IWMPI)*, Mar. 2013, pp. 1–1. DOI: 10.1109/IWMPI.2013.6528373 (page 59).

[111] P. Goodwill, K. Lu, B. Zheng, and S. Conolly, "Water-cooled two-axis rigid excitation coil assembly", in *4th International Workshop on Magnetic Particle Imaging*, 2014 (pages 59, 83).

[112] I. Schmale, J. Rahmer, B. Gleich, J. Kanzenbach, J. D. Schmidt, C. Bontus, O. Woywode, and J. Borgert, "First phantom and in vivo MPI images with an extended field of view", in *Medical Imaging 2011: Biomedical Applications in Molecular, Structural, and Functional Imaging*, J. B. Weaver and R. C. Molthen, Eds., SPIE, Mar. 2011. DOI: 10.1117/12.877339 (page 59).

[113] K. Gräfe, A. von Gladiss, G. Bringout, M. Ahlborg, and T. M. Buzug, "2D Images Recorded With a Single-Sided Magnetic Particle Imaging Scanner", *IEEE Transactions on Medical Imaging*, vol. 35, no. 4, pp. 1056–1065, Apr. 2016, ISSN: 0278-0062. DOI: 10.1109/TMI.2015.2507187 (page 59).

[114] B. Zheng, P. Goodwill, and S. Conolly, "Transmit filter design methods for magnetic particle imaging", *Proc.SPIE*, vol. 7965, pp. 7965 - 7965 - 6, 2011. DOI: 10.1117/12.878443 (page 59).

[115] T. F. Sattel, O. Woywode, J. Weizenecker, J. Rahmer, B. Gleich, and J. Borgert, "Setup and Validation of an MPI Signal Chain for a Drive Field Frequency of 150 kHz", *IEEE Transactions on Magnetics*, vol. 51, no. 2, pp. 1–3, Feb. 2015, ISSN: 0018-9464. DOI: 10.1109/TMAG.2014.2326256 (pages 59–60).

[116] G. Bringout, "Field Free Line Magnetic Particle Imaging Characterisation and imaging device up-scaling", PhD thesis, Universität zu Lübeck, Oct. 2016. DOI: 10.5281/zenodo.162417 (pages 59, 77, 83).

[117] J. Stelzner, M. Graeser, A. Bakenecker, A. von Gladiss, G. Bringout, and T. M. Buzug, "Measurements Inside a Rabbit Sized FFL-MPI Device Using a Gradiometric Receive Coil", *International Journal on Magnetic Particle Imaging*, vol. 3, no. 1, 2017, ISSN: 2365-9033 (pages 59–60).

[118] B. Zheng, W. Yang, T. Massey, P. W. Goodwill, and S. M. Conolly, "High-power active interference suppression in magnetic particle imaging", in *2013 International Workshop on Magnetic Particle Imaging (IWMPI)*, Mar. 2013, pp. 1–1. DOI: 10.1109/IWMPI.2013.6528381 (pages 59, 122).

[119] M. Graeser, T. Knopp, M. Grüttner, T. F. Sattel, G. Bringout, W. Tenner, H. Wojtczyk, and T. M. Buzug, "Cancellation techniques for MPI", in *2013 International Workshop on Magnetic Particle Imaging (IWMPI)*, Mar. 2013, pp. 1–1. DOI: 10.1109/IWMPI.2013.6528331 (pages 59, 122).

[120] I. Schmale, B. Gleich, J. Schmidt, J. Rahmer, C. Bontus, R. Eckart, B. David, M. Heinrich, O. Mende, O. Woywode, J. Jokram, and J. Borgert, "Human PNS and SAR study in the frequency range from 24 to 162 kHz", in *2013 International Workshop on Magnetic Particle Imaging (IWMPI)*, Mar. 2013, pp. 1–1. DOI: 10.1109/IWMPI.2013.6528346 (pages 60, 152).

[121] E. U. Saritas, P. W. Goodwill, G. Z. Zhang, and S. M. Conolly, "Magnetostimulation Limits in Magnetic Particle Imaging", *IEEE Transactions on Medical Imaging*, vol. 32, no. 9, pp. 1600–1610, Sep. 2013. DOI: 10.1109/tmi.2013.2260764 (pages 60, 152).

[122] F. Ludwig, D. Eberbeck, N. Löwa, U. Steinhoff, T. Wawrzik, M. Schilling, and L. Trahms, "Characterization of magnetic nanoparticle systems with respect to their magnetic particle imaging performance", *Biomedizinische Technik/Biomedical Engineering*, vol. 58, no. 6, Jan. 2013. DOI: 10.1515/bmt-2013-0013 (page 60).

[123] K. Murase, S. Hiratsuka, R. Song, and Y. Takeuchi, "Development of a system for magnetic particle imaging using neodymium magnets and gradiometer", *Japanese Journal of Applied Physics*, vol. 53, no. 6, p. 067 001, 2014 (page 60).

[124] I. Schmale, B. Gleich, J. Kanzenbach, J. Rahmer, J. Schmidt, J. Weizenecker, and J. Borgert, "An Introduction to the Hardware of Magnetic Particle Imaging", in *IFMBE Proceedings*, Springer Berlin Heidelberg, 2009, pp. 450–453. DOI: 10.1007/978-3-642-03879-2_127 (page 60).

[125] J. B. Weaver, A. M. Rauwerdink, C. R. Sullivan, and I. Baker, "Frequency distribution of the nanoparticle magnetization in the presence of a static as well as a harmonic magnetic field", *Medical Physics*, vol. 35, no. 5, pp. 1988–1994, 2008, ISSN: 2473-4209. DOI: 10.1118/1.2903449 (page 62).

[126] S. Biederer, T. Knopp, T. F. Sattel, K. Lüdtke-Buzug, B. Gleich, J. Weizenecker, J. Borgert, and T. M. Buzug, "Magnetization response spectroscopy of superparamagnetic nanoparticles for magnetic particle imaging", *Journal of Physics D: Applied Physics*, vol. 42, no. 20, p. 205 007, 2009 (page 62).

[127] A. C. Fraser-Smith, "The Magnetic Field Gradiometer", Stanford Electronics Labs. Office of Naval Technology/Naval Postgraduate School, Tech. Rep. E723-1, Contract N002228-81-C-AB56, Feb. 1983 (page 62).

[128] M. Graeser, A. von Gladiss, M. Weber, and T. M. Buzug, "Two dimensional magnetic particle spectrometry", *Physics in Medicine & Biology*, vol. 62, no. 9, p. 3378, 2017 (page 62).

[129] T. Wawrzik, J. Hahn, F. Ludwig, and M. Schilling, "Magnetic particle spectroscopy for the evaluation of field-dependent harmonics generation", in *Magnetic Nanoparticles: Particle Science, Imaging Technology, and Clinical Applications: Proceedings of the First International Workshop on Magnetic Particle Imaging*, World Scientific, 2010, p. 86 (page 64).

[130] C. R. Sullivan, "Optimal choice for number of strands in a litz-wire transformer winding", *IEEE Transactions on Power Electronics*, vol. 14, no. 2, pp. 283–291, Mar. 1999, ISSN: 0885-8993. DOI: 10.1109/63.750181 (page 64).

[131] J. Lammeraner and M. Štafl, *Eddy Currents*, Translated by Miloš Štafl, G. A. Toombs, Ed. Iliffe Books Ltd., London SNTL, Prague, 1966 (page 64).

[132] Agilent, *Agilent 4294A Precision Impedance Analyzer Data Sheet*, 5968-3809E, Agilent Technologies, Santa Rosa, CA, USA, 2008 (page 68).

[133] *7224 Operator's Manual*, 574.295.9495, AE Techron, Inc., 2507 Warren Street Elkhart, IN 46516 U.S.A., 2012 (page 68).

[134] C. Kuhlmann, A. P. Khandhar, R. M. Ferguson, S. Kemp, T. Wawrzik, M. Schilling, K. M. Krishnan, and F. Ludwig, "Drive-Field Frequency Dependent MPI Performance of Single-Core Magnetite Nanoparticle Tracers", *IEEE Transactions on Magnetics*, vol. 51, no. 2, pp. 1–4, Feb. 2015, ISSN: 0018-9464. DOI: 10.1109/TMAG.2014.2329772 (pages 71, 152–154).

[135] W. Haynes, "Magnetic susceptibility of the elements and inorganic compounds", *CRC Handbook of Chemistry and Physics,*, pp. 4–131, 1998 (pages 73–74).

[136] D. Lide, *CRC Handbook of Chemistry and Physics, 84th Edition*, ser. CRC HANDBOOK OF CHEMISTRY AND PHYSICS. Taylor & Francis, 2003, ISBN: 9780849304842 (page 74).

[137] F. Ludwig, T. Wawrzik, T. Yoshida, N. Gehrke, A. Briel, D. Eberbeck, and M. Schilling, "Optimization of Magnetic Nanoparticles for Magnetic Particle Imaging", *IEEE Transactions on Magnetics*, vol. 48, no. 11, pp. 3780–3783, Nov. 2012, ISSN: 0018-9464. DOI: 10.1109/TMAG.2012.2197601 (pages 74, 153).

[138] S. Draack, "Magnetic Particle Imaging System zur Demonstration von mobilityMPI", Master's thesis, Institut für Elektrische Messtechnik und Grundlagen der Elektrotechnik, Technische Universität Braunschweig, Jun. 2015 (page 77).

[139] T. Knopp and T. M. Buzug, *Magnetic Particle Imaging*. Springer-Verlag GmbH, May 30, 2012, ISBN: 3642041981 (page 77).

[140] P. Murgatroyd and D. Eastaugh, "Optimum shapes for multilayered toroidal inductors", English, *IEE Proceedings - Electric Power Applications*, vol. 147, 75–81(6), 1 Jan. 2000, ISSN: 1350-2352 (pages 85, 108).

[141] K. F. Man, K. S. Tang, and S. Kwong, "Genetic algorithms: concepts and applications [in engineering design]", *IEEE Transactions on Industrial Electronics*, vol. 43, no. 5, pp. 519–534, Oct. 1996, ISSN: 0278-0046. DOI: 10.1109/41.538609 (page 85).

[142] M. Erbe, T. F. Sattel, and T. M. Buzug, "Improved field free line magnetic particle imaging using saddle coils", *Biomedizinische Technik/Biomedical Engineering*, vol. 58, no. 6, Jan. 2013. DOI: 10.1515/bmt-2013-0030 (page 88).

[143] K. Wirgau, "Inductance calculation of an air-core disk winding", *IEEE Transactions on Power Apparatus and Systems*, vol. 95, no. 1, pp. 394–400, Jan. 1976. DOI: 10.1109/t-pas.1976.32117 (page 90).

[144] C.-W. Ho, A. Ruehli, and P. Brennan, "The modified nodal approach to network analysis", *IEEE Transactions on Circuits and Systems*, vol. 22, no. 6, pp. 504–509, Jun. 1975, ISSN: 0098-4094. DOI: 10.1109/TCS.1975.1084079 (page 96).

[145] L. W. Nagel, "SPICE2 : A Computer Program to Simulate Semiconductor Circuits", *Ph. D. dissertation, University of California at Berkeley*, 1975 (page 96).

[146] M. Engelhardt, "LTspice XVII", Linear Technology Corporation, Tech. Rep., 2017 (page 96).

[147] F. Taylor and A. Williams, *Electronic Filter Design Handbook*, Fourth Edition. New York: McGraw-Hill Education, 2006, ISBN: 978-0-071-47171-8 (pages 105–106).

[148] J. Stelzner, M. Graeser, and T. M. Buzug, "Design and Construction of a Toroidal Filter Coil for a Magnetic Particle Imaging Device", in *Deutsche Gesellschaft für Biomedizinische Technik, Jahrestagung*, vol. 59, Walter De Gruyter, 2014, pp. 679–682. DOI: 10.1515/bmt-2014-4280 (page 108).

[149] M. Schilling, F. Ludwig, C. Kuhlmann, and T. Wawrzik, "Magnetic particle imaging scanner with 10-kHz drive-field frequency", *Biomedizinische Technik/Biomedical Engineering*, vol. 58, p. 557, 2013, ISSN: 1862278 (page 111).

[150] C. Kuhlmann, T. Viereck, F. Ludwig, and M. Schilling, "Sensitivity and Dynamic Range Improvement in MPI by Means of a Differential Detection System", in *2015 5th International Workshop on Magnetic Particle Imaging (IWMPI 2015) Istanbul, Turkey, 26-28 March 2015*, ser. Conference Talk, 2015 (page 112).

[151] K. Lu, P. W. Goodwill, E. U. Saritas, B. Zheng, and S. M. Conolly, "Linearity and Shift Invariance for Quantitative Magnetic Particle Imaging", *IEEE Transactions on Medical Imaging*, vol. 32, no. 9, pp. 1565–1575, Sep. 2013, ISSN: 0278-0062. DOI: 10.1109/TMI.2013.2257177 (page 112).

[152] R. Raut and M. N. S. Swamy, *Modern Analog Filter Analysis and Design*. Wiley VCH Verlag GmbH, Oct. 11, 2010, ISBN: 3527407669 (page 117).

[153] *NI 6132/6133 Specifications*, 371231D-01, 371231D-01, National Instruments Corporation, Jul. 2006 (page 121).

[154] H. W. Kang, Y. S. Cho, and D. H. Youn, "On compensating nonlinear distortions of an OFDM system using an efficient adaptive predistorter", *IEEE Transactions on Communications*, vol. 47, no. 4, pp. 522–526, Apr. 1999, ISSN: 0090-6778. DOI: 10.1109/26.764925 (page 123).

[155] *7548/7794/7796 Operator's Manual*, 574.295.9495, AE Techron, Inc., 2507 Warren Street Elkhart, IN 46516 U.S.A., 2016 (page 125).

[156] *7548 SPECIFICATION SHEET*, 574.295.9495, AE Techron, Inc., 2507 Warren Street Elkhart, IN 46516 U.S.A., 2015 (page 125).

[157] *TMCM-310 Hardware Manual*, Version 1.25, Trinamic Motion Control GmbH & Co KG, Sternstraße 67 D-20357 Hamburg, Germany, Sep. 2009 (page 129).

[158] Rohde & Schwarz, *R&S®ZVL Vector Network Analyzer Specifications*, 10.00, Rohde & Schwarz, ROHDE & SCHWARZ GmbH & Co. KG Mühldorfstraße 15 81671 München Deutschland, 2017 (pages 131, 136).

[159] G. Heinzel, A. Rüdiger, and R. Schilling, "Spectrum and spectral density estimation by the Discrete Fourier transform (DFT), including a comprehensive list of window functions and some new at-top windows", 2002 (pages 134, 146).

[160] J. Franke, C. Bontus, B. Gleich, U. Heinen, F. Jaspard, T. Knopp, W. Ruhm, M. Heidenreich, and T. Buzug, "Drive-field decoupling and control network for magnetic particle imaging", in *Proc. Int. Workshop Magn. Particle Imag.*, 2014, p. 6 (page 142).

[161] T. Okada, R. Ishige, and S. Ando, "Analysis of Thermal Radiation Properties of Polyimide and Polymeric Materials Based on ATR-IR spectroscopy", *Journal of Photopolymer Science and Technology*, vol. 29, no. 2, pp. 251–254, 2016. DOI: 10.2494/photopolymer.29.251 (page 143).

[162] N. Gehrke, D. Heinke, D. Eberbeck, F. Ludwig, T. Wawrzik, C. Kuhlmann, and A. Briel, "Magnetic Characterization of Clustered Core Magnetic Nanoparticles for MPI", *IEEE Transactions on Magnetics*, vol. 51, no. 2, pp. 1–4, Feb. 2015, ISSN: 0018-9464. DOI: 10.1109/TMAG.2014.2358275 (page 152).

[163] I. N. Weinberg, P. Y. Stepanov, S. T. Fricke, R. Probst, M. Urdaneta, D. Warnow, H. Sanders, S. C. Glidden, A. McMillan, P. M. Starewicz, and J. P. Reilly, "Increasing the oscillation frequency of strong magnetic fields above 101 kHz significantly raises peripheral nerve excitation thresholds", *Medical Physics*, vol. 39, no. 5, pp. 2578–2583, 2012, ISSN: 2473-4209. DOI: 10.1118/1.3702775 (page 152).

[164] R. M. Ferguson, A. P. Khandhar, and K. M. Krishnan, "Tracer design for magnetic particle imaging (invited)", *Journal of Applied Physics*, vol. 111, no. 7, 07B318, 2012. DOI: 10.1063/1.3676053 (page 152).

[165] F. Ludwig, C. Kuhlmann, T. Wawrzik, J. Dieckhoff, A. Lak, A. P. Kandhar, R. M. Ferguson, S. J. Kemp, and K. M. Krishnan, "Dynamic Magnetic Properties of Optimized Magnetic Nanoparticles for Magnetic Particle Imaging", *IEEE Transactions on Magnetics*, vol. 50, no. 11, pp. 1–4, Nov. 2014, ISSN: 0018-9464. DOI: 10.1109/TMAG.2014.2329504 (page 152).

[166] N.-S. Cheng, "Formula for the Viscosity of a Glycerol-Water Mixture", *Industrial & Engineering Chemistry Research*, vol. 47, no. 9, pp. 3285–3288, May 2008. DOI: 10.1021/ie071349z (page 154).

[167] T. Wawrzik, C. Kuhlmann, H. Remmer, N. Gehrke, A. Briel, M. Schilling, and F. Ludwig, "Effect of Brownian relaxation in frequency-dependent magnetic particle spectroscopy measurements", in *2013 International Workshop on Magnetic Particle Imaging (IWMPI)*, Mar. 2013, pp. 1–1. DOI: 10.1109/IWMPI.2013.6528371 (page 156).

Publications and Contributions

[36] T. Wawrzik, C. Kuhlmann, F. Ludwig, and M. Schilling, *Scanner setup and reconstruction for three-dimensional magnetic particle imaging*, 2013. DOI: 10.1117/12.2006392 (page 17).

[45] ——, "Estimating particle mobility in MPI", in *2013 International Workshop on Magnetic Particle Imaging (IWMPI)*, Mar. 2013, pp. 1–1. DOI: 10.1109/IWMPI.2013.6528372 (page 25).

[48] T. Viereck, C. Kuhlmann, S. Draack, M. Schilling, and F. Ludwig, "Dual-frequency magnetic particle imaging of the Brownian particle contribution", *Journal of Magnetism and Magnetic Materials*, vol. 427, pp. 156–161, 2017, ISSN: 0304-8853. DOI: 10.1016/j.jmmm.2016.11.003 (pages 26, 161).

[74] C. Kuhlmann, S. Draack, T. Viereck, M. Schilling, and F. Ludwig, "Modeling the impedance of water-cooled core-less multi-layered solenoid coils for MPI drive field generation", *International Journal on Magnetic Particle Imaging*, vol. 4, no. 1, Apr. 2018, ISSN: 2365-9033. DOI: 10.18416/ijmpi.2018.1804001 (pages 36, 93–94, 99).

[110] C. Kuhlmann, T. Wawrzik, F. Ludwig, and M. Schilling, "A 3D MPI system for biological studies on mice", in *2013 International Workshop on Magnetic Particle Imaging (IWMPI)*, Mar. 2013, pp. 1–1. DOI: 10.1109/IWMPI.2013.6528373 (page 59).

[134] C. Kuhlmann, A. P. Khandhar, R. M. Ferguson, S. Kemp, T. Wawrzik, M. Schilling, K. M. Krishnan, and F. Ludwig, "Drive-Field Frequency Dependent MPI Performance of Single-Core Magnetite Nanoparticle Tracers", *IEEE Transactions on Magnetics*, vol. 51, no. 2, pp. 1–4, Feb. 2015, ISSN: 0018-9464. DOI: 10.1109/TMAG.2014.2329772 (pages 71, 152–154).

[149] M. Schilling, F. Ludwig, C. Kuhlmann, and T. Wawrzik, "Magnetic particle imaging scanner with 10-kHz drive-field frequency", *Biomedizinische Technik/Biomedical Engineering*, vol. 58, p. 557, 2013, ISSN: 1862278 (page 111).

[150] C. Kuhlmann, T. Viereck, F. Ludwig, and M. Schilling, "Sensitivity and Dynamic Range Improvement in MPI by Means of a Differential Detection System", in *2015 5th International Workshop on Magnetic Particle Imaging (IWMPI 2015) Istanbul, Turkey, 26-28 March 2015*, ser. Conference Talk, 2015 (page 112).

[162] N. Gehrke, D. Heinke, D. Eberbeck, F. Ludwig, T. Wawrzik, C. Kuhlmann, and A. Briel, "Magnetic Characterization of Clustered Core Magnetic Nanoparticles for MPI", *IEEE Transactions on Magnetics*, vol. 51, no. 2, pp. 1–4, Feb. 2015, ISSN: 0018-9464. DOI: 10.1109/TMAG.2014.2358275 (page 152).

[165] F. Ludwig, C. Kuhlmann, T. Wawrzik, J. Dieckhoff, A. Lak, A. P. Kandhar, R. M. Ferguson, S. J. Kemp, and K. M. Krishnan, "Dynamic Magnetic Properties of Optimized Magnetic Nanoparticles for Magnetic Particle Imaging", *IEEE Transactions on Magnetics*, vol. 50, no. 11, pp. 1–4, Nov. 2014, ISSN: 0018-9464. DOI: 10.1109/TMAG.2014.2329504 (page 152).

[167] T. Wawrzik, C. Kuhlmann, H. Remmer, N. Gehrke, A. Briel, M. Schilling, and F. Ludwig, "Effect of Brownian relaxation in frequency-dependent magnetic particle spectroscopy measurements", in *2013 International Workshop on Magnetic Particle Imaging (IWMPI)*, Mar. 2013, pp. 1–1. DOI: 10.1109/IWMPI.2013.6528371 (page 156).

Acknowledgements

I want to express my gratitude to *Prof. Meinhard Schilling* and *Dr. Thilo Viereck* for their continuous support, for introducing me to the fascinating topic of Magnetic Particle Imaging and for providing me with the opportunity to work in this field.

I also want to thank the PhD committee constituted by *Prof. Achim Enders* and *apl. Prof. Frank Ludwig* for evaluating my work.

This thesis would not have been possible without the continuous guidance by *Dr. Frank Ludwig*, who played a major part in many fruitful discussions and supported the project with his organizational talent and by securing external funding.

Sebastian Draack has made an essential contribution to the scanner construction during his master thesis and continues to support the project as a colleague with his excellent and exemplary work. I consider him a good friend and wish to thank him for his enthusiastic assistance along the way. I'm certain his broad knowledge and keen mind will continue to serve him well.

Special thanks are also in order to *Hilke Remmer*, who carefully prepared many of the nanoparticle samples used in this work and conducted accompanying measurements with other magnetic characterization methods.

I also want to thank *Dr. Thilo Viereck* for performing image reconstruction on the acquired data and his competent advice on how to interpret the imaging results.

Harald Schmidt, *Hartmut Müller* and *Jan Pförtner* from the institute's mechanical workshop did an outstanding job by building the scanner precisely to specifications, against all odds. Their constructive suggestions and vast experience were an essential prerequisite for getting the scanner design right first time.

Kerstin Franke deserves thanks for manufacturing many of our PCBs and keeping us all safe in the lab.

I also want to thank the people that collaborated with us, *Daniel Schmidt*, *Uwe Steinhoff*, *David Heinke*, *Joachim Landers*, *A. Khandhar*, *M. Ferguson*, *K. Krishnan*, as well as the MPI community (especially *I. Schmale*, *U. Heinen*, *J. Franke*, *P. Goodwill*, *B. Zheng*), for many stimulating conversations and their scientific contributions.

Additionally, I want to thank my fellow colleagues and lab mates for intriguing discussions as well as many unforgettable and joyful moments. In particular, I want to thank *Christof Wehrmann* for being a great office mate and a good friend. *Dr. Jan Scholtyssek* and *Dr. Jan Dieckhoff* deserve thanks for their cheerful character and their competent suggestions. I want to thank *Christoph Balceris* for providing an endless supply of astonishing scientific facts and for his preparation of dysprosium oxide samples. *Felix Nording* was of great value during many discussions about electronics and *Benedikt Hampel* and *Pieter Greeff* supported the project by managing the intitute's 3D printers. *Dr. Alexander Guillaume*, *Dr. Michael Martens* and *Sara Nazari Asl* were always welcome company and provided regular opportunities to broaden my mind with respect to other research activities.

This list would not be complete without thanking the administrative and technical staff at the Institute of Electrical Measurement and Fundamentals of Electrical Engineering at the TU Braunschweig, among who are *G. Weise* and *G. Kurbach*. *Ralf Behme* was of great help for all IT related matters, *Tanja Coenen* supported the print preparations of the manuscript and took some of the photographs.

Thanks to my bachelor and master students *Jiquing Fu*, *Fabian Fillmer*, *Sebastian Bögeholz*, *Sebastian Draack* and *Oliver Thiel*. They all contributed to my projects with their theses and helped me with their astute questions and fresh ideas.

I'd also like to thank *Anja*, *Markus* and *Marcus* for many dancing lessons which were a great experience and which helped me to clear my mind.

Special thanks to my friends, who were an immense source of inspiration and balance.

Finally, I want to thank the people to whom I dedicate this work:
My parents, who have supported me in every endeavor since my childhood,
my sister, who has always helped me sharpen my mind during funny discussions,
Dr. Krishnabhakdi and *Mr. Brinkmann-Boyagian*, who helped me in a difficult time that luckily had a positive outcome, and
Dr. Katharina Olze, who (among many other things) made the few hours not filled with work during the past years feel shorter – and much more precious.